2014

CFD Assessment of Respiratory Drug Delivery Efficiency in Adults and Improvements Using Controlled Condensational Growth

Ross L. Walenga
Virginia Commonwealth University

CFD ASSESSMENT OF RESPIRATORY DRUG DELIVERY EFFICIENCY IN ADULTS AND IMPROVEMENTS USING CONTROLLED CONDENSATIONAL GROWTH

A dissertation submitted in partial fulfillment of the requirements for the degree of Doctor of Philosophy at Virginia Commonwealth University.

by

ROSS LAWRENCE WALENGA
Bachelor of Science, Virginia Polytechnic Institute and State University, USA, 2000

Director: Dr. P. WORTH LONGEST
Professor, Department of Mechanical and Nuclear Engineering and
Department of Pharmaceutics

Virginia Commonwealth University
Richmond, Virginia
December, 2014

Acknowledgment

The completion of my doctorate has been a period of rapid personal and professional growth for me. At the beginning, I was able to execute a plan of action, but I had not yet developed my ability to see the big picture. Now, I find that I am able to use my natural inquisitiveness to guide my work and to confidently make meaningful decisions about the direction of my research. That does not discount the value of all the technical skill that I have developed during my time at VCU, which is significant too, but merely places it in perspective. Over the course of this process I have discovered that I love the creative and dynamic process of research with all of its unpredictability and meaningful discussion.

Many people have helped tremendously during this process, for all of whom I am deeply grateful. My loving wife Amanda has been there to celebrate my accomplishments and to provide emotional support during times of difficulty. I cannot truly measure the sacrifices that she has made to ensure the successful completion of this degree, but I do know that without her I would not be where I am now. I also want to acknowledge our two beautiful daughters Abigail and Miriam, who, along with Amanda, have given me more joy than they can ever know.

My advisor Dr. P. Worth Longest has made this degree possible with his generous and knowledgeable support. He told me from the start that there would be three phases of progression that I would pass through: a training phase, an application phase, and an innovation phase. I believe it is a great credit to him that I have been able to navigate these three stages and that I now have the confidence to engage in research on my own. I believe his greatest attribute

as an advisor has been the ability to balance thoughtful support while still providing space for me to operate individually. It has always been about more than just the successful completion of a given project, as he has always had my professional development in mind.

My colleagues Karl Bass, Katelyn Boone, Dr. Navvab Khajeh-Hosseini-Dalasm, Dale Farkas, Landon Holbrook, Dr. Alex Rygg, and Dr. Geng Tian have all been great partners to work with during these past few years. It was my pleasure to collaborate on a number of projects with them and to share our experiences as members of Dr. Longest's lab. Current and former members of the VCU Department of Pharmaceutics including Dr. Michael Hindle, Dr. Ravi Behara, Dr. Renishkumar Delvadia, Dr. Laleh Golshahi, Dr. Anubhav Kaviratna, and Xiangyin Wei have all provided immense help with the *in vitro* experiments that are so instrumental to our research. My Ph.D. committee members were Dr. Heise, Dr. Hindle, Dr. Mossi, and Dr. Tafreshi, and I am grateful for their thoughtful comments and guidance during this process

Finally, I want to acknowledge the grant funding that has made my dissertation research possible. An FDA U-award supported the characteristic tracheobronchial model and asthma constricted studies, while an NIH R01 grant supported the development of the mixer-heaters and the studies of nose-to-lung delivery in an NIV setting.

Table of Contents

List of Tables

List of Figures

Abstract

CFD ASSESSMENT OF RESPIRATORY DRUG DELIVERY EFFICIENCY IN ADULTS AND IMPROVEMENTS USING CONTROLLED CONDENSATIONAL GROWTH

By Ross Lawrence Walenga

A dissertation submitted in partial fulfillment of the requirements for the degree of Doctor of Philosophy at Virginia Commonwealth University.

Virginia Commonwealth University, 2014

Director: Dr. P. Worth Longest
Professor, Department of Mechanical and Nuclear Engineering and
Department of Pharmaceutics

Pharmaceutical aerosols provide a number of advantages for treating respiratory diseases that include targeting high doses directly to the lungs and reducing exposure of other organs to the medication, which improve effectiveness and minimize side effects. However, difficulties associated with aerosolized drug delivery to the lungs include drug losses in delivery devices and in the extrathoracic region of human upper airways. Intersubject variability of extrathoracic and thoracic drug deposition is a key issue as well and should be minimized. Improvements to respiratory drug delivery efficiency have been recently proposed by Dr. P. Worth Longest and Dr. Michael Hindle through the use controlled condensational growth methods, which include enhanced condensational growth (ECG) and excipient enhanced growth (EEG). These methods reduce inhaled drug loss through the introduction of an aerosol with an initial submicrometer aerodynamic diameter, which then experiences condensational growth to increase droplet size and enhance thoracic deposition. Tracheobronchial and nasal human airway computational

models were developed for this study to assess drug delivery using conventional and EEG methods. Computational versions of these models are used to assess drug delivery and variability with computational fluid dynamics (CFD) simulations, which are validated with experimental data where possible. Using CFD, steady state delivery of albuterol sulfate (AS) during high flow therapy (HFT) through a nasal cannula was characterized with four nasal models developed for this study, with results indicating an increase in average delivered dose from 24.0% with a conventional method to 82.2% with the EEG technique and an initially sized 0.9 μm aerosol, with a corresponding decrease in the coefficient of variation from 15% to 3%. Transient CFD simulations of nebulized AS administration through a mask during noninvasive positive pressure ventilation (NPPV) were performed and validated with experimental data, which resulted in 40.5% delivered dose with the EEG method as compared with 19.5% for a conventional method and a common inhalation profile. Using two newly created face-nose-mouth-throat models, dry powder delivery of ciprofloxacin during NPPV was assessed for the first time with steady state CFD predictions, which showed an increase in average delivered lung dose through a new mask design of 78.2% for the EEG method as compared with 36.2% for conventional delivery, while corresponding differences in delivered dose between the two models were reduced from 45.4% to 12.8% with EEG. In conclusion, results of this study demonstrate (i) the use of highly realistic *in silico* and *in vitro* models to predict the lung delivery of inhaled pharmaceutical aerosols, (ii) indicate that the EEG approach can reduce variability in nose-to-lung aerosol delivery through a nasal cannula by a factor of five, and (iii) introduce new high efficiency methods for administering aerosols during NPPV, which represents an area of current clinical need.

Chapter 1 Specific Aims

The goals of this dissertation are the improvement of adult respiratory drug delivery prediction accuracy and the development of more efficient methods of pharmaceutical drug delivery. A majority of the work accomplished in this dissertation utilized computational fluid dynamics (CFD) as a predictive and illustrative tool, and the simulations were validated with experimental *in vitro* data collected by members of the VCU Department of Pharmaceutics (Dr. Michael Hindle). Additionally, some experimental data was collected by the author for the development of new methods of aerosol size control and upper airway characterization. The numerical and experimental work in this manuscript was made possible by an active FDA U-Award and an NIH R01 grant. Expected results of this study include improvements in both anatomical upper airway model characterization and methods of delivery for nasally administered aerosols that target lung deposition. Deliverables of this dissertation include:

- a characteristic adult male tracheobronchial (TB) model that may be used to predict average deposition of aerosols
- a set of nasal airway models that may characterize aerosol deposition variability in adults
- improvements to an aerosol mixer-heater that may be used to produce submicrometer particles for excipient enhanced growth (EEG) delivery

- noninvasive positive pressure ventilation (NPPV) masks and delivery methods that optimize both nebulized and dry powder aerosol delivery

Objective 1: Airway and Mask Model Construction and Development

Current characteristic upper airway tracheobronchial models either omit realistic aspects for the sake of simplicity and general applicability (Isaacs *et al.*, 2006; Jin *et al.*, 2007; Kleinstreuer & Zhang, 2009; Russo *et al.*, 2008; Walters & Luke, 2011; Zhang & Finlay, 2005; Zhang *et al.*, 2005; Zhang *et al.*, 2009), or are highly realistic but do not account for intersubject variability and therefore have limited scope (Choi *et al.*, 2009; De Backer *et al.*, 2010a; Inthavong *et al.*, 2010a; Lambert *et al.*, 2011; Lin *et al.*, 2007, 2009; Ma & Lutchen, 2009; Montesantos *et al.*, 2010; Robinson *et al.*, 2009; Sauret *et al.*, 2002). One objective of this dissertation is to address this limitation through the construction of a patient specific model that matches certain average geometric characteristics and may be used for computational or *in vitro* analysis. Aerosol deposition in the nasal cavity is known to be highly variable (Cheng, 2003; Garcia *et al.*, 2009; Golshahi *et al.*, 2011; Storey-Bishoff *et al.*, 2008), but a new method of lung-targeted aerosol delivery, excipient enhanced growth (EEG), seeks to reduce depositional losses and concurrently reduce variability. Another goal of this study is to construct four nasal cavity models for CFD analysis that are capable of characterizing variability of aerosol deposition in standard cases and the expected reduction in variability using the EEG method for nose-to-lung delivery through a nasal cannula. Additionally, improvements in lung-targeted nasal aerosol delivery will be sought for this study through the optimization of currently existing noninvasive positive pressure ventilation (NPPV) masks for both dry powder and nebulized aerosol intake. The goals of Objective 1 will be accomplished with the following three tasks:

Task 1.1. Development of Model D: A realistic upper tracheobronchial (TB) geometry with a hexahedral mesh

Task 1.2. Development of nasal anatomies covering the range of surface area-to-volume ratio (SA/V) measurements for assessing aerosol delivery during noninvasive ventilation (NIV)

Task 1.3. Review existing NIV interfaces for aerosol delivery and develop a streamlined nasal or oronasal mask device that minimizes aerosol loss to adults receiving NPPV

To facilitate the creation of a characteristic adult male tracheobronchial model, a database will be compiled that consists of dimensional data from collected CT scans and published studies. An appropriate adult male CT scan will be selected from the database that is consistent with average geometric data for that population subset. The CT scan data will then be converted into a computer aided design (CAD) model and subsequently a hexahedral mesh will be constructed that fits the geometry. Similarly, a nasal dimensional database will be constructed from collected CT scans and published studies (Garcia, et al., 2009; Xi *et al.*, 2012; Yokley, 2006) to aid in the development of four nasal cavity models that characterize the range of variability with respect to assessed airway openness or constriction. Selection of the four nasal models will be based on SA/V, which is a measure of nasal cavity constriction. The selected sets of CT scan data will then be exported and CAD models will be constructed along with the accompanying CFD meshes. Regarding NPPV mask development, state-of-the-art nasal and oronasal masks for noninvasive ventilation (NIV) delivery will be identified, analyzed for performance limitations, and optimized to minimize system and expected upper airway depositional losses.

Objective 2: Application of CFD to Assess Conventional Respiratory Drug Delivery in Adults Using an MDI and a DPI

Metered dose inhalers (MDI) and dry powder inhalers (DPI) are two commonly used devices for pharmaceutical aerosolized drug delivery (Byron, 2004) that may be analyzed for delivery efficiency using either *in vivo*, *in vitro*, or computational (*in silico*) data. Computational fluid dynamics (CFD) is an *in silico* method that may be used to characterize the deposition in MDIs and DPIs, as well as the resulting deposition in any airway model with which the device may be paired. The accuracy of CFD characterization may be validated through comparison with either *in vitro* data from the same model, or if possible, with *in vivo* data. In addition to predicting MDI and DPI deposition in human airways, CFD is a useful tool for comparing different airway models under the same flow conditions and with the same injected particle profile. One goal of this study is to compare the aerosol deposition in the newly developed characteristic adult male TB model from Objective 1 (Model D) with a previously existing adult TB model that also may be considered characteristic (Model C). In addition to model comparison, the effect of asthmatic constriction on aerosol deposition in the upper and lower airways will be predicted with CFD, using a modified version of Model C for the upper airways and a stochastic individual pathway (SIP) modeling approach for the lower airways. These goals are accomplished with the two following tasks:

Task 2.1. CFD model validation and assessment of delivery to the upper TB airways based on Models C and D

Task 2.2. Effects of asthma constriction on delivery of MDI and DPI aerosols throughout the conducting airways using a SIP modeling approach

Predictions of MDI and DPI aerosol delivery in human airways will be obtained using CFD with both proposed characteristic TB models (Models C and D) and used to compare their performance. To ensure the viability of the data, a validation for CFD predictions of MDI and DPI aerosol delivery in Model C will be performed through a comparison with *in vitro* results collected by Longest et al. (2012d) for the same model. A flow field comparison is expected to yield a greater understanding of regional differences in the two models. Deposition analysis of both monodisperse and polydisperse boluses is projected to provide information regarding the applicability of each model to a given population segment. To examine the effect of constriction on upper airway aerosol deposition, an asthma-constricted version of Model C will be constructed with a 30% diameter reduction in the tracheobronchial region, based on the canine *in vivo* constricted airway measurements of Brown and Mitzner (2003). Deposition analysis of a polydisperse distribution will be performed to assess the difference between healthy and constricted versions of Model C through the third bifurcation, for both MDI and DPI delivery. Additionally, deposition in the lower airways of both healthy and asthmatic models from the fourth through the fifteenth generation of the lung airways will be compared using the SIP modeling approach, where deposition data in five individual lobar paths are averaged to provide branch-averaged deposition efficiency (DE) estimates.

Objective 3: Improved Aerosol Delivery during NIV

Patients with respiratory insufficiency are often supported using NIV, which uses a mask or nasal cannula to deliver oxygen rich gas in lieu of more invasive approaches such as endotracheal intubation (Dhand, 2012). One version of NIV is high flow therapy (HFT), also referred to as high flow nasal cannula (HFNC) delivery, where a heated and humidified gas flow

is continuously applied through a nasal cannula at flow rates that may be as high as 60 L/min (Dysart *et al.*, 2009; Parke *et al.*, 2011b). It is often desirable to deliver lung-targeted pharmaceutical aerosols to patients requiring NIV, but depositional losses in a humidified high flow system through the narrow nasal cavity are expected to be prohibitively high (Longest *et al.*, 2013c). The newly developed EEG method is capable of greatly reducing expected losses by introducing a submicrometer particle that contains an excipient along with the medication (Longest & Hindle, 2011). The combination particle then undergoes hygroscopic growth in the extrathoracic airways that allows for lung-targeted deposition (Longest & Hindle, 2011). An objective of this dissertation is to aid in the development of a mixer-heater device that is capable of producing the submicrometer particles required for EEG delivery. Additionally, previously developed models (as part of Objective 1) will be used to characterize the variability of nasal aerosol delivery in a control case and in the EEG case, where variability is expected to decrease. Another method of NIV is NPPV where differing levels of airstream pressure are provided during inhalation and exhalation to the patient by means of a nasal or oronasal mask (Masip, 2007; Mehta & Hill, 2001). Optimized mask development for both dry powder and nebulized aerosol delivery are goals of this dissertation, which include fabrication of new mask designs and nasal models along with CFD and *in vitro* testing. The CFD testing will also characterize variability of dry powder aerosol delivery. The goals of Objective 3 will be accomplished through the five following tasks:

Task 3.1. CFD testing, construction, and optimization of an aerosol drying and heating device for use with HFT and for ECG or direct nasal EEG delivery

Task 3.2. Evaluation of variability in nasal deposition for controlled condensational growth aerosol delivered during HFT

Task 3.3. Develop an efficient method for the delivery of *nebulized* aerosols to adults receiving NPPV with a mask

Task 3.4. Develop an efficient method for the delivery of *dry powder* aerosols to adults receiving NPPV with a mask

Task 3.5. Assessment of nasal deposition variability for aerosols delivered to adults receiving NPPV with a mask

A new mixer-heater for EEG delivery based on the design of Longest et al. (2013c) will be constructed and tested that will be capable of producing submicrometer particles in steady state flow with an outlet airstream temperature near human body temperature. After testing the steady state dryer, a transient dryer will be built with the aim of reducing expected losses during exhalation. Particle trajectories of the transient aerosol dryer will be illustrated using CFD and are expected to enhance the understanding of regional deposition. For the study which characterizes variability of nose-to-lung drug delivery through a nasal cannula, a new mesh will be developed using the previously existing nasal model of Golshahi et al. (2013) and will be used to validate CFD methods through comparison with *in vitro* data collected by Golshahi et al. (2013). Using the four developed nasal models from Objective 1, monodisperse aerosol deposition predictions will be produced using CFD with particles injected during control and EEG conditions, both at 30 L/min. Particle size change predictions at the exits of the nasal models will also be provided. Aerosol delivery through a NPPV system will be optimized through development of improved masks for both nebulized and dry powder aerosol

applications, as well as any other component of the different systems that may be altered to yield reduced depositional losses. The masks and any other components will be fabricated and then tested for deposition efficiency using both *in vitro* and *in silico* methods. Additionally, CFD will be used to assess variability of the dry powder aerosol delivery system.

Contributions

Elements of graduate student education reported in this work represent the phases of training in relevant areas of research, application of existing ideas, and innovation to solve significant problems. Areas of study include CFD simulation of multiphase flows, aerosol science, medical device development and design, and respiratory drug delivery. Projects completed in the training phase include the construction an *in vitro* version of an improved mixer-heater design, the design and development of a characteristic tracheobronchial model, and the assessment of the effect of asthmatic constriction on deposition efficiency throughout the lung. The application phase was based on implementing existing controlled condensational growth technology to improve delivered dose and reduce variability of lung targeted aerosols through a nasal cannula and new oronasal mask designs. Novel innovations produced in this work include new mask designs for nebulized and dry powder aerosol delivery during NPPV that utilize condensational growth techniques to maximize efficiency and reduce variability.

Chapter 2 Background

2.1 Objective 1: Airway and Mask Model Development

The development of realistic nasal, mouth-throat, and lung models is essential for the production of accurate correlations between *in vivo* data and data collected by *in vitro* or *in silico* means. An ideal model provides balance between simplicity and realism, such that the production of *in vitro* models is not hindered by unnecessary complexity and the computational time of *in silico* models is not excessive. However, it must capture enough realistic details to simulate the flow field characteristics most relevant to particle deposition, and it should be applicable to a large segment of the population, where such a model may be referred to as 'characteristic'. Currently available models are not typically 'characteristic', and the state of the art is provided here in this literature review. A number of studies have characterized nasal cavity variability, especially as it relates to aerosol deposition, through the use of various geometric parameters. Those studies are described in this chapter, including relevant information regarding the construction of those models. The accurate modeling of aerosol delivery devices is another important facet of deposition predictions. It is well known that much of the particle deposition in the upper airways occurs in the mouth and throat (or the nose, depending on the mode of delivery), and the amount of deposition is sensitive to the type and velocity of the aerosol-entrained flow field at the mouth or nose inlet. Existing noninvasive ventilation (NIV) delivery devices and their respective advantages and limitations are described.

2.1.1 Characteristic Upper Airway Models

Due to the large number of pharmaceutical aerosol delivery devices that target the tracheobronchial (TB) region of the upper airways, there is a need for accurate, easily reproducible models of this region. Upper airway models may be classified as either simplified, patient specific, or characteristic. Simplified models typically involve a number of assumptions that may include a constant branching angle or symmetric branch lengths and widths, for example. The result is a model that is more easily manufactured, meshed, and analyzed conceptually, though it sacrifices some accuracy by leaving out realistic features that may be relevant to pharmaceutical aerosol deposition. In contrast, patient specific models include as much morphometric information as possible, but may be more difficult to manufacture and mesh due to the added complexity of the models. Also problematic is the fact that results obtained from a patient specific model may be difficult to generalize to any given population due to the potential presence of individual abnormal airway features. Characteristic models include all realistic features that are relevant to the variables of interest, while introducing enough simplification to allow for better reproducibility, more effective meshing, and improved experimental visualization. The removal of extraneous information also allows for the creation of average, realistic models that may be considered representative of a certain population.

Mouth-throat (MT) characteristic models have been developed by both Stapleton et al. (2000) and Xi and Longest (2007) and studied extensively in the literature. The Alberta MT model (Stapleton, et al., 2000) was constructed using data from 10 CT scans and 5 observations of living models. The airspace was divided into sections represented by geometric forms, which improved manufacturability and allowed for the use a hexahedral mesh (Stapleton, et al., 2000). Several studies have used both *in vitro* and *in silico* versions of the Alberta MT model (DeHaan

& Finlay, 2001; Grgic *et al.*, 2004a; Grgic *et al.*, 2004b; Matida *et al.*, 2004; Wang *et al.*, 2006; Zhang *et al.*, 2004; Zhang *et al.*, 2007), and deposition predictions in the model have been matched with *in vivo* data by both Zhang et al. (2007) and Grgic et al. (2004a). Its ability to predict MT deposition has been validated through comparison with *in vivo* data (Grgic, et al., 2004b; Zhang, et al., 2007). Xi and Longest (2007) constructed a characteristic MT model through the use of both cast and CT data, and the application of dimensions reported by Cheng et al. (1997). The model was transformed through a series of simplifications and tested to identify key features that were required for accurately measuring particle deposition (Xi & Longest, 2007), which included a wedge-shaped glottic aperture. The simplified circular and elliptical cross-section MT models were shown to have good agreement with total deposition *in vitro* data from Cheng et al. (1997), though accurate prediction of local deposition required the most realistic model (Xi & Longest, 2007). Other cross-correlations of the Xi and Longest (2007) MT model with *in silico*, *in vitro*, and *in vivo* data have been performed and shown to match closely (Longest *et al.*, 2008b; Zhou *et al.*, 2011). Delvadia et al. (2012; 2013) used the MT model of Xi and Longest (2007) as a part of a set of three scaled models that were used to represent 95% of the adult population, and were shown to match well with the MT geometric variability study of Burnell et al. (2007). Additionally, the medium MT model from Delvadia et al. (2013) was used to correlate collected *in vitro* deposition data with previously published *in vivo* results for five commercial DPIs, where it was observed to correlate mean total lung deposition within 2% error for four of the five inhalers.

The existence of widely available pharmaceutical aerosols that target the TB region indicates a need for characteristic models of those airspaces. However, while many available TB models may be classified as simplified or patient-specific, none would appear to be characteristic

or representative of an average population. Several simplified TB models exist (Isaacs, et al., 2006; Jin, et al., 2007; Kleinstreuer & Zhang, 2009; Russo, et al., 2008; Walters & Luke, 2011; Zhang & Finlay, 2005; Zhang, et al., 2005; Zhang, et al., 2009), which most frequently employ symmetric bifurcations and straight tubes. Generally, these models may be effective at predicting total lung deposition, but lack the anatomical realism necessary to capture local effects. Patient specific models in the literature (Choi, et al., 2009; De Backer, et al., 2010a; Inthavong, et al., 2010a; Lambert, et al., 2011; Lin, et al., 2007, 2009; Ma & Lutchen, 2009; Montesantos, et al., 2010; Robinson, et al., 2009; Sauret, et al., 2002) are generally selected without any accompanying feature simplification that would imply a characteristic model. Some simplification of the model is present in Robinson et al. (2009), Montesantos et al. (2010), and Lin et al. (2009), but none of the changes result in models that are more easily meshed or manufactured. Additionally, though some studies compare model measurements to anatomical data (Inthavong, et al., 2010a; Robinson, et al., 2009), none select a model with the aim of producing an average model. Other studies consider cast data (Sauret, et al., 2002; Xi & Longest, 2008a), but do not perform any feature simplification.

A potential characteristic MT and upper TB model was constructed by using the elliptical MT model of Xi and Longest (2007) along with an upper TB geometry extending to the third bifurcation. The TB model was assembled using physically realistic bifurcations (Heistracher & Hofmann, 1995) and morphometric data from various sources (Hammersley & Olson, 1992; Horsfield *et al.*, 1971; Yeh & Schum, 1980), and it included cartilaginous rings, asymmetric branching, and out-of-plane rotations. One primary advantage of Model C is its ability to accept a hexahedral mesh, which has been shown to provide faster and more accurate predictions of aerosol dynamics and deposition (Longest & Vinchurkar, 2007a; Vinchurkar & Longest, 2008).

A free reproduction of the model is available at Respiratory Drug Delivery (RDD) online (http://www.rddonline.com). For the completion of Task 1.1, upper airway dimensions measured from a collected set of CT scans will be used to select a patient specific model representative of an average adult male (Model D), and compared with the previously existing Model C to assess the applicability of either as a characteristic model.

2.1.2 Nasal Cavity Models of Variable Constriction

Various parameters have been used to characterize the geometric variability in human nasal cavities. Minimum cross-sectional area (A_{min}) and a nondimensional shape factor have been used with both adult and infant *in vitro* methods to quantify differences in nasal deposition, where changes in A_{min} and shape factor have been associated with differences in deposition due to impaction and diffusion, respectively (Cheng, 2003; Storey-Bishoff, et al., 2008). Garcia et al. (2009) used measured pressure drop and nasal cavity length to collapse the data from five healthy adult *in vitro* models into a correlation that showed excellent agreement with experimental data. Golshahi et al. (2011) investigated the use of several different characteristic diameters for the purpose of collapsing the data from thirteen healthy child and five healthy adult *in vitro* models, and found that a parameter that included volume and length provided the best fit. Segal et al. (2008) used the surface area-to-volume ratio (SA/V), which is a measure of nasal constriction, to select four adult models for a study that described differences in nasal flow due to changes in SA/V. Others have also reported values of SA/V (Garcia, et al., 2009; Golshahi, et al., 2011; Storey-Bishoff, et al., 2008; Taylor *et al.*, 2010), which is deemed a suitable measure of geometric variability for this dissertation because of the relatively large amount of data available in the literature for the compilation of a database. Also, since deposition by impaction

is expected to dominate for the particle sizes considered, nasal cavity constriction (SA/V) should provide an accurate prediction of deposition.

Other factors may influence the flow and aerosol transport of nasal cavity airways in addition to the geometric variability of the nasal cavity itself. The airway following the nasopharynx, which includes the space between the hard palate and the uvula, can vary greatly depending on posture (Van Holsbeke *et al.*, 2013), which may affect the pressure drop across the nasal cavity at a given flow rate. Nostril hydraulic diameter is reported by Segal et al. (2008), but its effect on nasal flow has not been well characterized in the literature, as the nasal cavity dimensions are often reported without the inclusion of nostril dimensions. The termination point of the model is another variable to be considered, since not all models end after the nasopharynx, but may extend as far as the upper trachea, as is the case with the study performed by Golshahi et al. (2011). Additionally, care must be taken when comparing data from different sources as the nasal cavity region has several published definitions. Another factor that may influence variability is the resolution of the CT or MRI scan from which the *in vitro* or *in silico* model is created, which may range anywhere from 0.5 to 3 mm in axial thickness (Cheng, 2003; Segal, et al., 2008; Storey-Bishoff, et al., 2008; Taylor, et al., 2010). This may be particularly important for aerosol deposition predictions, as lower resolution models are expected to have a rougher surface. The CT scans selected for this study had a resolution of 1 mm or better to reduce any artificial roughness that may be induced by scan quality and its potential effect on deposition predictions. For this manuscript, the selection and construction of nasal models for the completion of Task 1.2 will be based on the variability of SA/V in the collected data set, but the effect of other variables on depositional variability measured by CFD predictions as part of Task 3.2 will be examined as well.

2.1.3 Existing NIV Interfaces for Aerosol Delivery

Noninvasive ventilation (NIV) describes a number of procedures used as alternatives to invasive measures, and has gained popularity over the last thirty years, particularly as treatment options for patients with obstructive sleep apnea (OSA) or chronic obstructive pulmonary disease (COPD) (Mehta & Hill, 2001). The first use of NIV dates back to the early part of the twentieth century, when negative pressure ventilation through the use of an iron lung was used, but during the 1960s invasive ventilation became increasingly popular and eventually replaced NIV (Mehta & Hill, 2001). However, NIV found its way back into regular use after Sullivan et al. (1981) proposed the continuous positive airway pressure (CPAP) mask for amelioration of sleep apnea symptoms. Though there has been some recent interest in negative pressure ventilation (DiMarco *et al.*, 2005), the most prominent forms of NIV are noninvasive positive pressure ventilation (NPPV), traditional nasal low flow therapy (LFT) with a nasal cannula, and more recently introduced nasal high flow therapy (HFT). Continuous positive airway pressure (CPAP) is also included by many as a form of NPPV, though it is not a true form of ventilation (Mehta & Hill, 2001; Nava & Hill, 2009). As opposed to the application of constant pressure that CPAP provides, bi-level NPPV applies an input that varies with the aim of matching pressure or volume limits during inspiration and expiration, denoted as inspiratory positive airway pressure (IPAP) and expiratory positive airway pressure (EPAP) for the case of pressure limiting operation (Masip, 2007; Mehta & Hill, 2001). For the sake of clarity, the rest of this manuscript will refer to CPAP separately from NPPV, and all mentions of NPPV will strictly reference bi-level NPPV. Additionally, while nasal HFT is also not strictly a form of ventilation, it has previously been included as a form of NPPV (Dhand, 2012) and is referred to as such in this manuscript.

Noninvasive positive pressure ventilation (NPPV) and nasal high flow therapy (HFT) are two frequently utilized forms of respiratory aide in cases of hypoxemia and acute respiratory failure (Aboussouan & Ricaurte, 2010; Lightowler *et al.*, 2003; Parke, McGuinness, and Eccleston, 2011b; Rea *et al.*, 2010). The primary indication for NPPV is for use with COPD patients, where it has been found through controlled trials to provide greater treatment success, reduced durations of hospital stays, a lower need for intubation, and lower mortality rates (Lightowler, et al., 2003). Additionally, hypercapnic patients have shown improved chances of avoiding intubation and decreased hospital stay durations through the use of NPPV (Celikel *et al.*, 1998). However, precaution must be used when selecting NPPV for use with patients showing general respiratory failure, as a series of trials with 221 patients not selected for pathology showed either no statistical improvement or even worse conditions through the application of NPPV as opposed to standard therapy (Esteban *et al.*, 2004). The implication of that finding is that while NPPV may aid certain patients it may hinder others who may require more intensive interventions. Indications for CPAP include its original use for treating patients with sleep apnea (McDaid *et al.*, 2009; Mehta & Hill, 2001), asthma (Shivaram *et al.*, 1987), and its well-documented success with treating pulmonary edema (Bersten *et al.*, 1991; Lin & Chiang, 1991; Lin *et al.*, 1995; Rasanen *et al.*, 1985; Vaisanen & Rasanen, 1987). There is even some indication that CPAP may provide some temporary benefits for COPD patients (Lopes *et al.*, 2011).

Several interfaces are available for NPPV, including mouthpieces, helmets, nasal pillows, and nasal, oronasal, and facial masks (Hess, 2007; Mehta & Hill, 2001). A recent survey of 272 European physicians showed that oronasal masks were the most frequently used device, followed by nasal masks, helmets, and mouthpieces (Crimi *et al.*, 2010). Due to the

greater frequency of use for masks and the stated goal of this manuscript of developing new masks, this background will only focus on those devices. Girault et al. (2009) performed trials with 90 chronic lung disease patients and found an 83% success rate of mask use with NPPV. As opposed to nasal masks, oronasal masks offer an improved seal between the face and the device, but are also associated with less tolerance and problems of asphyxiation should a power failure occur (Girault, et al., 2009; Mehta & Hill, 2001; Navalesi *et al.*, 2000), though one study did find better tolerance for oronasal masks used to treat general acute respiratory failure (Kwok *et al.*, 2003). Though some leakage is an accepted feature of NPPV masks (Mehta & Hill, 2001; Schettino *et al.*, 2001) because skin irritation may be caused by masks that are too tight-fitting (Nava *et al.*, 2009), too much leakage can cause problems of sleep disruption during nocturnal use, exposure, and asynchrony between patient breathing and device triggering (Bach *et al.*, 1995; Hui *et al.*, 2006; Miyoshi *et al.*, 2005). However, in spite of the increased leakage observed in nasal masks, they are still effective (Girault, et al., 2009; Nava, et al., 2009; Navalesi, et al., 2000) and due to their overall better tolerance they are preferred for milder cases of chronic acute respiratory failure (Nava, et al., 2009).

Nasal HFT employs a steady, heated, humidified stream of air or mixed oxygen at flow rates up to 60 L/min through a nasal cannula to improve respiratory function through several processes, including the removal of nasopharyngeal dead space which promotes enhanced oxygenation and improvement of compliance through the enhanced comfort of the warm and humid airstream (Dysart, et al., 2009; Parke, et al., 2011b). Previously, nasal cannulas were only used for LFT applications between 2-6 L/min (O'Driscoll *et al.*, 2008), but the use of heated and humidified airflow with HFT has allowed for higher flows and more oxygen delivery (Parke, et al., 2011b). Usage of HFT has been indicated for patients with acute respiratory failure (Roca *et*

al., 2010), bronchiectasis, and COPD (Rea, et al., 2010). Researchers have associated a number of positive outcomes with nasal HFT, including a reduction in the duration of respiratory distress, an improvement of patient reported comfort, increased blood oxygenation, reduced respiratory rate, and improved quality of life scores (Parke, et al., 2011b; Price *et al.*, 2008; Rea, et al., 2010; Roca, et al., 2010). Additionally, nasal HFT has been demonstrated to provide low levels of CPAP as long as the patient's mouth was closed, with pressures as high as 3.31 ± 1.05 cm H_2O (Parke *et al.*, 2011a).

Many patients that receive NPPV or nasal HFT may also benefit from the administration of pharmaceutical aerosols, typically bronchodilators, which are best delivered without interrupting respiratory support (Dhand, 2008, 2012; Hess, 2007). Added benefits of aerosol delivery with nasal HFT include the ability to administer drugs continuously or frequently through the nasal cannula (Longest, et al., 2013c). However, delivered dose of drug to the lungs is typically very low due to losses caused by high flow rates, a humidified airstream, device inefficiencies, difficulties in synchronizing aerosol release with inhalation, and nasal cavity filtration (Dhand, 2008, 2012; Hess, 2007). Since depositional losses are minimized in low flow applications, previous studies have focused on pediatric lung delivery, which utilizes flow rates <10 L/min (Longest, et al., 2013c). Ari et al. (2011) characterized pediatric delivery at 3 and 6 L/min using an Aeroneb Solo for aerosol generation and either oxygen or a helium-oxygen mixture (heliox) for ventilation, which is known to reduce turbulence and improve deposition efficiency (DE). The delivered dose from the Optiflow nasal cannula (Fisher & Paykel, Irvine, CA, USA) was similar for both ventilation gases at 3 L/min (~10%), while heliox yielded much better efficiency at 6 L/min as compared with oxygen, delivering about 6% as opposed to nearly 2%, respectively (Ari, et al., 2011). A vibrating mesh nebulizer (Aeroneb Solo, Aerogen/Nektar,

Mountain View, CA, USA) was used by Bhashyam et al. (2008) to evaluate the dose output through infant, pediatric, and adult sized nasal cannulas at 3 L/min. Using a heated, humidified airstream, the delivered dose through the various cannulas ranged from 18.6-26.9% when an inhalation flow was applied with a Harvard Lung connected to the outlets (Bhashyam, et al., 2008). In addition to the depositional losses reported by Bhashyam et al. (2008) and Ari et al. (2011), significant losses in the nasal cavity are expected before the dose may be delivered to the lung (Cheng, 2003; Garcia, et al., 2009; Longest *et al.*, 2011). However, the usage of NPPV and HFT with adults requires higher flow rates than with pediatric patients, and deposition data under these conditions are not available (Longest, et al., 2013c). Other forms of aerosol delivery with NPPV, namely those which typically employ a mask, have been characterized using *in vivo* data, and total delivery rates were found to be 1-7% for asthmatic adults during CPAP treatment (Parkes & Bersten, 1997). Further information on aerosol delivery through the nasal cavity and NPPV masks is available in Sections 2.3.2 through 2.3.5. Moreover, aerosol delivery through a nasal cannula or a mask during nasal HFT and NPPV, respectively, will be the primary focus of Tasks 3.1 through 3.5.

2.2 Objective 2: CFD Assessment of MDI and DPI Delivery

Ideally all measurements of aerosolized drug deposition would be accomplished *in vivo*, but due to the expense and lengthy duration of *in vivo* methods it is desirable to pursue other means (Meyer *et al.*, 2004). Predictions based on deposition in hollow airway models (*in vitro*) and computational fluid dynamics (CFD) simulations (*in silico*) are produced instead to provide correlations that may be used in place of *in vivo* data (Byron *et al.*, 2010). This objective is centered on the use of *in silico* methods to predict extrathoracic and lung deposition in realistic

mouth-throat and lung models. However, the *in silico* data is compared with and supplemented by *in vitro* data as a means of validating both methods.

The two most common methods of pharmaceutical aerosol drug delivery through the mouth are with a pressurized metered dose inhaler (MDI) and a dry powder inhaler (DPI). An MDI produces a sonic jet with the drug suspended or dissolved in an HFA propellant which is actuated by depressing the canister manually, while a DPI delivers drug in a dry powder form that is entrained in the inhaled airstream (Longest, et al., 2012d). In addition to the significantly different jets that the two inhalers produce, the instructions for inhalation differ as well, with in general the MDI and DPI requiring the patient to inhale "slowly and deeply" and "quickly and deeply", respectively (Longest, et al., 2012d). These two markedly different methods of oral aerosol delivery are investigated for this dissertation using two different models under consideration for the label 'characteristic', which include a previously existing model (Model C) (Xi & Longest, 2007) and one developed for this dissertation (Model D) (Walenga *et al.*, 2013). Additionally, the effects of asthma constriction are considered here in this study with Model C and a version of Model C with 30% diameter reduction in the tracheobronchial (TB) airways, using both an MDI and a DPI. An FDA U-Award provided the funding for the asthma constriction study, as well as the development of the *in vitro* version of Model C.

2.2.1 Characterization of MDI and DPI Aerosol Delivery in the TB Airways

The most commonly available pharmaceutical aerosol delivery devices are metered dose inhalers (MDIs) and dry powder inhalers (DPIs), which are also relatively inexpensive to produce (Byron, 2004). Several advantages and limitations are inherent in both delivery methods (Byron, 2004; Finlay, 2001; Newman & Busse, 2002; Newman, 2005). A consistent

dose is a notable feature of MDIs, however patient misuse is a common issue due to the difficulties associated with actuating the device at the proper point in the breathing cycle (Newman, 2005). DPIs solve this issue by only actuating when the patient inhales, but a consistent dose is often hard to deliver with those devices (Newman & Busse, 2002; Ross & Schultz, 1996), though some devices are more dependent on inhalation flow rate than others (Tarsin *et al.*, 2006). Lung deposition of MDIs and DPIs is frequently characterized through the use of radionuclide or pharmacokinetic methods, but both of these methods have significant limitations, including cost, safety concerns, and difficulty identifying regional deposition (Scheuch *et al.*, 2010). Though some characterization of MDI and DPI performance has been done at different flow rates by Ross and Schultz (1996), who used an *in vitro* method which quantified delivered dose and MMAD from the device, more data using both *in vitro* and *in silico* methods is needed that captures differences in regional and total lung deposition.

Performance comparisons between MDI and DPI devices have produced a variety of results using *in vivo* methods. Several pharmacokinetic studies have shown significantly greater drug absorption through the use of a DPI as opposed to an MDI that used a chlorofluorocarbon propellant (Bollert *et al.*, 1997; Bondesson *et al.*, 1998; Borgström *et al.*, 1996). However, another pharmacokinetic study performed by Hindle et al. (1995) indicated bioequivalence between DPI and MDI delivered medication. Environmental concerns have led to the development of hydrofluoroalkane (HFA) propelled MDIs, which has been shown via gamma scintigraphy methods to produce superior lung deposition results to those of DPIs, when used with a spacer (Hirst *et al.*, 2001). The variety of results indicates that more data is needed, and owing to the limitations of *in vivo* studies mentioned previously, *in vitro* and *in silico* data are desirable. Both of those methods lack the safety concerns that come with exposing patients to

radiation through radionuclide methods and both provide far greater regional deposition resolution than *in vivo* methods are capable of yielding (Longest, et al., 2012d).

Though *in silico* models are now capable of modeling aerosol effects due to inhaler type and polydisperse distributions, a majority of existing studies have only considered monodisperse boluses without the inclusion of inhaler effects (Longest & Holbrook, 2012). Deterministic, one-dimensional whole lung models are available that may accurately predict branch-averaged deposition and characterize certain flow effects, such as hygroscopicity (Asgharian *et al.*, 2001; Kim, 2009; Martonen *et al.*, 2000), though such models neglect inhaler spray and jet effects that are relevant to estimating MDI and DPI deposition. Several three-dimensional *in silico* studies have considered deposition in the extrathoracic and upper tracheobronchial (TB) airways (Lambert, et al., 2011; Longest & Xi, 2008; Ma & Lutchen, 2009; Zhang & Kleinstreuer, 2011), while others have considered lower TB airways (Kleinstreuer & Zhang, 2009; Zhang, et al., 2009). However, none of those studies considered polydisperse distributions and inhaler flow field conditions, which are important considerations for DPI and MDI performance characterization (Longest & Holbrook, 2012). Aerosol deposition from a DPI spray has been shown to vary considerably from ambient monodisperse distributions (DeHaan & Finlay, 2004; Longest, et al., 2008b). Spray momentum (Longest, et al., 2008b; Longest *et al.*, 2009), inlet jet effects (Matida *et al.*, 2003), and turbulence modeling (Ilie *et al.*, 2008; Longest & Hindle, 2009b) have all been shown to have significant effects on upper airway deposition. A correlation developed by DeHaan and Finlay (2004) which predicts mouth deposition of DPI aerosols based on inlet opening was validated by Finlay and Martin (2007), but no similar correlations for softmist inhalers and MDIs are known to exist. Considering both MDI and DPI delivery, the numerous, often contrasting effects of both forms of aerosol delivery may produce significantly

different predictions of regional and total deposition. For the completion of Task 2.1, both types of inhaler devices will be modeled with as much flow and aerosol transport accuracy as possible to provide a thorough comparison of the previously existing Model C and the newly constructed Model D for the evaluation of each as a characteristic model.

2.2.2 Effect of Asthma Constriction on Upper and Lower Airway Aerosol Deposition

Asthmatic airway constriction is difficult to quantify because it is known to be heterogeneous and patient specific (Inthavong *et al.*, 2010b; Martonen *et al.*, 2003; Yang *et al.*, 2006). From patient specific CT scan data, Inthavong et al. (2010b) observed the diameter increase from the asthmatic model (one day after hospital admission due to an attack, where spirometric testing indicated severe obstruction) to the recovered model (thirty days later) and found it to be, on a branch–averaged basis from the trachea through approximately the fourth bifurcation level, twice as much in the right side as the left side (10.4% vs. 4.8%). However, constriction was not the same throughout each side, with diameter increases as high as 30% (Inthavong, et al., 2010b). Using *in vivo* data, Brown and Mitzner (2003) noted a minimum of 30% diameter reduction in the constricted airways of canines, with complete closure present in some airways of several subjects at varying flow rates. Several CFD studies have constructed models with diameter constriction ranging from 20-50% (Farkas & Balashazy, 2007; Longest *et al.*, 2006; Martonen, et al., 2003). However, only Longest et al. (2006) used *in vivo* data (Brown & Mitzner, 2003) as a basis for the selection of diameter constriction, who used a 30% diameter reduction as a conservative estimate.

Several studies have used *in silico* methods to characterize aerosol deposition in the upper and lower airways of asthma constricted patients (Farkas & Balashazy, 2007; Inthavong, et

al., 2010b; Longest, et al., 2006; Martonen, et al., 2003; Vinchurkar *et al.*, 2012; Yang, et al., 2006; Zhang & Papadakis, 2010). Vinchurkar et al. (2012) constructed five patient specific models using CT scan data and used CFD with a large eddy turbulence model that was validated through comparison with *in vivo* data (De Backer *et al.*, 2010b) to characterize total lung deposition, which was estimated to be 30% on average. Inthavong et al. (2010b) used CT scan data to produce a patient specific model of a patient immediately following an asthma attack, and then another model was created 30 days following the attack to serve as a control case. At 30 L/min, a maximum absolute increase in DE through the entire six generation model of 13% for particles greater than 10 μm in the asthmatic model was observed, with a relative difference of about 50% (2010b). Other studies have used the dimensions of Weibel (1963) to create symmetric models at various regions of interest in the upper and lower TB airways for healthy and asthmatic subjects using varying degrees of diameter constriction for the diseased model (Farkas & Balashazy, 2007; Longest, et al., 2006; Yang, et al., 2006). Zhang and Papadakis (2010) also used Weibel (1963) dimensions to investigate a single bifurcation model, but the constriction was applied through the use of a sinusoidal indentation to better approximate morphology of an asthmatic airway. All of these *in silico* studies that compared healthy and asthmatic models have indicated a potential increase in tracheobronchial DE for asthmatic patients, due to the greater particle inertia caused by higher velocities in the constricted airways.

A symmetric human lung model that extends to the fifteenth bifurcation will have 32,768 outlets, and so a complete model to this level would be intractable for most CFD simulation applications. To provide an evaluation of aerosol deposition characteristics throughout the upper and lower lung airways, a method is required to estimate aerosol deposition characteristics deep into the lung without producing a full model. An individual path CFD model of the TB lower

airways has been proposed by Dr. P. Worth Longest and colleagues, entitled the stochastic individual path (SIP) model (Tian *et al.*, 2011a; Tian *et al.*, 2011b). The physically realistic bifurcation (PRB) units of Heistracher and Hofmann (1995) are adopted as the principal bifurcation unit (Tian, et al., 2011a). Using Model C as the upper airway model, the SIP models begin at the fourth bifurcation (B4), and for each successive bifurcation level a unit is randomly selected to be placed on the left or right side and oriented at 90° from the previous unit (Tian, et al., 2011a). However, deviation from the lobar region is not permitted and some combinations are disallowed (Tian, et al., 2011a). While it was shown that transient inhalation from a DPI produced significantly different upper airway deposition as opposed to a steady state approximation, it was found that a steady state condition was sufficient for the SIP model of the right lower (RL) lobe (Tian, et al., 2011b).

Hygroscopic size change of pharmaceutical aerosols considered for the newly proposed enhanced condensational growth (ECG) was evaluated using Model C (Tian, et al., 2011a). Aerosol deposition in the lower TB airways was estimated using Model C with the use of SIP models, where five lobar paths consisting of randomly oriented, regularly sized bifurcations are added to the model to approximate average deposition at each bifurcation level (Tian, et al., 2011a; Tian, et al., 2011b). The delivery of metered dose inhaler (MDI) and dry powder inhaler (DPI) delivery was predicted using Model C and a SIP approach with both an *in vitro* and an *in silico* model. Delvadia et al. (2013) found that the mean diameters of TB airways in Model C matched well with a collected sample of anatomical data. Additionally, an *in vitro* Model C was used to predict MT and total lung deposition, which presented a good match to published *in vivo* data from subjects of varied size (Delvadia, et al., 2012; Delvadia, et al., 2013). Considering drug delivery from a DPI and a softmist inhaler, Longest et al. (2012b) used the five SIP models

to produce the first known CFD predictions of deposition fraction (DF) in the small lower airways (B8-B15) of a healthy lung. The successful application of the SIP model approach in these studies provides confidence that it may be utilized for the completion of Task 2.2. Both non-constricted and constricted versions of Model C will be adapted for use with the SIP approach to compare upper and lower airway deposition predictions using CFD, including estimates of DF in the B8-B15 region for both healthy and asthmatic airways.

2.3 Objective 3: Improved Aerosol Delivery during NIV

With patients that require noninvasive ventilation (NIV) for respiratory augmentation it may be desirable to administer pharmaceutical aerosols for lung delivery through the NIV interface, so as to provide uninterrupted therapy and to allow for continuous aerosol delivery, which may be advantageous in some cases. However, a significant amount of drug loss in the nasal cavity is expected due to its well known function as a particle filtration system. It has been shown that the use of excipient enhanced growth (EEG) can greatly reduce the system losses by the introduction of a submicrometer particle that includes a hygroscopic excipient, which allows for continuous growth of the aerosol and deposition in the lungs (Hindle & Longest, 2012). An aerosol mixer-heater device is needed to reduce nebulized aerosol spray to a dried submicrometer solid particle for EEG delivery. A system that accomplishes this is built, tested, and optimized for this dissertation. The performance of a submicrometer aerosol containing an excipient is evaluated for delivery through a nasal cannula to four different adult nasal cavity models as a means of both predicting depositional losses in the nasal cavity and assessing intersubject variability. The means of nasal aerosol delivery is also addressed, with two new noninvasive positive pressure ventilation (NPPV) masks proposed for nebulized and dry powder

aerosols, respectively, that attempt to minimize aerosol losses in the system. Using these new mask designs, the depositional variability between masks and the repeatability of each mask is examined. Effects of mask design and EEG delivery on lung targeting is considered using a SIP approach, which allows for characterization of the lung through the fifteenth bifurcation (B15). The nasal aerosol delivery research completed for this dissertation is funded by an NIH R01 grant.

2.3.1 Submicrometer Particle Production for ECG and EEG delivery

Enhanced condensational growth (ECG) is a new aerosol delivery method (Hindle & Longest, 2010; Longest *et al.*, 2010) that has been shown to reduce depositional losses significantly for lung-targeted aerosols that are nasally delivered under HFT conditions (Longest, et al., 2011). Conceptually, ECG circumvents the high expected depositional losses in the extrathoracic airways by introducing a submicrometer particle through one side of the nasal cavity (Longest, et al., 2010). A separate, saturated or supersaturated heated airstream (39 °C) is delivered to the other side of the nasal cavity, which joins with the aerosol airstream in the nasopharynx, resulting in hygroscopic growth (Hindle & Longest, 2010). Particle growth is then expected to aid lung deposition and limit losses due to exhalation (Longest, et al., 2011). Depositional losses were reduced by a factor of five from ~75% in the control case to ~15% in the ECG case, with particles reaching a mass median aerodynamic diameter (MMAD) of ~2 μm at the exit of the extrathoracic airway (Longest, et al., 2011). Excipient enhanced growth (EEG) is another newly proposed technique that utilizes submicrometer particles to avoid high depositional losses in the extrathoracic airways (Longest & Hindle, 2011). As opposed to ECG, where particle growth is achieved through the use of a warm saturated airstream, a hygroscopic

excipient is combined with the aerosol to promote growth in the naturally humidified human upper airways (Longest & Hindle, 2011). Particle growth through the use of EEG has been shown to occur in acceptable ranges through an *in vitro* model (Longest & Hindle, 2012).

Previously, a radial mixer design has been implemented using *in vitro* and *in silico* methods to produce submicrometer aerosols suitable for ECG delivery during HFT therapy (Longest *et al.*, 2012a). A commercially available mesh nebulizer was used to create the initial droplets, and the system was heated via a wire or through a counter-flow design to induce evaporation and reduce droplet size (Longest, et al., 2012a). The wire heated design was found to heat the airstream to unsafe levels when the nebulizer ceased droplet production, while the counter-flow design produced a consistent, safely heated flow with submicrometer particles at rates between 5 and 30 L/min (Longest, et al., 2012a). However, a later study showed that device deposition was quite high (~30%) at a flow rate of 15 L/min, which indicates a potential area of improvement (Longest, et al., 2013c). Additionally, the device produces a continuous airstream (Longest, et al., 2012a), while it is has been shown that actuating an MDI during exhalation significantly reduces delivered dose (Diot *et al.*, 1995), so this represents another area of improvement.

An improved mixer-heater design was presented by Longest et al. (2013c), where CFD was used to optimize several features of the radial mixer-heater (Figure 5.1a) presented by Longest et al. (2012a). Characterizations of the previous design showed that the porous shell induced excessive turbulence and the radial cross section did not allow for a large enough surface area to produce the required heat transfer (Longest, et al., 2013c). The new design increased available surface area by implementing a channel based heat exchange region, which was vertically oriented downstream of the aerosol mixing region (Longest, et al., 2013c), as

shown in Figure 5.1b. Heat transfer was enhanced in the exchange region through the addition of aluminum conducting plates. An Aeroneb Lab nebulizer (Aerogen, Galway, Ireland) was used to generate the initial aerosol, which utilizes a vibrating mesh with micro-orifices (Longest, et al., 2012a). Longest et al. (2012a) reported that using a monodisperse aerosol assumption, the nebulizer produced an initial aerosol with an MMAD of 3.9 μm at a rate of 0.2 mL/min in an airflow of 15 L/min. The initial aerosol entered through a 2.4 cm diameter opening in the top of the design, which then combined with the heated inlet airstream in the mixing region, which was increased in volume to reduce depositional losses (Longest, et al., 2013c). As a consequence of the new setup, the inlet airstream was recirculated through the mixing region into the heat exchange region, which allowed for only one inlet airstream to be necessary (Longest, et al., 2013c). Dimensions of the inlet airstream side channels and inner heat exchange channel were 0.7 x 8 cm and 1.2 x 8 cm, respectively, and the outlet diameter was about 10 mm (Longest, et al., 2013c). The initial design also included vents (pictured in Figure 5.1b) near the mixing region which allowed for a higher inlet flow rate than that of the outlet, which was considered important for providing sufficient convective heat transfer at the conducting plates. The construction and optimization of the *in vitro* version of the improved mixer-heater design is accomplished for the completion of Task 3.1.

2.3.2 Depositional Loss and Variability during HFT Aerosol Delivery

Though it is desirable to deliver aerosols while administering various forms of NIV, including HFT, the high expected losses in the nasal cavity for lung targeted medicine is a significant obstacle. Pharmaceutical and environmental aerosol deposition in the nasal cavity has been characterized by a number of *in vivo* (Cheng, 2003; Stahlhofen *et al.*, 1989; Swift &

Strong, 1996), *in vitro* (Garcia, et al., 2009; Golshahi, et al., 2011; Guilmette *et al.*, 1994; Kelly *et al.*, 2004a, 2004b; Longest, et al., 2011; Storey-Bishoff, et al., 2008), and *in silico* (Inthavong *et al.*, 2011; Kimbell *et al.*, 2007; Liu *et al.*, 2007; Xi & Longest, 2008b; Xi *et al.*, 2011) studies. A primary outcome for most of these studies is an empirical relationship that may be used to predict nasal cavity deposition of pharmaceutical aerosols. Results can vary widely, particularly between *in vivo* and *in vitro* correlations. For example, Stahlhofen et al. (1989) compiled data from several *in vivo* studies and produced a correlation that may be used to predict 80% deposition for a 5 μm aerosol during inhalation at a rate of 30 L/min, while the *in vitro* relationship produced by Kelly et al. (2004b) estimated 40% under the same conditions. Several studies have collapsed predictions of nasal deposition onto a single curve that depend on patient specific characteristics such a pressure drop and nasal cavity dimensions, as well flow and aerosol specific parameters (Garcia, et al., 2009; Golshahi, et al., 2011; Storey-Bishoff, et al., 2008). Overall, the high expected nasal cavity losses represent an area of needed improvement for the further development of nasally delivered, lung targeted pharmaceutical aerosols.

Another obstacle to aerosol delivery during HFT is the high expected variability of delivered dose to the lungs. As outlined in Section 2.1.2, several studies have used various geometric parameters to characterize the variability of aerosol deposition in the nasal cavity (Cheng, 2003; Garcia, et al., 2009; Golshahi, et al., 2011; Storey-Bishoff, et al., 2008). Each of those studies used an impaction parameter as the independent variable (with deposition efficiency as the dependent variable), which is expressed as d_{ae}^2Q, where d_{ae} is aerodynamic diameter of the particle and Q is the flow rate. For example, a 3 μm particle at 30 L/min is reported to have a difference in minimum and maximum deposition efficiency as high as about 70% (Golshahi, et al., 2011), and as low as about 20% (Garcia, et al., 2009), but in either case

variability is significant. Borgström et al. (2006) found that variability in mouth-throat (MT) deposition was reduced as total deposition was reduced. If the same principle applies to the nasal cavity, then one of the enhanced growth techniques outlined in Section 2.3.1 (ECG or EEG) may reduce variability by reducing deposition with the injection of smaller particles. Regarding this dissertation, it is notable that all the previous studies considered placed the nasal cavity in an environmental chamber, which produces a situation similar to mask delivery or natural breathing, but would not necessarily capture the flow effects from a nasal cannula. An expected outcome for the completion of Task 3.2 is then the effect of ECG or EEG on aerosol deposition variability in the nasal cavity and the effect of nasal cannula delivered airflow on total deposition and depositional variability, using the four models completed for Task 1.2.

2.3.3 Nebulized Aerosol Delivery during NPPV

Though Sections 2.3.1 and 2.3.2 have focused on the optimization of HFT aerosol delivery, there are patients that require levels of CPAP or NPPV that HFT may not be able to provide, as it has been shown by Parke et al. (2011a) that even at 50 L/min nasal HFT only provides CPAP support at 3.31 ± 1.05 cm H_2O, and only while the patient's mouth is closed. A recent survey of 611 physicians representing 70 different countries showed that 99% used some sort of aerosol therapy during mechanical ventilation (including NIV), and that 87% used a nebulizer either exclusively or with an MDI (Ehrmann *et al.*, 2013). Further evidence of the efficacy of the combination of nebulized aerosol therapy and NPPV can be found through several *in vivo* studies, which have shown improvements in spirometric data from adult asthmatic patients receiving nebulized pharmaceutical aerosols with NPPV as opposed to those only receiving aerosol therapy (Brandão *et al.*, 2009; Galindo-Filho *et al.*, 2013; Pollack *et al.*, 1995).

However, França et al. (2006) found through an *in vivo* study of 13 healthy adults that nebulized therapy alone resulted in greater total lung deposition than when it was combined with NPPV, and it was postulated that the unfavorable contrast was explained by differences in patient morphometry between healthy and diseased patients. A recent study by Gupta et al. (2010) suggested that the combination of aerosol delivery and NPPV effects creates a complicated relationship between delivered dose and patient improvement. The results of the *in vivo* study with oronasal mask delivery of bronchodilators to 53 asthmatic patients showed that while ICU and hospital stay durations were decreased by the combination of aerosol therapy and NPPV as opposed to aerosol delivery alone, the spirometric data showed no significant differences and deposition efficiency actually decreased significantly, suggesting that the addition of NPPV reduced the needed amount of bronchodilators (Gupta, et al., 2010). Additionally, Parkes and Bersten (1997) evaluated the effect of aerosol delivery during CPAP with a combination *in vitro*/*in vivo* study that showed that the addition of CPAP while delivering nebulized bronchodilators reduced *in vitro* mask delivery from 6.9% to 1.3%, but the *in vivo* spirometric data from 10 asthmatic patients showed no significant difference, suggesting that aerosol therapy can be conducted without interrupting CPAP.

Several *in vivo* pediatric studies predicting nebulized delivery have been conducted, which are expected to provide significantly different data than those from adults due to smaller airways and contrasting breathing patterns of that demographic (Erzinger *et al.*, 2007; Fauroux *et al.*, 2000; Fok *et al.*, 1996; Wildhaber *et al.*, 1999). However, the only study conducted that included the effect of NPPV was performed by Fauroux et al. (2000), who observed that 18 children with cystic fibrosis showed increased total lung deposition when NPPV was used with a mouthpiece interface in combination with bronchodilator or corticosteroid delivery as opposed to

aerosol therapy alone (15 ± 8.3% vs. 11.5 ± 5.7%). Several *in vivo* studies of children who received aerosol therapy alone indicate trends in nebulized mask delivery that may be present when combined with NPPV. Wildhaber et al. (1999) showed through a study of 17 asthmatic children aged 2-9 years that delivery of nebulized salbutamol through a face mask without mechanical ventilation differed greatly among age sub-groups, with those aged less than 4 years receiving 5.4% delivered dose and those older than 4 years accepting 11.1%. The effect of face mask seal on nebulized aerosol delivery without mechanical ventilation was investigated by Erzinger et al. (2007) through the delivery of radiolabeled salbutamol to four children, and they found that the two children with a tight face seal (aided by the application of Vaseline) had average total lung deposition of 6.5%, while the screaming child with a tightly sealed mask received only 1.4% of the delivered dose, and the child with a poorly fitted mask only received 0.3% of the initial dose. Nebulized mask delivery without mechanical ventilation to infants has been found through several *in vivo* studies to be significantly less than for older children, with deposition efficiencies ranging from 0.3-2% when aerosol therapy alone was applied to infants with cystic fibrosis (Chua *et al.*, 1994; Mallol *et al.*, 1996) and from 1.5-2.4% for children with bronchiolitus or with general wheezing symptoms (Amirav *et al.*, 2002; Amirav *et al.*, 2003). The effect of nebulized therapy combined with invasive mechanical ventilation in infants was investigated by Fok et al. (1996), who reported delivery of 0.95 ± 0.23% of the nebulized salbutamol dose for 10 infants with bronchopulmonary dysplasia (BPD).

Though the efficacy of nebulized aerosol delivery with NPPV has been demonstrated for adults and children through several *in vivo* studies, delivery efficiency is still poorly characterized and expected to be low. Consequently, a better understanding of the factors that influence efficiency is needed for future development. As part of a review, Dhand (2012)

outlined several factors to consider regarding efficiency of nebulized aerosol delivery during NPPV, including particle size, interface type (nasal mask, oronasal mask, cannula, etc.), circuit-related factors, mode of ventilation, humidity, ventilator type, breathing parameters, and patient factors (e.g. patient pathology). Studies in the literature have largely focused on the effects of differing locations of the jet nebulizer with respect to the exhalation valve in the circuit and on the influence of various values of inspiratory positive airway pressure (IPAP) and expiratory positive airway pressure (EPAP). Chatmongkolchart et al. (2002) examined the effect of valve location, breathing parameters, and IPAP/EPAP settings, and observed a variation of 5% to 25% among *in vitro* mask delivered dose rates. The optimal case placed the jet nebulizer between the mask and the exhalation valve (as opposed to between the valve and the ventilator) and simulated 20 breaths per minutes with IPAP/EPAP settings of 20/5 cm H_2O (Chatmongkolchart, et al., 2002). The effect of valve placement on the mask rather than the circuit was characterized by Branconnier and Hess (2005), who found that placing the valve in the circuit produced approximately twice as much delivered dose through an *in vitro* experimental setup as opposed to mask placement. The effect of exhalation valve type was investigated by Dai et al. (2013), who varied the jet nebulizer position and IPAP/EPAP settings of an *in vitro* setup, and a complicated relationship between the nebulizer position and the valve type was found, while a higher IPAP was found to also positively influence delivered dose. Then, in contrast to Chatmongkolchart et al. (2002), it was found that placing the jet nebulizer between the valve and the ventilator was optimal, provided that a plateau exhalation valve was used, and so combined with IPAP/EPAP settings of 25/5 cm H_2O the mean delivery was 28.22 ± 1.59% (Dai, et al., 2013). The results of the study indicated that a complicated relationship between valve placement and type may exist (Dai, et al., 2013). The effect of a vibrating mesh nebulizer (as

opposed to a jet nebulizer) was included in a humidified *in vitro* pediatric NPPV circuit by White et al. (2013), who also included an approximated pediatric nasal lung model and varied the placement of the nebulizer. In spite of the presence of the humidifier, which is known to increase depositional loss of conventionally sized aerosols (Fink *et al.*, 1999), and the nasal lung model, White et al. (2013) found that placing the vibrating mesh nebulizer on the mask delivered about 10% of the initial dose.

Though mask design has not been investigated as it relates to nebulized aerosol delivery rates when therapy is used with NPPV, several studies have examined the effect of mask design when aerosol therapy is used alone. The *in vivo* short report published by Hayden et al. (2004) indicated that three different commercially available facemasks combined with an MDI and a spacer produced a range of 6-30% delivered dose in 24 wheezy children, showing that facemask design is an important variable for certain types of aerosol delivery. Sangwan et al. (2004) tested seven different oronasal masks with three different jet nebulizers in an *in vitro* pediatric model, and observed a range of deposition from 2.24-5.96% and that leakage was a significant source of depositional loss and facial and eye deposition (0.44-2.34% and 0.09-1.78%, respectively). Smaldone et al. (2005) modeled nebulized budesonide delivery through a pediatric *in vitro* model and found that facemask seal had a large effect, producing nearly twice as much delivered dose (as high at 19.3%) to the mask for the artificially sealed case as opposed to the naturally unsealed case. As noted above, Erzinger et al. (2007) observed a difference of 0.3-6.5% in delivered dose depending on face mask seal, who also mentioned that minimizing mask dead space may be a key factor to reducing drug loss. A key factor in minimizing mask leakage may be the difference in mask fit pressure on the face and airway pressure, which was found by Schettino et al. (2001) to minimize leak flow rate of a NPPV mask attached to a mannequin when the difference was

greater than 1.7 cm H_2O. The effect of mask design on nebulized aerosol therapy with NPPV will be investigated for the completion of Task 3.3, which will attempt to identify key design characteristics that may influence aerosol delivery, such as inhalation port location with respect to the face/nose and streamlining of the inlet. In order to accomplish this goal, the significant effect of mask seal will be omitted to isolate these contributions of mask design. However, mask sealing issues will be explored in the subsequent dry powder delivery study.

2.3.4 Dry Powder Aerosol Delivery during NPPV

Though most dry powder inhalers (DPI) typically rely on patient inspiratory effort to aerosolize the powder for delivery (Newman & Busse, 2002), there has been some development with DPIs that require an additional energy input (Everard *et al.*, 1996; Laube *et al.*, 2012; Pohlmann *et al.*, 2013; Tang *et al.*, 2011). Researchers have then classified DPIs as either 'passive' or 'active', where the former refers to those that rely entirely on patient effort while the latter employs some energy augmentation to enhance delivery (Crowder & Hickey, 2006; Newman & Busse, 2002). While passive DPIs help solve the problem of patient misuse that MDIs have by only actuating upon patient inhalation (Newman & Busse, 2002), active devices are useful for situations where the patient's effort may be limited, such as cases of mechanical ventilation (Tang, et al., 2011), lung targeted aerosol delivery during nasal HFT (Golshahi, et al., 2013), and pediatric delivery (Laube, et al., 2012; Pohlmann, et al., 2013).

Several studies have considered the use of active DPI devices (Everard, et al., 1996; Laube, et al., 2012; Pohlmann, et al., 2013; Tang, et al., 2011). The integration of an active DPI device with a mechanical ventilation circuit was considered by Everard et al. (1996), who investigated the delivery of budesonide with the commercially available Turbuhaler® through a

9 mm endotracheal tube (ETT) in series with a Servo 900C volume cycled ventilator and observed 20% mean delivered dose at the ETT exit. A manual ventilation bag was considered for airflow augmentation of a DPI (Osmohaler™) by Tang et al. (2011), which was placed in series with an invasive ventilation circuit and was capable of delivering mannitol powder at a flow rate of 111-116 L/min through endotracheal and tracheostomy tubes ranging in size from 7-9 mm internal diameter and 95-300 mm in length. It was observed that the active DPI device was capable of delivering 50-60% of the loaded dose with a fine particle fraction (FPF) of 20-31%, where FPF was defined as the fraction of all particles smaller than 5 μm (Tang, et al., 2011). Regarding pediatric aerosol delivery through a face mask in the absence of mechanical ventilation, Laube et al. (2012) used the *in vitro* Sophia anatomical infant nose-throat (SAINT) model of a 9 month old baby to demonstrate that a syringe may be used in combination with a Solovent™ DPI to aerosolize a radiolabeled dry powder to deliver 90% of the initial dose from the device. However, only 0.3-4% of the dry powder was collected on a filter positioned after the SAINT model due to significant losses in a spacer used prior to the mask (Laube, et al., 2012). Delivery of dry powder surfactant to preterm neonates was considered by Pohlmann et al. (2013), who reported a 55% mean delivery rate to the nasal prongs in a system that used a pressure pulse to actuate the device and deagglomerate the aerosol, which was heated and humidified prior to interface delivery to avoid the collection of aggregates in the lungs.

The previously described EEG delivery approach may provide an effective means of dry powder delivery for both passive and active devices. Recently, Son et al. (2013a) developed a new dry powder formulation for EEG delivery through a passive DPI (Aerolizer®) consisting of albuterol sulfate (AS) and mannitol (MN) as the drug and hygroscopic excipient, respectively. The inhaler was connected in series with the MT model from Model C to assess deposition of the

new formulation, which was observed to reduce losses in the MT model from 80% to less than 5% when compared with a commercially available formulation (Salbulin) loaded in the same device (Aerolizer®) (Son, et al., 2013a). Using this new formulation, Son et al. (2013b) implemented *in vitro* and *in silico* methods to evaluate its performance with regard to deposition and hygroscopic growth through five commercial passive inhalers and one with a modified mouthpiece, for a flow rate of 45 L/min and a pressure drop of 4 kPa. The modified mouthpiece contained a 3D rod array designed to deaggregate the aerosol particles, which when combined with the HandiHaler® produced FPFs for particles less than 1 μm and 5 μm of 38.8% and 97.3% from the device, respectively (Son, et al., 2013b). Depositional losses in the MT of an *in vitro* Model C placed in a humid chamber were only 2.6% and the MMAD at the system exit was 2.8 μm, which was considered to represent sufficient growth for maximal lung retention (Son, et al., 2013b). Using the 3D rod array design optimized for delivery of carrier-free dry powder formulations by Longest et al. (2013b), Behara et al. (2014a) developed a new passive DPI device with a redesigned capsule chamber which oriented the capsule perpendicular to the flow. When combined with a polytetrafluoroethylene (PTFE) surface coating, *in vitro* testing showed that the new inhaler provided an emitted dose greater than 80%, an MMAD of 1.3 μm, and an FPF for particles smaller than 5 μm that was greater than 90%, which compared favorably with existing commercial and modified designs (Behara, et al., 2014a). Furthermore, Behara et al. (2013) developed another new DPI capable high performance without PTFE coating, which, along with the other design of Behara et al. (2014a), were observed to reduce variability of FPF and MMAD when different inhalation profiles were applied, as compared to existing commercial inhalers.

Several active DPI systems were recently tested by Behara et al. (2014b), which were designed to be placed in-line with a nasal HFT circuit and received additional energy input from a ventilation bag. The new in-line DPI devices included 3D rod arrays as described above and a flow control orifice for which the diameter was varied to investigate the effect of flow rate on system performance (Behara, et al., 2014b). Different arrangements of the 3D rod array were also investigated to evaluate their effect as well (Behara, et al., 2014b). The nasal cannula implemented was previously designed for ECG delivery by Longest et al. (2013c), with a streamlined nasal prong on the anatomical right side for powder delivery and a prong on the left side for delivery of heated, humidified gas (Behara, et al., 2014b). Testing of the *in vitro* setup showed that a flow control orifice size of 2.3 mm produced a flow rate of 15 L/min, while a size of 3.1 mm yielded 30 L/min, which may be considered applicable to low and high flow delivery, respectively (Behara, et al., 2014b). Two optimal designs, one of each for a low and high flow application, provided emitted doses greater than 70%, FPFs for particles smaller than 5 μm up to 80%, and MMADs that were approximately 1.5 μm (Behara, et al., 2014b).

Mask delivery of an active DPI during NIV has yet to be explored in the literature. Though nasal HFT is known to provide low levels of CPAP under certain conditions (Parke, et al., 2011a), some patients may require stronger intervention in more severe cases or may need a true ventilator system. Dr. P. Worth Longest and colleagues have demonstrated effective delivery of active DPI through a nasal HFT system with an EEG approach (Behara, et al., 2014b), which is thought to be a promising method for mask delivery during NPPV and CPAP. Dry powder delivery during NPPV using the EEG technique will be explored for the completion of Task 3.4. A new mask will be developed which will characterize EEG delivery using the

active DPI system proposed by Behara et al. (2014b) to interface with a portable home ventilator for NPPV.

2.3.5 Variability of NPPV Aerosol Delivery

Deposition variability during NIV aerosol delivery can be assessed by considering several different factors, including repeatability, intersubject factors, mask design differences, face mask seal and other system specifics including nebulizer type and breathing pattern. Only two studies are known to have reported variability estimates from *in vitro* and *in vivo* studies for aerosol delivery combined with NPPV (Fauroux, et al., 2000; Parkes & Bersten, 1997). Repeatability of bronchodilator delivery during CPAP with a face mask (Vital Signs, Totowa, New Jersey, USA) was reported after four *in vitro* trials, with a mean delivered dose at the interface of 1.3% and a standard deviation (SD) of 0.37% (Parkes & Bersten, 1997). High intersubject variability of radiolabeled aerosol delivery through a mouthpiece to 18 children with cystic fibrosis during NPPV was observed by Fauroux et al. (2000), who noted a mean delivered lung dose of 15% with an SD of 8.3%.

Several others have considered variability of face mask aerosol delivery without NPPV (Erzinger, et al., 2007; Hayden, et al., 2004; Smaldone, et al., 2005). Smaldone et al. (2005) considered repeatability in a study designed to examine the effect of nebulizer type, breathing pattern, and facemask seal on delivered dose through an *in vitro* system without NPPV. Ten nebulizers of a specific brand were purchased and tested, but only five that were within 5% of the mean were selected for use in the study and three trials were performed on each nebulizer, where it was found for an ideal case that the average delivered dose was 24.3% with an SD of 3.1% (Smaldone, et al., 2005). Variability of MDI aerosol delivery due to mask design

differences was investigated by Hayden et al. (2004) through an *in vivo* study with 24 children who used a facemask and a spacer, and it was found that while two commercial masks yielded a delivered mask dose of about 30% another only yielded 6%. Additionally, Hayden et al. (2004) noted poor repeatability with each of the three commercial masks, with coefficient of variation (CV) values of 42-259%, though the high values of CV may be due to the difficulties associated with ensuring correct usage with pediatric patients. Significant variability due to face mask seal has been reported by the *in vivo* study of Erzinger et al. (2007), who noted that a loose mask may reduce deposition from 6.5% to 0.3% as compared to a normally fitted mask.

Owing to the fact that few studies have considered the variability of nebulized and dry powder aerosol delivery during the application of NPPV, significant gaps of knowledge currently exist. Several studies have indicated that variability in this situation may be substantial, particularly due to issues of face mask design or seal. Due to the influences of several factors, including face mask seal, intersubject variability, mask design differences, and repeatability, the characterization of the variability of aerosol delivery during NPPV is intertwined and complicated. This manuscript will attempt to address drug deposition variability for the completion of Task 3.5 with *in silico* analysis of dry powder delivery through two newly developed face-nose-mouth-throat (FNMT) models. The two FNMT models will have significantly different dimensions and the interplay of those features on the effect of mask seal will be explored.

Chapter 3 Characteristic Tracheobronchial Model

The primary objective of this study is to create a new tracheobronchial (TB) airway model that uses a patient-specific scan representing average adult male dimensions, striking a balance between simplification and anatomical realism. CFD is used to compare the flow and aerosol transport characteristics of a previously existing model and the new model under both metered dose inhaler (MDI) and dry powder inhaler (DPI) conditions. The data obtained is expected to examine each model's applicability as a characteristic tracheobronchial (TB) model and to compare lung delivery from the two most common inhalers.

3.1 Introduction

Computed tomography (CT) scans were collected from various sources to compile an adult database of upper tracheobronchial (TB) airway dimensions. From this database, a scan was selected that represented average adult male dimensions, which was then converted to a 3D surface file that was further reconstructed into a 3D computer aided design (CAD) model. This model was then joined with a previously existing mouth-throat (MT) model (Xi & Longest, 2007), using published average tracheal length as a guideline (Griscom & Wohl, 1986). The resulting upper airway geometry was connected to metered dose inhaler (MDI) and dry powder inhaler (DPI) interfaces and hexahedral meshes were applied. Additionally, a previously existing geometry (Model C), as defined by (Tian, et al., 2011b), was connected to the same MT model

and MDI and DPI interfaces following the same protocol. Comparisons of the two models showed that the new geometry (Model D) provided added anatomical realism through the inclusion of realistic curvature in the trachea and main bronchi and through the definition of anatomically correct main bronchi lengths.

To assess the applicability of Models C and D to the concept of a characteristic model, the models were compared using CFD to evaluate aerosol deposition and transport under both MDI and DPI conditions. Simulation methods were validated using the *in vitro* data of Model C for both MDI and DPI delivery produced by Longest et al. (2012d). Predictions of fluid and aerosol transport were produced to provide a basis for comparison between the two models. Flow field characterizations showed several phenomena present in Model D that were not captured by Model C, including a leftward bias of the laryngeal jet, a recirculation region in the trachea, and increased velocity in the left main bronchus. Comparisons of total upper airway deposition from a polydisperse distribution showed negligible differences between Model C and Model D, but flow field differences produced significant contrast in regional TB deposition fraction (DF) and deposition enhancement factor (DEF) predictions. Monodisperse aerosol predictions yielded good agreement in some upper airway regions with the *in vitro* data of Zhou and Cheng (2005) and indicated substantial regional differences between Model C and D, but more data is required to better characterize monodisperse predictions with the two models. Hexahedral and tetrahedral meshes were applied to both models and comparisons of regional DFs under MDI and DPI conditions showed that while a tetrahedral mesh may be adequate for some DPI applications, the MDI predictions were greatly improved through the use of a hexahedral mesh.

3.2 Methods

A model is developed using CT scan data chosen to be consistent with the measurements of an average adult male, and then it is compared with a previously existing anatomical geometry (Model C) which includes MT and TB regions. To facilitate comparison, both models terminate at the third bifurcation of the upper TB airways (denoted as B3, where B1 is the bifurcation from the trachea to the main bronchi). This allows for flow at each outlet to be proportional to the outlet diameter when a constant negative pressure is applied to an enclosed model. The TB airway dimensions of Model C, as outlined by Tian et al. (2011b) are based on the anatomical cast data of Yeh and Schum (1980), which are then scaled to a lung volume (3.5 L) representative of an average adult male while using an inhaler (ICRP, 1994). Heistracher and Hofmann (1995) published physiologically realistic bifurcation (PRB) parameters that were used to design the bifurcation units for Model C, though some modifications were necessary to facilitate smooth asymmetrical branching. The branch radii of curvatures and the carinal ridge features were adopted from the measurements of Hammersley and Olson (1992) and Horsfield et al. (1971). The branch gravity angles reported by Yeh and Schum (1980) were utilized to define bifurcation unit rotations. Since the TB airways terminated at the third bifurcation level each lobe had one bifurcation, with the exception of the right lower and right middle lobes. Using measurements from the *ex vivo* study of Russo et al. (2008) and other collected CT scans, a D-shaped tracheal cross section was formed and cartilaginous rings were added to the Model C trachea (Tian, et al., 2011b).

Model D was developed using a patient-specific CT scan that represented average adult male dimensions as defined by a collected data set of pre-existing scans. The high resolution scans were procured using an approved IRB protocol from VCU Medical Center, which were de-

identified before acquisition. Each scan included both lungs in their entirety and the TB airways up to below the larynx, and was acquired from a SIEMENS Sensation 16 scanner with an axial thickness of 1 mm or less. The new data set of scans consisted of eight subjects with five males and three females, ages ranging from 20 to 60 years, and body heights ranging from 170 to 180 cm. Average upper TB airway dimensions were assessed by considering this data set, available data from previous airway cast studies, and other publically available scan data. Based on critical dimensions of airway diameters, cross-sectional areas, and branch lengths, a single representative scan was selected from the data set that provided a reasonable approximation to average data for an adult male. Comparisons of the Model D dimensions are made with available data later in this section. The scan selected for Model D was from a 50 year old male with a body mass of approximately 82 kg and a height of approximately 178 cm. The development of an average female model or a set of models that includes small, medium, and large males and females is left for future study.

Existing patient-specific models have been constructed from surface models with an .stl file type that are produced by converting the set of 2D CT scan images through the use of commercial or custom software. One disadvantage of this process is that the .stl file type is only capable of accepting a tetrahedral mesh. For this study, the commercial software Mimics 14.0 (Materialise, Belgium) was used to extract a 3D surface file. Cross-sections were then defined using six to eight points, which were extracted to describe the geometry and imported into solid the modeling and mesh generation software package GAMBIT 2.4 (ANSYS, Inc., Canonsburg, PA, USA). These points then formed the basis of the surfaces and volumes that were used to generate the hexahedral mesh, which was formed using a cross-blocking pattern as outlined by Vinchurkar and Longest (2008).

Some smoothing of the airway surfaces was a byproduct of this process, though the original 3D surface file did not differ greatly from the reconstructed version. Data from Griscom and Wohl (1986) was used to determine the length of the trachea, since some intermediate reconstruction was necessary between the newly formed TB model and the MT model. The angle of the trachea with respect to the horizontal plane from the supine CT scan was used directly in the reconstructed model. The outlet branches were terminated at approximately 80% of the distance from the third to the fourth bifurcation. Both Model C and D were connected to standard MDI and DPI devices, as described later in this section.

A previously developed elliptical MT model (Xi & Longest, 2007) was joined to both of the TB geometries. Cast and scan data was used by Xi and Longest (2007) to create a realistic geometry, which was then simplified as much as possible without significantly altering deposition characteristics. It was found that an important feature was a noncircular glottic aperture, which was vital for accurate modeling of the laryngeal jet (Xi & Longest, 2007), which has been identified as important for the correct prediction of TB airway deposition (Xi *et al.*, 2008). The MT and TB regions of each model were joined using the tracheal length data from Griscom and Wohl (1986), with lengths from the glottic aperture to the main carina for Models C and D that were 137 mm and 131 mm, respectively. For Model C, there is a transition region below the glottis where the coronal angle is at approximately 22 deg, which then meets with the remainder of the trachea. This lower section of the trachea is vertical (coronal angle of zero), which is not anatomically correct for a typical standing position. The trachea of Model D is connected to the MT model in a more realistic way. As it is known that the trachea follows the upper thoracic region of the spinal column, the coronal angle of the trachea in Model D is set to match the upper thoracic angle of the spine in the selected CT scan. The coronal angle of the

upper thoracic spine (T1–T3) in the selected CT scan (30.6 deg) was found to be consistent with the measurements of Kuo et al. (2009), who recorded the mean upper thoracic angle for a standing male to be 30.1 deg. Moreover, the measured angle gives confidence that Model D may be used to approximate the upper airway geometry in a standing subject, which is most relevant to the evaluation of inhaler use in ambulatory patients.

The MDI and DPI devices selected for CFD analysis of Models C and D were Flovent HFA MDI and Flovent Diskus DPI (GlaxoSmithKline, Raleigh, NC, USA). The nominal dose from both inhalers is 250 μg of fluticasone propionate. The metered dose of the Flovent HFA MDI is 250 μg, while the emitted dose is 220 μg, indicating an estimated 12% deposited device loss from the suspension formulation. The nonhygroscopic active ingredient, micronized fluticasone propionate, is suspended without any additional excipients in HFA 134a and has a total metered mass of 75 mg per actuation. Micronized fluticasone propionate is blended with lactose in the Flovent DPI with a total mass of 12.5 mg.

The flow from each device was modeled by including geometric details of the MDI and DPI at the MT inlet of each model (Figure 3.1). Aerosolized powder and air entered through a 5 mm orifice in the DPI mouthpiece, while the MDI included a 0.5 mm spray nozzle which formed the aerosol, the actuator and the airflow around the canister, and the mouthpiece. More details on the smooth connection of both devices is available from Longest et al. (2012d).

The computational mesh for each model was created with GAMBIT 2.4, using primarily hexahedral cells, which are expected to produce more accurate results than a mesh consisting of tetrahedral elements (Longest & Vinchurkar, 2007a; Vinchurkar & Longest, 2008). The mesh density in each model was greater in the MT region than the TB region due to the presence of inlet jets from each inhaler that require a finer mesh to properly resolve. Additionally, a

structured hexahedral mesh with a butterfly blocking pattern was used in the MT region of the MDI models due to the presence of compressible supersonic flow (Vinchurkar & Longest, 2008). Elsewhere, an unstructured hexahedral mesh with a cross blocking pattern was deemed adequate for resolving the flow in the MT region of the DPI models and in the TB regions of all models. Due to the use of different blocking patterns in the MDI models and variable mesh densities in all models, the MT and TB regions were impossible to join using hexahedral blocks. For the DPI model, this issue was resolved by using an interpolation feature of the CFD software, with only a small discontinuity in velocity visible in the solution. However, the transient compressible MDI simulations showed a large discontinuity when using this feature, so a small region of tetrahedral cells was used to join the MT and TB regions, consisting of ~4% of the total number of elements.

Grid convergence was previously established for the MDI and DPI Model C geometries for meshes with 1.4×10^6 and 1.8×10^6 elements, respectively (Longest, et al., 2012d). Considering the similarities in the Model C and D geometries, approximately similar numbers of control volumes were implemented. In this study, the MDI mesh was adjusted to provide similar distances to the first near-wall control volume height consistent with the DPI mesh. The resulting MDI mesh consisted of approximately 1×10^6 cells. Reduction of the MDI grid resolution also allowed for the compressible, transient, multispecies solution to run in a more efficient manner with only a small increase in grid resolution error. For both DPI models, a mesh of $\sim 1.4 \times 10^6$ elements was used. The average distances and range of distances to the first near-wall control volume height are summarized in Table 3.1 for both models and inhalers.

The y^+ values of the meshes were considered to assess the applicability of the k-ω turbulence model. The nondimensional variable y^+ provides an estimate of which turbulence

zone (laminar sublayer, transition, fully turbulent) a near-wall node is within, and is calculated with the equation

$$y^+ = \frac{\sqrt{\frac{\tau_w}{\rho}}y}{\upsilon} \quad (3.1)$$

where τ_w is the shear stress at the wall, y is the distance from the node to the wall, ρ is the local density, and υ is the local kinematic viscosity. Since the y^+ values depend on shear, density, and kinematic viscosity, they are solution dependent and must be checked after running the simulations. Theoretically, ideal y^+ values for use with the k-ω model are greater than 30, or less than 5 (with the Low Reynolds number feature that has been utilized in this study), though y^+ values between 5 and 11.2 are considered accurate as well.

The simulations used for this study were checked for their y^+ values, and it was found that while most of the of the y^+ values (> 90%) in each simulation were within the acceptable ranges, there were a few localized areas of y^+ values between 11.2 and 17. Finer hexahedral meshes of the MDI and DPI versions of Model C, each consisting of $1.8x10^6$ cells, were used to compare depositional changes associated with y^+ values. Tetrahedral meshes were not considered as the near-wall heights of cells were virtually identical in those simulations, while Model D was not considered because the y^+ values for both models were similar with both the MDI and DPI. It was found that the change in total DF was small (< 7% relative difference for the MDI, <2% relative difference for the DPI), and that the finer mesh did not provide a consistent improvement in deposition predictions compared with the *in vitro* results. Therefore, it was determined that the original meshes (consisting of $1x10^6$ and $1.4x10^6$ cells, respectively) offered enough accuracy to provide a meaningful comparison of Model C and Model D.

Longest et al. (2012d) described typical inhalation boundary conditions for both an MDI and a DPI by considering common patient instructions ('slowly and deeply' or 'quickly and

deeply', respectively) and airflow resistance of each device. The mean flow rates for each transient profile were 37 and 75 L/min for the MDI and DPI, respectively. Aerosol deposition prediction methods under both MDI and DPI conditions were validated using the adapted versions of Model C (as shown in Figure 3.1a and Figure 3.1c) and the *in vitro* data and methods of Longest et al. (2012d). Regarding the MDI validation, steady state flow at 37 L/min was initially simulated and run to convergence, after which the actuation of the device was modeled with a 0.2 s transient jet that was then allowed to develop throughout the system for ~2 s after actuation ceased. Drug particles and HFA 134a vapor both entered the flowstream through the 0.5 mm nozzle during the transient portion of the simulation. For the DPI validation simulations, a square waveform with a maximum value of 75 L/min was implemented to approximate the *in vitro* conditions. However, in the experiments, a true square-wave cannot be achieved as there is some ramp-up time to the maximum velocity. In this study, the ramp-up time was assumed to be the first 0.05 s of flow. DPI particles were injected as a bolus into the transient square wave in the middle of the ramp-up time period. Other studies have suggested ramp-up times of 0.1 s and even higher (Martin *et al.*, 2007). However, sensitivity to the ramp-up time employed is not considered to be large.

An overview of simulation parameters for the validation and comparison cases is provided in Table 3.2. Deposition predictions of pharmaceutical aerosols in the upper TB airways are known to be sensitive to the choice of steady state or transient inhalation profiles (Tian, et al., 2011b). Though a transient profile is typically more accurate, steady state approximations are significantly more computational efficient, and may provide sufficient accuracy under the right circumstances. Since the focus of this study was the comparison of aerosol deposition and transport in Models C and D under different inhaler boundary conditions,

a steady state approximation was deemed to offer enough accuracy for the DPI comparison simulations. However, due to the highly transient nature of the MDI actuation required for those simulations, a steady state approximation was not considered feasible and so those comparison simulations were modeled as transient flow. For all transient simulations (MDI and DPI validation, MDI comparison), each case was run for long enough (~2 s) to allow for most (~99%) of the particles to escape.

Initial boundary conditions at the transient MDI spray nozzle were obtained by assuming isentropic flow. Flow rate at the nozzle exit was found by assuming sonic velocity, while temperature was yielded through the assumption that the formulation was at the HFA 134a boiling point for atmospheric pressure. The density of the mixture at the nozzle exit was estimated by applying conservation of mass. As mentioned above, the particles in the DPI were injected as a single burst for the polydisperse validation, which is released after 0.025 s (the middle of the ramp). Additional boundary condition information is available from Longest et al. (2012d) for both inhalers.

Regarding CFD simulations of upper TB airways, outlet conditions are typically specified using a mass-flow distribution or a constant pressure. The *in vitro* experiments of Longest et al. (2012d) were performed by placing the TB geometry in an environmental chamber and applying a constant negative pressure, as described in Delvadia et al. (2012). Both the MDI and DPI validations performed for this task utilize constant pressure outlet conditions in order to match the *in vitro* conditions applied by Longest et al. (2012d). However, for the simulations that compare Models C and D, a mass-flow distribution was applied at the outlets to better approximate *in vivo* conditions. Distribution of mass between the five lung lobes has been characterized using CT scan data (Yin *et al.*, 2010) and analytical models (Asgharian & Price,

2006). Based on the data from these two studies, the following mass distribution approximation was used for this task: left upper 15%, left lower 31%, right upper 14%, right middle 7%, and right lower 33%. This produced an asymmetrical split of 54% ventilation to the right side and 46% to the left. Symmetric outflow was assumed for branches extending beyond the lobar bronchi.

Measurements from a Next Generation Impactor (NGI) were taken by Longest et al. (2012d) and used to produce size distributions of the fully dried MDI aerosol and the initial DPI aerosol. The mass median aerodynamic diameter (MMAD) of the MDI aerosol at 30 L/min was 2.64 μm with an SD of 0.1, while the geometric standard deviation (GSD) was 1.51. DPI characterization is slightly more complicated, as 30% of the particles that exited the DPI were smaller particles (<10 μm) that had de-agglomerated from the lactose carrier, while the other 70% represented large particles that had failed to break apart during device actuation. Among the smaller particles, the MMAD of the DPI aerosol was 2.99 μm with an SD of 0.2 and a GSD of 2.09 at 75 L/min. The MMADs reported for both the MDI and DPI exclude the drug mass depositing in the preseparator, which is standard convention for reporting pharmaceutical aerosol size. However, the full polydisperse aerosol distribution including the preseparator component was included in the simulations.

For the polydisperse validation of the DPI, the particle distribution was adjusted to take into account the predicted drug mass that deposited in the NGI preseparator. Previous simulations have assumed that only large particles (>12 μm) deposit in the preseparator, leaving the smaller particles free to pass through. However, some fraction of smaller particles is also lost in the preseparator due to turbulence. To determine the fraction of smaller particles lost in the preseparator and correct the inlet particle distribution leaving the inhaler and entering the MT,

separate CFD simulations of the NGI preseparator were conducted. The particle injection at the inlet of the preseparator was modeled as an initial burst of 90,000 particles that was released and then tracked over 4 s of continuous flow at 75 L/min, consistent with the experiments. The correction factor used for adjusting the particle distribution was calculated as

$$CF = \frac{DF_{<12\mu m} + FR}{FR} \tag{3.2}$$

where FR is fraction remaining of particle mass at the outlet, and $DF_{<12\ \mu m}$ is the deposition fraction (DF) of particles smaller than 12 μm. This correction factor was then multiplied by the drug mass percentage of each particle size, and mass percentages were then normalized. The FR found for this case was 11.1% and the $DF_{<12\ \mu m}$ was 16.7%, so the distribution was altered significantly. The new distribution consisted of 51% particles greater than 10 μm and 49% smaller particles with an adjusted MMAD of 3.00 μm.

For the simulations considered, the discrete phase was modeled as one-way coupled since the energy, mass, and momentum of the flow field was not expected to be significantly affected by particle changes. Since Lagrangian particle tracking (which was used for this study) does not realistically allow for a complete characterization of all delivered particles, the distribution is estimated by splitting the polydisperse aerosol into several monodisperse bins. The bin sizes were divided according to the different NGI stage midpoint diameters. The MDI simulations used 8,000 particles for each bin, while the DPI cases used 10,000. Deposition estimates for each simulation were then produced by taking the number fraction of each size bin and factoring it with the mass distribution of each NGI stage that was obtained from experiments. The number of particles used for each bin was considered adequate since an increase by a factor of two did not produce any appreciable change.

The solution methods of the MDI and DPI simulations are significantly different due to the contrasting flow fields produced at the respective inlets. The MDI requires modeling of species transport (HFA 134a and air), temperature gradients, turbulence, compressibility effects and transient effects. In contrast, the DPI is approximated with isothermal, incompressible, turbulent, and steady state or transient flow (depending on whether or not it is a comparison or validation simulation, respectively). Species transport modeling is not necessary for the DPI since hygroscopic growth is not considered and therefore the flow may be described using only air as the gas phase. Details of the previous CFD simulations of MDIs and DPIs may be found in other papers published by our group (Longest *et al.*, 2007; Longest, et al., 2012d; Tian, et al., 2011a; Tian, et al., 2011b). However, the approach used in this current study is concisely summarized in the following paragraphs.

Since the low Reynolds number (LRN) k–ω turbulence model has been shown to produce good predictions of monodisperse aerosol deposition and transport in human upper airway models (Longest & Vinchurkar, 2007b; Xi, et al., 2008), it was selected for use with this task. In addition, polydisperse estimates of pharmaceutical aerosol deposition and transport have provided good predictions for softmist inhalers and MDIs (Longest, et al., 2007; Longest *et al.*, 2008a; Longest & Hindle, 2009a), as well as DPIs (Tian, et al., 2011b). Species concentration and temperature gradients of the MDI were modeled using interconnected relations that describe the mass and heat transfer of HFA 134a, which are reported in more detail by Longest and Xi (2008) and Longest et al. (2007).

Particle trajectories were modeled using a Lagrangian particle tracking method, which was applied through a mixture of custom in-house code and commercial routines (FLUENT 12.0.16, ANSYS, Inc., Canonsburg, PA, USA). Matida et al. (2004) has shown that the

assumption of isotropic turbulence may over-predict aerosol deposition. Since the LRN k–ω model uses this approximation, the user-defined functions (UDFs) were applied to describe anisotropic near-wall turbulence, as outlined by Longest et al. (2007). The custom routines also included near-wall fluid velocity interpolation and a Brownian motion correction (Longest & Xi, 2007).

Since fluticasone propionate is known to lack hygroscopic properties, the DPI aerosols were modeled without considering size change. However, MDI aerosols are composed of drug particles suspended in HFA 134a, which evaporates quickly under typical conditions (Stein & Myrdal, 2006). Particle size distributions at the MDI exit are very difficult to procure due to the rapid changes inherent in the process. However, Longest et al. (2012d) proposed a method for estimating aerosol deposition without including size change predictions, and validated the method through a comparison of *in vitro* and *in silico* results. Using the aerosol size distribution of dried particles obtained from the NGI, and assuming that the dry particles contain only fluticasone propionate, the final dried particle distribution was used for the CFD simulations to estimate trajectories without considering size change.

As an additional component of this study, the effect of mesh style on solution performance was also considered. Based on previous studies, hexahedral elements are expected to provide the most accurate solution for biofluid-type simulations (Longest & Vinchurkar, 2007a). However, hexahedral meshes cannot always be generated for complex bifurcating airway geometries. In this study, CFD solutions in Models C and D were also conducted using a similar tetrahedral mesh. The primary condition on the tetrahedral mesh size was an equal height of the first near-wall control volume compared with the hexahedral mesh. For the MDI and DPI geometries, the resulting tetrahedral meshes contained 3.3×10^6 and 4.0×10^6 cells, respectively.

As with the hexahedral meshes, a spatial grading was applied to the tetrahedral meshes such that smaller elements were used in the near-wall locations to better resolve regions of high velocity gradients. Tetrahedral cell counts were similar for Models C and D. These tetrahedral meshes were considered to be the largest computational meshes that could be evaluated in a practical amount of time on a current single computational workstation.

Deposition within regions of the respiratory tract can be reported as either a fraction or efficiency. The DF for the *i*th region based on drug mass is calculated as

$$DF_i = \frac{mass\ of\ drug\ depositing\ in\ region\ i}{mass\ of\ drug\ released\ in\ inhaler} \tag{3.3}$$

The corresponding deposition efficiency (DE) for region *i* is calculated as

$$DE_i = \frac{mass\ of\ drug\ depositing\ in\ region\ i}{mass\ of\ drug\ entering\ region\ i} \tag{3.4}$$

To determine a total deposition fraction, DF_i values in individual regions (e.g., MT and TB) can be directly summed. The use of deposition efficiency is an effective method to report the deposition characteristics of an individual section of the respiratory tract without the influence of upstream aerosol losses. In addition, the fraction remaining, FR_i, represents the fraction of aerosol remaining at the inlet of the *i* region (e.g., inlet to a lung lobe).

Localized deposition can be presented in terms of a deposition enhancement factor (DEF), which quantifies local deposition as a fraction of the total or regional deposition efficiency. A DEF, similar to the enhancement factor suggested by Balashazy et al. (1999), for local region *j* can be defined as

$$DEF_j = \frac{DF_j / A_j}{\sum_{j=1}^{N} DF_j / \sum_{j=1}^{N} A_j} \tag{3.5}$$

where the summation is performed over the region of interest, i.e., the upper airway model. In this study, the local area A_j is assumed to be a region with a diameter of 1600 μm and 2500 μm for DPI and MDI simulations, respectively, or approximately 160–250 lung epithelial cells in length.

The deposition of monodisperse particles ranging from 0.93–30 μm at an inhalation flow rate of 30 L/min was predicted for both Model C and Model D and compared with the empirical formulations of Zhou and Cheng (2005) based on *in vitro* experiments of polystyrene latex particles. In this study, the geometric regions of the upper TB airways are defined in Model C based on the PRB units and in Model D based on similar bifurcation definitions. Numerical predictions of DE from a monodisperse distribution were compared with the empirical results of Zhou and Cheng (2005). The general empirical formulation used by Zhou and Cheng (2005) is

$$DE = 1 - e^{-a*Stk^b} \tag{3.6}$$

where St_k is the Stokes number and a and b are empirical constants. Stokes number is defined in Zhou and Cheng (2005) as

$$St_k = d^2V/36\mu R_0 \tag{3.7}$$

where d is the particle aerodynamic diameter, V is the average velocity, μ is the dynamic viscosity, and R_0 is the average radius of the parent branch in the region of interest. The empirical constants differ according to the airway of interest; for the trachea, they are constants (a is 6.4 and b is 1.19), but for bifurcations B1–B3, the constant a is a function of branching angle and the daughter to parent branch radius ratio.

For the numerical simulations, an open mouth inlet (2 cm wide) was employed with a blunt particle inlet profile. Calculation of the monodisperse DE for each airway is found by dividing the number of depositing particles in each section by the number of entering particles.

3.3 Results

Model D provides several realistic features lacking in Model C, as a visual comparison of the two models demonstrates (Figure 3.1). The model dimensions of the trachea, left main bronchus (LMB), right main bronchus (RMB), and main bifurcation (B1) angle are provided in Table 3.3 for further comparison. Bronchial lengths are obtained from the intersection of centerlines at the first bifurcation to the intersection of centerlines at the respective second bifurcation (right or left). The curvature in both main bronchi, the shorter RMB, and the longer LMB are all anatomically correct features that are present in Model D that were absent in Model C. Additionally, the presence of the aorta produces significant curvature in the trachea of Model D which may also be observed in other patient-specific models (Lambert, et al., 2011). However, cartilaginous rings were not included as they were not fully resolved in the CT scan. Other notable differences in Model D include a larger tracheal diameter and smaller main bifurcation angle. Anatomical data of TB dimensions were collected and summarized (Table 3.4) from the scans used for this study, the Early Lung Cancer Action Program (ELCAP) Public Lung Database (www.via.cornell.edu/databases/lungdb.html), and other studies. The data is divided into three categories: sets collected from lung casts (Horsfield, et al., 1971; Phalen *et al.*, 1985; Raabe *et al.*, 1976), patient-specific CT scans, and simplified models (Soong *et al.*, 1979; Weibel, 1963). The patient-specific data consists of 21 sets in total, including the eight scans collected for this study, 11 scans from ELCAP, and two from other studies (Choi, et al., 2009; Lin, et al., 2007). The ELCAP scans were obtained from patient screening for early stages of lung cancer, from which 50 sets of data are published and publically available in the database. The scan resolution is 1.25 mm between slices, and nodule locations are provided along with the scan data. For this study, the data sets that were chosen from the ELCAP database did not have

any obvious morphological defects. Average diameter measurements were obtained from scans by first taking area measurements along several locations of the relevant airway, averaging those measurements, then finding the diameter based on an approximation of the area as a circle. Length measurements in the main bronchi were taken from the intersection of centerlines on the surface of the airway at the first bifurcation to the relevant second bifurcation intersection. Although the length measurements were desired from the interior of the airways, the software only allowed for surface measurements, which was deemed to provide an accurate estimate. Cast length and diameter measurements are larger than patient-specific measurements in all cases except for tracheal length, which is not surprising given that lung casts are known to expand due to the injection pressure of the cast material. Cast data in Table 3.4 was not scaled to a corrected lung volume, which is sometimes performed. Tracheal length is difficult to accurately compare between studies due to inconsistencies in the definition of the beginning and end points of the trachea. The main bifurcation angle is observed to have one of the largest standard deviations (SD). Of the 21 scans, five were from adult men and five were from adult women, while the other 11 scans were from the ELCAP database, which does not provide gender information. Additional information on patient characteristics was not available for the complete data set.

In comparison with the patient-specific measurements of Table 3.4, the Model D measurements (Table 3.3) are all within one standard deviation, except for tracheal length (for which patient specific data was not available due to the starting location of the scan). It is noted that the length of the LMB in Model D is reported from the interior intersection of centerlines in the first bifurcation to the second bifurcation, as this is considered the more anatomically correct measurement. However, the surface measurement of the LMB length is 59.9 mm, which is just outside of the SD tolerance. Considering the difficulty in obtaining a single scan that fits within

all parameters, the match between the Model D measurements and the patient-specific data is very good. The Model D data is also within the SD tolerances of the cast data, except for the tracheal length and the average LMB diameter. In contrast, Model C is well outside of the SD tolerances for the RMB and LMB lengths from the patient-specific measurements as well as the tracheal length. Overall, Model D is a better fit with the compiled anatomical TB data compared with Model C and appears to reasonably represent mean airway dimensions for an adult male.

Regarding CFD predictions of monodisperse particle deposition, the DE in the trachea, first, second, and third bifurcations for Models C and D are shown in Figure 3.2 and Figure 3.3, respectively. The airway regions of interest are clearly illustrated in Figure 3.2 and Figure 3.3 for both models. The Model C trachea and first bifurcation data provide a close fit to the Zhou and Cheng (2005) data, particularly for particles smaller than 10 μm (Figure 3.2). The DE for the second and third bifurcations shows a similar trend as the empirical data, though it is consistently under-predicted, which appears to be explained by the significantly wider airways (~40–50% increase in diameter) in Model C versus the patient specific cast model used by Zhou and Cheng (2005) (Figure 3.2). Comparing the boundaries illustrated in Figure 3.2 with the boundaries implemented by Zhou and Cheng (2005) also reveals some discrepancies, which are partially responsible for differences between the predictions and experimental results.

Considering Model D, DE in the trachea is over-predicted, which is most likely due to the curvature of the trachea around the aorta that is absent in the Zhou and Cheng (2005) model. The Zhou and Cheng (2005) model was based on a cast, which is known to expand and may have removed the tracheal curvature around the aorta. The differences in the first generation bifurcation DE may be explained by a different definition of what physically constitutes this bifurcation. For the Zhou and Cheng (2005) study, it begins at the point where the centerlines of

the daughter branches meet and extends until the airways bifurcate again. However, the first bifurcation for Model D, as defined for the comparison with the Zhou and Cheng (2005) model, begins at a higher location that is consistent with the PRB units employed in Model C so that the tracheal lengths of both the Zhou and Cheng (2005) model and Model D would be equivalent. In addition, the first bifurcation in the Zhou and Cheng (2005) model extends further than in Model D. The DE values for the second and third generations are remarkably similar, despite the relatively larger size of the Model D airways, and differences in the bifurcation definition region. In contrast with Model C, agreement between the Model D and Zhou and Cheng (2005) data in the second and third bifurcations implies that including irregular cross-sections and bronchi curvature in this region is important.

To summarize the monodisperse comparisons, large differences are observed between the results of Model C versus D and between the computational predictions and experimental results of Zhou and Cheng (2005) on a regional basis. It is noted that the Zhou and Cheng (2005) geometry is different from the airway model considered here and some differences in regional definitions exist. Higher deposition in the trachea of Model D highlights the importance of tracheal curvature, the laryngeal jet, and potential differences between the experimental and CFD model. Good agreement between Model D predictions and the experimental data in the second and third bifurcations indicates the importance of including realistic irregular bronchial cross-sections and curvature in this region. The additional geometric features included in Model D appear to have a significant impact on the regional deposition of monodisperse aerosols.

The regional DFs of polydisperse particles were predicted for Model C using CFD and compared with previous *in vitro* results for an MDI inhaler and a DPI inhaler in the exact same geometry. A full description of the experimental setup and methods are provided in previous

publications for both the MDI (Longest, et al., 2012d) and DPI (Tian, et al., 2011b). For the MDI, the total DF (experimental 50.3% versus CFD 48.7%) provided a good match, though some regional differences were found (Figure 3.4). The results for the MDI inhaler show a close match in the MT region (4% relative difference), while the mouthpiece (MP) and TB regions are not as close (42% relative difference in the MP region; 233% in the TB region) (Figure 3.4a). The differences in these regions may be explained by the omission of evaporation and two-way coupling effects in the model, both of which would greatly increase the computational time required. An evaporating aerosol would increase deposition in the inhaler and decrease deposition in the TB region. However, considering the focus of the study is to provide a comparison between Model C and Model D, the predictions were deemed adequately close to the experimental results. For comparison with previous *in vivo* results, MT deposition was not found in the literature for the Flovent HFA MDI. However, a similar MDI using HFA 134a as the propellant was reported to produce 29 ± 18% deposition in the MT *in vivo*, which is similar to the results shown in Figure 3.4a (Leach et al., 1998). It is noted that the aerosol considered in the *in vivo* study is known to have a smaller MMAD than the Flovent HFA MDI, which is likely responsible for the lower deposition.

For the case of the DPI aerosol, the CFD predictions do an excellent job of matching the *in vitro* experiments on a total and regional basis Figure 3.4b. Specifically, the relative differences between the experiments and model for total deposition, MT deposition, and upper TB deposition are 1%, 2%, and 14%, respectively. This good agreement is impressive considering the complexity of the system, which includes a polydisperse pharmaceutical aerosol, a high velocity turbulent jet into the MT, turbulent to laminar transition, multiple system outlets, and multiple aerosol deposition mechanisms. As with the MDI, *in vivo* deposition data for the

Diskus inhaler could not be found in the literature. However, approximately 70% MT deposition is consistent with most commercial DPIs (Delvadia, et al., 2012; Delvadia, et al., 2013; Islam & Cleary, 2012; Newman *et al.*, 2000).

Flow velocity fields for both Model C and Model D are shown in Figure 3.5 and Figure 3.6, for the MDI and DPI solutions, respectively. Sagittal velocity contours with midplane vector fields are displayed for all cases, along with selected axial cross-sectional contours and inplane streamlines. As described for model comparisons, the inlet flow condition for the MDI is steady state at 37 L/min with a transient 0.2 s spray producing a time-dependent solution. The MDI results shown in Figure 3.5 are for 0.1 s after spray actuation. For the DPI and model comparisons (Figure 3.6), the inlet flow is constant in time at 75 L/min producing a steady state solution. Contours, vector fields, and streamlines in the MDI (Figure 3.5) and DPI (Figure 3.6) cases are somewhat similar for both models, except for the increase in magnitude that comes from a higher flow rate (75 L/min) with the DPI as opposed to the MDI (37 L/min).

One major difference between the flow fields of both models is that the laryngeal jet of Model C is symmetric whereas the jet of Model D is skewed to the anatomical left side of the trachea. This phenomena is observed with Model D for both inhalers and is enhanced with the higher velocity field of the DPI (Figure 3.6b) compared with the MDI (Figure 3.5b). The occurrence of a skewed laryngeal jet was previously reported by Xi et al. (2008) using a cast-based CFD representation of the upper airways and was postulated to enhance gas mixing (reducing the effect of anatomical dead space) and enhance upper airway particle filtration. In the current study, this asymmetrical laryngeal jet is observed to create some flow recirculation in the upper part of the trachea. The skewed laryngeal jet travels along the left side of the trachea and along the curvature created by the aorta. As the flow separates on the downstream side of

the aortic curvature, the associated negative pressure helps to pull the flow into the left main bronchus. Although the average diameters of the bronchi in both Model C and Model D are similar, the velocity magnitude in the left bronchi of Model D is significantly larger than that of Model C, which again may be explained by the curvature caused by the presence of the aorta. It appears to direct the flow towards the left lung, whereas in Model C the flow strikes the carina almost directly. This shift in flow may create the vortices in the main bronchi of Model C that are absent in Model D. A combination of the skewed laryngeal jet, recirculating tracheal flow, and interaction of the laryngeal jet with the tracheal walls likely accounts for the significantly enhanced tracheal deposition of monodisperse aerosols for Model D compared with Model C observed in Figure 3.3 versus Figure 3.2.

Predictions of DF along with FR and mass median aerodynamic diameter (MMAD) exiting B3 and entering each of the five lung lobes for both models are displayed in Figure 3.7, including data for the MDI (Figure 3.7a and Figure 3.7b) and DPI (Figure 3.7c and Figure 3.7d) simulations. The lung lobes are denoted right upper (RU), right middle (RM), right lower (RL), left upper (LU) and left lower (LL) in the figure. Total DFs including both the MT and upper TB components are similar between Models C and D for both the MDI (48.7% versus 47.2%) and DPI (91.7% versus 89.9%). However, this similarity is largely due to the MT geometries being almost identical between Models C and D coupled with the fact that most of the deposition occurs in the MT. Small differences in MT deposition between Models C and D are due to differences in the connecting region between the glottic aperture and upper trachea. Larger differences in deposition between Models C and D are observed in the TB portion of the models. For both inhalers, TB deposition for Model D is higher than with Model C. Specifically, Model D produces a 160% relative increase in deposition with the MDI and a 533% relative increase for

the DPI compared with Model C. Reasons for this increased deposition include the skewed laryngeal jet, recirculation in the upper trachea, interaction of the jet with the curved tracheal walls, and increased velocity in the LMB. Fractions of aerosol remaining at the outlet of each lung lobe and exiting MMADs appear similar between Models C and D for both inhalers. One exception is the RM outlet, which has an FR in Model D that is two to three times larger than with Model C.

Differences in deposited drug mass between Model C and Model D are further highlighted in Figure 3.8, which presents DFs in the trachea, first, second, and third bifurcations. For both inhalers, higher deposition is consistently observed for Model D in the trachea and the second and third bifurcations. These differences in deposition are increased with the higher flow rate of the DPI aerosol. As with the monodisperse aerosol, it appears that the skewed laryngeal jet, tracheal curvature, branch curvature, and more realistic cross-sectional profiles contribute to increased deposition in these three TB regions. The only departure from this trend is the higher deposition noted for Model C in the first bifurcation with the MDI. The leftward shift in the velocity field in the first bifurcation due to the skewed laryngeal jet and the tracheal curvature is likely responsible for the reduction of deposition (60% relative difference) in B1 of Model D, as the flow is channeled away from directly striking the carina, as it does in Model C.

Highly localized deposition in the airways can affect the dissolution of drug molecules, uptake, and airway irritation. The DEF parameter captures highly localized deposition as a proportion of the total surface-area-averaged deposition. DEF values are compared for Models C and D with both inhalers in Figure 3.9. Maximum values of DEF are reported directly on the figure for the MT and upper TB regions. In general, DEF values are higher with Model D compared with Model C. One exception is the MT maximum of Model D with the DPI (Figure

3.9d). This local value of deposition may be lower than the Model C case due to differences in total surface area of the geometries as well as different deposition patterns in the MT arising from differences in the downstream pressure profiles in the glottic region. The maximum DEF value less than 1 in the TB region of Model C with the DPI (Figure 3.9c) is due to much higher DEF values in the MT region and evaluation of the entire MT and upper TB model together for calculating local deposition values.

Deposition characteristics in tetrahedral meshes of Model C and Model D are displayed in Figure 3.10, with the results from the hexahedral meshes (shown in Figure 3.7) under the same flow conditions for comparison. For both models with the MDI, the DF in the tetrahedral meshes is significantly under-predicted in the MP and the MT regions, but greatly over-predicted in the TB region as compared to the hexahedral results. Also shown with the MDI results of Model C (Figure 3.10) are the *in vitro* experimental results previously shown in Figure 3.4 of this study (originally from Longest et al. (2012d)). For Model C and the MDI, the tetrahedral DF predictions are 45% less in the MT region and 80% less in the MP region, while they are 680% greater in the TB region compared with the *in vitro* results. As a result, the predictions from the tetrahedral mesh are considered inadequate for the simulation of both models with the MDI. Also problematic is the increased computation time for the tetrahedral MDI simulations (Figure 3.11) of both models, due to the increased number of cells required by the tetrahedral mesh to maintain the same distance to the first near-wall control volume and the complexity of the MDI solution. Similarly for the DPI inhaler, simulations with a tetrahedral mesh under-predict MT deposition, over-predict TB deposition, and significantly increase solution time compared with the more accurate hexahedral approach (results not shown).

3.4 Discussion

A key feature of this study is the use of a CT scan to create a characteristic TB model that was verified through comparisons of the relevant dimensions of the model to average measurements reported in the literature and new measurements. The scan selected for use in the construction of the model, titled Model D, was shown to provide a good match to the average length and diameter measurements of the trachea and main bronchi obtained from an adult data set derived from 21 CT scans. As the scan selected for use was from an adult male, and because the measurements were within the range of average values, the model was considered to represent an average-sized adult male based on a limited data set. For Model C, it was shown that while the diameters of the main bronchi fell within the range of average values, the lengths of the main bronchi were somewhat different. Model D was designed to include realistic characteristics that Model C lacked, including curvature in the asymmetrical trachea that accounts for the presence of the aorta, an accurate tracheal gravity angle, curvature in the main bronchi, and irregular cross sections (as opposed to the circular cross-sections of the connecting branches from Model C).

Comparisons between monodisperse Model C and D results with the Zhou and Cheng (2005) data provided very good agreement in some regions. However, observed differences in other areas are likely due to differences between the computational and experimental geometries as well as differences in regional definitions. Comparisons with the Zhou and Cheng (2005) data set for a single geometry are not intended to validate the selection of a characteristic model or the CFD predictions. Instead, these comparisons highlight variability associated with different geometries in predicting regional deposition as well as the effects of different regional

definitions. A consistent method of defining and reporting deposition results within the upper TB airways appears to be needed.

CFD predictions of polydisperse deposition in Model C for both the MDI and DPI were first used to validate the model with existing *in vitro* data, and found to provide a good match using experimentally similar flow conditions, which provided confidence that the CFD methods produced a realistic approximation of the multiple deposition mechanisms for the polydisperse aerosol. Comparisons of Model C and D deposition results indicated that total deposition was similar, mainly due to the use of identical MT geometries. In contrast, both regional and highly localized deposition was consistently higher in the TB portion of Model D, except for the first bifurcation where a reduction was noted. The comparisons showed a leftward shift in particle deposition from Model C to Model D, apparently due to the inclusion of geometric features that produced a realistic skewed inlet laryngeal jet. This leftward shift in the TB deposition pattern was also reflected in the DEF values. These results suggest that both models may be considered characteristic for cases where only total DF is considered, but in cases where more specific information is required, Model D is preferable due to its inclusion of realistic features that are absent in Model C.

It appears that most of the realistic features included in Model D had an effect on the TB deposition. Both the asymmetric trachea and accurate tracheal angle related to gravity contributed to the laryngeal jet shifting sharply to the anatomical left side of the airway. This finding is similar to the CFD TB model of Xi et al. (2008), who demonstrated instability in the laryngeal jet and a tendency to shift away from the tracheal center. In the current study, a combination of the laryngeal jet, recirculation in the trachea, and interaction of the tracheal flow with wall curvature caused by the aorta increased tracheal deposition compared with Model C.

As a result, Model D tracheal deposition was much larger than observed with Model C for both inhalers, even in the absence of tracheal rings. The skewed tracheal flow, curvature of the bronchi, and irregular cross-sections of the connecting branches all influenced and increased deposition in Model D. This increase was observed for both monodisperse particles and polydisperse realistic pharmaceutical aerosols from inhalers. As a result of these observations, all of the new features included in Model D are considered necessary in a characteristic upper TB model for evaluating pharmaceutical aerosol delivery.

The leftward skew of deposition observed in Model D was also noted by Lambert et al. (2011), who predicted polydisperse deposition at 20 L/min in a patient-specific geometry that extended to the seventh bifurcation and included tracheal curvature due to the presence of the aorta, an LMB that is significantly longer than the RMB, and pronounced curvature in the LMB. The left-to-right ratio of deposition was 1.01–1.60, depending on the particle size (2.5–30 μm), which was greater for larger particles. This leftward shift was observed in spite of greater ventilation to the right side (50.6% of the airflow went to the right). Although the ratio discussed in this study includes the sum of all particle size contributions, and in Lambert et al. (2011) the data is presented on an individual particle size basis, both studies show a bias in deposition toward the anatomical left hand side. Moreover, this trend is noted in both studies in spite of greater ventilation to the right (54% to the right for this study). Although both Xi et al. (2008) and this study observed a skewed laryngeal jet, Xi et al. (2008) noted a laryngeal jet that was shifted to the right, as opposed to the leftward shift observed in Model D. The tracheal curvature of Model D causes the left side of the trachea to be closer to the center line of the glottis, which may induce the Coandă effect, a phenomenon whereby an unsteady jet is known to attach to the closest surface. The cast-based model of Xi et al. (2008) lacks the tracheal curvature due to the

presence of the aorta that is present in Model D, which results in a trachea that is closer to symmetric. In addition to the effect that tracheal curvature may have on the direction of the laryngeal jet, the greater right lung ventilation of Xi et al. (2008) as compared to this study (60% versus 54%) may have contributed to the rightward bias in that model.

The type of mesh style selected is important for evaluating aerosols within the characteristic models. Previous studies demonstrated that hexahedral results are superior to tetrahedral solutions due to improved grid convergence, reduced numerical error, and faster solution times. However, a vast majority of studies on transport and deposition in the airways employ a tetrahedral mesh solution. The original motivation behind the Model C geometry was a mathematically reproducible model that could support a highly accurate hexahedral mesh, at the expense of some geometric realism. The current study illustrates the development of a hexahedral mesh starting with the inhaler and continuing through the third respiratory bifurcation. Comparisons of the hexahedral and tetrahedral solutions (with approximately three times more control volumes) demonstrated large differences in deposition predictions. As a result, both realistic geometric models and high quality hexahedral mesh solutions appear to be important for generating the best CFD predictions. Conversely, a highly realistic geometry that requires a tetrahedral mesh and does not sufficiently resolve the flow field may not improve the realism of the solution compared with *in vitro* and *in vivo* conditions.

One potential limitation of the current study is the simulation of constant flow rate inhalation compared with a more realistic transient inhalation profile. Previous studies with a DPI and the Model C geometry demonstrated that transient inhalation increased deposition in the MT and upper TB regions whereas deposition in the TB region beyond approximately B3 was unchanged compared with steady state conditions (Tian, et al., 2011b). The study of Longest et

al. (2012d) demonstrated that correct versus incorrect transient inhalation profiles with inhalers had little effect on MT deposition for both the MDI and DPI, but had a significant impact on deposition in the upper TB region. Regarding the findings of this study, transient inhalation will influence the overall deposition in the TB region. However, the relative differences observed between Model C and D arising from geometry changes are expected to remain the same with transient inhalation. Considering the skewed laryngeal jet, Xi et al. (2008) documented a symmetric jet entering the trachea through approximately 10% of the inhalation time cycle, which then quickly attached to the tracheal side wall and remained skewed for the remainder of the inhalation breath cycle. As a result, the laryngeal jet pattern observed in this study is not expected to largely change with transient inhalation.

In addition to steady state inhalation, limitations of the study include the exclusion of cartilaginous rings, the size of the CT scan data set, and the lack of models from other gender and age demographics. Additionally, the definition of age demographics may require further refinement, as the current data set includes subjects between 20 and 60 years of age, where a tighter range may be more appropriate to isolate the effects of aging on TB dimensions. The CT scan lacked sufficient resolution to include cartilaginous rings in Model D. It is known that cartilaginous rings of a certain size will increase tracheal deposition (Russo, et al., 2008; Zhang & Finlay, 2005). However, results of this study indicate an even larger increase in tracheal deposition associated with the skewed inlet jet, inclusion of tracheal curvature, and an accurate tracheal gravity angle. Although Model D has been shown to fit within average adult dimensions, it is obtained from an adult male and the trachea is in the upper range of average dimensions. Models of other age and gender demographics are desirable for the prediction of aerosol deposition among a larger segment of the population, and development of these models

is left to future studies. Although the size of the scan data set (21 individuals) was deemed satisfactory for this study, a larger data set would provide even greater confidence that the dimensions of Model D are characteristic.

This study has produced an upper airway TB model (Model D) that includes a number of key anatomical and physiological characteristics, which were proven to influence deposition, and falls within the limits of average dimensions for an adult male. When compared with a previously existing model (Model C), the total deposition of realistic polydisperse pharmaceutical aerosols (MDI and DPI) was found to be similar, but the additional realistic features of Model D were found to significantly affect regional and local deposition with both the MDI and the DPI. This led to the conclusion that both models may be considered characteristic for predictions of total deposition of polydisperse aerosols, but Model D has clear advantages for evaluating regional and local deposition. The use of a hexahedral mesh versus a tetrahedral mesh was considered for both models with both inhalers, and it was found that a hexahedral mesh was preferable in all situations. Unfortunately, branch-averaged or bifurcation scale deposition results are not available from living subjects for test or pharmaceutical aerosols. Considering pharmaceutical aerosols, *in vivo* data is available that compares central lung to peripheral lung deposition, forming a C/P ratio (Newman, et al., 2000). Future studies will seek correlations between results with Model D and C/P ratios based on *in vivo* data with pharmaceutical aerosols. Other recent studies have just begun to report highly localized deposition of test aerosols from nebulizers within the airways (Conway *et al.*, 2012; Majoral *et al.*, 2014), which will serve as an additional source of *in vivo* model verification. Overall, Model D appears to be useful for studying the deposition of polydisperse aerosols in the upper TB

airways of an adult male, and provides a template from which other characteristic upper TB airway models may be constructed.

Table 3.1 Mean distance from the wall to the first control volume height in the MT and TB regions of Model C and Model D, for the MDI and DPI meshes. Also included in parentheses are the ranges of values in each region.

	MDI		DPI	
	MT	**TB**	**MT**	**TB**
Model C	0.147 (0.0467-0.271)	0.101 (0.0673-0.188)	0.126 (0.0515-0.358)	0.101 (0.0673-0.188)
Model D	0.140 (0.0467-0.242)	0.096 (0.0376-0.229)	0.142 (0.0534-0.36)	0.096 (0.0376-0.229)

Table 3.2 Summary of CFD simulation conditions.

Simulation	Conditions before particle injection	Particle injection conditions	Flow field time treatment	Outlet boundary conditions
1. *MDI Validation*	Steady airflow at 37 L/min	Spray period of 0.2 s with HFA 134a vapor and polydisperse particles entering the flow field	Transient solution	Constant pressure (flow proportional to outlet diameter)
2. *DPI Validation*	Zero velocity and pressure fields	Airflow introduced as a square-wave at 75 L/min with a ramp-up time of 0.05 s Polydisperse particles injected as a bolus at 0.025 s	Transient solution	Constant pressure (flow proportional to outlet diameter)
3. *MDI Comparison Study*	Steady airflow at 37 L/min	Spray period of 0.2 s with HFA 134a vapor and polydisperse particles entering the flow field	Transient solution	Predetermined mass flow condition at each lung lobe
4. *DPI Comparison Study*	Steady airflow at 75 L/min	Polydisperse particles evaluated in steady state flow field	Steady state solution	Predetermined mass flow condition at each lung lobe

Table 3.3 Lengths and average diameters (in mm) of trachea and main bronchi for Models C and D. Total angle of the main bifurcation (in degrees) is shown as well.

	Trachea		RMB		LMB		Branching
	L	**D_{avg}**	**L**	**D_{avg}**	**L**	**D_{avg}**	**Angle**
Model C	137.0	16.1	34.8	14.8	34.1	12.0	66.4
Model D	131.0	19.4	23.8	14.9	55.6	11.6	57.3

Table 3.4 Summary of morphological data reported in literature for cast, patient specific, and simplified models. Patient specific data includes 13 scans from ELCAP Public Lung Database and 8 scans from those collected for this study. Mean values of length and diameter are reported in mm while the branching angle is reported in degrees. Mean values are reported along with +/- one SD.

	Data	Trachea		RMB		LMB		Branching
	Sets	L	D_{avg}	L	D_{avg}	L	D_{avg}	Angle
Cast	7	106.4 ± 20.4	19.7 ± 2.2	29.5 ± 6.4	15.7 ± 2.4	57.0 ± 5.9	13.1 ± 0.9	55.0 ± 10.0
Patient Specific	21	NA	17.5 ± 2.1	25.2 ± 5.7	14.4 ± 1.8	53.8 ± 4.9	11.8 ± 1.9	73.1 ± 18.5
Simplified	2	112.5 ± 7.3	16.9 ± 1.1	NA	NA	NA	NA	NA

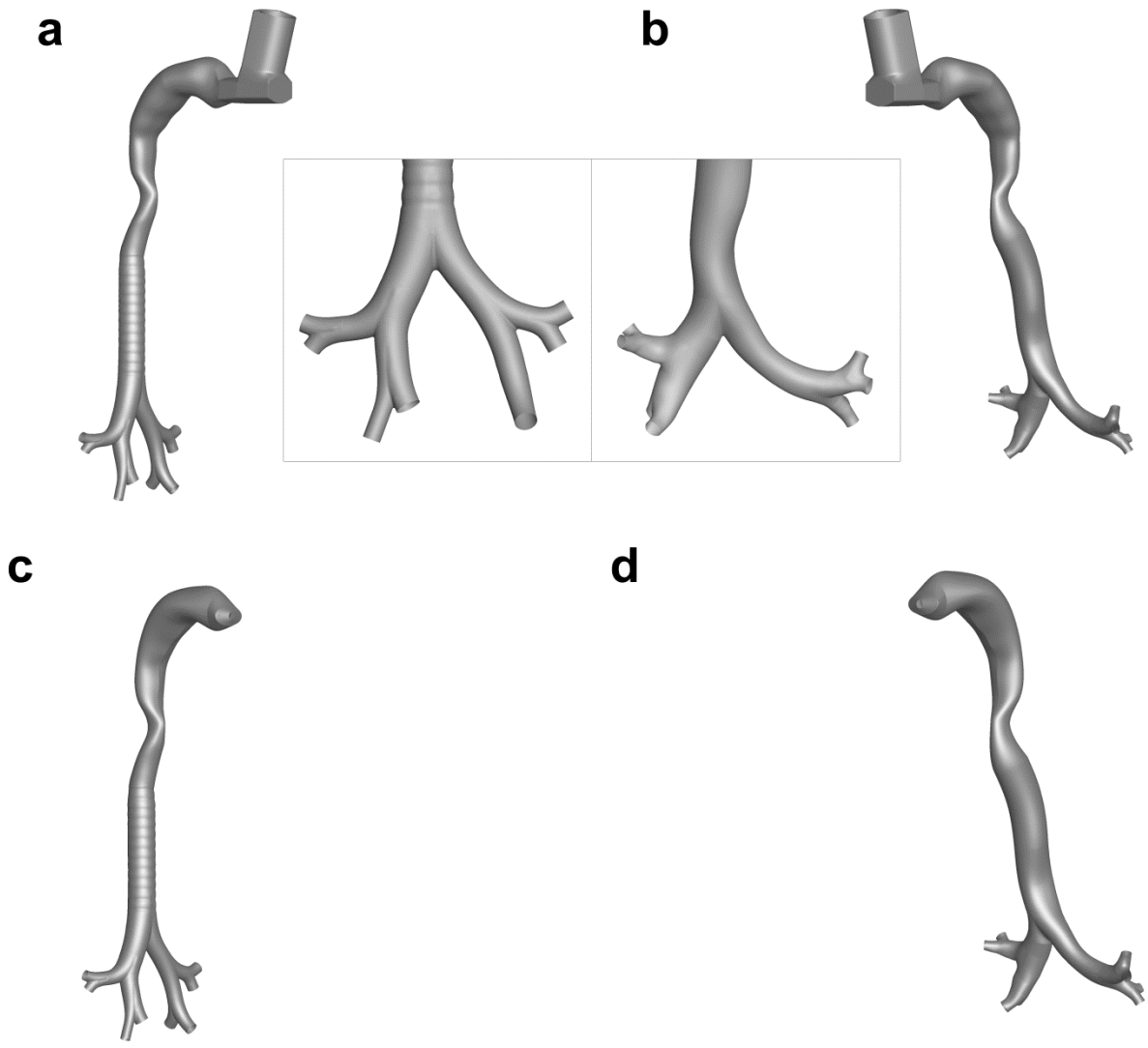

Figure 3.1 Surface geometries of (a and c) Model C compared with (b and d) Model D, with a metered dose inhaler (MDI) (a and b) and dry powder inhaler (DPI) (c and d) attached to each model.

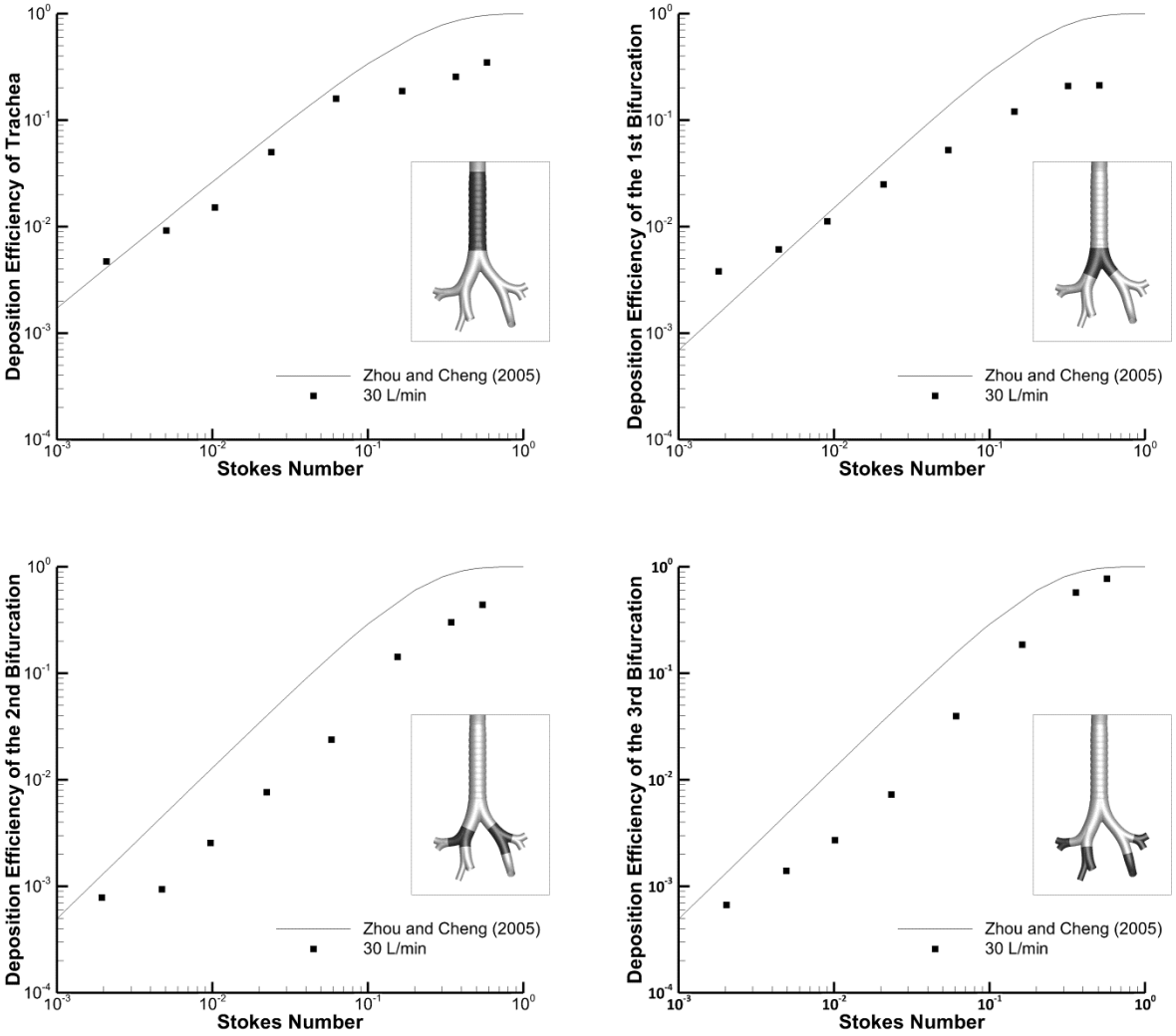

Figure 3.2 Deposition efficiency (DE) of monodisperse aerosols in Model C using the Zhou and Cheng (2005) empirical formulations compared to CFD predictions at 30 L/min within different regions of the upper TB airways. The regions of interest are highlighted for each case.

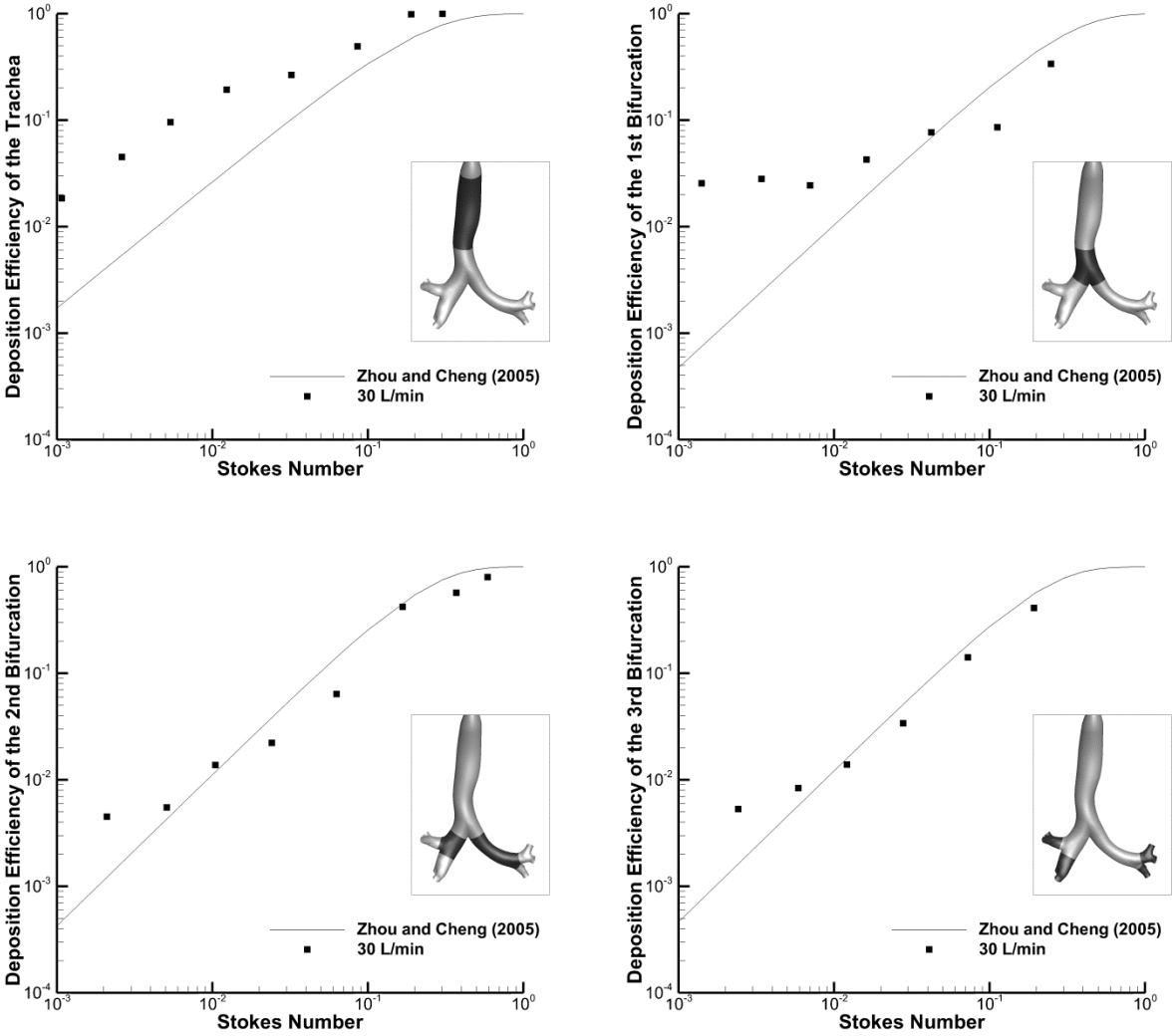

Figure 3.3 Deposition efficiency (DE) of monodisperse aerosols in Model D using Zhou and Cheng (2005) empirical formulations compared to CFD predictions at 30 L/min within different regions of the upper TB airways. The regions of interest are highlighted for each case.

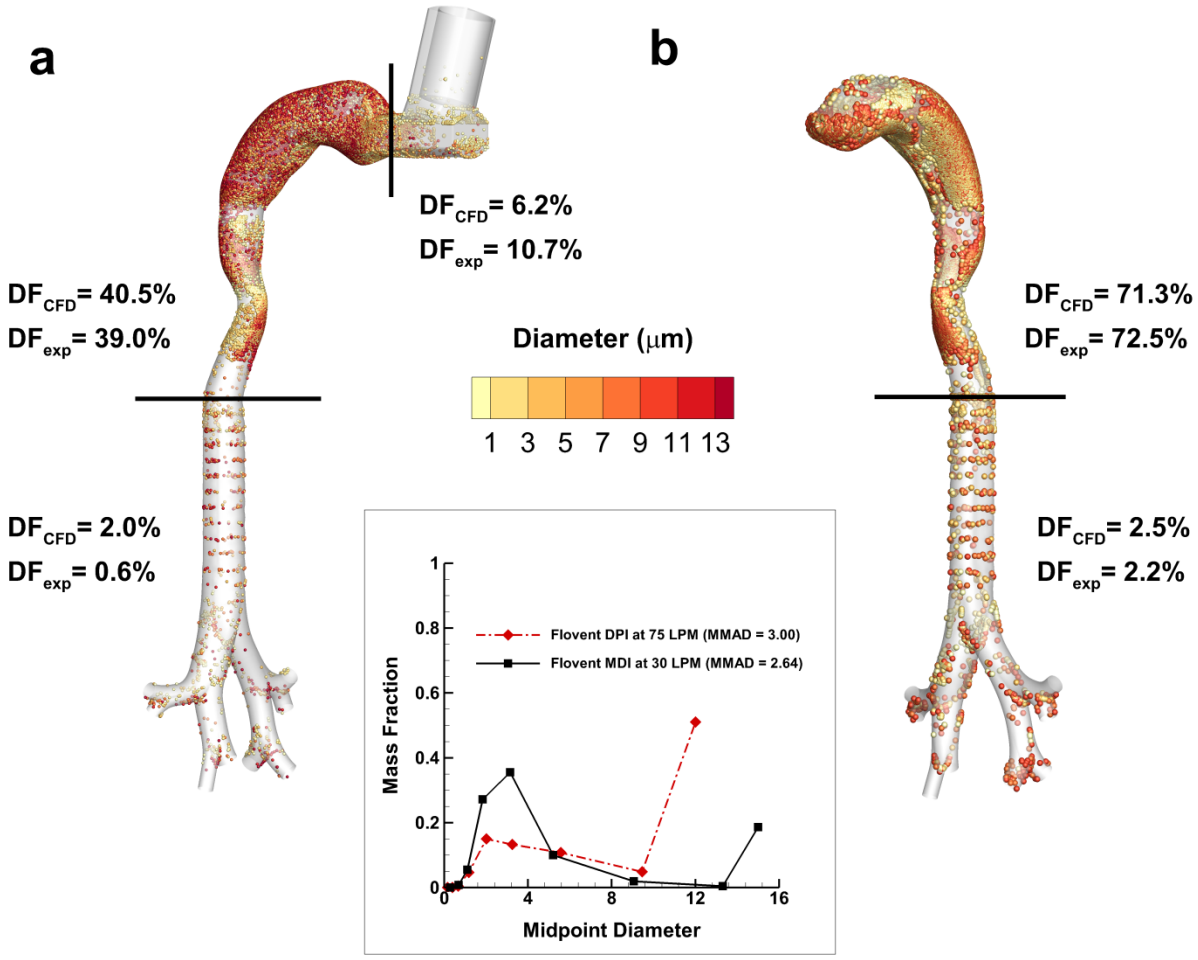

Figure 3.4 CFD predictions of deposition fraction (DF) for polydisperse pharmaceutical aerosols in Model C with both the (a) DPI and (b) MDI as compared with existing experimental data in the same geometry. The experimentally determined polydisperse particle profiles for both the DPI and MDI are shown as figure inserts. The DPI profile was corrected for deposition in the preseparator based on additional CFD simulations.

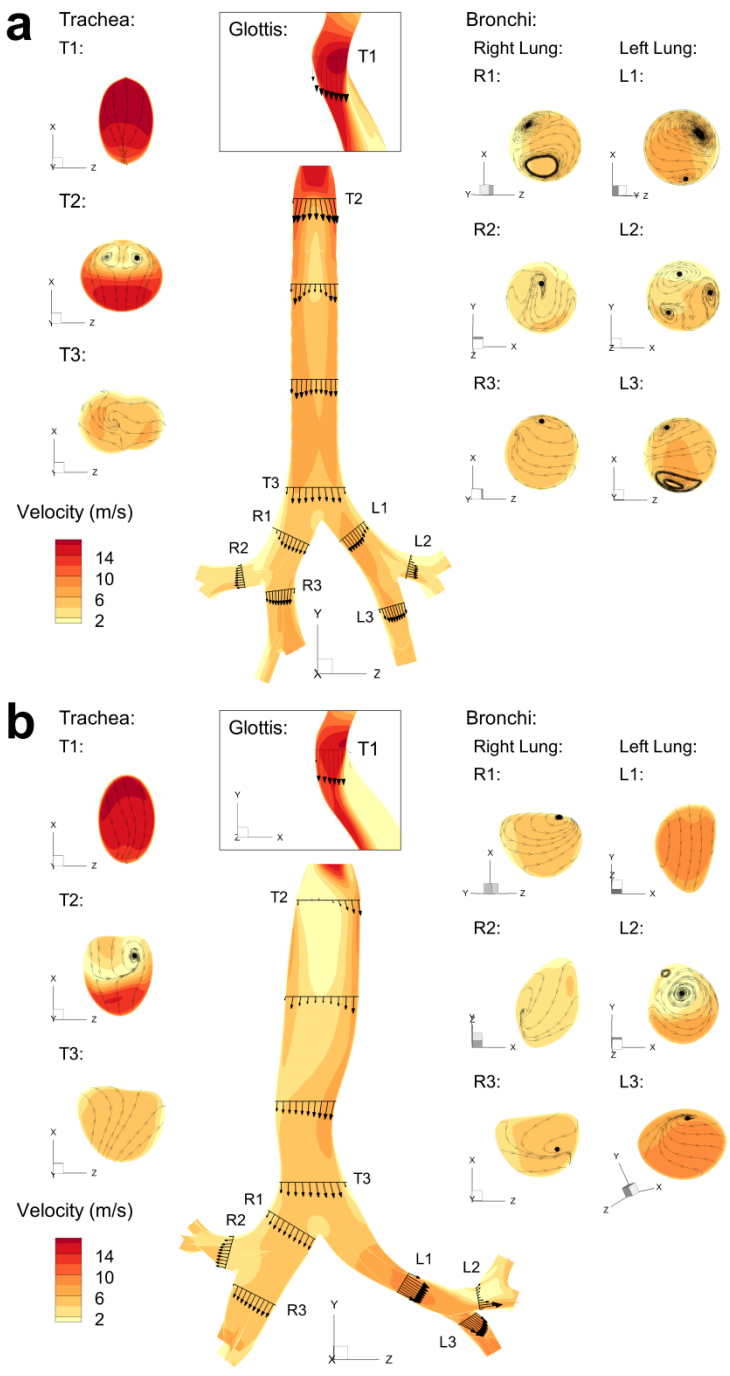

Figure 3.5 Sagittal plane velocity contours with midplane vector fields, along with selected axial cross-sectional contours and streamlines, in (a) Model C and (b) Model D for the MDI.

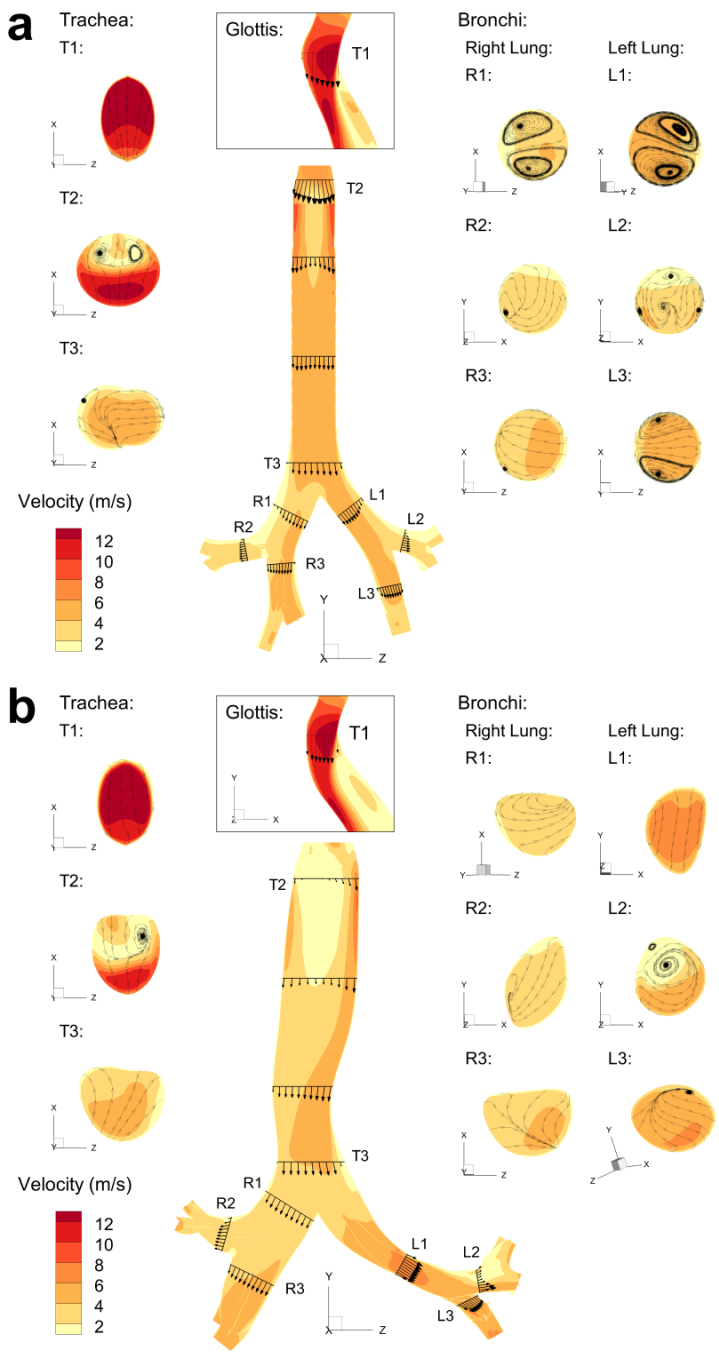

Figure 3.6 Sagittal plane velocity contours with midplane vector fields, along with selected axial cross-sectional contours and streamlines, in (a) Model C and (b) Model D for the DPI.

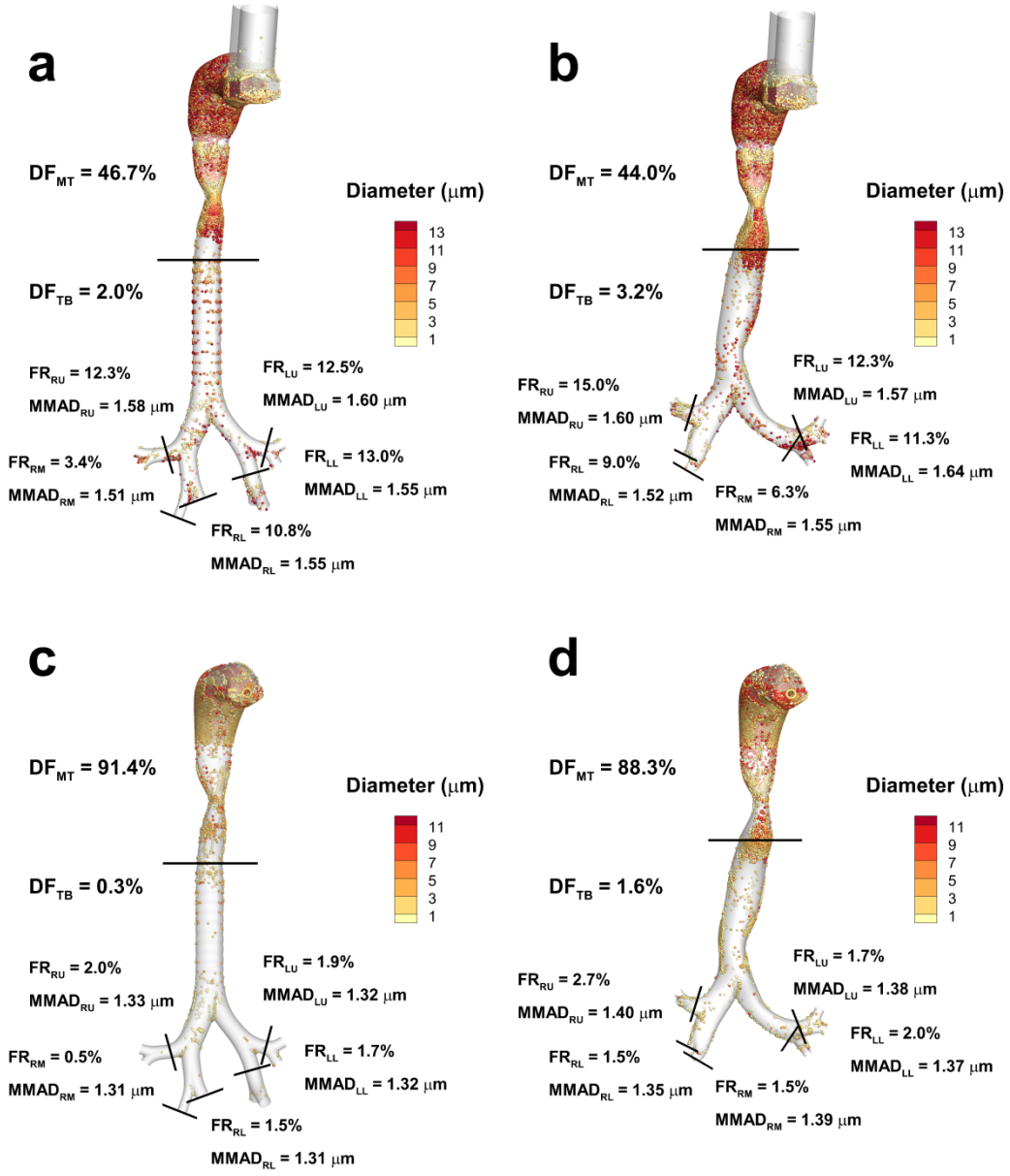

Figure 3.7 Deposition fraction (DF) in the mouth-throat (MT) and tracheobronchial (TB) airways for the MDI used in (a) Model C and (b) Model D, and for the DPI used in (c) Model C and (d) Model D. Also shown at the five lobar outlets are the fractions remaining (FR) and the mass median aerodynamic diameter (MMAD) of the remaining aerosol.

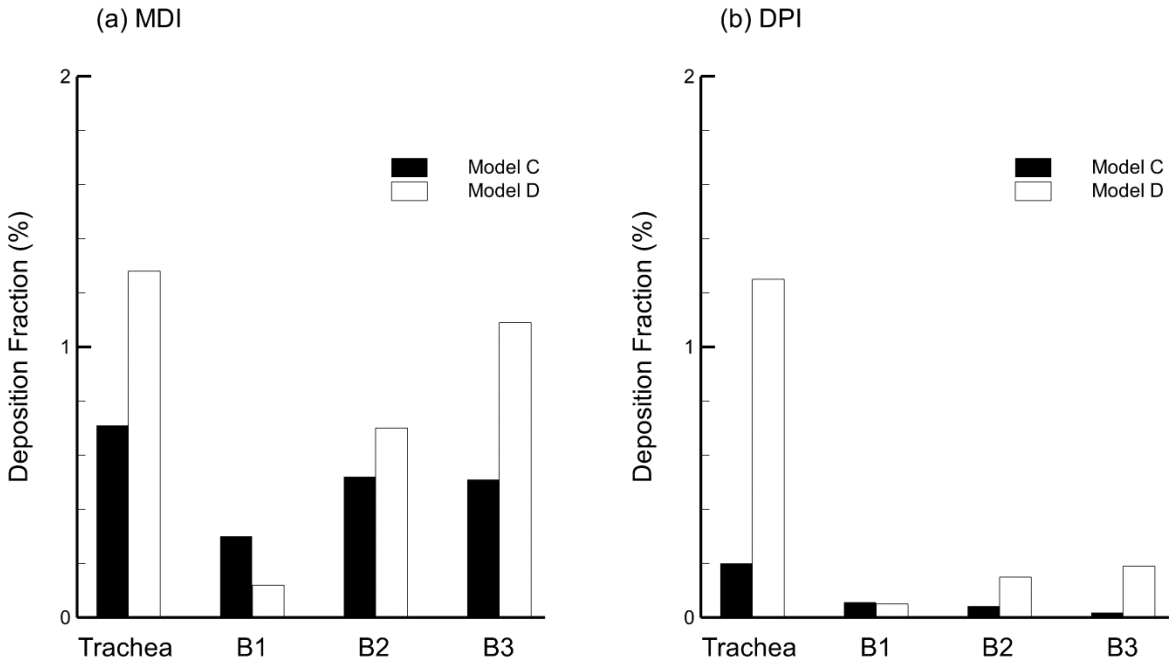

Figure 3.8 Regional deposition fraction (DF) in the TB airways through the third bifurcation (B3) for Model C and Model D with the (a) MDI and (b) DPI. The total deposition in B2 and B3 is shown.

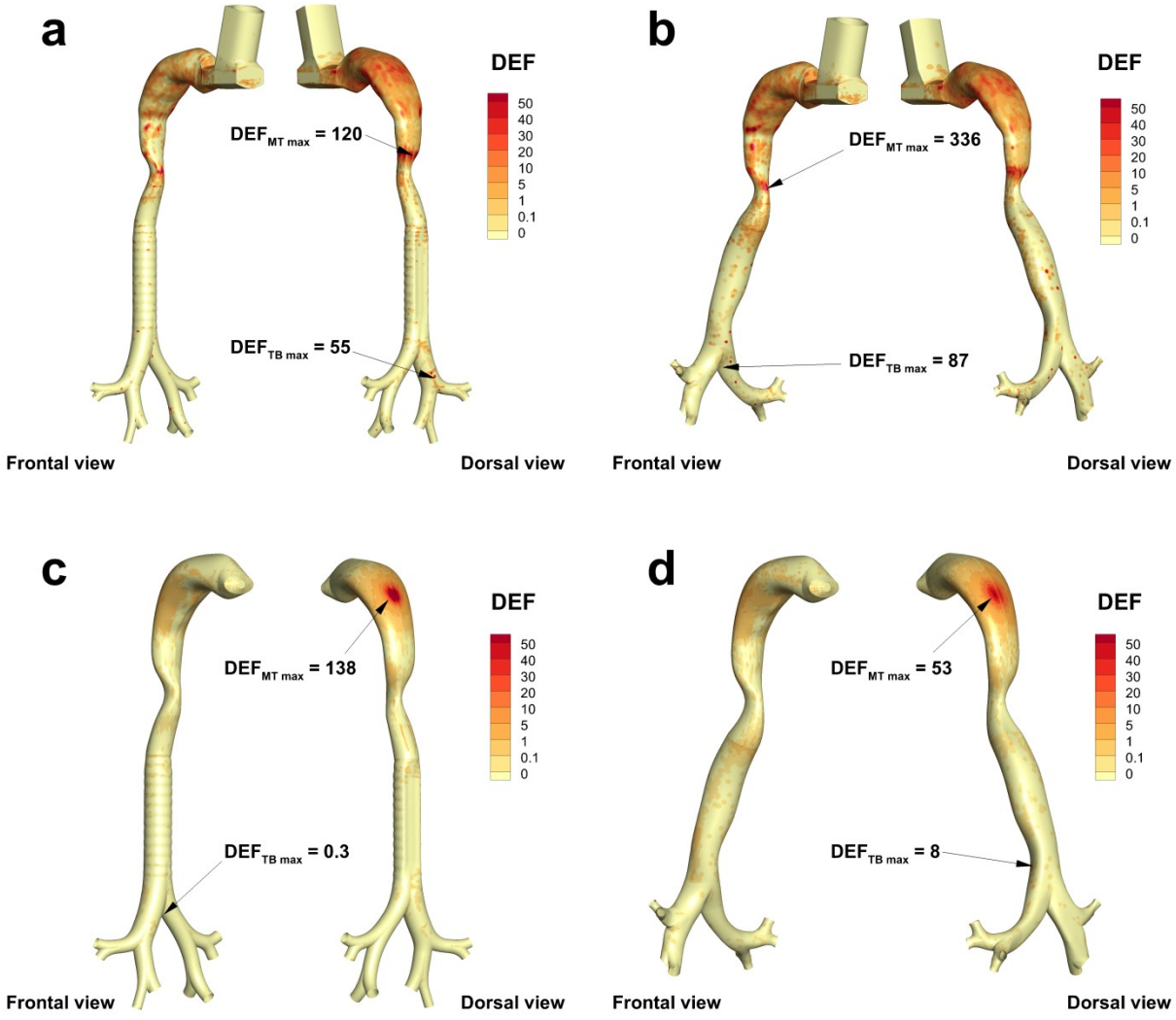

Figure 3.9 Deposition enhancement factor (DEF) for the MDI used in (a) Model C and (b) Model D, and the DPI used in (c) Model C and (d) Model D.

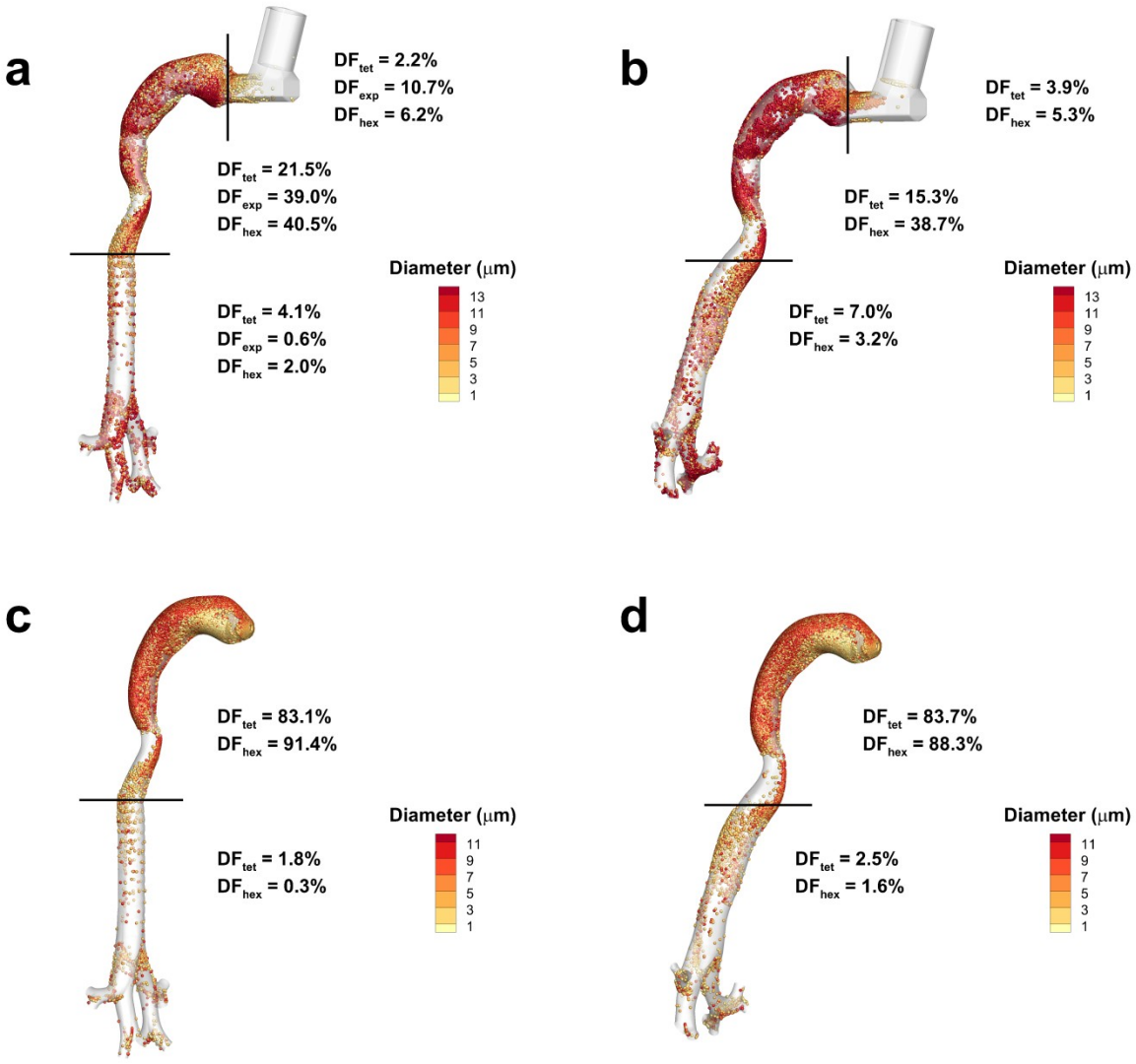

Figure 3.10 Deposition fraction (DF) in tetrahedral meshes as compared with hexahedral mesh results for the MDI used in (a) Model C and (b) Model D, and for the DPI used in (c) Model C and (d) Model D. Experimental values for DF are also included with Model C data.

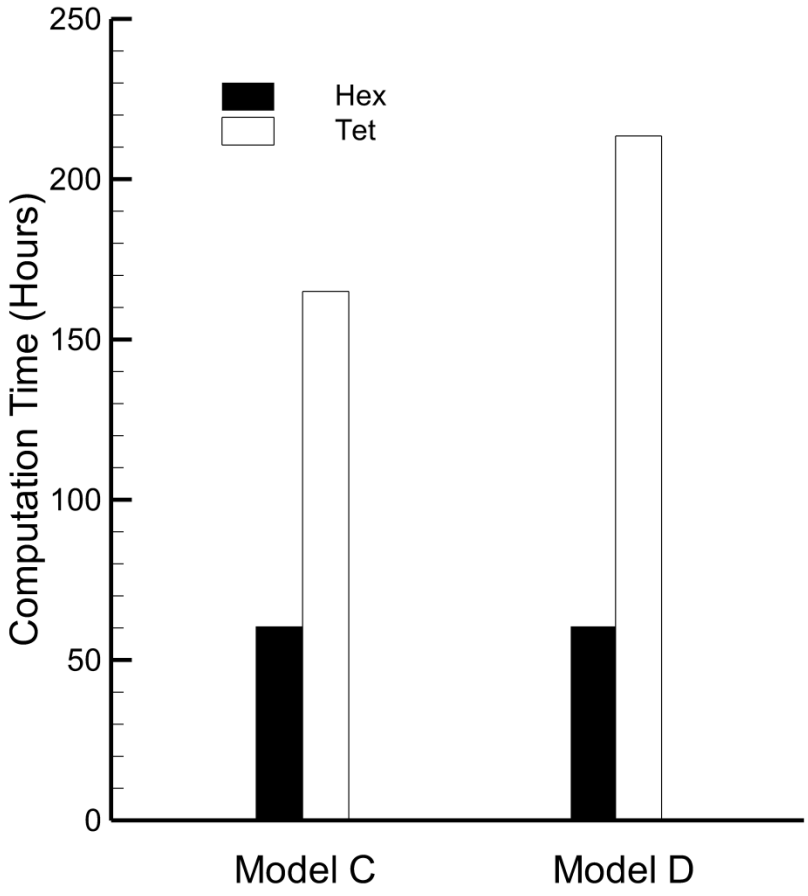

Figure 3.11 Computation time for tetrahedral and hexahedral meshes for Model C and Model D with the (a) MDI and (b) DPI.

Chapter 4 Effects of Asthma Constriction

The effects of asthma constriction on deposition characteristics of metered dose inhaler (MDI) and dry powder inhaler (DPI) aerosols are quantified in this study with CFD simulations in the mouth-throat (MT) through the fifteenth bifurcation (B15). One of the primary expected outcomes is a method for improved near-wall fluid velocity predictions and turbulence corrections that may reduce mesh dependence and provide more accurate estimates of particle trajectories, branch-averaged deposition efficiency (DE), and regional deposition fractions (DFs). Additionally, differences between non-constricted and constricted airways in the tracheobronchial (TB) regions are assessed through changes in DF, while differences throughout the lower airways are represented by branch-averaged DE and regional DF.

4.1 Introduction

Model C was used to represent the tracheobronchial airways from the mouth-throat (MT) region through the fifteenth bifurcation (B15), and a 30% diameter reduction was applied to the bifurcating airways to create asthma-constricted versions of Model C with MDI and DPI mouthpieces. Stochastic individual pathway (SIP) models, as described by Tian et al. (2011a; 2011b), were used to represent both the non-constricted and constricted lower airways from the fourth bifurcation (B4) to B15. Previously developed user-defined functions (UDFs) for near-wall corrections of fluid velocities and turbulence were altered to allow for mesh independence

of those routines which in turn promoted greater consistency of their application. The effect of constriction in the upper airways was quantified by a comparison of DF values in the MT and upper TB regions, which showed approximately twice as much TB deposition for the MDI and DPI cases, and a slight increase in extrathoracic deposition in both cases as well. Deposition efficiency (DE) in the SIP models was calculated using CFD and compared with data produced using a correlation developed by Chan and Lippmann (1980). Branch-averaged DE values as predicted by the correlation data were approximately twice as high for the constricted MDI case as compared with the non-constricted case, and smaller increases for DPI delivery were observed as well. Regarding the CFD data, differences in branch-averaged DE values for the constricted cases as opposed to the non-constricted cases were not as pronounced. Using the CFD estimates of branch-averaged DE, regional DF values were produced for all cases, where it was observed that DF in the B8-B15 region was reduced in the non-constricted as compared with the constricted models by 0.24% and 0.27% for MDI and DPI delivery, respectively. Though the magnitudes of DE values as predicted by CFD for all cases were less than those estimated using the correlation from Chan and Lippmann (1980), the relative differences in adjacent bifurcations of branch-averaged DE in the SIP models as predicted using both methods showed good agreement. This provided confidence that future study may use the improved near-wall corrections for accurate predictions of DF and branch-averaged DE from the MT through B15 using a combination of transient and steady state simulations.

4.2 Methods

For this study, the previously developed Model C (Tian, et al., 2011b) was used to create non-constricted and constricted airways with MDI and DPI mouthpieces, as illustrated in Figure

4.1. The construction details of Model C are outlined by Tian et al. (2011b) and in Section 3.2 of this dissertation. The inhalers used were Flovent HFA MDI and Flovent Diskus DPI (GlaxoSmithKline, Raleigh, NC, USA), which were also described in more detail in Section 3.2. Model C was chosen since this study was in progress during the development of Model D, and as such it was the only available characteristic TB model. Consistent with the canine *in vivo* data of Brown and Mitzner (2003), the constricted models were produced by applying a 30% diameter reduction in the trachea through the third bifurcation (B3) while the lengths of each airway were held constant. Reduction of the airway diameters required re-surfacing the new models and applying the appropriate smoothing, which was accomplished using GAMBIT 2.4 (ANSYS, Inc., Canonsburg, PA, USA).

The lower airways from B4 to B15 were modeled using the SIP approach as described by Tian et al. (2011a; 2011b) and in Section 2.2.2 of this dissertation. Five SIP models were scaled by Tian et al. (2011a; 2011b) to simulate flow and particle transport in the lobar paths of non-constricted models for MDI and DPI delivery. For this study, constricted versions of the five SIP models were constructed by applying a 30% diameter reduction in the same manner as with the upper airway models in Figure 4.1. The five SIP models are designated as the left lower (LL), left upper (LU), right lower (RL), right middle (RM), and right upper (RU) lobar paths for the non-constricted and constricted cases. The LL, LU, and RU models begin at the third bifurcation (B3), but the RL and RM models begin at B4 and are unique. Non-constricted and constricted versions of the LL model are shown in Figure 4.2, while the other models which are similar in appearance are not pictured. The average diameters of the SIP models, given in mm, are displayed in Table 4.1. The RL SIP model is based on dimensional data from Yeh and Schum (1980) and scaled to represent a functional residual capacity (FRC) of 3.5 L, as described by

Tian et al. (2011b), while the four other SIP models are scaled from the RL SIP model to match the lobar outlets of Model C. The models are split between B4-B7 and B8-B15, which is done to reduce the number of particles needed for particle trajectory predictions, as described in more detail later in this section.

The non-constricted upper airway computational meshes were identical to those used with Model C, as described in Section 3.2 and in Walenga et al. (2013), with ~$1x10^6$ and ~$1.4x10^6$ cells used for the MDI and DPI models. The constricted models were constructed in the same manner, while the near-wall cell heights were based on the same gradient used in the non-constricted models, which resulted in smaller cell heights near the wall. This mismatch of near-wall cell heights has been known to cause discrepancies in Lagrangian particle tracking corrections due to drag and turbulence, and in this study the UDFs used for these corrections were altered to avoid this issue, as described later in this section. The y^+ values of each constricted case were checked and were found to be similar those from the non-constricted cases. The numerical extensions at the outlets were omitted to allow for interpolation of flow field and particle tracking information to the SIP models. Any potential loss in accuracy at the outlets due to any artificially increased turbulence that may result from the lack of extensions was deemed to be sufficiently small as to still allow for comparison of the DFs between the non-constricted and constricted models. Moreover, Tian et al. (2011b) showed that DE predictions in SIP models are not significantly affected by the removal of numerical extensions in the corresponding upper airway model.

The non-constricted and constricted SIP meshes were constructed with GAMBIT 2.4 (ANSYS, Inc., Canonsburg, PA, USA) using hexahedral elements in the same manner as the upper airway meshes. Two versions of each SIP model were constructed, one with numerical

extensions at the outlets to avoid the development of unrealistic turbulence, and the other without to allow for a more realistic pressure distribution at the outlets, since it was unknown which would have a greater effect on particle deposition. Since the models were split between B4-B7 and B8-B15, the numerical extension at B7 was omitted in both cases to allow for interpolation of flow and particle data. The meshes from B4-B7 had approximately $2.4x10^5$ and $1.8x10^5$ cells with and without extensions, respectively, while the meshes from B8-B15 had approximately $4.2x10^5$ and $3.0x10^5$ cells, respectively.

The inhalation waveforms of the MDI and DPI models were modeled after Longest et al. (2012d). In that study, slow and deep (SD) and quick and deep (QD) transient inhalation waveforms were developed to represent correct patient usage boundary conditions for the MDI and DPI, respectively. The waveforms were based on a 3 L inhaled volume for both the MDI and DPI, which was found to be consistent with the study of Broeders et al. (2003), and resulted in 37 L/min and 75 L/min mean flow rate for MDI and DPI inhalation, respectively. Other parameters reported by Longest et al. (2012d) were the peak inspiratory flow rate (PIFR) and the period of inhalation (T), which were found to be 61.4 L/min and 4.86 s for the SD profile and 122.2 L/min and 2.40 s for the QD profile. Longest et al. (2012d) considered both correct and incorrect usage of MDI and DPI inhalers, but for this study only correct usage is considered. Specifically, the MDI upper airway models are simulated under transient conditions with the SD waveform, while the DPI predictions use the QD waveform. The reader is referred to Longest et al. (2012d) for further details on the SD and QD waveforms.

The velocity inlet boundary conditions for the SIP predictions were interpolated from the upper airway models at the time steps when the inhalation flow rates of the MDI and DPI simulations are at their mean accelerating values (i.e. 37 and 75 L/min, respectively). The SIP

model simulations were run under steady state conditions for computational efficiency, and also because it was impractical to interpolate fluid velocities from the upper airway model at every transient time step. Moreover, it was necessary to split the models because the particle trajectory calculations would be nearly intractable as described later in this section. Tian et al. (2011b) compared DE predictions in three different RL lobe SIP models under steady state and QD conditions, and found differences in the predictions to be less than 0.2%, indicating that the steady state approximation is adequate.

Flow field simulations were conducted using ANSYS FLUENT 14.5 (ANSYS, Inc., Canonsburg, PA, USA). Many of the CFD simulation methods and boundary conditions for the MDI and DPI upper airway predictions were similar to those employed in Chapter 3 of this dissertation and in other studies by our group (Longest, et al., 2007; Longest, et al., 2012d; Tian, et al., 2011a; Tian, et al., 2011b; Walenga, et al., 2013). The MDI simulations from the mouth-throat (MT) through B3 were turbulent, compressible, transient, and required both temperature gradient and species transport calculations. As before, the temperature and concentration gradient calculations of the MDI were based on the methods of Longest and Xi (2008) and Longest et al. (2007). The DPI upper airway solutions were based on turbulent, incompressible, and isothermal flow without species transport, but only transient simulation of the upper airway models was considered. Regarding the SIP models, the flow fields were modeled as turbulent, incompressible, isothermal, without a species concentration gradient, and steady state as indicated above. While these conditions were consistent with the DPI upper airway models, they differed from the MDI upper airway models but were located far enough away from the inlet jet that the density, temperature, and species concentrations were considered to be nearly constant. All simulations used the low Reynolds number (LRN) k–ω turbulence model, which has been

shown to provide good polydisperse predictions of particle transport and deposition for MDIs (Longest, et al., 2007, 2008a; Longest & Hindle, 2009a) and DPIs (Tian, et al., 2011b). The outlet conditions for the MDI upper airway simulations were specified using pressures at the boundaries that were obtained by first predicting flow with the mass-flow distribution specified in Chapter 3 and based on Yin et al. (2010) and Asgharian and Price (2006). Pressure outlets were necessary for the compressible MDI simulations, but not for the incompressible DPI simulations, which employed the mass-flow distribution directly. The SIP model outlets utilized symmetric mass-flow distributions.

Particle trajectory calculations were performed using a Lagrangian particle tracking model, while turbulent dispersion was applied using a random walk method. Since particle size change was not considered, the effects of the particles on energy, mass, and momentum of the flow field were considered to be negligible and thus the discrete phase was modeled as one-way coupled. The polydisperse particle distributions were the same that were used in Chapter 3 and Walenga et al. (2013) for both the MDI and DPI predictions. A combination of code from ANSYS FLUENT 14.5 and custom UDFs was used to apply a near-wall correction to model anisotropic turbulence as implemented by Longest et al. (2007), since the LRN k–ω model uses a near-wall isotropic turbulence assumption that may over-predict aerosol deposition (Matida, et al., 2004). Additionally, a linear interpolation of near-wall velocities was applied in a similar fashion.

A key feature of this study was an adjustment to the near-wall drag and turbulence corrections for Lagrangian particle tracking. As described by Longest and Xi (2007), the particle trajectory calculations are updated using mean fluid velocities at each time-step, which are determined through interpolation from nodal values or control volume centers. However,

Longest and Xi (2007) found that fluid velocities at near-wall control volumes do not approach zero at the wall, and thus a linear interpolation of fluid velocities was performed using UDFs in combination with the commercial code, which in effect creates a first order approximation of the boundary layer between the cell center and wall. However, a disadvantage of this approach is that mesh dependence is a factor, since any alteration in the size of near-wall control volume heights may have a large effect on particle deposition. Also, local changes of near-wall control volume heights within the model create inconsistent reduction of fluid velocities in relation to the particle trajectory. For example, a particle may pass from the upper half of a smaller near-wall cell volume where no fluid velocity correction is applied, but then pass into a larger cell volume where it is now within the linear interpolation region, leading to an unnaturally disjointed trajectory. For this reason, the fluid-velocity correction UDF was updated to be applied only when it is within a certain pre-defined near-wall limit (nw_{limit}), independent of its position in relation to near-wall cell volumes. Also, the code was written to allow for application of different values of nw_{limit} in different regions, in much the same manner that physical boundary layers change with diameter. Caution must still be used though when creating the mesh, since though the near-wall fluid velocity corrections are now mesh independent, the y^+ values at the wall must still be checked. The updated near-wall fluid velocity prediction UDF is titled "nw_drag_2.1c.c" and is further described in Appendix A.

The near-wall turbulence corrections were updated for mesh independence as well. The random walk method employed by the CFD simulations to model particle turbulent dispersion implements an eddy interaction model that does not reduce turbulent near-wall normal fluctuations (Kim *et al.*, 1987; Longest, et al., 2007; Matida *et al.*, 2000; Matida, et al., 2004).

The near-wall fluctuating velocity is updated as described by Longest et al. (2007) and others (Matida, et al., 2004; Wang & James, 1999) as

$$u_n' = f_n \xi_n \sqrt{\frac{2}{3}k} \quad \text{where} \quad f_n = 1 - e^{-0.02n^+} \quad \text{and} \quad n^+ = u_\tau n/\upsilon \qquad (4.1a\text{-}c)$$

The near-wall fluctuating velocity u_n' is at the wall-normal coordinate n, while the near-wall damping function f_n and the randomly generated Gaussian distributed numbers ξ_n are at the same location. The energy k from the LRN k–ω model is also used to calculate u_n'. The n^+ value is evaluated using the turbulent friction velocity u_τ and the kinematic viscosity ν. Within the code, a limit of n^+ is defined below which the anisotropic fluctuating velocity correction is applied, which is referred to as n^+_{limit} here. Similar to the fluid velocity correction, the previous turbulent correction UDF implemented a linear interpolation of the k energy value based on the distance between the near-wall control volume center and the wall. The UDF used for this study applied a mesh independent interpolation based on the same values of nw_{limit} used for the fluid velocity interpolation in the corresponding zones. Unlike the values of nw_{limit}, the value of n^+_{limit} was not varied according to zone. The updated near-wall turbulence correction UDF is titled "nw_turb_2.4c.c" and is further described in Appendix A.

Validations of the non-constricted MDI and DPI models were performed to obtain values of nw_{limit} in the MT and tracheobronchial (TB) regions and the value of n^+_{limit} that best approximates the available *in vitro* data from Longest et al. (2012d) and Tian et al. (2011b), respectively. The inlet and outlet conditions of the MDI and DPI validations are the same as those used in Chapter 3 and Walenga et al. (2013), where a transient square wave was used with particle release during the first 0.2 s for the MDI non-constricted model, and where a transient square wave with a ramp-up from 0 to 0.05 s with a bolus of particles released at 0.025 s was used for the DPI non-constricted model. The particle distributions were the same as well, the

only change was that the new near-wall correction UDFs were used. For the MDI validation, the optimal values of nw_{limit} for the MT and TB were 0.05 mm and 0.1 mm, respectively, and the value of n^{+}_{limit} was 60. The mouthpiece (MP) and the MT region were considered as one region for this validation since the value of nw_{limit} for the TB region was needed for the SIP model inlet conditions and, moreover, because constriction was not applied in the MP or MT regions of the constricted models. The resulting predictions of DF in the MT and TB regions were 50.3% and 0.6%, which showed good agreement with the *in vitro* data of 49.7% and 0.6%, respectively. For the DPI validation, the optimal values of nw_{limit} for the MT and TB were 0.1 mm and 0.05 mm, respectively, and the value of n^{+}_{limit} was 60. The predicted values of DF using those parameters in the MT and TB regions were 72.0% and 2.3%, which showed good agreement with the *in vitro* data of 72.5% and 2.2%, respectively. The values of nw_{limit} and n^{+}_{limit} that were obtained from the MDI and DPI validations were then applied to the non-constricted MDI and DPI simulations with the SD and QD waveforms, respectively. For the constricted simulations the same values of nw_{limit} and n^{+}_{limit} were used except in the TB region, where the nw_{limit} values were scaled to 70% of the non-constricted value, which came to be 0.07 mm for the MDI predictions and 0.035 mm for the DPI predictions. The adjustment of nw_{limit} was applied for the constricted simulations based on the hypothesis that nw_{limit} should be proportional to boundary layer thickness, and it is known that boundary layer thickness in fully developed pipe flow is equal to the radius of the pipe.

Particles at the B3 outlets (LL, LU, RL, RM, RU) of the upper airway models were allowed to accumulate over the entire course of those transient simulations and then injected into the inlets of the corresponding SIP models. The polydisperse particle distribution at the B3 outlets from all of the upper airway simulations consisted of ~3,000 particles, which were too

few to provide an accurate characterization of the DE in the lower regions of the SIP models, which extend from B4 to B15. Thus, the models were split into two sections from B4-B7 and B8-B15 in the same manner as Longest et al. (2012d) to reduce the number of particles necessary, which was estimated to be ~45,000 particles for the B4-B7 section and ~1,500,000 particles for the B8-B15 section. The fluid velocities and particle profiles at the outlets of the B4-B7 models were interpolated to the corresponding B8-B15 models. To provide the required number of particles for each SIP model, multiple copies of the particle profile were simulated concurrently. The inclusion of turbulent dispersion modeling in the particle trajectory calculations ensured a unique path for each particle from a copied profile due to the randomness inherent in that method.

Regarding the application of the nw_{limit} and n^{+}_{limit} values for the fluid velocity and turbulence corrections in the SIP models particle trajectory calculations, three methods were used. The first method, labeled as 'constant', takes the nw_{limit} from the TB regions of the corresponding MDI and DPI non-constricted and constricted simulations with the SD and QD waveforms and applies it to every section from B4-B15. The 'proportional decrease' method applied the nw_{limit} from the corresponding TB regions and applied it to the B4 regions, and then the value of nw_{limit} was decreased proportionally according to the decrease in average airway diameter from one bifurcation to the next. The 'trachea scaled proportional decrease' method is the same as the 'proportional decrease' method except that the value nw_{limit} was decreased proportionally from the trachea down to B15 according to diameter, which yielded a unique set of values for each lobar SIP model. For n^{+}_{limit}, the value from the upper airway simulations (n^{+}_{limit} = 60) was applied to all of the B4-B7 sections, while it is set to zero for B8-B15

simulations since it is expected that those bifurcations should have nearly laminar flow and the application of a turbulence correction may under-predict deposition.

The CFD predicted values of branch-averaged DE in the SIP models were compared with the empirical correlation for deposition probability due to impaction that was developed by Chan and Lippmann (1980), which is calculated as

$$DE = 1.606 * St_k + 0.0023 \tag{4.2}$$

where St_k is the Stokes number that is calculated as

$$St_k = \frac{u_{\text{avg}} \rho_{part} {d_{part}}^2 C_c}{18 \mu D_{bifurcation}} \tag{4.3}$$

where u_{avg} is the average velocity at the inlet of each bifurcation, ρ_{part} is the density of the particle, d_{part} is the diameter of the particle, μ is the dynamic viscosity of the fluid, and $D_{bifurcation}$ is the average bifurcation diameter. The Cunningham correction factor C_c is calculated as

$$C_c = 1 + \frac{2.52\lambda}{d_{part}} \tag{4.4}$$

where λ is the mean free path in the fluid of interest. As noted by Finlay (2001), the Chan and Lippmann (1980) correlation uses data from a lung cast with a larynx and multiple generations rather than a single generation as is the case with some available correlations. Moreover, the Chan and Lippmann (1980) correlation falls in the middle of several known correlations, which makes it an appropriate choice for comparison with CFD data from a characteristic TB model (Finlay, 2001). However, since the Chan and Lippmann (1980) correlation is based on *in vitro* data from a cast model extending to the sixth bifurcation level, it is not intended to represent a perfect match of *in vivo* data. Rather, it is used to provide a means for comparing relative changes in DE as predicted by CFD. In addition to the estimates of deposition by impaction provided by the Chan and Lippmann (1980) correlation, the contribution of sedimentation to DE

was also included, based on the equations of Finlay (2001), but the overall contribution was negligible in nearly every case and thus the equations are not repeated here.

Since the impaction and sedimentation correlations used are intended to be predictive of a monodisperse distribution, some extrapolation was necessary to provide a polydisperse prediction. To accomplish this, the total mass from each particle size bin was determined at the SIP model inlets, and from that the correlation of Chan and Lippmann (1980) was used to predict DE due to impaction in the B4 region for each particle bin contribution. The total amount of mass deposited in the B4 region was then subtracted from the total entering, and the calculation was performed again for the next level, and the process was repeated until reaching B15.

The calculations for upper airway DF and branch-averaged lower airway DE values for the CFD simulations were performed using equations 3.3 and 3.4 of this dissertation. Upper airway deposition values were quantified using DF because a comparison of MT and TB regions was sought, and the TB region included the trachea through B3 leaving the calculation of branch-averaged DE values unnecessary. Regarding the branch-averaged DE calculations in the SIP models, the values were weighted according to the mass entering each SIP model. One difficulty with applying a mass-weighted average was that the LL, LU, and RU lobes begin at B3, while the RL and RM lobes begin at B4. As a consequence, simply taking the amount of mass entering the LL, LU, and RU SIP models (which begin at B4) does not account for approximately half of the mass in each lobe. To handle this, the mass amounts exiting both B3 outlets for the three lobes were summed and used for the mass-weighted average, which carries the inherent assumption that DE predictions are the same through the other B4 pathways of the LL, LU, and RU lobes. Considering that the diameters and ventilation at B4 for the other pathways are identical to the B4 pathways of the LL, LU, and RU SIP models, this was taken to be a

reasonable assumption. The empirically predicted DE values from the Chan and Lippmann (1980) correlation were also branch-averaged on a mass-weighted basis in an identical fashion.

Values of DF in the SIP models were evaluated on a regional basis from B4-B7, B8-B15, and B4-B15 using the DE values from the CFD predictions. In the same manner as Longest et al. (2012b) and ICRP (1994), the DE of the given region from the *i*th bifurcation to the *j*th bifurcation was first calculated as

$$DE_{region} = 1 - (1 - DE_{Bi})\left(1 - DE_{B(i+1)}\right) \dots (1 - DE_{Bj}) \quad (4.5).$$

Then, the regional DF was calculated as

$$DF_{region} = DE_{region} * FR_{Bi} \quad (4.6)$$

where FR_{Bi} is the fraction remaining of drug entering the *i*th bifurcation. These calculations were performed for each SIP model and the DF values were then summed to provide total regional DF values. As with the branch-averaged DE calculations, the values of FR_{B4} for the LL, LU, and RU SIP models were applied using the summed amounts of mass from both B3 outlets of those lobes.

The methods of near-wall parameter (nw_{limit} and n^{+}_{limit}) application in the SIP models were evaluated by taking the relative differences between bifurcations for the correlation and CFD data, which is calculated as

$$\Delta_{Bi-B(i+1)} = \frac{DE_{Bi} - DE_{B(i+1)}}{\mu_{B4-B15}} \quad (4.7)$$

where $\Delta_{Bi\text{-}B(i+1)}$ is the relative difference in DE between the *i*th and the *i*th+1 bifurcations, DE_{Bi} and $DE_{B(i+1)}$ are the deposition efficiencies of the *i*th and the *i*th+1 bifurcations predicted by correlation or CFD data, and $\mu_{B4\text{-}B15}$ is the mean value of DE extending from B4 to B15 in the given SIP model. A Shapiro-Wilk normality test was performed on all sets of $\Delta_{Bi\text{-}Bi+1}$ to determine if a paired Student's t-test or a Wilcoxon signed-rank test would be more appropriate

for analyzing the data. Once the appropriate test was determined, the p-values were tabulated and if any case and method combination (e.g. 'constant' and DPI constricted) had $p < 0.05$ that method was rejected. The average p-value for each method was tabulated and the highest result was taken to indicate the most effective method for the CFD data to match the relative differences of the correlation data.

4.3 Results

In the upper TB airways, the constricted MDI and DPI models show approximately twice as much drug deposition as compared with their non-constricted counterparts, where the DF values increase from 1.2% to 2.7% and from 2.9% to 5.7%, respectively, as illustrated in Figure 4.3. The increased particle inertia as a result of the constricted airways explains the dramatic increase in deposition in this region, where deposition is known to be dominated by impaction as opposed to sedimentation or diffusion. Additionally, the extrathoracic regions for both the MDI and DPI models show a small increase in DF from the non-constricted to the constricted versions, where the total DF in the combination of the MP and MT regions in the MDI models increases from 51.1% to 53.4%, while the DF in the MT region of the of DPI models increases from 71.3% to 75.3%. This may be partly explained by the decrease in diameter from the glottis to the trachea entrance, which comprises a small section of the MT region in both the MDI and DPI models. However, upstream effects of the increased pressure drop in the constricted model are clearly present in the MDI case, as the MP deposition fraction increases from 5.4% to 9.1% while the MT region shows a slight decrease from 45.7% to 44.3%. Since there is no MP deposition fraction recorded for the DPI case, these upstream effects are not observable. Compressible flow in the MDI case may enhance these effects compared with the incompressible

flow in the DPI case. The relative difference in MP values from the healthy to the asthmatic cases for MDI delivery is notably large at 69%, and determining whether or not this is a realistic change may be a good topic for future study.

Initial testing showed that the B4 near-wall correction values for nw_{limit} of 0.1 and 0.07 mm for the MDI non-constricted and constricted SIP models along with 0.05 and 0.035 mm for the DPI non-constricted and constricted SIP models yielded consistently lower DE values for all cases and all methods compared with the predictions based on the Chan and Lippmann (1980) correlation. Attempts were made to increase these values but a threshold was reached in each case where DE values would continue to increase until they showed good agreement with the correlation data for the B4-B7 sections, but the values in the B8-B15 sections would plateau well below the data compiled using the correlation from Chan and Lippmann (1980). Changes in n^{+}_{limit} did not yield any observable increase in overall DE predictions. After testing numerous cases, it was determined that setting the nw_{limit} parameter to 0.05 and 0.035 mm for the non-constricted and constricted models of both the MDI and the DPI cases showed the best approximation of the relative changes in DE from one branch to the next as compared with the Chan and Lippmann (1980) estimates.

Deposition efficiency (DE) results (given in %) are shown for non-constricted and constricted SIP models with MDI and DPI delivery in Tables 4.2-4.5. Data is only presented for the 'constant' and 'proportional decrease' near-wall correction methods as the 'trachea scaled proportional decrease' method showed higher values for all cases of DE in the B4-B7 sections as compared with the Chan and Lippmann (1980) correlation data, but lower values in the B8-B15 sections. As a result, the data produced by the 'trachea scaled proportional decrease' method was the least consistent with the Chan and Lippmann (1980) data since the other methods

yielded relative changes in DE that compared well. Initial inspection of the data shows that DE values as predicted by Chan and Lippmann (1980) in the upper sections (B4-B7) are approximately 2-4 times higher than those predicted by CFD in most cases, but are 2-10 times higher in the lower sections (B8-B15). However, using the 'proportional decrease' method with the SIP models that have numerical extensions appears to yield the most consistent ratio of correlation versus CFD predicted DE values, as in this case the B4-B7 percentages are about 2-4 times greater while the B8-B15 values are about 2-7 times greater.

Statistical analysis of the data confirms that the 'proportional decrease' method applied to SIP models with numerical extensions yields the best approximation with the CFD data of the $\Delta_{Bi\text{-}B(i+1)}$ results from the Chan and Lippmann (1980) data. The Shapiro-Wilk normality test indicated non-normality for the 'constant' and 'proportional decrease' methods that included numerical extensions with the MDI constricted case ($p < 0.0005$ and $p < 0.003$, respectively) and with the DPI constricted case as well ($p < 0.0005$ and $p < 0.002$). Additionally, when the 'constant' and 'proportional decrease' methods were used for the DPI constricted case without numerical extensions, non-normality was shown as well ($p < 0.0009$ and $p < 0.003$). Thus, the Wilcoxon signed-rank test was chosen to evaluate the null hypothesis that the relative differences estimated by the four methods for each case were the same as the correlation data relative differences, as shown in Table 4.6. None of the method and case combinations showed p-values that rejected the null hypothesis. Both methods that used numerical extensions had much higher p-values in nearly every case, except for the MDI constricted case, where the p-values for each method were similarly low. The highest average p-value found was for the 'constant' method when numerical extensions were included ($p = 0.745$), but the 'proportional decrease' method was chosen as the best CFD representation of the correlation data throughout the conducting

airways because it had a similar average p-value (0.616) and provided a better representation of the MDI constricted case.

The distribution of particle mass at the B3 outlets of the upper airway model is given in Table 4.7, which includes the summation of mass amounts leaving both B3 outlets for the LL, LU, and RU lobes. In three out of four cases the LL lobe contains the largest particle mass, which is consistent with the findings of Longest et al. (2012b), where it was found that the LL SIP model was the most representative of branch-averaged DE predictions for delivery from a DPI and a softmist inhaler. For the MDI constricted case, the RU lobe has the greatest particle mass. Particle deposition is illustrated with the LL SIP models in the B4-B7 and B8-B15 sections for all cases in Figure 4.4 and Figure 4.5, since it is most likely to be representative. Deposition efficiency (DE) values in the B4-B7 sections (Figure 4.4) show generally decreasing patterns from B4 to B7, though a small rise in DE is observed from B5 to B6 for both MDI cases, and the DE values for the DPI non-constricted case are nearly steady. As expected, larger particles (> 5 μm) deposit in the B4 and B5 regions. Also notable is that deposition location is typically centered on the carina of each bifurcation, but in the B4 and B5 regions particle deposition is also observed along the straight portions of the airways. The DE values in the B8-B15 sections (Figure 4.5) show an overall decrease from B8 to B12 or B13, but there is a significant increase from that point until B15 for all cases, except the MDI non-constricted case where DE is reduced from B14 to B15. As with the B4-B7 sections there is an initial rise in DE values from B8 to B9, followed by a decreasing pattern. Similar to the pattern in the B4-B7 sections, the location of particle deposition is centered on the carina for all bifurcations, while deposition is also observed on the straight sections of B8 and B9.

A comparison of the CFD data from the 'proportional decrease' method for all cases with that of Chan and Lippmann (1980) is provided in Figure 4.6. The correlation data indicates that for MDI delivery, constriction in the SIP models increases DE approximately two-fold, while for DPI delivery smaller increases are visible. The CFD data does not show dramatic differences, but only smaller local differences, with the largest increase visible from B4-B7 for MDI delivery. Some decrease in DE is visible for the DPI constricted case from B13-B15 as compared with the non-constricted case. Considering the visible trends of the MDI cases in both the correlation and the CFD data, the values of DE rise and fall throughout the SIP models. Generally, the CFD data follows the correlation data for the MDI cases with no large departures, but it does show consistently lower values of DE values as noted above. The changes in DE for both the DPI cases are more dramatic with an initial decrease from B4 to B7, a peak from B7 to B11, and an increase from B11 to B15. The CFD data follows these trends well, with the lone exception occurring from B4 to B5 for the non-constricted DPI case, where a sharp increase is seen rather than a decrease in DE. As with the MDI cases, the CFD predictions of DE are consistently about half as much as the correlation data indicates. Overall, while CFD estimates showed lower DE values as compared with the correlation data, they did show good agreement with the trends in data and consequently the relative changes in DE from one branch to the next were similar.

Regional DF values for the lower airways are given in Table 4.8. For both inhaler types, the amount of drug deposited in the B8-B15 region decreases from the non-constricted cases to the constricted cases, with a reduction from 1.13% to 0.89% for MDI delivery and from 1.08% to 0.81% for DPI delivery. Considering the B4-B7 region, the DPI cases show a decrease from 1.85% in the non-constricted model to 1.38% in the constricted model, while for the MDI cases an increase is observed from 0.73% to 1.40%. This is most likely explained by the rise in DE

values in the B4-B7 regions from the MDI non-constricted case to the MDI constricted case, while a similar rise was not observed for the DPI cases. Similar to the B4-B7 region, DF values in the total lower airway region (B4-B15) show an increase from the MDI non-constricted case to the MDI constricted case of 1.86% to 2.29%, while from the DPI non-constricted case to the DPI constricted case a reduction of 2.93% to 2.19% is observed.

4.4 Discussion

Although inhaled pharmaceutical aerosols are nearly always polydisperse in nature, a direct comparison of the polydisperse data from this study with other published figures was difficult to obtain. Generally, CFD investigations into DF or DE values between non-constricted and constricted airways are conducted by simulating multiple cases with monodisperse particle injections over a certain range as a means of capturing the filtering capacity of the airways of interest (Farkas & Balashazy, 2007; Inthavong, et al., 2010b; Longest, et al., 2006). Moreover, the models considered often focus on a region of interest of only a few bifurcations, as opposed to the comprehensive models considered here (Farkas & Balashazy, 2007; Longest, et al., 2006). Vinchurkar et al. (2012) evaluated thoracic deposition in five patient specific models of asthmatic patients using CFD to predict MDI delivery of beclomethasone propionate/formoterol at 15, 30, and 60 L/min. Thoracic deposition was estimated by Vinchurkar et al. (2012) to be 28.3 ± 8.3%, 26.3 ± 8.6%, and 22.9 ± 8.6% when the aerosol was released between 0 and 0.3 s for the three flow rates, respectively, which were all lower than the 43.9% reported for MDI delivery in this study. This is unexpected since the MMAD of the formulation used by Vinchurkar et al. (2012) was 1.30 μm, which was significantly smaller than the MDI particle distribution used for this study (2.64 μm). However, a true comparison is difficult since the drug

modeled in this study is different (fluticasone propionate), the amount of constriction in the models constructed by Vinchurkar et al. (2012) was not made available, and the boundary conditions used by Vinchurkar et al. (2012) were outlet pressures obtained from an *in vivo* study (De Backer, et al., 2010b) as opposed to velocity inlet boundary condition used by this study that was validated with *in vitro* data from Longest et al. (2012d). All of these differences may lead to significantly different predictions, and it would be useful for future study to focus on acquisition of *in vivo* or *in vitro* data of fluticasone propionate with asthmatic subjects and/or models with defined levels of constriction.

The first known DF estimates in the small lower airway region (B8-B15) of an asthmatic airway were produced for this study considering both MDI and DPI delivery. Comparison of the DPI non-constricted DF value in the B8-B15 region with the results of Longest et al. (2012b) indicate 1.08% for the Flovent Diskus DPI in this study as opposed to 0.9% with the Novolizer DPI (Longest, et al., 2012b). Though the results from the different inhalers are not expected to be equal, the similar values lend confidence to the methods employed by this study. The reductions in DF values in the B8-B15 region for both MDI and DPI delivery from the non-constricted to the constricted models were 0.24% and 0.27%, respectively. On a relative basis these are significant decreases (21% and 25%, respectively), though clinical testing is desired for further understanding of the impact of these predicted differences.

Statistical analysis showed that the values of $\Delta_{Bi\text{-}B(i+1)}$ obtained from CFD with the 'proportional decrease' with numerical extensions method were not significantly different from those taken from the correlation data of Chan and Lippmann (1980). However, as expected, a Wilcoxon signed-rank test confirmed that all sets of DE values from each case as predicted by CFD were significantly different from the correlation data. One potential cause of the

discrepancy in the raw data is the method for transitioning from the transient upper airway models to the steady state SIP models. For this study, the flow field was interpolated to each SIP model at the time step when the mean flow rate occurred for each inhaler, though this may not capture all of the relevant features of the flow that contribute to deposition. For instance, a flow rate closer to the peak value may be a more appropriate choice, since the bulk of deposition by impaction may occur in that time frame. Since the primary focus was the improvement of near-wall corrections of particle trajectories in CFD to improve accuracy of DF and DE predictions, the flow rate of interpolated fluid velocities was not a study design variable, but would be an excellent focus for future study.

Several other limitations may explain differences in the CFD and correlation data. It was assumed that five SIP models would provide an adequate representation of branch-averaged DE, but the addition of more models may significantly affect the data. Also, since the study was commenced during the development of Model D, that model was not available, and it was shown in Chapter 3 and Walenga et al. (2013) to provide more accurate estimates of DF in the MT and TB regions. The constricted models were constructed assuming a 30% diameter reduction based on the data from Brown and Mitzner (2003), but a heterogeneous reduction of diameter based on lung imaging of asthmatic patients would provide greater physiological accuracy. The combination of transient and steady simulations with interpolation of fluid velocities and particle trajectories is a large assumption that was necessary for practical implementation of CFD predictions, but any method that could reasonably circumvent these assumptions would presumably improve accuracy significantly. For computational efficiency turbulence was modeled using a RANS approximation, but a model that captures more of the eddy characteristics, such as a large eddy model, would provide a more complete physical

representation of the deposition mechanisms. Lastly, though the data of Chan and Lippmann (1980) presumably provides good estimates of branch-averaged DE, *in vitro* data from Model C in the SIP models would provide a more exact basis of comparison, though the practical difficulties associated with obtaining experimental data with airways as small as 0.45 mm present a significant challenge.

Though a significantly similar data set was desired from the CFD predictions as compared with the correlation data, the Chan and Lippmann (1980) correlation has limitations. It was derived from a cast model that extended to the sixth bifurcation, so it is unknown how accurate it may be considered past that bifurcation. In addition, the *in vitro* data from which it is derived showed a great deal of scatter, with as much as an order of magnitude difference between DE values for a given Stokes number. Finally, the predictions of the Chan and Lippmann (1980) data are based on a cast model with a glottic aperture, which is likely different from the Model C dimensions (Xi, et al., 2008). However, the purpose of comparing the CFD data with the correlation predictions was not to provide a validation, but rather a confirmation of expected trends in the lower airways and to determine if the estimates are within an order of magnitude of each other. Both of those objectives were accomplished through that comparison. For a true validation of the CFD data, a comparison with *in vivo* data on a branch-averaged basis is required. A recent study by Majoral et al. (2014) has provided this kind of data using 2D and 3D lung imaging, and it would be a good source of comparison for future study with CFD.

Regional DF and branch-averaged DE values were predicted using CFD methods in conjunction with improved near-wall corrections of particle trajectories for MDI and DPI delivery through non-constricted and asthma constricted lung models from the MT through B15. Branch-averaged values of DE were compared in the lower airways with data from an existing

correlation. For both MDI and DPI delivery, airway constriction yielded predictions of upper airway DF that were about twice as high as the non-constricted counterparts. The effect of constriction on lower airway branch-averaged DE values was more complicated, with obvious increases visible in the correlation data for the constricted cases and opposed to the non-constricted cases, while the CFD data did not show many large differences. The branch-averaged DE predictions obtained from the CFD data were used to provide the first known CFD estimates of DF in the small lower airways (B8-B15) for an asthmatic subject, where it was shown that values were reduced from the non-constricted to the constricted models by 0.24% and 0.27% for MDI and DPI delivery, respectively. Values of branch-averaged DE predicted with CFD showed significant differences as compared with the correlation data as predicted by Chan and Lippmann (1980). However, relative differences in DE between adjacent bifurcations did not show significant statistical differences between the CFD and correlation data. Future study may focus on adjustment of interpolated flow rate value from the transient upper airway models to the steady state SIP models as a means of validating branch-averaged *in vivo* DE data using CFD predictions.

Table 4.1 Average bifurcation diameter (given in mm) from the fourth bifurcation (B4) to the fifteenth bifurcation (B15) for the non-constricted and constricted pathways in the five SIP models: left lower left (LL), left upper right (LU), right lower (RL), right middle (RM), and right upper right (RU).

	Non-Constricted					Constricted				
Bifurcation	**LL**	**LU**	**RL**	**RM**	**RU**	**LL**	**LU**	**RL**	**RM**	**RU**
B4	7.38	7.14	8.64	6.16	6.50	5.42	5.00	6.04	4.31	4.55
B5	6.13	5.65	6.84	4.88	5.15	4.29	3.96	4.79	3.41	3.60
B6	4.98	4.60	5.56	3.96	4.18	3.49	3.22	3.89	2.77	2.93
B7	4.46	4.12	4.98	3.55	3.75	3.12	2.88	3.49	2.49	2.62
B8	3.61	3.33	4.03	2.87	3.03	2.53	2.33	2.82	2.01	2.12
B9	2.81	2.60	3.14	2.24	2.36	1.97	1.82	2.20	1.57	1.65
B10	2.66	2.46	2.97	2.12	2.23	1.86	1.72	2.08	1.48	1.56
B11	2.43	2.24	2.71	1.93	2.04	1.70	1.57	1.90	1.35	1.43
B12	1.91	1.76	2.13	1.52	1.60	1.34	1.23	1.49	1.06	1.12
B13	1.39	1.28	1.55	1.10	1.17	0.97	0.90	1.09	0.77	0.82
B14	1.03	0.95	1.15	0.82	0.87	0.72	0.67	0.81	0.57	0.61
B15	0.77	0.71	0.86	0.61	0.65	0.54	0.50	0.60	0.43	0.45

Table 4.2 Deposition efficiency (DE) predictions (given in %) for metered dose inhaler (MDI) delivery in non-constricted lung airways from the fourth bifurcation (B4) through the fifteenth bifurcation (B15). Analytical predictions are based on the correlation developed by Chan and Lippmann (1980), while the other data is based on CFD predictions from this study for models with and without numerical extensions, and with and without proportional decrease of near-wall limits of drag and turbulence corrections.

		Extensions		No Extensions	
Bifurcation	**Chan and Lippmann (1980)**	**Constant**	**Proportional Decrease**	**Constant**	**Proportional Decrease**
B4	1.09	0.34	0.38	0.33	0.32
B5	1.09	0.43	0.46	0.36	0.40
B6	1.04	0.43	0.52	0.34	0.42
B7	0.86	0.20	0.18	0.25	0.20
B8	0.86	0.20	0.24	0.22	0.29
B9	0.97	0.30	0.43	0.32	0.40
B10	0.82	0.26	0.34	0.18	0.28
B11	0.97	0.22	0.28	0.14	0.23
B12	1.22	0.11	0.18	0.13	0.25
B13	0.96	0.09	0.23	0.02	0.12
B14	1.10	0.07	0.38	0.03	0.10
B15	1.27	0.35	0.38	0.04	0.13

Table 4.3 Deposition efficiency (DE) predictions (given in %) for metered dose inhaler (MDI) delivery in constricted lung airways from the fourth bifurcation (B4) through the fifteenth bifurcation (B15). Analytical predictions are based on the correlation developed by Chan and Lippmann (1980), while the other data is based on CFD predictions from this study for models with and without numerical extensions, and with and without proportional decrease of near-wall limits of drag and turbulence corrections.

		Extensions		No Extensions	
Bifurcation	**Chan and Lippmann (1980)**	**Constant**	**Proportional Decrease**	**Constant**	**Proportional Decrease**
B4	3.47	1.96	1.82	1.56	1.59
B5	2.37	0.84	0.98	0.88	0.98
B6	3.14	0.71	1.26	0.87	1.14
B7	2.07	0.35	0.52	0.46	0.68
B8	2.22	0.28	0.44	0.48	0.63
B9	2.38	0.21	0.55	0.67	1.13
B10	1.67	0.22	0.44	0.59	0.71
B11	1.53	0.19	0.29	0.40	0.64
B12	1.79	0.17	0.27	0.52	0.35
B13	1.69	0.07	0.35	0.10	0.21
B14	1.98	0.07	0.36	0.14	0.31
B15	2.10	0.17	0.33	0.17	0.09

Table 4.4 Deposition efficiency (DE) predictions (given in %) for dry powder inhaler (DPI) delivery in non-constricted lung airways from the fourth bifurcation (B4) through the fifteenth bifurcation (B15). Analytical predictions are based on the correlation developed by Chan and Lippmann (1980), while the other data is based on CFD predictions from this study for models with and without numerical extensions, and with and without proportional decrease of near-wall limits of drag and turbulence corrections.

		Extensions		No Extensions	
Bifurcation	**Chan and Lippmann (1980)**	**Constant**	**Proportional Decrease**	**Constant**	**Proportional Decrease**
B4	5.10	2.53	2.64	2.53	2.57
B5	4.21	3.64	3.85	3.70	3.90
B6	3.49	2.43	2.55	2.05	2.39
B7	2.39	1.41	1.80	1.46	1.49
B8	2.20	0.31	0.92	0.44	0.77
B9	2.29	1.39	1.37	1.11	1.41
B10	1.56	0.56	0.65	0.49	0.68
B11	1.38	0.35	0.42	0.34	0.46
B12	1.56	0.30	0.35	0.28	0.49
B13	1.50	0.60	0.74	0.21	0.36
B14	1.72	0.41	0.83	0.23	0.41
B15	1.97	1.22	1.51	0.23	0.52

Table 4.5 Deposition efficiency (DE) predictions (given in %) for dry powder inhaler (DPI) delivery in constricted lung airways from the fourth bifurcation (B4) through the fifteenth bifurcation (B15). Analytical predictions are based on the correlation developed by Chan and Lippmann (1980), while the other data is based on CFD predictions from this study for models with and without numerical extensions, and with and without proportional decrease of near-wall limits of drag and turbulence corrections.

		Extensions		No Extensions	
Bifurcation	**Chan and Lippmann (1980)**	**Constant**	**Proportional Decrease**	**Constant**	**Proportional Decrease**
B4	5.97	3.20	3.19	3.00	3.03
B5	4.58	2.60	2.80	3.99	4.18
B6	4.02	1.01	1.22	1.78	2.22
B7	1.69	0.52	0.57	0.71	0.82
B8	2.59	0.55	0.97	0.71	1.03
B9	2.69	0.62	0.89	0.93	1.16
B10	1.68	0.34	0.60	0.44	0.70
B11	1.26	0.20	0.26	0.33	0.41
B12	1.34	0.27	0.30	0.45	0.43
B13	1.52	0.36	0.51	0.38	0.54
B14	1.79	0.22	0.62	0.47	0.61
B15	2.02	0.52	0.79	0.49	0.58

Table 4.6 Wilcoxon signed-rank test p-values for method and case combinations, with the average p-value for each method listed below.

		Extension		No Extension	
		Constant	Proportional Decrease	Constant	Proportional Decrease
MDI	**Non-constricted**	0.966	0.831	0.102	0.577
	Constricted	0.083	0.148	0.175	0.068
DPI	**Non-constricted**	0.966	0.966	0.240	0.240
	Constricted	0.966	0.520	0.700	0.322
	Average	0.745	0.616	0.304	0.302

Table 4.7 Distribution of particle mass at B4 inlets of the five SIP models for MDI and DPI cases in non-constricted and constricted geometries. The mass values of each case are normalized against the mean.

	MDI		DPI	
	Non-Constricted	**Constricted**	**Non-Constricted**	**Constricted**
LLL	1.332	1.010	1.316	1.308
LUR	1.066	1.130	1.051	1.032
RL	1.154	1.079	1.274	1.245
RM	0.366	0.395	0.361	0.365
RUR	1.082	1.386	0.997	1.050

Table 4.8 Deposition fraction (DF) values (given in %) in the B4-B7, B8-B15 and B4-B15 regions for all cases. The values of DF in each region are the summation of results from all five lobes.

		Deposition Fraction (DF)		
		B4-B7	**B8-B15**	**B4-B15**
MDI	**Non-constricted**	0.73	1.13	1.86
	Constricted	1.40	0.89	2.29
DPI	**Non-constricted**	1.85	1.08	2.93
	Constricted	1.38	0.81	2.19

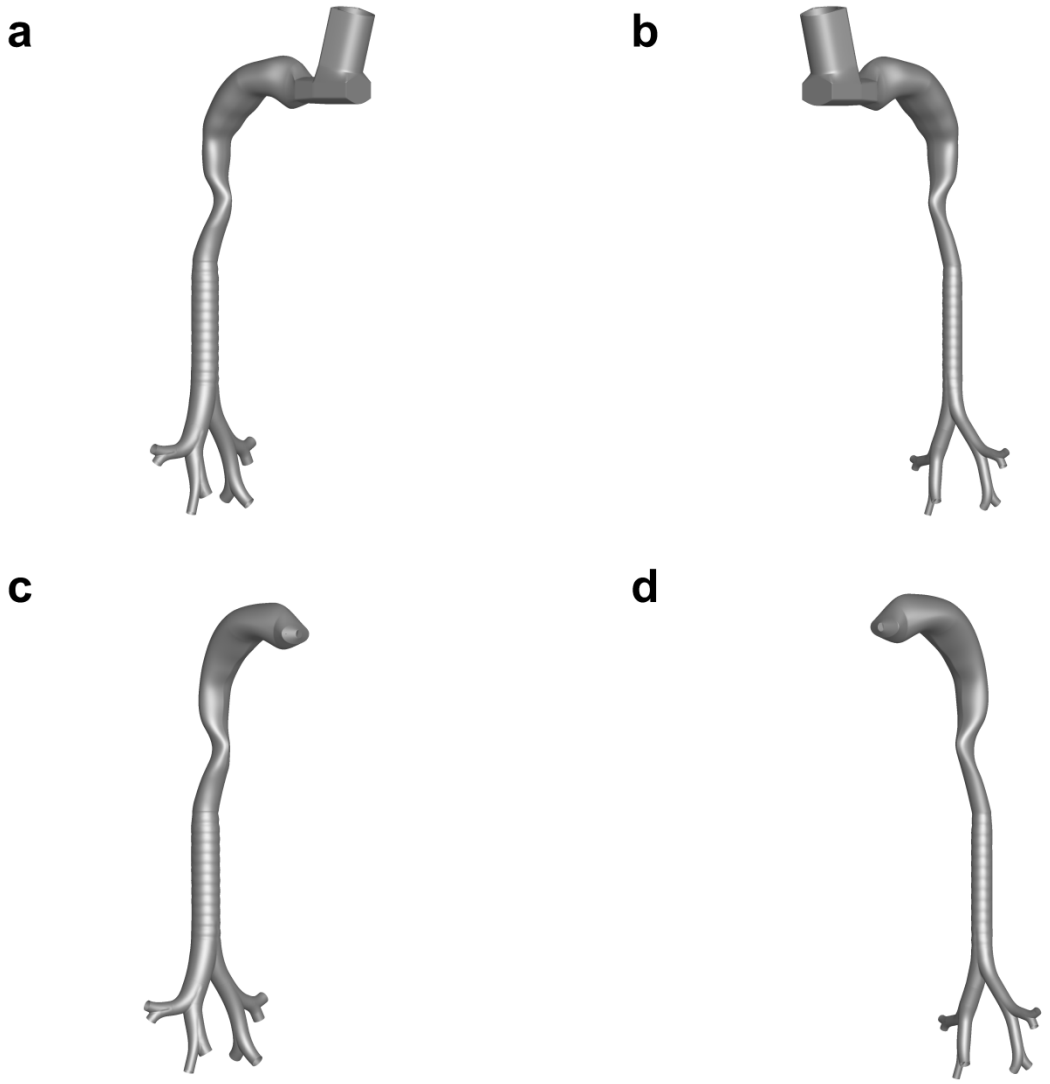

Figure 4.1 Interior airspace of non-constricted and constricted Model C with a metered dose inhaler (MDI) (a and b) and with a dry powder inhaler (DPI) (c and d).

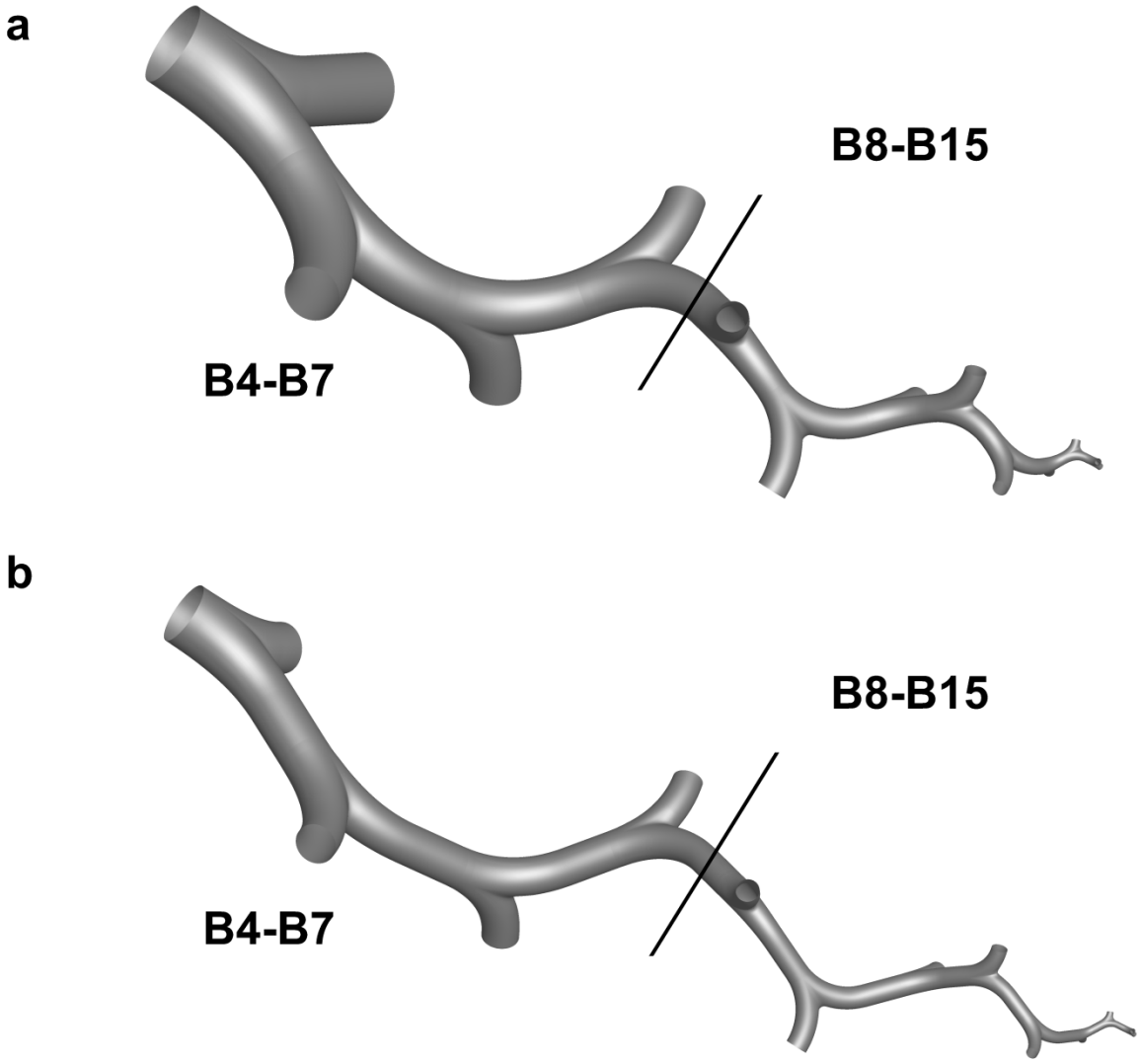

Figure 4.2 Stochastic individual path (SIP) models of the left lower (LL) lobe from the fourth bifurcation (B4) through the fifteenth bifurcation (B15) for the (a) non-constricted and (b) constricted case. The models are divided at the interface of B4-B7 and B8-B15 to illustrate the division in the CFD predictions.

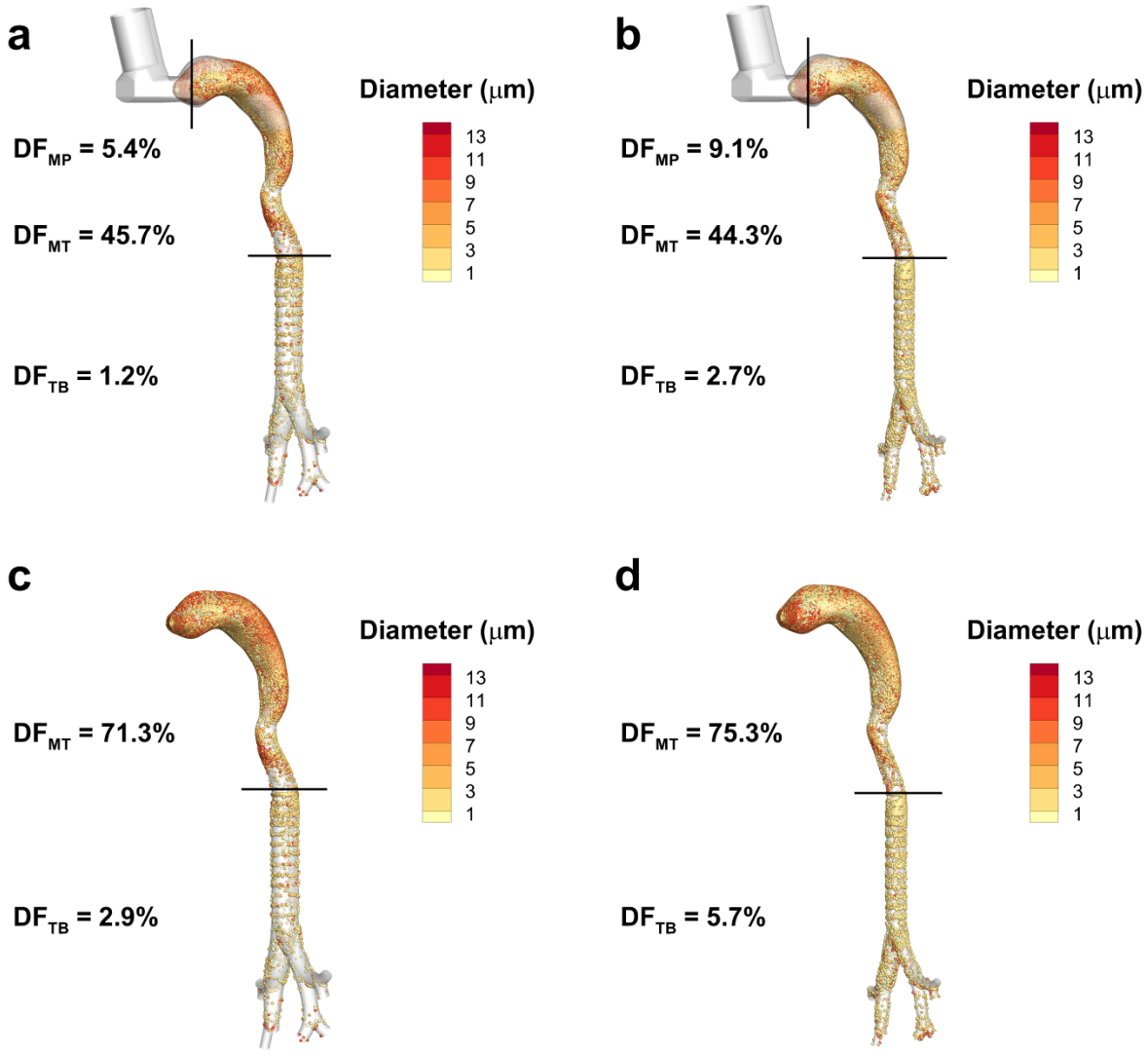

Figure 4.3 Deposition fraction (DF) predictions in the mouthpiece (MP), mouth-throat (MT) and tracheobronchial (TB) regions for the non-constricted and constricted airways with metered dose inhaler (MDI) delivery (a and b) and with dry powder inhaler (DPI) delivery (c and d). Deposition in the MP is only considered for MDI delivery.

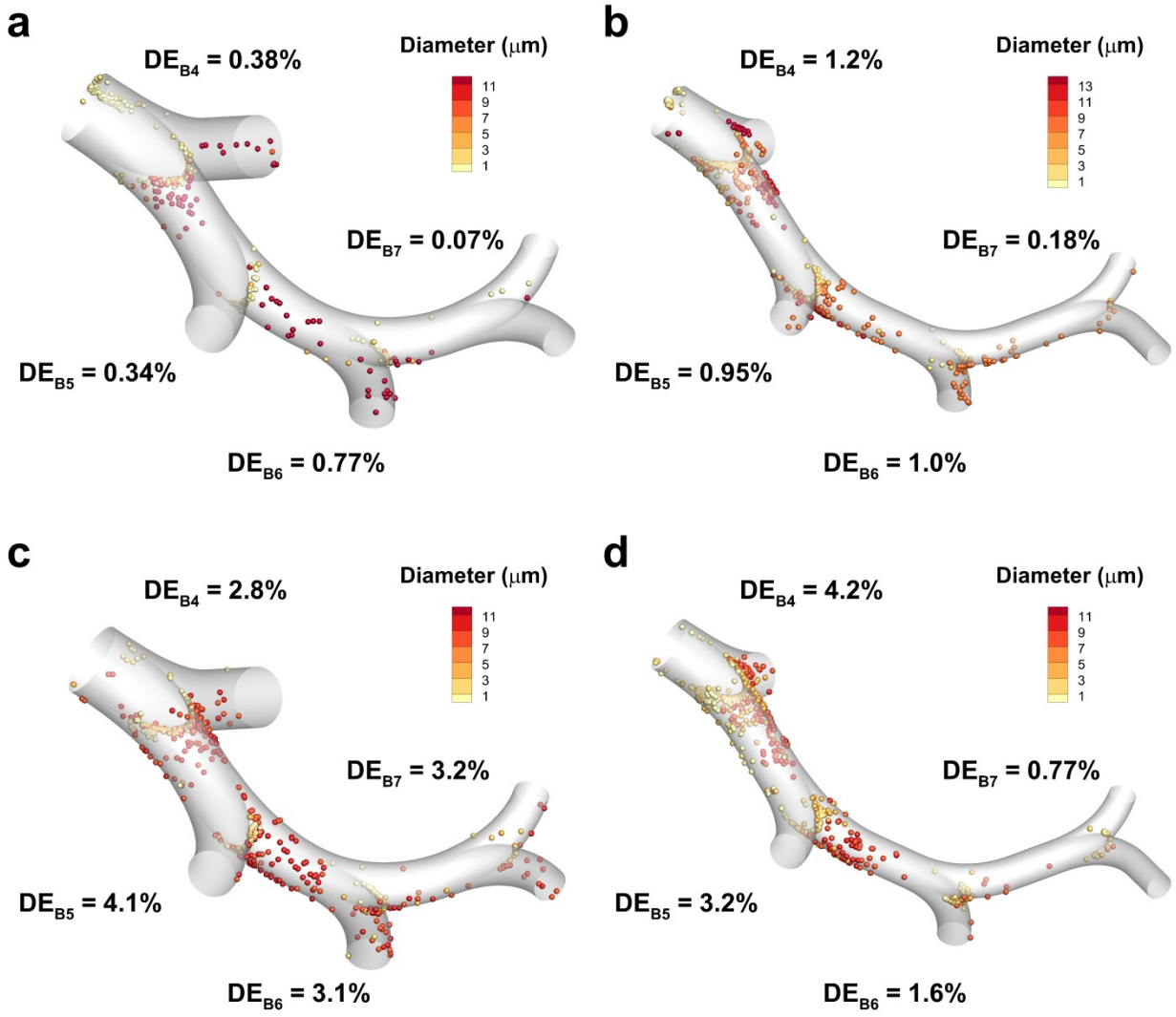

Figure 4.4 Deposition efficiency (DE) estimates based on CFD predictions for the fourth through the seventh bifurcation (B4-B7) of the left lower (LL) lobe stochastic individual path (SIP) model. The cases presented are for non-constricted and constricted airways with metered dose inhaler (MDI) delivery (a and b) and with dry powder inhaler (DPI) delivery (c and d)

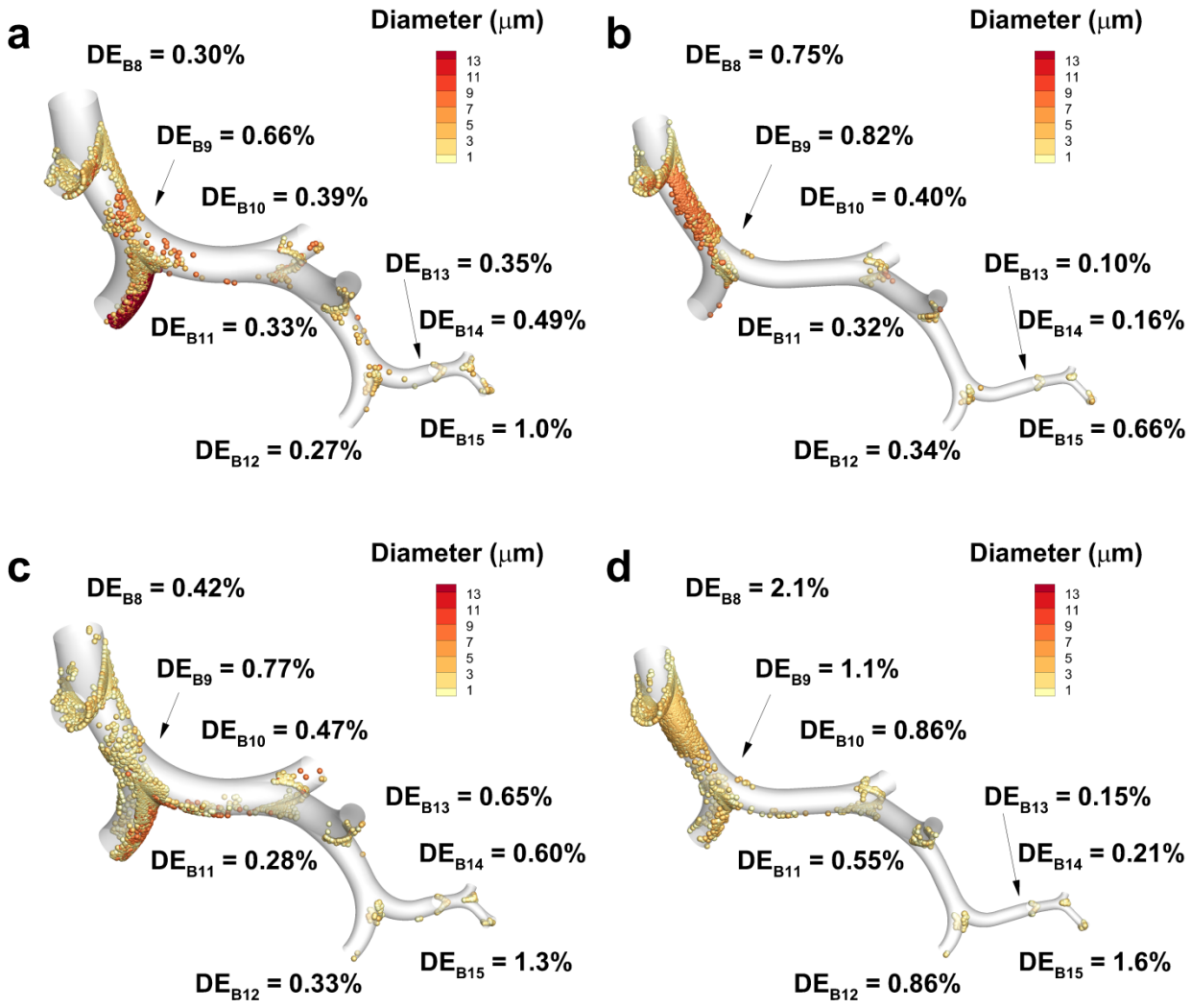

Figure 4.5 Deposition efficiency (DE) estimates based on CFD predictions for the eighth through the fifteenth bifurcation (B8-B15) of the right lower (RL) lobe stochastic individual path (SIP) model. The cases presented are for non-constricted and constricted airways with metered dose inhaler (MDI) delivery (a and b) and with dry powder inhaler (DPI) delivery (c and d).

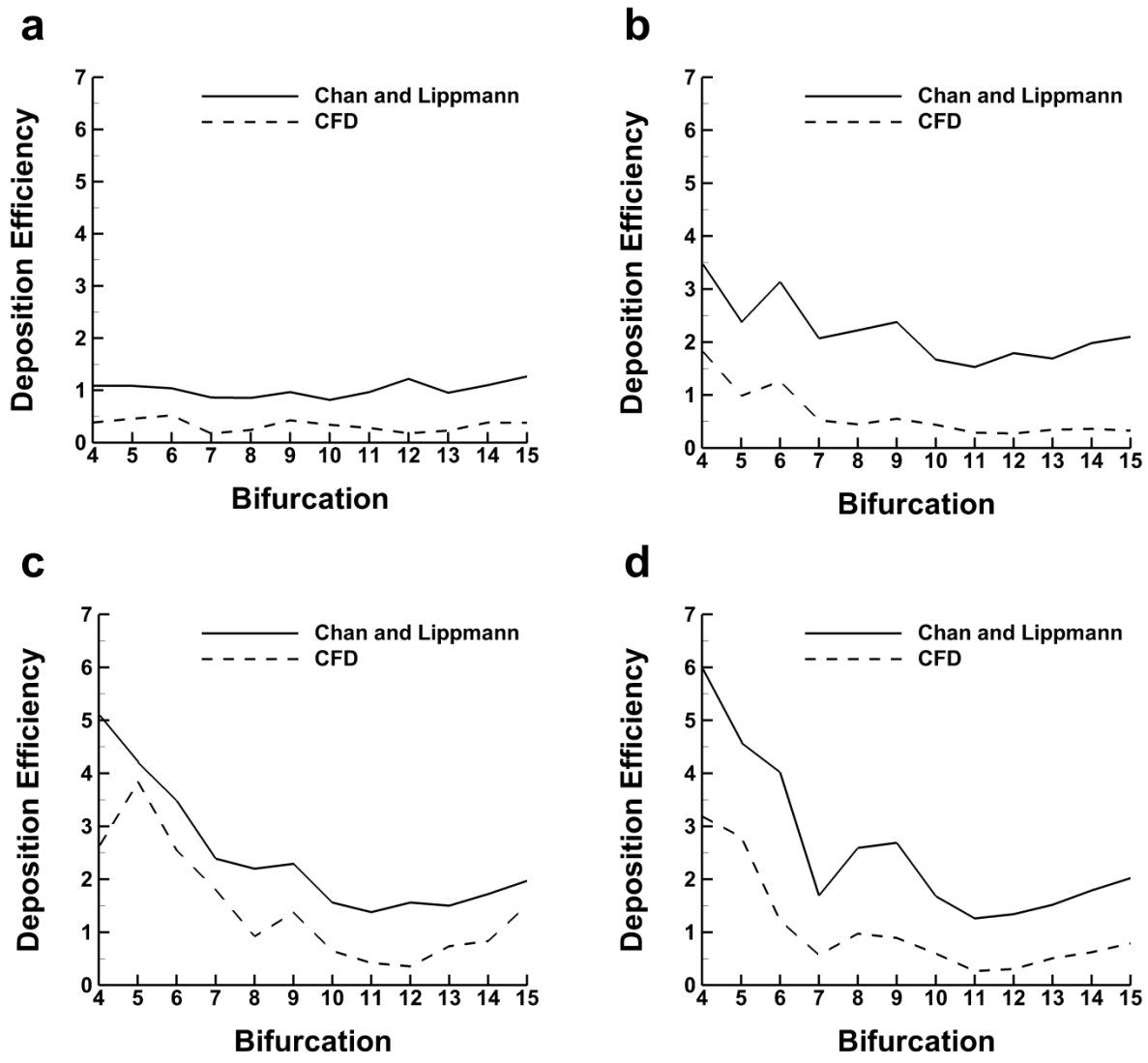

Figure 4.6 Deposition efficiency (DE) predictions from the fourth bifurcation (B4) through the fifteenth bifurcation (B15) for the non-constricted and constricted airways with metered dose inhaler (MDI) delivery (a and b) and with dry powder inhaler (DPI) delivery (c and d). The empirical correlation from Chan and Lippmann (1980) is applied to each case and compared with CFD results.

Chapter 5 Mixer-Heater Construction and Development

The objective of this study was to construct, test, and optimize an improved mixer-heater capable of drying and heating nebulized aerosols at room temperature with an initial mass median aerodynamic diameter (MMAD) of 3.9 μm to an outlet MMAD of about 0.9 μm at human body temperature for flow rates up to 15 L/min.

5.1 Introduction

An *in vitro* version of an improved mixer-heater design proposed by Longest et al. (2013c) was constructed, tested and optimized. The new design was predicted by Longest et al. (2013c) to be capable of producing dried, heated submicrometer particles for both excipient enhanced growth (EEG) and enhanced condensational growth (ECG) delivery, which are delivery techniques outlined in Section 2.3.1. Longest et al. (2013c) improved upon the previously existing radial design (shown in Figure 5.1a) of Longest et al. (2012a) through the use of CFD as a design and optimization tool. The improved mixer-heater computational design (pictured in Figure 5.1b) was then adapted for this study using CAD software to produce a physical model that was rapid prototyped using a stereolithography (SLA) machine, and then assembled to include aluminum conducting plates. Testing of the model yielded several improvements to the system, including the removal of initially designed vents, the addition of Kapton® film heaters, and the inclusion of diffuser plates. Respectively, these changes allowed

for the mixer-heater to be operated with a lower inlet flow rate, to eliminate the need for heating the inlet air supply, and for more even mixing of the aerosol. Experiments showed that the model was capable of delivering a heated flow at the outlet of about 35 °C at 15 L/min, which was considered acceptable. Longest et al. (2013c) used the new *in vitro* model to show that the improved mixer-heater was capable of providing submicrometer aerosols at the outlet and reducing depositional loss by a factor of three when compared with the original radial design. After the completion of the steady state *in vitro* improved mixer-heater, a transient version was designed and produced which included fans that may be controlled to provide aerosol delivery only during inhalation, with the goal of reducing losses during exhalation. The losses in the stand-alone model were predicted with CFD for this manuscript and compared with the experimental data of Golshahi et al. (2014b) with which good agreement was found. The predictions also indicated that the system was capable of producing submicrometer aerosols with minimal losses. Golshahi et al. (2014b) used the transient mixer-heater to show that for a patient receiving medication through the system with her mouth open to allow excess flow to escape, delivered doses of 83-93% and 72-77.5% may be possible for EEG and ECG delivery, respectively.

5.2 Methods

The *in vitro* improved mixer-heater was constructed with blowers and controls for the completion of this objective. In the initial improved mixer-heater design specified by Longest et al. (2013c), the inlet airstream flow rate was set at 80 L/min and then the outlet vents at the top of the mixer-heater were adjusted to produce the desired outlet flow rate (5-15 L/min). This was believed to provide a good balance between maximizing heat transfer at a safe temperature and

providing the desired flow rates (Longest, et al., 2013c). Air flow was provided by an in-house compressed air source, which had a measured relative humidity (RH) of 5%, and was divided by a custom built manifold (Longest, et al., 2013c). The initial design called for a heated inlet airstream, as indicated by Figure 5.1b, but the version tested for this objective used Kapton® film heaters (OMEGALUX KHLV-202; Omega Engineering, Inc.) that were adhered to the conducting plates in the inlet side channels.

A hollow version of the initial computational model outlined by Longest et al. (2013c) was created with CAD software (GAMBIT 2.4, ANSYS, Inc., Canonsburg, PA, USA), which was designed with 2 mm thick walls. Stereolithography (SLA) was implemented to rapid prototype the model with a Viper SLA system (3D Systems, Valencia, CA, USA) using Accura 60 clear plastic resin. Aluminum conducting plates (1 mm thick) were inserted into the model, which was built in sections and then joined with epoxy. For the purposes of testing the mixer-heater for heating capacity and the presence of excess condensation, a formulation of 0.1% w/v sucrose in water solution was used. Inlet airflow of 80 L/min was heated by employing a constant voltage in parallel with the two Kapton® film heaters and varying it on a trial by trial basis to find the correct value that produced at least 35°C at the outlet after two minutes.

After the final version of the *in vitro* steady state mixer-heater was completed (as described in Section 5.3), a transient mixer-heater was designed (Figure 5.2). The compressed air inlet of the original improved mixer-heater was replaced with two fans (Dynatron 12 V DC Blowers, Fremont, CA, USA) which allowed for a variable input that may be adjusted to produce a nearly sinusoidal inhalation profile. Additionally, the use of fans improved the portability of the design which did not require a compressed air source. The sinusoidal profile was produced by controlling the fans with a waveform generator (Agilent 33120A, Santa Clara, CA, USA)

which was connected an amplifier/power supply (Accel TS200-1B, Irvine, CA, USA). To produce the desired profile, a duty cycle of 25% was implemented to allow for activation of the fans during the 1st second of the 4 second period, which was set by using a sinusoidal profile in the waveform generator at a frequency of 250 mHz. Air flow rate was adjusted by varying waveform generator voltages between 200-990 mVpp, which was amplified to 9-17 V. Besides the addition of fans, the transient design was also reduced in size from a height, width, and depth of 12.4 x 16.8 x 13.7 cm in the improved design to 9 x 8 x 8 cm in the new design. Also, to prevent exposure of the aerosol through the fans, two low resistance one-way valves (Hudson RCI, Teleflex, Research Triangle Park, NC, USA) were attached to the external surfaces of the fans. As described is Section 5.3 of this study, optimization of the improved mixer-heater called for flow diffusers in the inlet side channels, which are added to the transient design as well, that include 10 cylindrical channels with height and radius of 0.2 x 0.2 cm.

The top section of the transient mixer-heater was optimized with the goal of reducing aerosol losses in the mixing region and in the backflow, through the creation of three different models (straight, curved, and perforated), as shown in Figure 5.3. The straight design represented the control case as it was identical to the original section. The perforated design used a porous wall to limit backflow through the inlet channels when the fans were not in operation (i.e. during exhalation conditions), while the curved design sought to achieve the same goal through the addition of curvature (radius of 0.8 cm) to the dividing plates at the entrance to the mixing region.

Particle deposition in the transient mixer-heater was predicted using computational fluid dynamics (CFD) to allow for visualization of the particle paths. The mesh was constructed using the ANSYS ICEM 10 package (ANSYS, Inc., Canonsburg, PA, USA), and it consisted of

approximately 1.1 million cells. A two-way coupled simulation was performed using ANSYS FLUENT 12.0.16 (ANSYS, Inc., Canonsburg, PA, USA) that modeled the interactions between the flow field and the injected droplets. Due to the computationally intensive nature of a two-way coupled simulation, a transient simulation was considered intractable, and thus the flow field was approximated with a steady state solution. Zhang et al. (2002) showed that the deposition efficiency (DE) in a transient system may be approximated by a steady state solution that employs a flow field with a Reynolds number that is the average of the periodic mean and the maximum. The periodic mean flow rate from breathing profile 1 was 7.7 L/min and the maximum was 23.1 L/min, which was averaged to a flow rate (15.4 L/min) that was utilized for the steady state solution. The simulation of a two-way coupled flow field accounting for droplet evaporation with hygroscopic effects, mass fraction of water vapor in the air, heat transfer, and turbulent mixing was previously described by Longest et al. (2013c) and those methods were included in the current study.

As described by Longest et al. (2013c), the CFD solution included the use of a Low Reynolds number (LRN) k-ω turbulence model, the implementation of user defined functions (UDFs) to provide near-wall corrections for turbulence and velocity, and the modeling of heat transfer and species transport (of the air-water vapor mixture). The LRN k-ω model has been shown to provide accurate predictions of aerosol trajectories and deposition (Longest & Vinchurkar, 2007b; Xi & Longest, 2007; Xi, et al., 2008). Regarding the boundary conditions of the model, the temperature of the heated plates was set as 50 °C, while the temperatures of the aerosol and air inlets were held at 21°C. The relative humidity (RH) of the aerosol and air inlets was set as 100% RH and 50% RH, respectively, whereas the walls were considered initially dry (zero diffusive mass flux of water vapor). The droplets from the Aeroneb Lab nebulizer were

modeled as a monodisperse bolus with an initial droplet size of 3.9 μm, which was the mass median aerodynamic diameter (MMAD) of the polydisperse aerosol as reported by Longest et al. (2012a). For the two-way coupled flow field corrections, a bolus of 1,500 droplets, representing the entire mass of injected droplets, was used in order to complete the simulation more efficiently. For predicting droplet deposition, following completion of the flow field simulation, a bolus of 6,000 droplets with a tracking accuracy tolerance of 10^{-5} was utilized to maximize accuracy.

5.3 Results

Regarding the two proposed methods of heating the airstream for the improved mixer-heater, the use of Kapton® film heaters was first tested. Upon testing the system at 80 L/min, it was found that 28 V was required to produce an outlet flow temperature of 35°C, but that sealing the vents allowed for a lower voltage (24 V) to be applied at a lower flow rate (about 23 L/min). The temperature of the model near the conducting plates was checked and found to be about 50°C, which is below the glass transition temperature of Accura 60 (~60°C). Since the system was capable of producing the required airflow at a reasonable outlet temperature at a lower flow rate and voltage, a sealed system (without vents) was constructed. Another consequence of the success of the film heaters is that the need for a heated airstream was eliminated in favor of the more easily operated film heaters. Another modification was made to the new sealed system after the initial testing, which was the inclusion of flow diffusers in the inlet side channels for the purpose of reducing asymmetry in the delivery of the inlet airstream, which was observed due the fact that the inlet airstream initially enters horizontally and then abruptly turns 90° to a vertical orientation. The new diffusers, which included 10 cylindrical holes that had a depth and

radius of 0.2 x 0.2 cm each, allowed the flow to be more evenly distributed and promoted more complete mixing. The new improved mixer-heater was tested by colleagues in the VCU Department of Pharmaceutics for depositional and sizing characteristics, and found to produce submicrometer aerosols at the exit and to reduce depositional losses by a factor of three as compared to the original radial design (Longest, et al., 2013c).

The transient mixer-heater was tested and found capable of producing the desired flow rates. Colleagues in the VCU Department of Pharmaceutics tested the three top section designs as outlined in Figure 5.3 and found that the emitted dose and peak flow rate through the outlet was higher for the straight version, so this section was adopted for further use (Golshahi, et al., 2014b). As shown in Figure 5.4, the CFD predictions of the transient mixer-heater are shown and compared with the experimental data of Golshahi et al. (2014b). The mixer-heater was tested by Golshahi et al. (2014b) without the *in vitro* setup (tube, nasal cannula, NMT model, and breathing simulator) by introducing aerosols generated by the Aeroneb Lab nebulizer from a solution of 0.2% AS: 0.2% NaCl in water. The average emitted dose was reported as 96.9% with a standard deviation (SD) of 2.2%, leading to the estimate of 3.1% depositional loss in the system (Golshahi, et al., 2014b). Then, as shown in Figure 5.4, the prediction of 2.5% depositional loss in the mixer-heater produced for this study was in good agreement with the experimental results of Golshahi et al. (2014b) and indicated that the system was capable of delivering the aerosol with minimal losses.

A brief summary of other findings from Golshahi et al. (2014b) is provided here for context. Colleagues in the VCU Department of Pharmaceutics found that when the mixer-heater was attached to an *in vitro* setup that included a tube, nasal cannula, realistic nose-mouth-throat (NMT) model, and breathing simulator, that high emitted doses were possible with both

excipient enhanced growth (EEG) and enhanced condensational growth (ECG), two methods that are outlined in Section 2.3.1 of this dissertation (Golshahi, et al., 2014b). Specifically, they showed that with a closed mouth model, the nasally delivered aerosol achieved delivery rates of 70-92% and 58-63% for the EEG and ECG cases (Golshahi, et al., 2014b). Allowing exhalation flow to escape through an open mouth improved delivered dose even more, resulting in rates of 83-93% and 72-77.5% of the initial drug for EEG and ECG delivery (Golshahi, et al., 2014b).

5.4 Discussion

The models produced for this study are intended to provide support to future proof of concept studies that will explore more specific applications of EEG and ECG delivery of dried and heated aerosols from the two designs. Potential delivery modes include high flow nasal cannula (HFNC) therapy and noninvasive positive pressure ventilation (NPPV), which are both explored in Chapters 6, 7, and 8. Current limitations of the models include a construction material with a low glass transition temperature, an inability of the transient model to adapt to a real patient's breathing cycle, and the potential for re-breathing of exhaled aerosols. The current models employ heating to temperatures near the glass transition temperature of Accura 60 such that they may be subjected to melting if higher output temperatures are desired. Moreover, if the models are to be developed for commercial production in the future, the safety concerns generated by models at ~50 °C would need to be addressed, perhaps by the addition of some outer insulation. The transient model is designed to output a fixed breathing profile, which is adequate for proof of concept studies, but commercial development would require that it adapt to the patient's breathing profile in a synchronous manner. Golshahi et al. (2014b) explored the effect of backflow on emitted dose and found that open-mouthed NMT model allowed for

reductions in backflow that were significantly related to an increase in emitted dose. However, the effect of possible exposure hazards due to exhaled aerosols has not been considered, and thus an optimal solution to the problem of emitted dose reduction due to backflow has yet to be identified.

In summary, steady state and transient versions of an improved mixer-heater design were adapted for three dimensional fabrication and *in vitro* testing. The process of adapting of the steady state design yielded several improvements, including the use of a sealed design that allowed for both a lower flow rate and applied voltage, the application of portable Kapton® film heaters as opposed to the more cumbersome heated air supply, and the addition of flow diffusers to even out the air supply prior to mixing. Testing showed that the rapid prototyped *in vitro* model was capable of producing 35°C flow with dried particles that were confirmed by colleagues in the VCU Department of Pharmaceutics to be in the submicrometer range and to reduce depositional losses by a factor of three. A transient version of the improved mixer-heater design was also adapted for fabrication and testing, and it was found to produce an approximately sinusoidal profile with a 4 s period that showed temperatures in the desired range. Golshahi et al. (2014b) performed a stand-alone test of the transient mixer heater and reported 96.9% delivery of 0.2% AS: 0.2% NaCl in water and those results were confirmed by CFD testing performed by the author of this study.

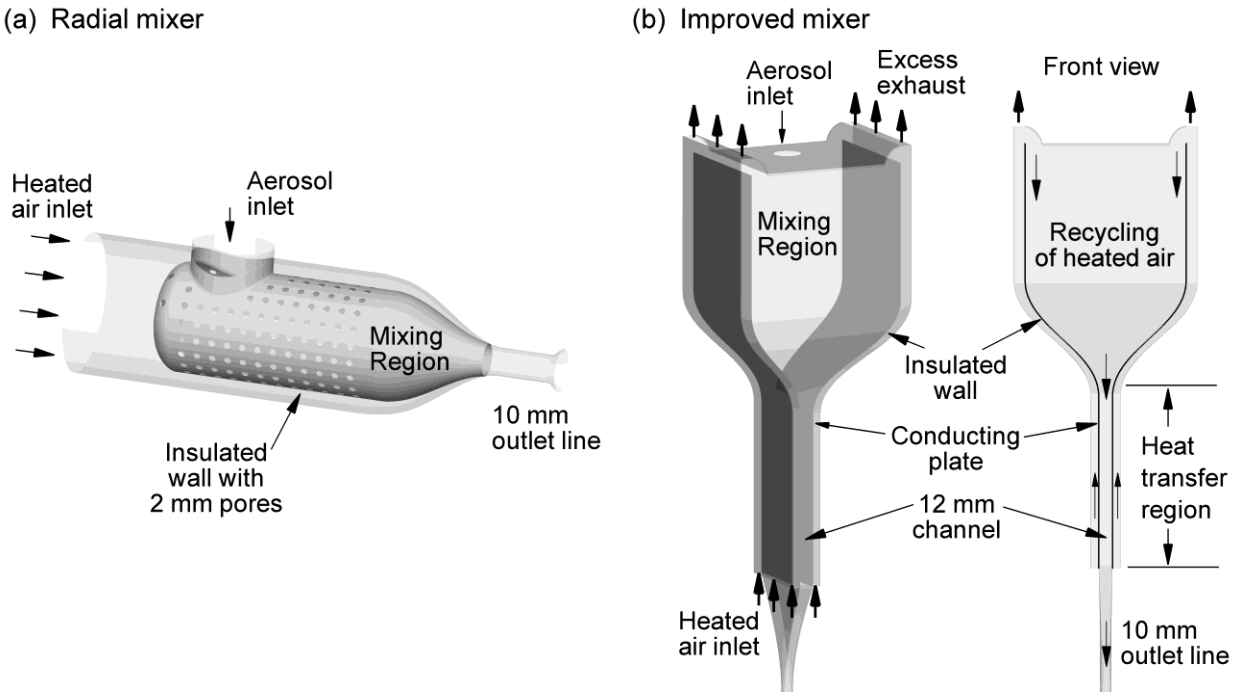

Figure 5.1 Mixer-heaters including (a) radial and (b) improved designs. An Aeroneb Lab nebulizer is used to produce the initial aerosol. The radial design evaporates the aerosol through the use of downstream counterflow heating. The original improved design introduced a single heated airstream which raised the temperature of the conducting plates and interacted with the aerosol to promote drying in the mixing region. Reprinted with permission of Dr. P. Worth Longest. Copyright © 2013. Cite: Longest, P.W., Walenga, R.L., Son, Y.-J., & Hindle, M. (2013c). High efficiency generation and delivery of aerosols through nasal cannula during noninvasive ventilation. Journal of Aerosol Medicine and Pulmonary Drug Delivery, 26, 266-279.

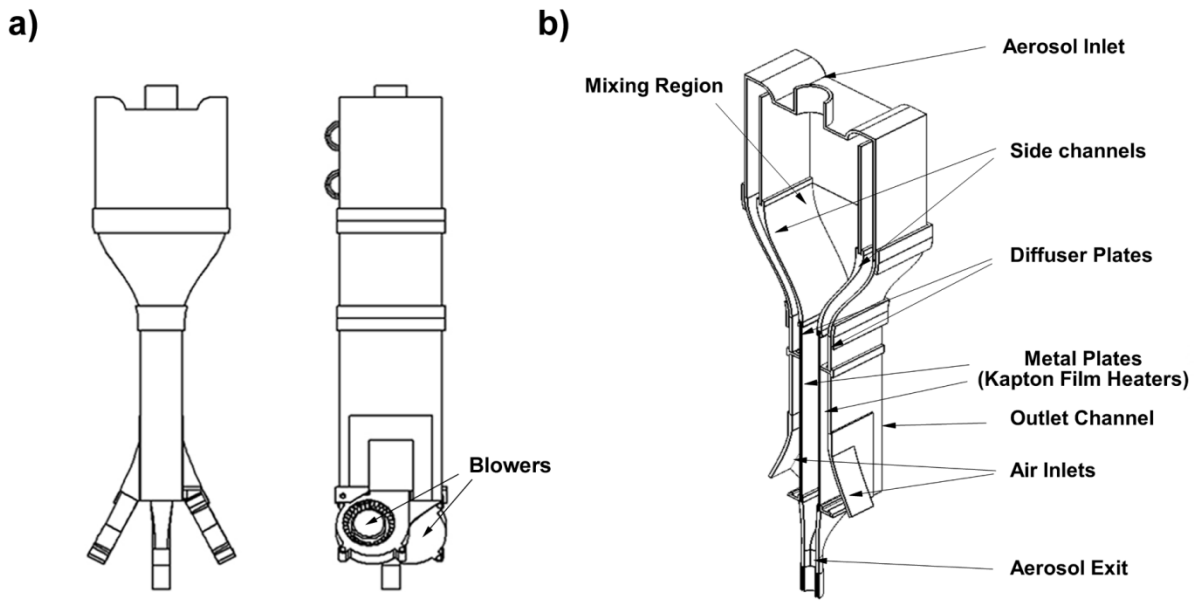

Figure 5.2 Schematic diagram of transient mixer-heater from (a) front and side views and (b) a cross-sectional perspective view.

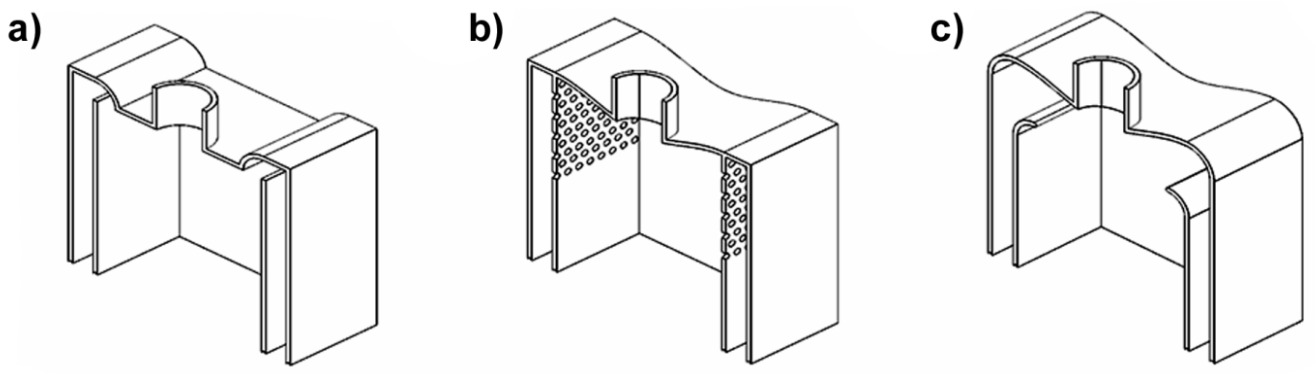

Figure 5.3 Various mixing region designs for transient mixer-heater, including the (a) straight, (b) perforated, and (c) curved models.

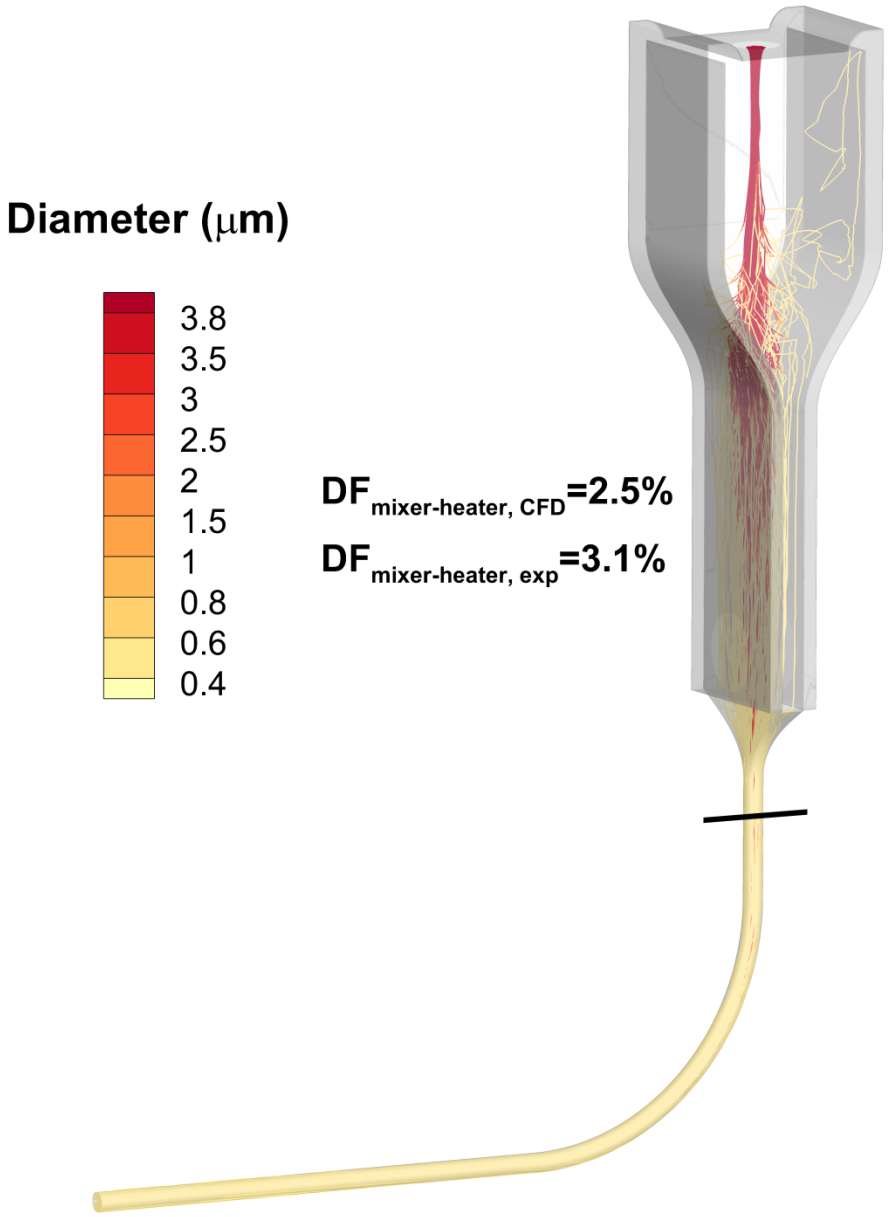

Figure 5.4 Computational fluid dynamics (CFD) results for deposition fraction (DF) and particle tracking visualization.

Chapter 6 Nasal Variability and EEG Delivery

The objective of this study is to create four patient specific nasal cavity models for *in silico* testing, that are selected from a collected database of dimensional measurements to be representative of the full range of surface area-to-volume (SA/V) ratio values for an adult population. In the four models, nasal deposition variability of albuterol sulfate (AS) delivered during high flow nasal cannula (HFNC) therapy is assessed by considering both control conditions with a 5 μm aerosol and excipient enhanced growth (EEG) delivery conditions with 0.9 μm and 1.5 μm aerosols.

6.1 Introduction

A database of anatomical nasal cavity dimensions was compiled that included data from 12 collected computed tomography (CT) scans and 54 CT scans from other sources. Measurements included surface area (SA) and volume (V), along with the hydraulic diameters of the minimum nasal cavity cross sectional area ($d_{h,min}$), nostril opening ($d_{h,nostril}$), and the nasopharynx outlet ($d_{h,nasopharynx}$). Four models representative of the range of adult surface area-to-volume (SA/V) ratios were selected, where three were built using data from the collected CT scans, while the other was adopted from a previously existing model (Golshahi, et al., 2013; Longest, et al., 2011; Xi & Longest, 2008b). A new streamlined nasal cannula developed by Longest, Golshahi, et al. (2013a) was implemented with a 20 cm inlet tube to allow for

characterization of nasal high flow therapy (HFT) aerosol delivery. The newly constructed database showed that SA/V measurements yielded an average (μ) and standard deviation (SD) of 1.07 and 0.24 mm^{-1}, respectively, and that the selected models covered the range of 0.74-1.42 mm^{-1}, which represents approximately 84% of the population variation from an assumed normal distribution. The SA/V values of the four models were found to have a linear correlation ($p < 0.03$) with $d_{h,min}$, indicating that SA/V may be a good measure of constriction. However, no other correlation was observed, showing that the other variables were allowed to vary in a realistic way.

A new mesh was applied to a previously existing nose-mouth-throat (NMT) model (Golshahi, et al., 2013), which is then used to validate CFD methods for this study through comparison with *in vitro* depositional data from Golshahi et al. (2013). Then, tetrahedral meshes were applied to the four nasal cavity models, while hexahedral meshes were used for the tube and streamlined nasal cannula inserted into each model. The four models were used to compare deposition efficiency (DE) and penetration fraction (PF) of aerosol delivery with conventional and EEG methods at a flow rate of 30 L/min flow through a streamlined nasal cannula. Aerosols considered were solid particles for excipient enhanced growth (EEG) delivery (0.9 μm and 1.5 μm) composed of a 50:50 mixture of albuterol sulfate (AS) and sodium chloride (NaCl) and large droplets (5 μm) of a 0.1% AS:0.1% NaCl solution for a control case. Deposition results from the four models were compared with a previously developed correlation that was based on data from an *in vitro* study of 13 children aged 4 to 14, which was observed to produce good predictions of adult deposition as well as from that age group (Golshahi, et al., 2011). Collected *in silico* data matched well with predictions based on the correlation developed by Golshahi et al. (2011). CFD predictions showed that the use of EEG as opposed to conventional methods reduced

delivered dose of aerosols through the nasopharynx, expressed as penetration fraction (PF), by approximately a factor of four. Variability of PF, expressed by the coefficient of variation (CV), was reduced by as much as a factor of five for the four models considered.

6.2 Methods

To test variability in the delivery of aerosols through the nose to the lungs, an anatomical data set was assembled that consisted of pre-existing adult computed tomography (CT) scans compiled for this study and from published sources. A set of 31 CT scans from VCU Medical Center was procured using a previously approved IRB protocol for pre-existing data. The in-house scans were produced by a SIEMENS Sensation 16 scanner with a slice thickness ranging from 0.4 mm to 1.5 mm and each included the entire nasal cavity. An otolaryngologist checked the scans for any morphological defects. The number of scans selected for use in the data set was reduced from 31 to 12, after scans were disqualified due to low resolution (slice thickness > 1.0 mm) or obvious anatomical defects that were noted by the otolaryngologist. The final set consisted of 3 males and 9 females, with ages ranging from 19-60, heights between 150-180 cm, and weights between 45-95 kg. CT scan data was then extracted into a 3D surface file using the commercial software package Mimics 16.0 (Materialise, Belgium). A feature of the software allowed for surface area and volume measurements to be calculated, which were evaluated within the airspace between the nasal valve area and the termination of the septum.

The regional definition of the nasal cavity boundaries varies in the literature (Garcia, et al., 2009; Liu *et al.*, 2009; Segal, et al., 2008; Taylor, et al., 2010; Xi, et al., 2012; Yokley, 2006; Zhu *et al.*, 2011), so only studies that measured surface area-to-volume ratios (SA/V) from the nasal valve area to the septum (Garcia, et al., 2009; Xi, et al., 2012; Yokley, 2006) were

considered for consistent comparisons. CT scan data set measurements were adopted from an anthropological study by Yokley (2006) on nasal cavity evolution (n = 49), a study by Garcia et al. (2009) regarding intersubject nasal filtration variability (n = 4), and a study by Xi et al. (2012) concerning ultrafine particle deposition in nasal-laryngeal airways of various models representative of different age groups, where only the adult model was used for this study. The SA/V values from Yokley (2006) were measured by only considering the least congested side to eliminate the transient effect of nasal cycling, which is known to produce a difference in congestion at nearly all times (Lang *et al.*, 2003). However, Garcia et al. (2009) and Xi et al. (2012) used an approach that included the measurements of both sides. Considering the CT scans collected for this study, the SA/V values were measured considering only the least congested side, similar to Yokley (2006). The overall effect of this minor discrepancy was not expected to be large enough to merit exclusion of the data from Garcia et al. (2009) and Xi et al. (2012). The complete database from both collected CT scans and published sources included 66 adult subjects, though the sex demographics were largely unknown because the literature data frequently did not include this information.

Analysis of the collected data set describing 66 subjects yielded an average SA/V value of 1.07 ± 0.24 mm^{-1}, and ideally the models chosen would cover two standard deviations from the mean (95% of the variation) or a range of values 0.59-1.55 mm^{-1} from a normal distribution. A complete test of the data set for normality was not possible, since the data from Yokley (2006) was only given as a mean and a standard deviation, but a Shapiro-Wilk test performed on the rest of the data set (n = 17) did not show any significant deviation from normality (p = 0.21). The data set did not include models that cover this desired range exactly. Selection among the available models covered a SA/V range of 0.74-1.42 mm^{-1}, which theoretically should

approximate 84% of the variation from a normal distribution and represents a large fraction of the population. The four nasal models chosen to represent the range of variability in SA/V measurements are depicted in Figure 6.1, and each includes nostrils, the nasal cavity, the nasopharynx, and the streamlined nasal cannula attached to a tube with a 90° bend. The throat regions were not included in the four models because it was available in only some of the CT scan data sets and a direct comparison was desired. Coronal cross sections of each model are shown in four different regions: (1) termination of the nasal valve area, (2) nasal cavity with two meatuses, (3) nasal cavity with three meatuses, and (4) entrance to the nasopharynx. The four models were named 'Open', 'Average', 'Constricted1', and 'Constricted2', with values of SA, V, SA/V, minimum coronal cross-sectional hydraulic diameter of the nasal cavity ($d_{h,min}$), average nostril entrance hydraulic diameter ($d_{h,nostril}$), and nasopharynx exit hydraulic diameter ($d_{h,nasopharynx}$), shown in Table 6.1. All of the models were derived from VCU Medical Center CT scans, except for the 'Open' geometry, which has been frequently used with *in vitro* (Golshahi, et al., 2013; Longest, et al., 2011) and CFD studies (Golshahi, et al., 2013; Longest, et al., 2011; Xi & Longest, 2008b) and represents the lower limit of the SA/V values.

The 3D surface files extracted from the Average, Constricted1, and Constricted2 models were exported as .stl files, a surface file type often used in rapid prototyping. In order to import these files into a CAD software package, the files were converted into a volumetric file type (.igs) using the mesh development software 3-matic (Materialise, Belgium). These files were then imported into the CAD software package SolidWorks 2011 (Dassault Systèmes Solidworks Corp., Waltham, MA, USA) for further modification. The inlet tips of the nostril airspaces were truncated to produce a flat surface that would be compatible with a velocity inlet for a computational mesh. The plane of truncation was chosen in each case to minimize the amount of

airspace removed. Additionally, the exit of the nasopharynx was truncated to produce a flat outlet surface, where the slicing plane was chosen to be perpendicular to the direction of flow. Numerical extensions were added to each of the three models through extrusions of the outlet cross section by 10 hydraulic diameter lengths. Regarding the Open model, it was initially available through GAMBIT 2.4 (ANSYS, Inc., Canonsburg, PA, USA), and after small modifications to the nostril outlets to produce a flat surface, it was imported into SolidWorks using a parasolid (.x_t) file format.

A previously developed (Longest, et al., 2013a) streamlined nasal cannula was added to the four models, along with a 20 cm inlet tube that was shaped into a 90° bend and positioned on a plane perpendicular to gravity (Figure 6.1e). The tube was imported from GAMBIT 2.4 into SolidWorks, as described above, and then the nasal prongs were placed into each nostril in a manner that maximized the space between the nostril and cannula walls, yet maintained an orientation that allowed for delivery of the aerosol to the middle region of the nasal cavity. Some enlargement of the nostril region was necessary to accommodate the cannula in two of the models, which seems reasonable given that nostrils are flexible and would expand if nasal prongs larger than the unstressed nares were inserted. However, as is consistent with HFNC gas delivery, each model remained an open system since enlargement was only necessary in a few select locations along the perimeter of the oblong nostril openings. Realistic wall thickness of the cannula was considered unimportant for flow determination and a potential obstacle for mesh development, and thus the wall was modeled with an infinitesimal thickness.

In addition to the four nasal models described above, a model of the NMT region was considered for comparison to existing *in vitro* results in order to validate the CFD model predictions of deposition. This NMT geometry consisted of the Open nasal model combined

with a CT scan model of the mouth and throat as previously described and evaluated in the study of Golshahi et al. (2013). In the previous study of Golshahi et al.(2013), the same cannula and flow rates were considered as in the current study for control and EEG aerosol formulations. Previous CFD simulations of these conditions matched the *in vitro* results to a high degree in terms of aerosol size change and depositional loss. However, minor modifications to the meshing approach and boundary conditions made in the current study require new validations of the CFD predictions.

The computational meshes for each model, including the new mesh of the NMT model from Golshahi et al. (2013) and the four models developed for this study, were constructed using ICEM CFD 12.0.1 (ANSYS, Inc., Canonsburg, PA, USA). The tube and cannula were modeled using a structured hexahedral mesh with a butterfly blocking pattern rather than the tetrahedral mesh employed by Golshahi et al. (2013), since hexahedral meshes are numerically preferred where possible (Longest & Vinchurkar, 2007a; Vinchurkar & Longest, 2008). The near-wall control volume height of the mesh in the tube and cannula for each model was approximately 0.025 mm throughout, and consisted of ~1 million control volumes. Due to the geometric complexity of the nasal cavity, an unstructured tetrahedral mesh was deemed necessary in that region. A surface mesh was first applied with the curvature sensitive feature that used smaller elements in regions of greater curvature. A Delauney mesh was applied to the volume of each nasal cavity with a spacing scaling factor of 1.2-1.3, and a maximum cell dimension of 1 mm. Pentahedral elements were added along the walls to increase the accuracy of the boundary layer simulations and particle deposition. Golshahi et al. (2013) utilized five near-wall layers with a near-wall control volume height of 0.05 mm, but it was found through several mesh construction iterations that decreasing the near-wall control volume height to 0.011 mm and increasing the

number of layers to seven improved resolution of flow field features. The mesh density of the new version of the NMT model from Golshahi et al. (2013) was increased from ~1.3 million cells to ~4.4 million cells using the new meshing scheme. The four models used for this study were meshed in the same manner, producing models with mesh densities between ~3 million (Open) and ~6 million (Constricted2) cells.

The applicability of the *k-ω* turbulence model used in this study was assessed by checking the y^+ values at the walls. The y^+ parameter is a nondimensional number that identifies the multiple turbulence zones at the wall (laminar sub-layer, transition, or fully turbulent). It is calculated as

$$y^+ = \sqrt{\frac{\frac{\tau_w}{\rho} y}{\nu}} \tag{6.1}$$

where τ_w is the shear stress at the wall, y is the normal distance from the control volume center to the wall, ρ is the local density, and υ is the kinematic viscosity. Values of $y^+ < 5$ indicate a laminar sub-layer, whereas values of $y^+ > 30$ indicate the fully turbulent layer, both of which are considered to be accurately resolved by ANSYS FLUENT 14.5 (ANSYS, Inc., Canonsburg, PA, USA). Accurate resolution of the laminar sub-layer requires the use of a low Reynolds number correction, which was utilized in this study. The transition layer ($5 < y^+ < 30$) is associated with a loss of resolution, though some accuracy is maintained for values of $5 < y^+ < 11.2$. The values of y^+ are solution dependent since they are based on shear stress at the wall, density, and kinematic viscosity and should be checked after running simulations. It was found that the y^+ values in each model did not exceed 6.5 in the tube at 30 L/min, so that the near-wall control volumes were mostly in the laminar sub-layer region. The y^+ values in the nasal cavity near-wall control volumes were all ~1, indicating adequate near-wall mesh resolution.

In this study, simulations are considered for both the NMT validation and to evaluate variability in the four nasal models across different aerosol sizes. A steady state flow rate of 30 L/min was used in all cases applied at the inlet tube and additional airflow was not introduced to the nostrils outside of the two nasal prongs. Considering the validation study, inlet conditions were consistent with conventional mesh nebulizer generated aerosols. In this case, the aerosol from the nebulizer evaporates until the relative humidity (RH) reaches 100% at the ambient temperature, which prevents additional droplet size change. Therefore, in the validation case study, the inlet temperature and RH were 25°C and 99%, respectively. The aerosol size for the validation case study at the tube inlet was 2.9 μm, which was measured by Golshahi et al. (2013) at the cannula outlets. For evaluating variability among the four nasal geometries, particle aerodynamic diameters at the tube inlet were 0.9, 1.5, and 5.0 μm. The 0.9 and 1.5 μm aerosols were dried particles with an EEG formulation and were assumed to be generated with a previously developed mixer-heater (Longest, et al., 2013c). The resulting inlet temperature and RH for these cases were 35°C and 40%, respectively. The 5 μm droplet aerosol was assumed to be generated with a mesh nebulizer without the mixer-heater. Therefore, as with the conventional aerosol in the validation study, the inlet T and RH from the mesh nebulizer were assumed to be 25°C and 99%, respectively.

Table 6.2 describes differences in the boundary conditions between the current study and the simulations performed in the study of Golshahi et al. (2013). In the current study, the particle size exiting the cannula was employed in the validations. Therefore, a RH of 99% was assumed at the inlet to prevent aerosol evaporation in the tubing. Moreover, a more comfortable RH with EEG delivery of 40% is assumed, compared with the previous low value of 14%. Finally, the current study considered a larger control aerosol of 5.0 μm, which is consistent with most

aerosols produced by mesh nebulizers (Longest, et al., 2013a; Martin *et al.*, 2010; Rao *et al.*, 2010; Scherer *et al.*, 2011).

Though it is known that transient effects play a role in particle deposition, the models were simulated with a steady state approximation. A steady state approximation is advantageous for computational efficiency and is sufficient for achieving the primary objective of this study, which is a relative quantification of the nasal deposition and its variation in the four models. Effects of transient breathing and the need to synchronize aerosol delivery with inhalation for efficient nose-to-lung aerosol delivery have recently been explored by Golshahi et al. (2014b).

For all cases, airway wall surfaces had an RH of 99% and a temperature of 37 °C. Additionally all cases had 0.0001% turbulent intensity at the tubing inlet, which is reasonable since laminar flow is expected in this region. The outlet conditions of the four models and the NMT model were selected to closely mimic envisioned EEG nose-to-lung delivery. For all simulations used in this study, including the validation of the NMT model, constant pressure outlets were used at the nostrils and the trachea exit. The nostrils were held at a gauge pressure of zero and the value of negative pressure at the trachea exit was determined iteratively to provide a constant flow rate of 30 L/min throughout the model.

Multiple particle/droplet sizes were used to characterize depositional variability in the nasal geometries, which represented control (conventional) and EEG delivery. For control conditions in the four nasal models and the NMT validation, the formulation used was 0.1% AS: 0.1% NaCl w/v in water, while the droplet aerodynamic size was 5 μm. The droplets or particles were injected as a monodisperse bolus of 9,000 discrete elements for each case in this study, with a parabolic profile at the inlet of the tube. For EEG conditions, solid combination EEG particles composed of 50:50 drug (AS):excipient (NaCl) were used. Two particle sizes were investigated

for the EEG delivery, 0.9 μm and 1.5 μm, where the sizes are given as aerodynamic diameters since the particle densities were significantly different than that of water. Aerodynamic diameter (d_{ae}) is defined as

$$d_{ae} = d_{geo}\sqrt{\frac{\rho_p}{\rho_w}} \tag{6.2}$$

where d_{geo} is the geometric diameter, ρ_p is the particle density, and ρ_w is the density of water. The hygroscopicity of each substance is quantified by its hygroscopic parameter (Longest & Hindle, 2011), where a large number indicates a greater potential for particle size increase due to water uptake. For the formulation used, the hygroscopic parameters were 77.9 kmol/m^3 for NaCl and 4.9 kmol/m^3 for AS, which indicated that NaCl has much greater growth potential than AS (Longest & Hindle, 2011).

A combination of user-defined routines and the commercially available CFD package ANSYS FLUENT 14.5 (ANSYS, Inc., Canonsburg, PA, USA) was used to simulate the fluid flow, heat, and mass transfer of the nasal models. Additionally, this combination was used to calculate the trajectories, size changes and deposition of all particulate matter. Since the maximum Reynolds number in the four models was estimated to be ~5,000 at 30 L/min, some regions of the models were considered to be in transition to turbulence or fully turbulent flow. A low-Reynolds number (LRN) k-ω model was selected for modeling both laminar and turbulent conditions, as it has been shown to accurately estimate flow field conditions in an upper respiratory geometry, particularly as they relate to aerosol deposition and transport (Xi, et al., 2008). The variable temperature and RH fields were resolved using coupled equations of heat and mass transfer previously reviewed in Longest et al. (2007) and Longest & Xi (2008).

Particle trajectories, including hygroscopic size change, were modeled using a Lagrangian transport set of equations (Longest & Hindle, 2010). Turbulent dispersion was

estimated using a random walk method, while user-defined functions were implemented to simulate Brownian motion, anisotropic near-wall turbulent dispersion, and near-wall interpolation of fluid velocities. The near-wall corrections were applied using the updated code developed in Chapter 4. Additionally, evaporation and condensation of the particles were modeled using user-defined functions. Particle size changes included the effects of both the droplet surface vapor pressure change due to temperature and the hygroscopicity of the excipients and drugs, as well as the Kelvin effect. Influences of the particles on the fluid phase were neglected, and thus the system was modeled as one-way coupled. Further details of the equations used can be found in previous studies (Longest, et al., 2011; Tian *et al.*, 2013).

Solution methods for ANSYS FLUENT 14.5 were selected to reflect previously implemented models and established best practices (Longest *et al.*, 2012c). Double precision was used for all calculations to improve accuracy, which is particularly important in regions of rapid change for flow, heat, and mass transport. The pressure-velocity coupling was modeled using the SIMPLEC algorithm, and the spatial discretization of all convective terms utilized a second order upwind scheme. Flow field convergence was achieved when the global mass-residual had been reduced five orders of magnitude and the residual rates of reduction for both mass and momentum approached the numerical precision limit.

Previously developed correlations for nasal deposition (Cheng, 2003; Golshahi, et al., 2011) were applied to the four nasal models from this study to provide initial DE estimates. However, unlike the CFD predictions of this study, neither correlation was based on data that included condensational size change effects, so comparison with each correlation is intended to provide a first order approximation rather than a nearly exact match. Cheng (2003) developed a correlation between Stokes number and DE in the nasal cavity due to impaction using *in vitro*

data reported by Swift (1991) for an adult and an infant model, with minimum coronal cross-sectional area (A_{min}) values of 1.61 and 0.54 cm^2, respectively. The models were built using MRI images with a 3 mm build layer thickness, and a polydisperse NaCl solution was generated and passed through the system at 7, 15, 30, and 50 L/min via a breathing chamber (Swift, 1991). The correlation that Cheng (2003) produced using the data from Swift (1991) was

$$DE = 1 - e^{-110St_k} \tag{6.3}$$

where DE is the depositional efficiency of the nasal cavity and St_k is the Stokes number. The nondimensional Stokes number from the study of Cheng (2003) was calculated as

$$St_k = \frac{\rho_w \sqrt{\pi} d_{ae}^2 Q}{18\mu\sqrt{A_{min}{}^2}} \tag{6.4}$$

where St_k is the Stokes number, ρ_w is the density of water, d_{ae} is the aerodynamic diameter, Q is the flow rate, μ is the dynamic viscosity of the fluid medium (in this case, air), and A_{min} is the minimum coronal cross-sectional area of the nasal cavity. The value of A_{min} for each of the four models used in this study is given in Table 6.3. A correlation for deposition due to diffusion was also developed by Cheng (2003), which is not reported here since it was for particles smaller (<500 nm) than those investigated for this study.

Nasal DE was correlated with Stokes number (St_k) and Reynolds number (Re) by Golshahi et al. (2011), using *in vitro* data from 13 pediatric upper airway models. The models were developed using CT scans of children age 4 to 14 years, and included the nasal cavity through the larynx and up to the beginning of the trachea (Golshahi, et al., 2011). Data was then collected by placing the models in a breathing chamber and passing polydisperse sunflower oil particles through each model, where the count median aerodynamic diameter (CMAD) was 0.4 μm (Golshahi, et al., 2011). The correlation developed by Cheng (2003) was explored by Golshahi et al. (2011) as a means of describing their *in vitro* data, but it produced a prediction

that was well above the experimental results. Cheng (2003) used $A_{min}^{1.5}$ to describe a characteristic diameter (d_c) which was aimed at capturing the geometric contribution to the variability of nasal deposition, but Golshahi et al. (2011) found another form of d_c that yielded a high R^2 value (0.91) with relatively easily collected variables, given as

$$d_c = \sqrt{V_{total}/L_{CP}} \tag{6.5}$$

where d_c is the characteristic diameter, V_{total} is the volume of the airway up to and including the larynx, and L_{CP} is the central path length. The values of V_{total}, L_{CP}, and d_c for each of the four models are shown in Table 6.3. The characteristic diameter d_c was then applied by Golshahi et al. (2011) to find the Reynolds (Re) and Stokes (St_k) numbers as

$$Re = \frac{4\rho_{air}Q}{\pi\mu d_c} \tag{6.6}$$

$$St_k = \frac{4\rho_{water}d_{ae}^2 C_{ca}Q}{9\pi\mu d_c^2} \tag{6.7}$$

where ρ is the density of air or water, d_{ae} is the aerodynamic diameter of the particle, Q is the flow rate, μ is the fluid dynamic viscosity, and C_{ca} is the Cunningham correction factor for the aerodynamic diameter. The final correlation from Golshahi et al. (2011) for the depositional efficiency (DE) was then stated as

$$DE = \left[1 - \left(\frac{119.4}{119.4+X}\right)^{0.57}\right] * 100\% \tag{6.8}$$

where X is defined as

$$X = {St_k}^{1.23} Re^{1.28} \tag{6.9}.$$

The percentage of initial drug mass that deposits in a given region is denoted by deposition fraction (DF), which is defined as

$$DF_i = \frac{drug\ mass\ deposited\ in\ region\ i}{drug\ mass\ released\ from\ nebulizer}\ x\ 100\% \tag{6.10}.$$

In this study the aerosol released from the nebulizer directly enters the inlet tube. The deposition efficiency (DE) is the percentage of drug mass that enters a given region and deposits within that region, given by

$$DE_i = \frac{drug\ mass\ deposited\ in\ region\ i}{drug\ mass\ entering\ region\ i}\ x\ 100\% \qquad (6.11).$$

Deposition efficiency values are calculated for the nasal region in this study to capture nasal deposition independent of loss in the cannula, which enables consistent comparison with predictions based on the existing correlations of Cheng (2003) and Golshahi et al. (2011). The penetration fraction (PF) is the percentage of initial drug mass that exits the nasopharynx, and is calculated as

$$PF = \frac{drug\ mass\ exiting\ nasopharynx}{drug\ mass\ released\ from\ nebulizer}\ x\ 100\% \qquad (6.12).$$

The variability of the DE, PF, and the MMAD at the nasopharynx exit is characterized using the coefficient of variation (CV), given as

$$CV = \frac{SD}{\mu} \qquad (6.13)$$

where SD is the standard deviation and μ is the mean value.

6.3 Results

As described, the selected nasal models represent a SA/V range of 0.74-1.42 mm^{-1}, which theoretically should approximate 84% of the variation from a normal distribution based on the assembled data set. Though the nasal cavity models are selected for constriction, expressed as SA/V, other parameters, including $d_{h,nostril}$, $d_{h,nasopharynx}$, and nasal cannula insertion depth vary without any apparent relationship to SA/V (Table 6.1). Minimum nasal cavity cross sectional hydraulic diameter ($d_{h,min}$) correlates inversely with SA/V (correlation coefficient R = -0.97, p <

0.03), indicating gradual constriction of the models from the Open model to the Constricted2 model. However, a linear correlation was not found for $d_{h,nostril}$ (R = 0.46) and $d_{h,nasopharynx}$ (R = 0.41) with SA/V. The insertion depth values of the cannula for each of the models, which are defined as the shortest and longest distances from the edge of the cannula opening to the plane of the nostril opening, had minimum and maximum value ranges of 0.17-3.24 mm and 4.39-8.12 mm, respectively. The right nostril cannula insertion of the Average model is illustrated in Figure 6.2 to provide further context and demonstrate that the prongs protrude into the nasal cavity by a small amount. These insertion depth values vary based on the open nostril volume available for prong insertion, and so they are also unrelated to nasal cavity constriction. Thus, the controlled variation in the four models (SA/V) is in the nasal cavity region, which has defined boundaries between the termination of the nasal valve area and the end of septum. Consequently, the collection of models should test the hypothesis that deposition fraction of the nasal cavity increases as SA/V values of the nasal cavity increase, since other variables (cannula insertion depth, $d_{h,nostril}$, and $d_{h,nasopharynx}$) are based on the patient specific dimensions.

Deposition of drug mass for the NMT model is compared in Figure 6.3 between the CFD predictions and previous *in vitro* study of Golshahi et al. (2013). Two formulations were tested, 0.1% AS: 0.1% mannitol (MN) and 0.1% AS: 0.1% NaCl, and the MMAD of the droplets at the inlet was 2.9 μm in both cases. The results are presented as deposition efficiency (DE) in the cannula and the NMT region, and the new mesh was found to provide a very close match to the experimental data. In particular, the NMT deposition efficiency of 0.1% AS:0.1% NaCl particles was predicted by CFD to be 9.5%, a 7% relative increase from the value of 8.9% that was found experimentally by Golshahi et al. (2013), while the relative increase for 0.1% AS:0.1% MN particles was even smaller (2%). This close agreement of nasal cannula predictions provides

confidence that the CFD methods employed for this study will provide a good estimate of aerosol deposition and transport.

Expected Reynolds numbers in the four different regions depicted in Figure 6.1 for each model are given in Table 6.5. The Reynolds numbers are calculated as

$$Re = \frac{Q d_h}{\upsilon A} \tag{6.14}$$

where Q is the flow rate, d_h is the hydraulic diameter of each region shown in Figure 6.1, υ is the kinematic viscosity, and A is the cross-sectional area of each region. The values of SA/V do not correlate well with the Re values of the various regions, where the strongest correlation was found between the SA/V and Re values of Region 3 (R = -0.79). A strong correlation exists between the $d_{h,nasopharynx}$ and Re values of Region 2 (R = -0.9996, $p < 0.0003$), and a weak correlation exists between the $d_{h,nasopharynx}$ and Re values of Region 3 (R = -0.88). However, reasons for this possible relationship are unclear. Static pressure profiles at the walls of each model are illustrated in Figure 6.4, with units given in Pa. The tube in each model shows a gradual decrease in pressure, while a sharp decrease in pressure is visible at the junction of the tube and cannula. The transition from the cannula to the nasal cavity shows another sharp decrease in pressure, while the pressure drop from the nostril inlet to the nasopharynx outlet is more gradual. The olfactory region (i.e. superior meatus) of each model has a higher pressure at the wall than the inferior and middle meatus, which is to be expected given that the airspace in this region is more confined. Table 6.6 shows the pressure drop (Δp) from the inlet of the tube to the exit of the nasopharynx, along with geometric measurements that may correlate with Δp, including SA/V and $d_{h,nasopharynx}$. While SA/V and $d_{h,nasopharynx}$ provide a poor linear fit for Δp, dividing SA/V by $d_{h,nasopharynx}$ provides a good fit (R = 0.98, $p < 0.03$), which shows that the pressure drop is affected by the constriction of both the nasal cavity (SA/V) and the nasopharynx

exit ($d_{h,nasopharynx}$). As the pressure drop is expected to influence particle deposition (Garcia, et al., 2009; Heyder & Rudolf, 1975; Hounam *et al.*, 1971; Kesavanathan *et al.*, 1998), the variability may not only correlate with SA/V as expected, but with $d_{h,nasopharynx}$ as well.

Cross sections of velocity magnitude for each model are presented in Figure 6.5, taken from the four regions illustrated in Figure 6.1. The peak global velocities of the nasal cavity occur in region 1 (termination of the nasal valve area) and have a magnitude of ~10 m/s in each model. In regions 2 and 3 (nasal cavity with two and three meatuses), the highest local velocities of each region occur in the middle meatuses as opposed to the inferior and superior meatuses. In region 4 (entrance to the nasopharynx), the local velocity is at a maximum in the upper left and right sides of each model, except for the Constricted1 geometry, where the anatomical left side has the only large region of heightened velocity. Areas of recirculation are noted in regions 1 and 4 for each model, at the entrance and at the exit of the nasal cavity, with the exception of the Open model, which lacks recirculation in region 1. The Open model instead has areas of recirculation in region 2 that are absent in the other three models, except for a small area in region 2 of the Constricted2 case. Since the Open model is the least constricted of the four geometries, it may be that a critical SA/V value exists for a given flow rate, above which recirculation in the nasal cavity (i.e. regions 2 and 3) is much less likely to occur.

The cross sectional turbulent viscosity ratio is shown in Figure 6.6 for each model, where the cross sections are taken at the four regions shown in Figure 6.1. The turbulent viscosity ratio (ζ) is defined as

$$\zeta = \frac{\nu+\nu_T}{\nu} \tag{6.15}$$

where ν and ν_T are the laminar and turbulent kinematic viscosities, respectively. Similar to the velocity magnitude, the maximum global turbulent viscosity ratio is found in region 1 for all four

models, and is denoted as ζ_{max} in Figure 6.6. There is no significant correlation between ζ_{max} and SA/V, as all values are similar with the exception of the Constricted1 model, which has a much smaller ζ_{max} value. The areas of local peak turbulent viscosity ratio in regions 2 and 3 are much more pronounced in the Open model than the other three models, which is consistent with the maximum velocity and recirculating flow profiles observed in Figure 6.5.

The correlation from Cheng (2003) was applied to each of the four models and the DE values were plotted against d_{ae}, as shown in Figure 6.7a. Also shown in the figure is the range between the maximum and minimum predicted values of DE in the nasal cavity region for each initial particle size (0.9 μm, 1.5 μm, 5 μm). The predictions show that the greatest and smallest ranges occur for 1.5 μm and 5 μm particles, which were 25.8-39.5% and 96.4-99.6%, respectively. According to the correlation, full nasal cavity retention is expected for particles greater than 6 μm, regardless of the SA/V value. Submicrometer particle deposition is predicted to be as low as 10%.

Predictions based on the correlation produced by Golshahi et al. (2011) for DE in the nasal cavity as a function of d_{ae} are shown in Figure 6.7b. Consistent with the findings of Golshahi et al. (2011), their correlation falls well below those of Cheng (2003) for each of the four models. The range of values follow a much different pattern than with the Cheng (2003) predictions, since the greatest and smallest ranges occur for 5 μm and 0.9 μm particles, which were 30.5-51.1% and 0.9-2.4%, respectively. These findings provide evidence that use of the smaller EEG formulation aerosols will yield significant reductions in variability of the nasal depositional drug loss. CFD simulations of this variability are explored below and nasal deposition predictions are then compared with the predictions of the correlations.

Predictions of regional DF and total nasal DE are presented in Table 6.7 and Table 6.8 for cases without and with size change, respectively. Size change was excluded in the first set of simulations so that its effects on deposition and variability as well as comparisons to the existing nasal deposition correlations could be assessed. Regional nasal cannula DF predictions showed that nearly half of the initial drug mass deposited in this region for the control case (5 μm), without and with size change, but that for the EEG cases (0.9 μm and 1.5 μm) very little of the initial mass deposited (<4%). Likewise, there is very little deposition of the initial drug mass in the nasal valve area for the EEG cases, and significantly more in the control case.

The total nasal DE values of 0.9 μm and 5 μm aerosols for cases with size change are illustrated in Figure 6.8 and Figure 6.9, respectively, for each of the four models. The mean, twice the SD, and the CV are shown for cases without and with size change in Table 6.7 and Table 6.8, respectively. The control aerosol size (5 μm) shows an average nasal DE that is an order of magnitude higher than the EEG cases, both without and with size change. Variability without and with condensational growth is also higher for the control case with CV's of 31% and 30% compared to the 0.9 μm cases (17% and 8%), and the 1.5 μm cases (15% and 12%), respectively. There is a small increase in the average total nasal DE for 0.9 μm and 1.5 μm particles in the presence of condensational size change compared to predictions without size change, but the values of DE remain about an order magnitude less than the control estimates. Condensational size change was also observed to decrease variability for the 0.9 μm and 1.5 μm cases and to increase it slightly for the 5 μm case. In terms of population DE range as estimated by the four geometries with size change considered, the 5 μm aerosol size produces a 95% CI of 15.5-64.1%, which is compared to the 95% CI for 0.9 μm EEG delivery of 2.3-3.1%.

Considering aerosol size change, mass median aerodynamic diameter (MMAD) predictions of the droplets at the exit of the nasopharynx are shown in Table 6.9 with the mean, 95% CI, and the CV. Very little evaporation is evident for the 5 μm case, which is expected given the high RH value throughout the system (99%). Significant size increase of EEG droplets is evident for both the 0.9 μm and 1.5 μm cases, with average values of 1.56 and 2.40 μm at the exits. There did appear to be an increased variability observed for the condensational growth of the 0.9 μm EEG aerosol with the 4 model geometries, however this represented a CV of only 10%, with a 95% CI population range of particle sizes at the exit of the nasal cavity of 1.24 – 1.88 μm.

Droplet trajectories are illustrated in Figure 6.10 for the 0.9 μm EEG case, with the MMADs at the nasopharynx exit also provided. The nasal cannula directs particles toward the middle and upper meatuses for all four models, with fewer trajectories visible in the lower meatus. Also of note are the recirculation regions present near the nostrils and nasal cannula of each model, presumably due to the pressure difference between the atmospheric nostril openings and the fast moving flow exiting the cannula.

Total nasal DE values for each model and aerosol size are shown in Figure 6.11a and Figure 6.11b, without and with condensational size change, and compared to the correlations developed by Golshahi et al. (2011). Differences were too great for direct comparison of the data to the correlation developed by Cheng (2003). The individual values as predicted by CFD show a good match with the correlation values of Golshahi et al. (2011) in terms of magnitude and rank order, despite the considerable size change observed with the EEG cases. The variation (expressed as CV) of 5 μm aerosols without and with size change (31% and 30%) are somewhat larger than predicted by Golshahi et al. (2011), who estimated a CV value of 21%. However, the variations predicted by Golshahi et al. (2011) for the 0.9 μm and 1.5 μm cases (39% and 38%)

are much higher than those predicted by CFD for this study (17% and 15% without condensational size change; 8% and 12% with condensational size change). A reduction in variability is observed in conjunction with the inclusion of condensational size change effects, though it does not fully explain the differences in the CFD predictions and those of Golshahi et al. (2011). The mode of aerosol delivery is an additional possible source of the discrepancy, as the correlation developed by Golshahi et al. (2011) was based on flow through an environmental chamber, while this study introduced aerosols through a nasal cannula.

Penetration fraction (PF) values through the entire geometry without and with condensational size change are provided in Table 6.10 along with the mean, 95% CI, and the CV. It is noted that the PF values only include aerosols that exited the nasopharynx and do not include those that exit through the nostrils, which was on the order of ~10% for all cases using the EEG technique with matched cannula and inhalation flow, but only ~1% for the four models under control conditions. The relative difference in losses through the nostril inlets is most likely due to the greater inertia of the 5 μm droplets, causing those particles to not enter the recirculation region. Average PF values for EEG cases were similar for both initial particle sizes as well as without and with condensational size change. The EEG delivery approach (0.9 μm and 1.5 μm particles) increased lung PF values by a factor of four compared with the control case. Variation of the control cases was about five times higher than the EEG cases, with average CV values of 17% and 15% without and with condensational size change, as opposed to 3-4% for the EEG simulations. While the PF values for the control cases without and with condensational size change correlated very strongly with SA/V ($R = -0.998$, $p < 0.002$ and $R = -0.997$, $p < 0.003$), the EEG PF values did not show the same dependence. However, some correlation was observed between the EEG PF values and $d_{h,nasopharynx}$ values, considering cases

without and with size change for initial particle sizes of 0.9 μm (R = -0.93 and R = -0.90) and 1.5 μm (R = -0.96, $p < 0.05$ and R = -0.93).

6.4 Discussion

A primary outcome of this study is that the EEG approach allows for significantly reduced depositional losses and variability during nose-to-lung pharmaceutical aerosol delivery. Other results of the study include the collection of CT scan nasal cavity measurements into a database and the creation of four models with their accompanying meshes, which were selected to represent a wide range of nasal airway SA/V values. Comparison of these four models using validated CFD methods showed that for the same flow rate, approximately four times as much delivered dose, expressed as PF, was observed at the nasopharynx outlet under EEG conditions compared with the control aerosol case. Regarding the initial goal of reducing system losses below a maximum of 15%, an average PF value of 82.2% for 0.9 μm particles under EEG conditions was predicted, which implied total average losses of 17.8% in the nasal airways, through the nostrils, and in the device. A majority of the lost fraction (~10%) was from aerosol exiting the nostrils due to the matched flow rate between the cannula and inhalation. Nonetheless, considering the high reported delivery device (Ari, et al., 2011; Bhashyam, et al., 2008; Longest, et al., 2013a) and nasal (Kelly, et al., 2004b; Stahlhofen, et al., 1989) depositional losses from other studies, the results indicated that EEG methods may provide an order of magnitude improvement compared with conventional aerosol sizes in terms of PF. Substantial reductions in variability were observed when EEG delivery was employed in favor of conventional sizes, with resulting PF coefficients of variation (CV) reduced from 15% to 3-4%.

In this study, the aerosol delivery flow rate of 30 L/min was matched by the tracheal inhalation flow rate. As a result, recirculation occurred in the nostrils and approximately 10% of the EEG dose was lost through the nostril openings to the atmosphere. To prevent this loss, an additional case was considered where the nasal inhalation flow rate was greater than the aerosol delivery flow rate. The Average model was considered with a cannula flow of 30 L/min and an additional flow of 15 L/min through the nostrils producing a tracheal flow rate of 45 L/min. Values of PF for the Average model under EEG conditions with condensational size change improved from 80% to 93% for the 0.9 μm aerosols and from 76% to 91% for the 1.5 μm aerosols. With the control aerosol, values of PF were reduced from 25% to 22% for the 5 μm cases. There were no losses observed through the nostril inlets for all cases. Regarding improvements of PF under EEG conditions, the aerosol recirculation regions in the nostrils were greatly reduced due to the presence of additional inhaled flow, which prevented depositional losses through the nostrils and potentially in the entrance of the nasal cavity. Moreover, depositional losses in the nasal cavity with the smaller EEG particles were low, so any relative increase due to the increased flow rate was expected to be small. Conversely, for control conditions, the presence of additional inhaled flow through the nostril inlets does not have a great effect on PF because losses near the nasal prongs were already low, and the increased flow rate increases nasal depositional losses. The predicted high efficiency delivery of aerosols using the EEG technique indicates that delivered dose may be maximized with a system that synchronizes aerosol delivery with inhalation and ceases delivery during exhalation (Golshahi *et al.*, 2014a).

Predicted delivery device losses under control conditions with a 5 μm aerosol were found to be about 55% on average when including tube and nasal cannula loss, which is less than the range of observed losses (67-98%) that other studies in the literature had reported for aerosol

delivery through commercial nasal cannulas under various flow conditions (Ari, et al., 2011; Bhashyam, et al., 2008; Longest, et al., 2013c). The improvement may be explained in part by the use of the streamlined nasal cannula as opposed to typically available cannulas like the Optiflow™ (Fisher & Paykel, Irvine, CA, USA), which was shown by Longest et al. (2013c) through computational and *in vitro* methods to exhibit greater depositional loss than a streamlined version. The comparison to Ari et al. (2011) and Bhashyam et al. (2008) is limited by demographics, since both studies considered pediatric and neonatal HFNC gas and aerosol delivery, where it is known that efficiency is reduced by the smaller cannula size as compared to adult cannulas. However, a recent study by Perry et al. (2013) suggested that adult delivery of nominal dose using a commercial cannula with a Vapotherm (Stevensville, MD, USA) HFNC system was not much greater than for a pediatric or infant case. For the adult case, nominal dose delivery was reported to be 2.5% or less, depending on flow rate, and for pediatric and infant cases it was 1.2% or less and 0.6% or less, respectively (Perry, et al., 2013). Another limitation to the comparison is the difference in tube positioning, where the current study utilized a 90° bend of tubing intended to mimic the Optiflow device with a single inlet, whereas the studies of Ari et al. (2011) and Bhashyam et al. (2008) considered *in vitro* systems with tubing in various positions. The positioning of the tubing was considered far less significant than the choice of cannula for EEG delivery, since the smaller particles are expected to pass through the gradual bend of the tubing more easily than the more rapid bend of the cannula. For EEG delivery, tube and cannula system losses predicted by this study were much less than for control conditions, with about 2% and 4% for the 0.9 μm and 1.5 μm initial particle sizes, respectively, which is due to the small initial aerosol size and the use of the streamlined cannula. For all cases, including condensational size change did not have a significant effect on average device losses.

Nasal cavity depositional loss comparisons are more difficult to characterize due to the disparity between *in vivo* and *in vitro* results present in the literature. Stahlhofen et al. (1989) provided a fit of *in vivo* data from several studies and measured 80% nasal loss (expressed as deposition efficiency) for a 5 μm aerosol at 30 L/min, while Kelly et al. (2004b) showed a 40% loss under the same conditions using an *in vitro* model. Moreover, a 0.9 μm aerosol at 30 L/min was predicted to produce a nasal loss of 7-8% by Stahlhofen et al. (1989), but Kelly et al. (2004b) predicted virtually no loss for the same conditions. However, Kelly et al. (2004b) also showed depositional loss predicted by *in vitro* models varied greatly when different build methods were employed using the same MRI scan data from Swift (1991), where estimated loss for a 5 μm aerosol at 30 L/min ranged from 40-95%. Despite the unresolved discrepancies between *in vivo* and *in vitro* data in the literature, the average predicted nasal losses for 5 μm and 0.9 μm aerosols at 30 L/min for this study (39.8% and 2.7% with condensational size change and 40.8% and 2.4% without condensational size change) agree reasonably well with published values. Comparisons with the correlation provided by Golshahi et al. (2011) in Figure 6.11 showed outstanding agreement. Moreover, the CFD predictions of nasal deposition produced by this study show an order of magnitude reduction based on initial particle size (i.e. a 5 μm aerosol as compared with a 0.9 μm aerosol), a trend also seen in Stahlhofen et al. (1989), Kelly et al. (2004b), and other studies throughout the literature.

Nasal cavity deposition variability has been predicted by other studies, including Garcia et al. (2009) and Golshahi et al. (2011). Estimates of CV and 95% CI population range were not available from those studies, so for the sake of comparison the range of predicted minimum and maximum nasal DE values are discussed here. Using a set of five adult *in vitro* models, Garcia et al. (2009) measured a range of depositional losses from 20-80% for a 5 μm aerosol at 30

L/min, while for the same conditions Golshahi et al. (2011) observed a range of 35-80% for fourteen *in vitro* models of children, where the range from each study is defined by the minimum and maximum data. For the same parameters, not including any condensational size change effects, this study predicted minimum and maximum depositional losses of 25% (Open model) and 55% (Constricted2 model), indicating a smaller range. However, both Garcia et al. (2009) and Golshahi et al. (2011) had experimental setups that would best approximate either aerosol delivery through a mask or environmental exposure, while this study simulated delivery with short nasal prongs. It is reasonable to conclude that aerosol delivery through a nasal cannula may reduce some variability by directing the flow in a more specific way, though more study is required to further elucidate the reported differences under control conditions. For a 0.9 μm aerosol, studies have shown low variability, where Garcia et al. (2009) reported a range of depositions around 0-3%, Golshahi et al. (2011) showed approximately 0-5%, and this study predicted a range of 2.5-2.9%. All three studies show that for a submicrometer particle size (0.9 μm in this case), variability is lower by an order of magnitude compared with conventional pharmaceutical aerosol size, which highlights the expected efficiency of EEG nasal delivery of lung targeted aerosols.

The two primary features of EEG nasal delivery are the use of submicrometer particles to reduce extrathoracic deposition and the addition of an excipient to promote aerosol growth and foster thoracic deposition. Prior to this study it was well known that deposition of submicrometer aerosols is significantly less than that of larger aerosols, but the effects of condensational size change on deposition and variability of deposition had not been characterized. Though it would seem logical that particle growth as a result of the use of EEG methods would lead to potentially significant increases in both deposition magnitude and

variability, the CFD data did not support this result. Instead, the 95% CI range for the DE of the 0.9 μm aerosol in the four models was reduced from 1.6-3.2% to 2.3-3.1%, and the mean was relatively unchanged, increasing from 2.4% to 2.7%. Consequently, the CV was reduced from 17% to 8% by including the effects of condensational size change for the 0.9 μm aerosol. A similar pattern was observed for the 1.5 μm aerosol, though not as pronounced. Condensational size change effects did not produce an observable change in the data for the 5 μm aerosol. Collectively, the data showed that the condensational size change effects of the EEG method produce a reduction in depositional variability that was more pronounced with the smaller aerosol.

A primary hypothesis of this study was that SA/V may be used as an indicator of nasal DE and associated variability. Several correlations exist in the literature that use a variety of parameters to characterize variability, including SA/V or V/SA (Carrigy *et al.*, 2014; Garcia, et al., 2009; Golshahi, et al., 2011; Storey-Bishoff, et al., 2008). Results showed that for control conditions without and with condensational size change considered, the nasal cavity DE correlated very strongly with SA/V ($R = 0.993$, $p < 0.007$ and $R = 0.991$, $p < 0.01$), but for EEG conditions the two parameters were not related. Instead, DE shows some correlation with the product of $d_{h,nasopharynx}$ and SA/V, where r-values of the 0.9 μm and 1.5 μm aerosols with size change considered were $R = 0.84$ and $R = 0.93$, respectively. Examining the relationships of PF with variables of interest provides what is perhaps a clearer picture. Delivered dose (i.e. PF) correlates strongly with SA/V for control conditions without and with condensational size change ($R = -0.998$, $p < 0.002$ and $R = -0.997$, $p < 0.003$), while for EEG conditions a relationship between PF and $d_{h,nasopharynx}$ was observed. With the inclusion of condensational size change effects, a correlation between the two parameters was noted for the 0.9 μm and 1.5 μm

cases ($R = -0.93$ and $R = -0.96$, $p < 0.05$), which was somewhat weaker when size change was considered for both particle sizes ($R = -0.90$ and $R = -0.93$).

Though it is interesting to observe that PF may be related to $d_{h,nasopharynx}$, the unsteady nature of this parameter presents a problem. PF has been shown to vary during a breathing cycle (Schwab *et al.*, 1993), during sleep (Trudo *et al.*, 1998), and according to posture (Van Holsbeke, et al., 2013). Therefore, the PF of smaller particles may be subject to intrasubject variability as well as intersubject variability. Regarding the scan data used in this study, CT scans are taken in a supine posture, which has been shown by Van Holsbeke et al. (2013) to reduce nasopharynx exit area, and the scans are not controlled for any particular point in the breathing cycle. Also, it is not clear whether $d_{h,nasopharynx}$ is the sole indicator of PF under these conditions.

Though this study has provided evidence that SA/V correlates well with DE and PF under control conditions (i.e. for an aerosol size of 5 μm), a limitation of the results is that a critical aerosol diameter for which this relationship is valid was not defined. More investigation is required to characterize a greater range of aerosol diameters and flow rates so that a related characteristic diameter may be identified. For aerosol sizes less than this critical diameter, a dependence of PF on $d_{h,nasopharynx}$ was suggested by the data, but the scan conditions were not controlled to isolate intrasubject and intersubject effects, nor has dependence on other parameters been ruled out. Also, future study is required to identify the effects of the MMAD at the nasopharynx exit on the total DF in the lungs.

In summary, the EEG approach can improve the lung PF of aerosols by a factor of four compared with conventional aerosol administration with a nasal cannula interface across a range of nasal anatomies. A database of nasal cavity dimensions obtained from CT scans was produced, from which the four models were chosen. The models were selected to represent a

broad range of nasal cavity constriction, which was characterized by SA/V, and evidence showed that the deposition of larger aerosols at the given flow rate correlate well with this parameter. For a 5 μm initial aerosol size, conventional methods resulted in delivery device and nasal losses around 80%, while a 0.9 μm initially sized aerosol under EEG conditions only resulted in about 20% total drug loss with only 6% depositing in the device and nasal airways. An investigation of nasal inhalation effects showed that the tracheal inhalation rate should be greater than the aerosol delivery rate, with PF values increased to 90% for one case. Furthermore, use of the EEG techniques reduced variability in PF as expressed by CV from 15% to 3-4% as compared with conventional aerosol sizes. With EEG delivery, differences in nasal cavity geometry had a larger effect on the size of the aerosol exiting the nasopharynx than for conventional delivery. Determining whether this size difference has an effect on lung deposition requires additional study.

Table 6.1 Geometric measurements of each nasal model, including surface area (SA), volume (V), surface area-to-volume ratio (SA/V), minimum nasal cavity hydraulic diameter ($d_{h,min}$), average nostril hydraulic diameter ($d_{h,nostril}$), and nasopharynx exit hydraulic diameter ($d_{h,nasopharynx}$).

	SA (mm^2)	V (mm^3)	SA/V (mm^{-1})	$d_{h,min}$ (mm)	$d_{h,nostril}$ (mm)	$d_{h,nasopharynx}$ (mm)
Open	8024.20	10832.35	0.74	3.83	12.06	5.94
Average	10509.34	10488.66	1.00	2.81	11.44	9.74
Constricted1	8237.14	7194.61	1.14	2.40	11.21	5.87
Constricted2	9661.46	6790.42	1.42	1.98	13.00	8.78

Table 6.2 Boundary conditions and particle parameters from the study of Golshahi et al. (2013) and the current study, including inlet relative humidity (RH), the total number of particles (n_{part}) and the initial aerodynamic diameters of the control ($d_{ae,control}$) and EEG ($d_{ae,EEG}$) aerosols.

	$RH_{Control}$	RH_{EEG}	n_{part}	$d_{control}$ (µm)	d_{EEG} (µm)
Golshahi et al. (2013)	90%	14%	9000	3.6	0.9
Current Study	99%	40%	3000	5.0	0.9, 1.5

Table 6.3 Nasal model measurements implemented in the Golshahi et al. (2011) correlation which include the central path length (L_{CP}), volume of the nasal-throat airways to the top of trachea (V_{total}), and the characteristic diameter (d_c). Also shown is the minimum coronal cross-sectional area of the nasal cavity (A_{min}), for use with the Cheng (2003) correlation.

Model	L_{CP} (mm)	V_{oro} (mm^3)	d_c	A_{min} (mm^2)
Open	212.34	52620.66	15.74	169.61
Average	224.45	45371.92	14.22	162.16
Constricted1	213.89	39153.94	13.53	130.33
Constricted2	224.19	36638.79	12.78	119.69

Table 6.4 Range of insertion depth values of the streamlined nasal cannula in each model. Insertion depth is defined as the range of the shortest and longest distance of the cannula opening to the plane of the nostril inlet.

	Left Nostril (mm)	Right Nostril (mm)
Open	1.27-7.27	1.72-8.12
Average	0.17-4.76	0.32-5.23
Constricted1	3.24-6.54	2.54-6.92
Constricted2	1.75-4.39	0.90-5.19

Table 6.5 Expected Reynolds numbers for each model in coronal cross-sectional Regions 1-4 (as shown in Figure 6.1), defined as (1) the termination of the nasal valve area, (2) location with two meatuses, (3) location with three meatuses, and (4) entrance to the nasopharynx.

Model	Region 1	Region 2	Region 3	Region 4
Open	799	361	419	1402
Average	861	304	345	1248
Constricted1	1058	361	392	1456
Constricted2	968	317	322	1510

Table 6.6 Pressure drop (Δp) from the tube inlet to the nasopharynx exit for each model. Variables that may correlate with pressure drop are also shown, including surface area-to-volume ratio (SA/V), hydraulic diameter at the exit of the nasopharynx ($d_{h,nasopharynx}$), and the surface area to volume ratio divided by the hydraulic diameter at the exit of the nasopharynx ($(SA/V)/d_{h,nasopharynx}$).

	Δp (Pa)	**SA/V (mm^{-1})**	**$d_{h,nasopharynx}$ (mm)**	**$(SA/V)/d_{h,nasopharynx}$ (mm^{-2})**
Open	128.59	0.74	5.94	0.12
Average	123.84	1.00	9.74	0.10
Constricted1	193.63	1.14	5.87	0.20
Constricted2	176.58	1.42	8.78	0.16

Table 6.7 Regional deposition fraction (DF) values (given in %) for simulations without condensational aerosol size change in the cannula, nasal valve area, and nasal cavity of each model. Also shown is the deposition efficiency (DE) of the total nasal region including the nasal valve area, nasal cavity, and nasopharynx. The particles considered include 0.9 μm and 1.5 μm solid formulations of 50:50 albuterol sulfate (AS):NaCl, and a 5 μm droplet of 0.1% AS:0.1% NaCl. The mean, 95% confidence interval (CI), and coefficient of variation (CV) for the total nasal DE of each initial particle size are also included.

	Cannula DF			Nostril DF			Nasal Cavity DF			Total Nasal DE		
	0.9 μm	**1.5 μm**	**5 μm**	**0.9 μm**	**1.5 μm**	**5 μm**	**0.9 μm**	**1.5 μm**	**5 μm**	**0.9 μm**	**1.5 μm**	**5 μm**
Open	1.6	3.7	50.2	0.1	0.3	2.8	1.5	2.4	7.3	1.8	3	24.5
Average	1.7	3.5	49.6	0.3	0.4	5.1	2.2	3.5	11.5	2.6	4.2	38.6
Constricted1	1.6	2.8	49.4	0.2	0.3	2.9	2	3	16.4	2.4	3.7	45.1
Constricted2	1.7	2.9	48.5	0.2	0.3	7.9	2.4	3.5	16.5	2.7	4.1	54.9
									Mean	2.4	3.8	40.8
									95% CI	1.6-3.2	2.7-4.8	15.3-66.3
									CV	17%	15%	31%

Table 6.8 Regional deposition fraction (DF) values (given in %) with condensational size change for the cannula, nasal valve area, and nasal cavity of each model. Also shown is the deposition efficiency (DE) of the total nose-throat region including the nasal valve area, nasal cavity, and nasopharynx. The particles considered include 0.9 μm and 1.5 μm solid formulations of 50:50 albuterol sulfate (AS): sodium chloride (NaCl), and a 5 μm droplet of 0.1% AS:0.1% NaCl. The mean, 95% confidence interval (CI), and coefficient of variation (CV) for the total nasal DE of each initial particle size are also included.

	Cannula DF			Nostril DF			Nasal Cavity DF			Total Nasal DE		
	0.9 μm	**1.5 μm**	**5 μm**	**0.9 μm**	**1.5 μm**	**5 μm**	**0.9 μm**	**1.5 μm**	**5 μm**	**0.9 μm**	**1.5 μm**	**5 μm**
Open	1.9	3.4	50.0	0.2	0.2	2.7	2.0	2.5	7.4	2.6	3.2	24.3
Average	2.0	3.7	49.9	0.3	0.3	4.7	2.4	3.5	11.2	2.9	4.1	37.4
Constricted1	1.4	3.1	48.8	0.1	0.3	3.3	2.2	3.1	15.9	2.5	3.8	44.5
Constricted2	1.5	3.1	48.5	0.3	0.4	7.9	2.4	3.6	15.9	2.9	4.2	53.0
									Mean	2.7	3.8	39.8
									95% CI	2.3-3.1	2.9-4.7	15.5-64.1
									CV	8%	12%	30%

Table 6.9 Mass median aerodynamic diameters (MMAD), given in μm, at the exit of the nasal cavity for the three initial aerodynamic diameter (d_{ae}) cases (0.9 μm and 1.5 μm for 50:50 albuterol sulfate (AS): sodium chloride (NaCl), 5 μm for 0.1% AS:0.1% NaCl). The mean, 95% confidence interval (CI), and coefficient of variation (CV) are listed for each initial particle size.

	Exit		
	0.9 μm	**1.5 μm**	**5 μm**
Open	1.33	2.2	4.9
Average	1.62	2.49	4.85
Constricted1	1.58	2.39	4.91
Constricted2	1.7	2.5	4.9
Mean	1.56 μm	2.40 μm	4.89 μm
95% CI	1.24 – 1.88 μm	2.12 – 2.67 μm	4.84 – 4.94 μm
CV	10%	6%	1%

Table 6.10 Penetration fraction (PF) values of each model, listed without simulated size change and with size change. The PF indicates the percentage of initial drug mass that exits the nasopharynx and enters the pharynx upstream of the larynx. Values include loss at the nostril inlets. The mean, 95% confidence interval (CI), and coefficient of variation (CV) are listed for each initial particle size.

	Without Size Change			**With Size Change**		
	0.9 µm	**1.5 µm**	**5 µm**	**0.9 µm**	**1.5 µm**	**5 µm**
Open	83.4	81.3	28.3	82.7	80.4	28.4
Average	80.0	77.3	24.6	79.6	76.4	25.0
Constricted1	85.7	83.3	22.1	85.5	83.4	22.7
Constricted2	80.6	78.4	18.6	81.1	77.5	19.7
Mean	82.4	80.1	23.4	82.2	79.4	24.0
95% CI	77.1 – 87.7	74.6 – 85.5	15.2 – 31.6	77.2 – 87.3	73.1 – 85.7	16.6 – 31.3
CV	3%	3%	17%	3%	4%	15%

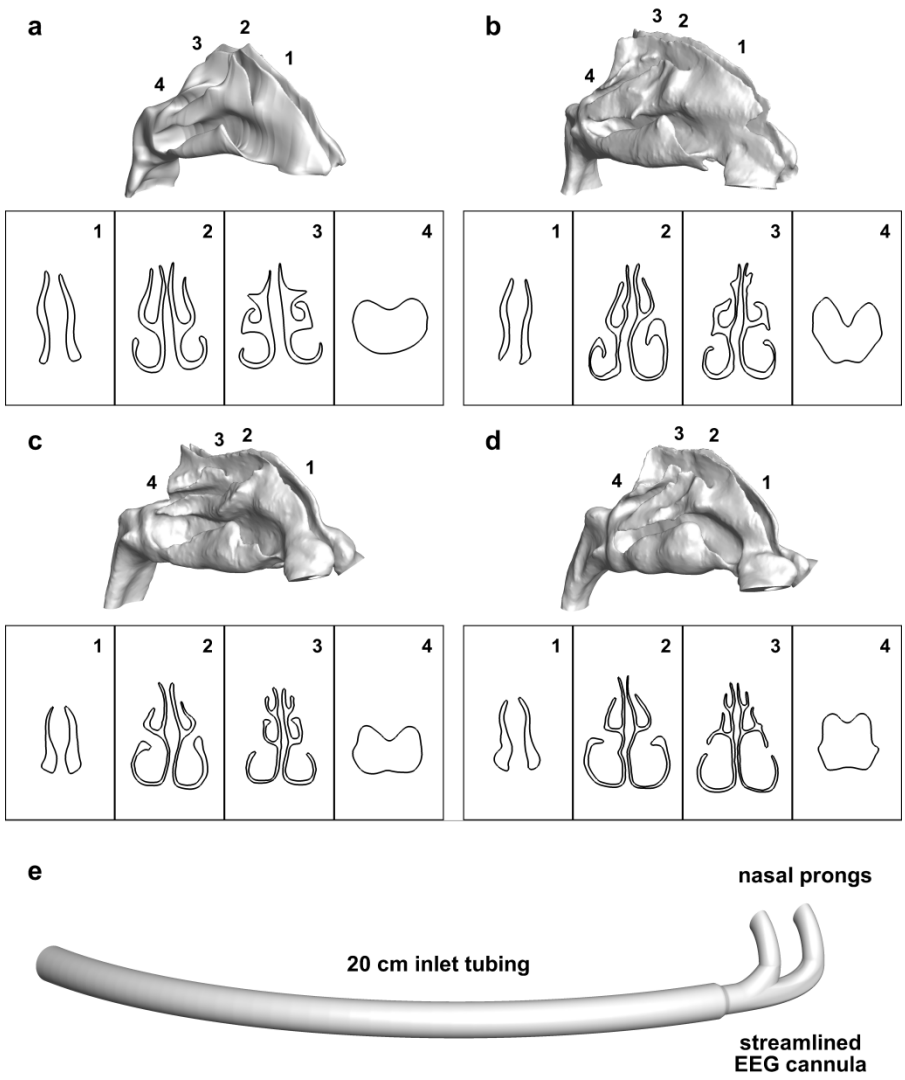

Figure 6.1 Four nasal models denoted (a) Open, (b) Average, (c) Constricted1, and (d) Constricted2. Coronal cross-sectional Regions (1 to 4) are depicted, beginning with the termination of the nasal valve area (1), followed by regions showing two and three meatuses (2 and 3, respectively), and ending with the entrance to the nasopharynx (4). The tube and nasal cannula used with each model is illustrated in part (e).

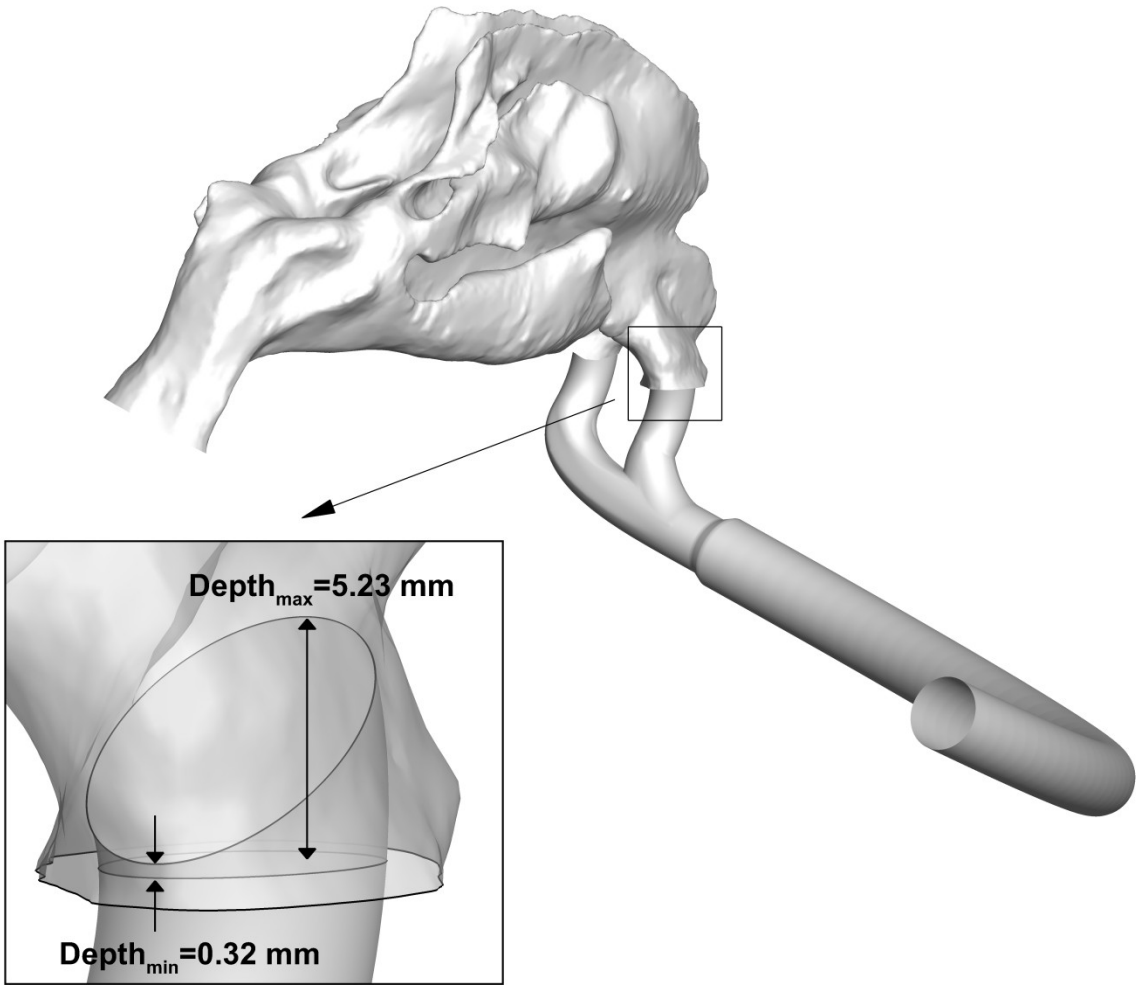

Figure 6.2 Minimum and maximum insertion depth values of the nasal cannula in the right nostril of the Average model. For clarity, a translucent close up of the model is shown in the same orientation as the far field view. The prongs are observed to protrude into the nasal vestibule by only a small amount.

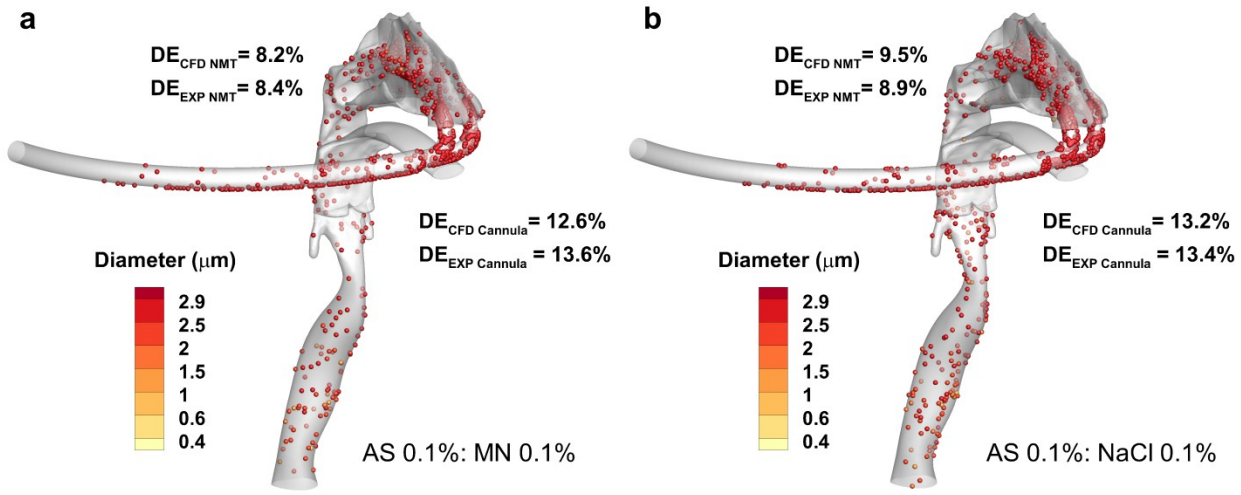

Figure 6.3 Comparison of CFD predictions with the experimental deposition fraction (DF) results from Golshahi et al. (2013) with formulations (a) 0.1% albuterol sulfate (AS): 0.1% mannitol (MN) and (b) 0.1% AS: 0.1% sodium chloride (NaCl).

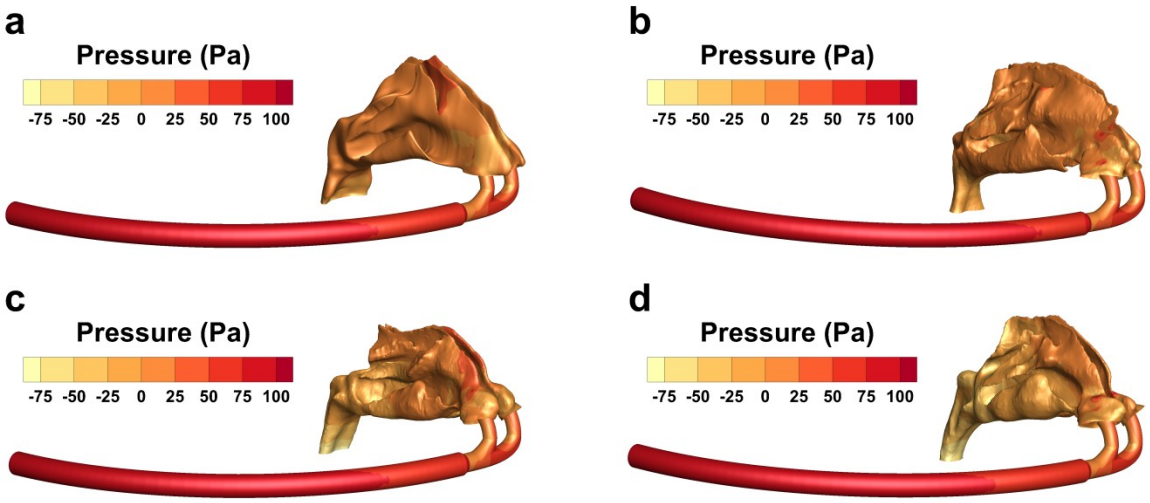

Figure 6.4 Wall pressure of (a) Open, (b) Average, (c) Constricted1, and (d) Constricted2 models, shown in Pa.

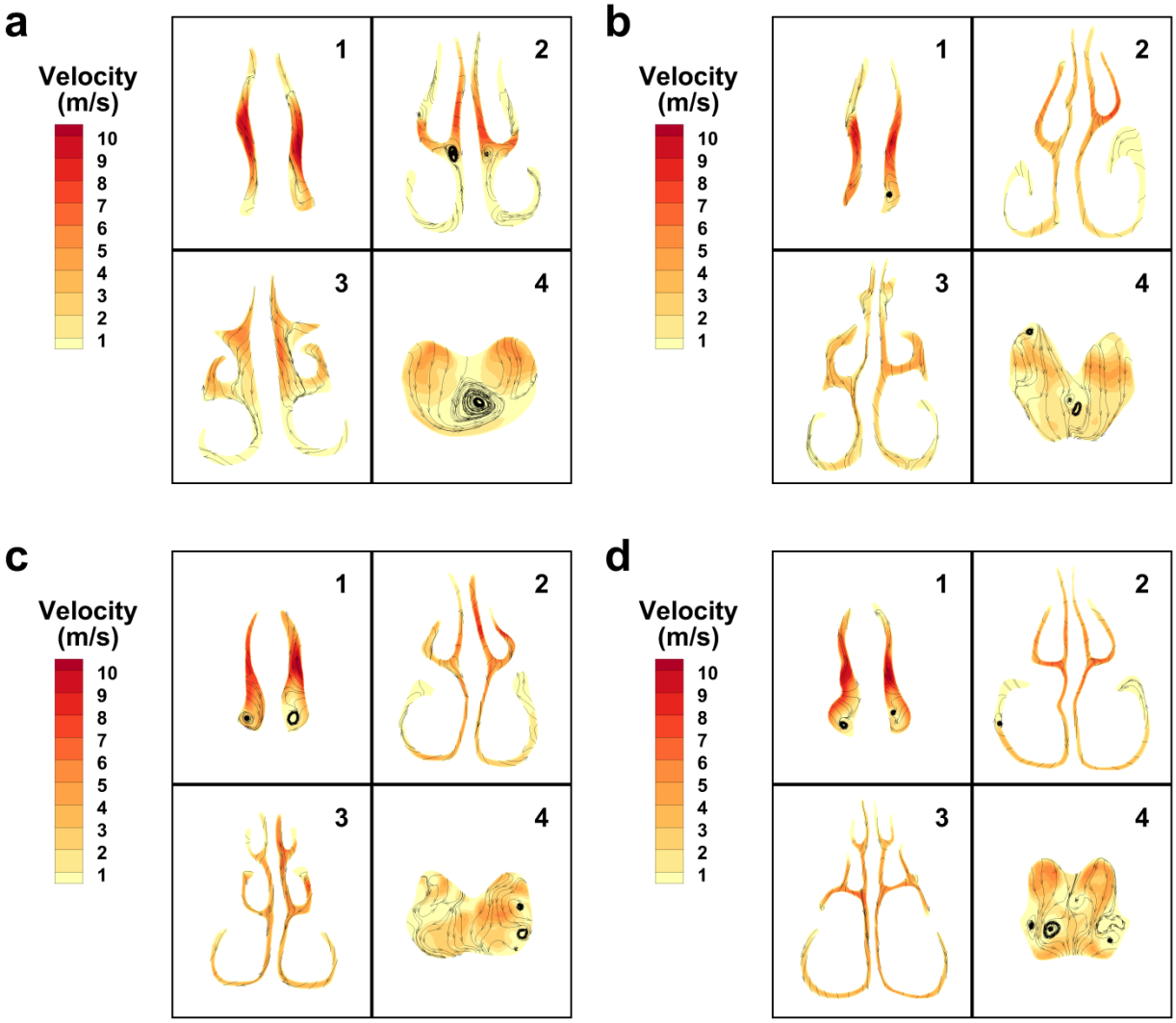

Figure 6.5 Velocity magnitude and contours of coronal cross-sections for (a) Open, (b) Average, (c) Constricted1, and (d) Constricted2 airway models. Cross-sections shown for regions (1) nasal valve area termination, (2) two meatuses, (3) three meatuses, and (4) nasopharynx entrance.

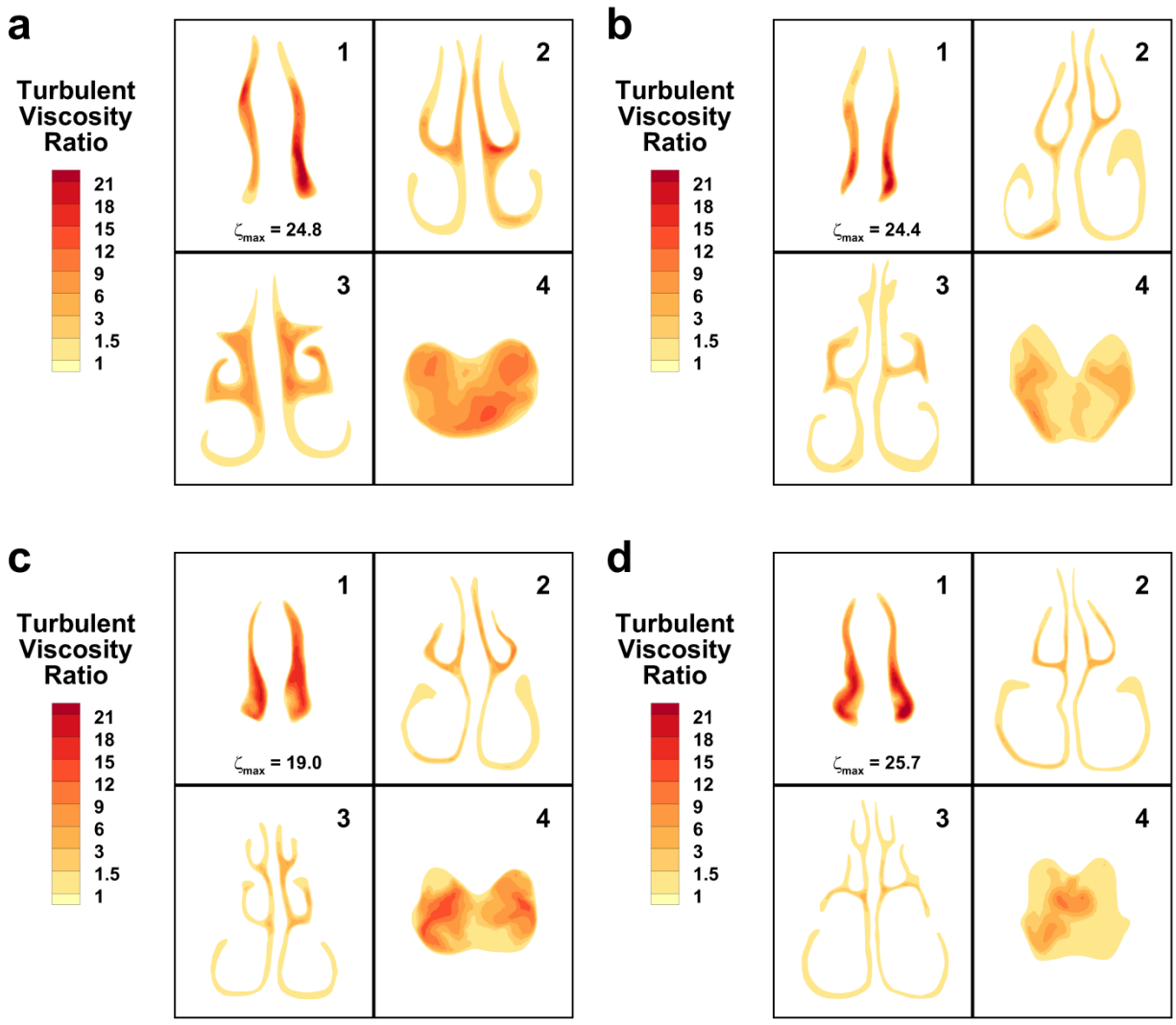

Figure 6.6 Turbulent viscosity ratio (ζ) of coronal cross-sections for (a) Open, (b) Average, (c) Constricted1, and (d) Constricted2 airway models. Cross-sections shown for regions (1) nasal valve area termination, (2) two meatuses, (3) three meatuses, and (4) nasopharynx entrance. The maximum turbulent viscosity ratio (ζ_{max}) is indicated for each model, which occurred in region 1 for all cases.

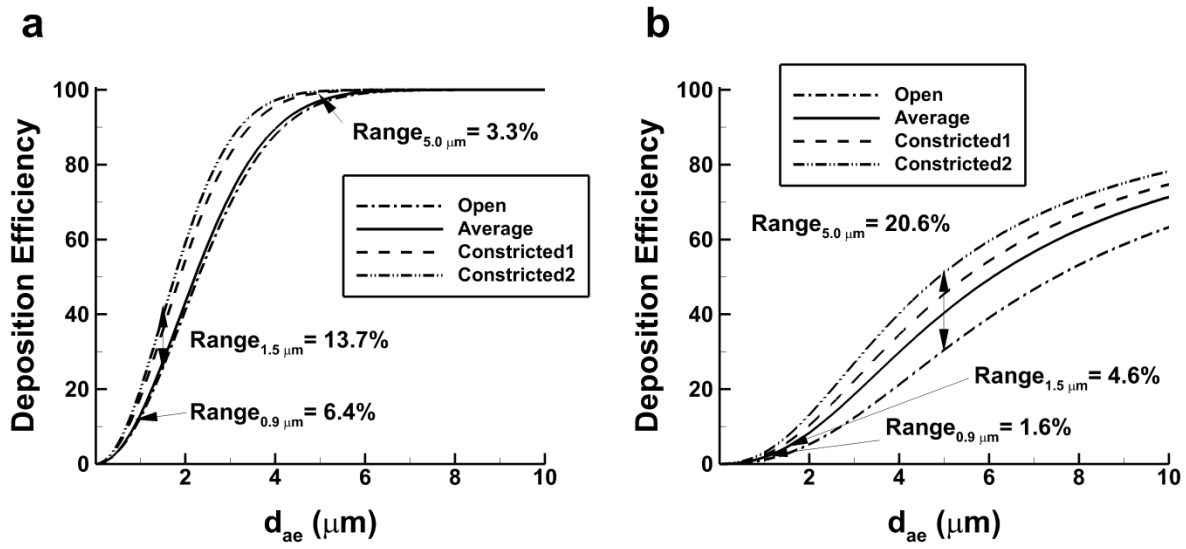

Figure 6.7 Predictions of deposition efficiency (DE) based on aerodynamic diameter (d_{ae}) from the correlations of (a) Cheng (2003) and (b) Golshahi et al. (2011) applied to the four nasal models. Range values representing the difference between maximum and minimum predicted DE are also presented for particles of initial size 0.9 μm, 1.5 μm, and 5.0 μm.

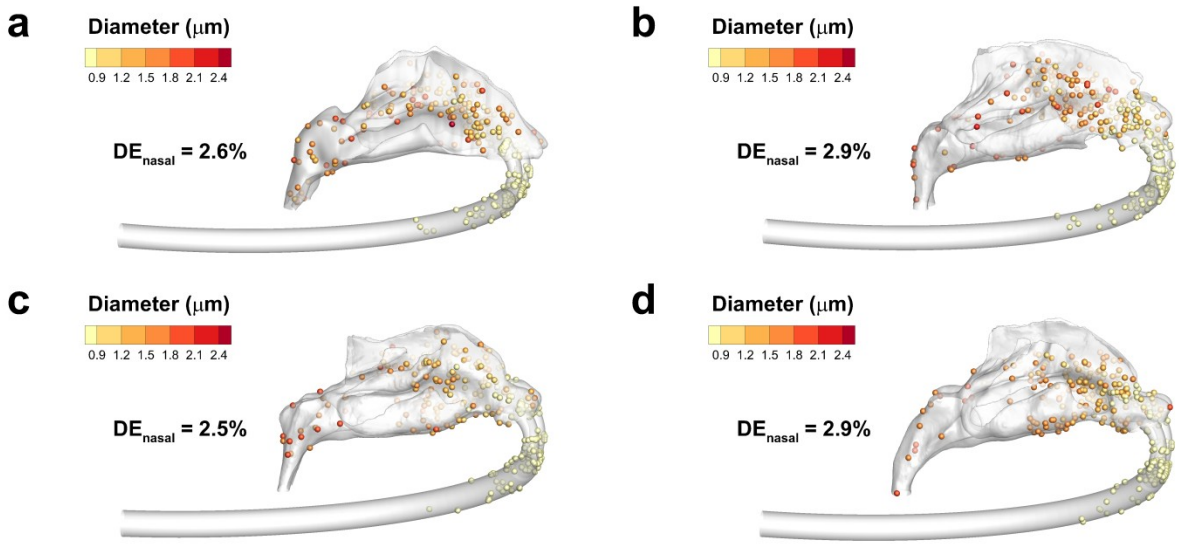

Figure 6.8 Deposition efficiency (DE) of droplets with an initial mass median aerodynamic diameter (MMAD) of 0.9 μm for (a) Open, (b) Average, (c) Constricted1, and (d) Constricted2 airway models.

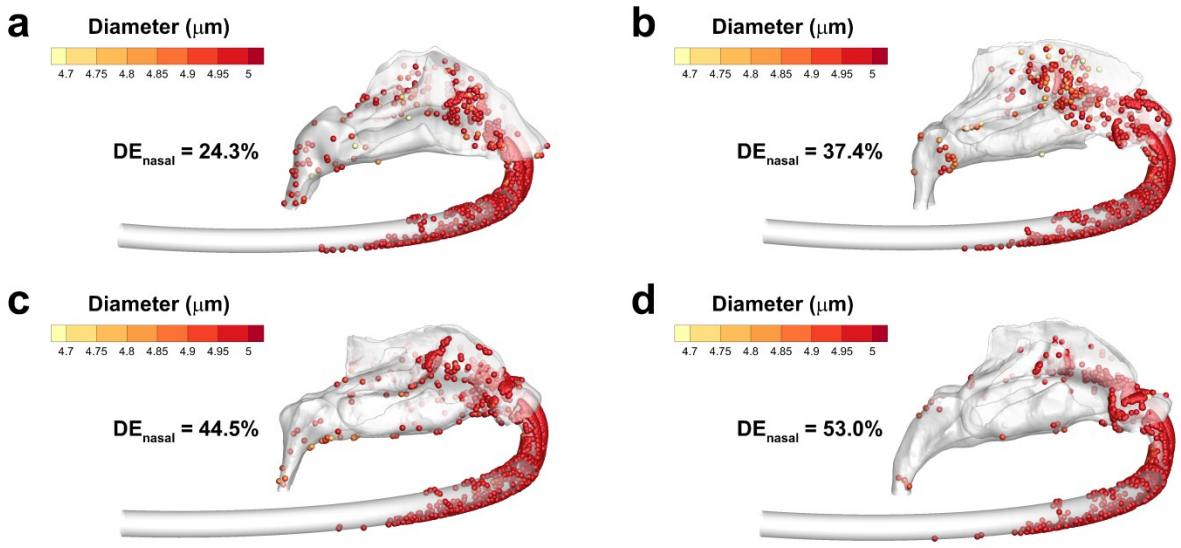

Figure 6.9 Deposition efficiency (DE) of droplets with an initial mass median aerodynamic diameter (MMAD) of 5 μm for (a) Open, (b) Average, (c) Constricted1, and (d) Constricted2 airway models.

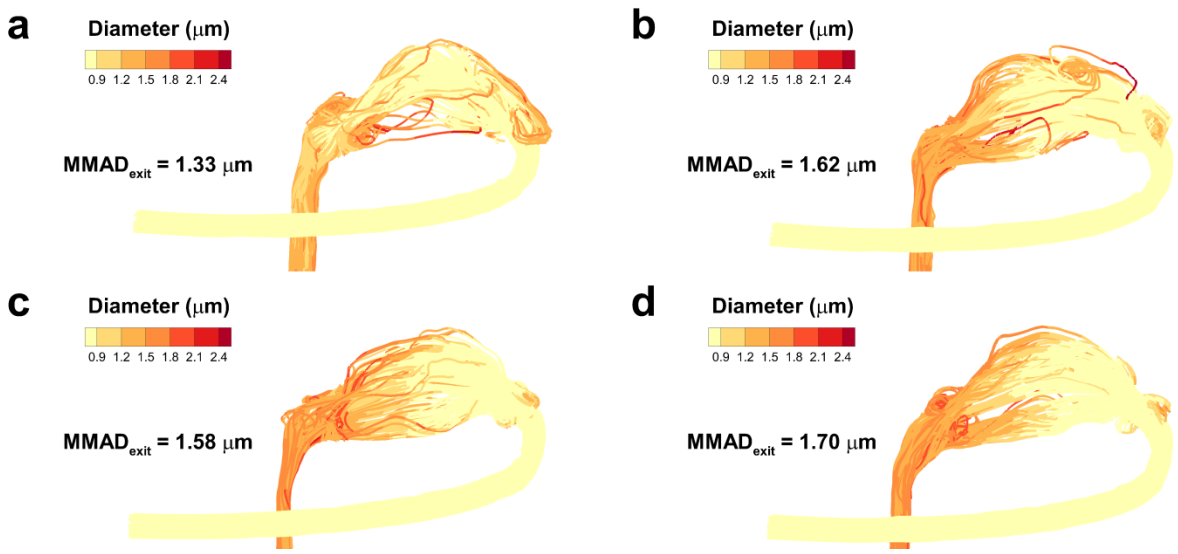

Figure 6.10 Growth and evaporation of particles with an MMAD of 0.9 μm for (a) Open, (b) Average, (c) Constricted1, and (d) Constricted2 airway models.

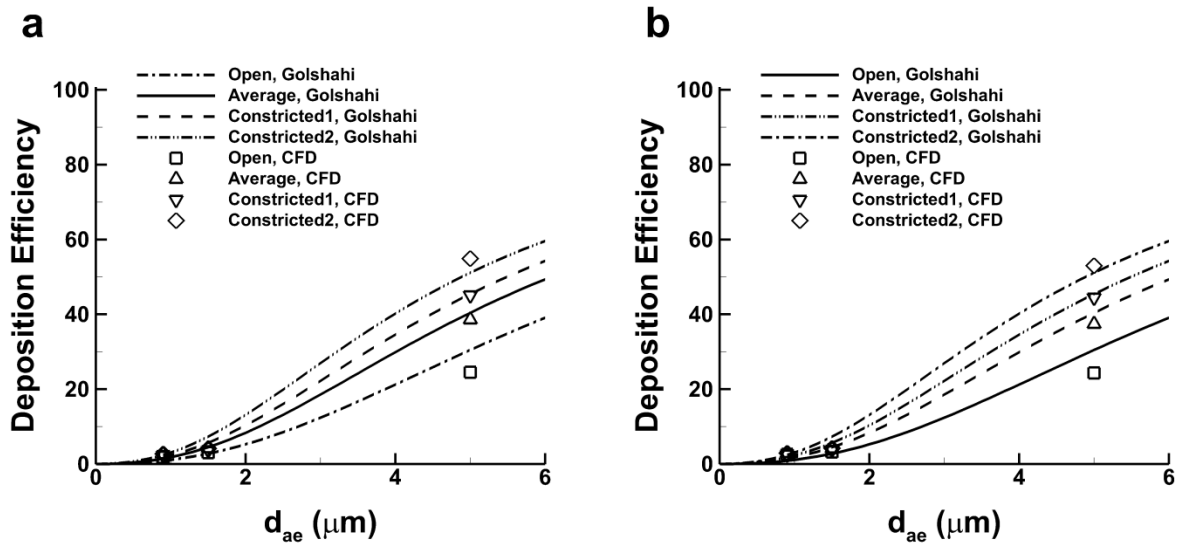

Figure 6.11 Deposition efficiency (DE) predicted with the Golshahi et al. (2011) correlation and compared with CFD predictions (a) without size change and (b) with size change.

Chapter 7 Nebulized Aerosol Delivery during NPPV

The objective of this study is to evaluate four oronasal mask designs as they relate to efficiency of nebulized aerosol delivery during noninvasive positive pressure ventilation (NPPV). A face-nose-mouth-throat (FNMT) model was constructed from CT scan data for both CFD simulations and *in vitro* experiments to test a commercial mask and three altered versions of that mask intended to improve aerosol transmission. Conventional and excipient enhanced growth (EEG) aerosol delivery are both considered to quantify potential improvements to nebulized aerosol delivery during NPPV using a condensational growth approach.

7.1 Introduction

To assess conventional and excipient enhanced growth (EEG) drug delivery through a mask during noninvasive positive pressure ventilation (NPPV), the computational version of the face-nose-mouth-throat (FNMT) model was constructed from the same CT scan data used to create the Constricted2 nasal model for Chapter 6 and Walenga et al. (2014). However, to allow for rapid prototyping to be used for model construction the septum was thickened, resulting in a surface area-to-volume ratio (SA/V) of 1.05 mm^{-1}, which represented an average value. A commercially designed mask (PerformaTrak SE®) was replicated using CAD software, and three new mask designs were created by applying various modifications to the commercial mask with the intent of improving aerosol transmission. Steady state delivery of a polydisperse

conventional aerosol was assessed using CFD to serve as a baseline, and deposition was measured using deposition fraction (DF). The drug delivery of a drug:excipient combination using the EEG method was assessed through monodisperse steady state simulations. Results indicated that the EEG technique reduced model deposition by an order of magnitude and that significant aerosol size increase occurred. The mask selected for further study featured two 8 mm diameter aerosol inlets that were directed toward the nostril openings.

An *in vitro* version of the FNMT model was created using rapid prototyping to facilitate experiments performed by Dr. Michael Hindle and co-workers in the VCU Department of Pharmaceutics. Conventional drug delivery was assessed with a prototyped version of the commercial mask and the FNMT model placed in-line with a critical care ventilator, a test lung, and an Aeroneb Pro nebulizer that was filled with a 0.5% albuterol sulfate (AS) w/v solution. The mixer-heater developed by our group and reported in Golshahi et al. (2014b) was selected to produce the submicrometer aerosol required for testing the EEG method. The EEG formulation chosen was a 50:50 combination of AS and sodium chloride (NaCl). Initial experiments showed that the most efficient system for EEG delivery placed the mixer-heater in-line with the inspiratory limb of the dual limb circuit, which eliminated the need for an extra flow source to deliver the aerosol. This indicated that the commercial mask (single inlet) would be a better choice for EEG delivery compared with the mask selected from the initial CFD trials (separate gas and aerosol delivery inlets). Results from the experiments showed that delivered dose was improved by about a factor of two with the EEG case as compared to the conventional case for two different test lung inhalation times (1 s and 2 s), while FNMT model deposition was reduced by about an order of magnitude.

Transient CFD predictions were obtained to provide additional insight into the drug deposition mechanisms in the system. To provide a one-to-one comparison with the experimental results, some assumptions were applied to estimate the amount of drug entering the mask in order to provide an approximate nominal dose for the transient simulations. Also, the amount of drug exiting the mask was estimated using the experimental data, which was then compared with the same CFD estimate. The results showed agreement of CFD with experimental estimates within a 4% absolute difference for all cases in each region. Of particular interest was the CFD estimate of mass median aerodynamic diameter (MMAD) at the FNMT outlet, which was unavailable from the experimental data. Predictions showed the MMAD for both EEG cases was comparable with those from the two conventional cases, which indicated that enough condensational growth occurred to allow for significantly enhanced thoracic deposition.

7.2 Methods

Prediction of nebulized aerosol delivery through a mask required the creation of a nose-mouth-throat (NMT) model with a facial interface. The Constricted2 model from Chapter 6 and Walenga et al. (2014) was chosen to represent the nasal model because the associated CT scan included the most complete face and throat data of the models created for that study. Additionally, the penetration fraction (PF) values for the Constricted2 model with size change were below the mean for all three particle sizes, so it represents a conservative case with regard to lung aerosol delivery. The commercial software package Mimics 16.0 (Materialise, Belgium) was used to augment the existing model to include the face and throat, which was exported as a 3D surface file with an .stl extension. Conversion of the surface file to a volumetric file with an

.igs extension was performed using 3-matic (Materialise, Belgium), which allowed for the model to be imported into SolidWorks 2011 (Dassault Systèmes Solidworks Corp., Waltham, MA, USA).

As described later in this section, the results of the steady state CFD simulations were used to guide the selection of a mask for subsequent *in vitro* experiments and transient CFD predictions. The *in vitro* FNMT model was constructed after the steady state simulations were performed, and it was discovered during that process that the septum thickness of Constricted2 was too small for stereolithography (SLA) rapid prototyping, and that it needed to be increased from a minimum of 0.2 to 0.6 mm. However, the steady state results with the original Constricted2 model were still considered valid because only a relative comparison of mask performance was sought. The altered FNMT model was then used for the in *vitro* experiments and transient CFD simulations. The new surface area-to-volume ratio (SA/V) of the altered Constricted2 nasal cavity was 1.05 mm^{-1}, which was significantly less than the previous value (1.42 mm^{-1}), and placed it near the mean of SA/V values collected for Chapter 6 and Walenga et al. (2014). However, Walenga et al. (2014) found that PF only showed a correlation for conventional aerosol delivery, and that the hydraulic nasopharynx diameter ($d_{h,nasopharynx}$) correlated weakly with PF. Using those findings as a guide, the alteration in SA/V makes the altered Constricted2 model an average case for conventional delivery, but it may still be taken as a conservative case for EEG delivery since the value of $d_{h,nasopharynx}$ (8.78 mm) was unaltered.

To facilitate further modification of the model, the SolidWorks file was saved as an .x_t file type and exported to ANSYS Workbench/DesignModeler 14.5 (ANSYS, Inc., Canonsburg, PA, USA). The face was truncated to allow for de-identification of the model and thus only the areas deemed necessary for mask delivery characterization were retained, namely the regions

around the nose and mouth. The mouth pathway was nearly occluded in the CT scan data, since patients that receive that type of imaging typically have their mouths closed. For this study, a closed mouth model was considered appropriate for inpatient NPPV. However, it was desirable for the model to have a mouth pathway to allow for the possibility of an open mouth model in future studies. The mouth pathway visible in the CT scan data was then augmented to similar dimensions as that of the NMT of Golshahi et al. (2013), and, to approximate a closed mouth position, the mouth pathway volume did not join with the volume defined by the face and mask boundaries. To aid with any future studies that may consider tracheobronchial regions, the throat was modified to allow for connection with Model D from Chapter 3. A numerical extension was added by extruding the outlet profile by ten outlet hydraulic diameter lengths. The final computational version of the FNMT model is pictured in Figure 7.1, where the numerical extension is not pictured. The dead space volumes (air space volumes) of the nasal valve area, nasal cavity, nasopharynx, mouth, and throat regions of the FNMT model are listed in Table 7.1. Also included is the volume of the commercial mask chosen for this study.

The four mask designs tested with steady state CFD simulations are pictured in Figure 7.2. For the first design, shown in Figure 7.2a, the commercially available PerformaTrak® SE oronasal mask (Philips Respironics, Inc., Pittsburgh, PA, USA) was selected and the computational model was built using careful measurements with a set of calipers. The other three mask designs were conceived by making alterations to the commercial design, with the idea that a separate aerosol stream proximal to the nares would perform more efficiently than direct delivery through the ventilation line. Illustrated in Figure 7.2b is Mask Design #1.1, where an inlet tube with an 8 mm inner diameter was inserted into the anatomical right side of the commercial mask, aimed at the nearest nostril opening, and extended about halfway between

the mask and nostril. Mask Design #1.2, depicted in Figure 7.2c, has two inlet tubes with 8 mm inner diameters aimed at both nostril openings, but they do not extend into the mask space as with Mask Design #1.1. For Mask Design #1.3, shown in Figure 7.2d, Mask Design #1.1 was altered such that the inlet tube extended all the way to the nostril opening.

To create the computational meshes for this study, the four masks were joined with the FNMT model and the meshing software ICEM CFD 12.0.1 (ANSYS, Inc., Canonsburg, PA, USA) was used. Though it is well known that the mask seal with the face may have a significant effect on drug delivery, the meshes were built without allowing a leak, to provide for a more concentrated focus on the effect of mask design. However, the effect of mask seal as it relates to dry powder delivery is explored in Chapter 8. A nearly identical meshing procedure as compared with Chapter 6 and Walenga et al. (2014) was implemented to create the four meshes. The only change in the method was that a tetrahedral mesh was applied to airspace between the mask and the face as opposed to the hexahedral mesh applied to the tube and nasal cannula in Walenga et al. (2014), because the irregular face surface made the application of a hexahedral boundary intractable. As before, seven near-wall layers were applied with a near-wall control volume height of 0.011 mm to the Delauney meshes. The four models all consisted of ~7 million cells. The simulations were checked for y^+ values of the near-wall control volumes, and in all cases the y^+ values were ~1 or less, indicating mesh independence.

To evaluate the four mask designs, steady state simulations were performed to obtain relative differences in DF in the mask, face, and NMT. The steady state assumption was made for computational efficiency and also because experimentally determined flow profiles had not yet been obtained. As mentioned above, the original Constricted2 nasal cavity was considered for these simulations. As is common with most NPPV systems, it was assumed that heated,

humidified inlet flow was provided to the models. Gas delivery from the ventilator was assumed to occur at an average rate of 30 L/min. For all of the models except the commercial version, the aerosol inlet temperature was 35 °C, the relative humidity (RH) was 99%, and the flow rate was 15 L/min, leaving the other 15 L/min to travel through the mask inlet from the ventilator at a temperature of 37 °C and an RH of 99%. For the commercial version, the inlet flow was simply 30 L/min at 37 °C and an RH of 99%. The outlet condition for all the four cases was specified as a constant pressure outlet of zero.

Excipient enhanced growth (EEG) drug delivery was considered for all four steady state cases. Drug and excipient combination particles consisting of AS and NaCl were injected into each of the four models as a monodisperse bolus of 9,000 particles, with an assumed initial aerodynamic diameter of 0.9 μm. This assumption was based on a similar experiment with the steady state mixer-heater described in Chapter 5, where 50:50 AS:NaCl was reduced to 0.9 μm for a flow rate of 30 L/min (Golshahi, et al., 2013). The hygroscopic parameters of both AS and NaCl are reported in Chapter 6 and in the literature (Longest & Hindle, 2011; Walenga, et al., 2014). The aerosols were considered as both 50:50 and 75:25 combinations of AS:NaCl. Additionally, the commercial mask was considered with a polydisperse conventional aerosol that was assumed to be produced by an Aeroneb Lab nebulizer (Aerogen, Galway, Ireland) with 0.2% AS w/v at a flow rate of 30 L/min. The polydisperse bolus consisted of 9,000 particles. The relevant particle size distribution was determined by Longest et al. (2013a; 2014a), where the mass median aerodynamic diameter (MMAD) was 4.84 μm.

To simulate the steady state fluid flow for the four cases considered, the commercially available CFD package ANSYS FLUENT 14.5 (ANSYS, Inc., Canonsburg, PA, USA) was used in conjunction with several user-defined routines. Using this blend of commercial and custom

software, fluid heat and mass transfer and were also modeled, along with particle deposition, size change, and trajectories. To simulate both turbulent and laminar flow, a low-Reynolds number (LRN) k-ω model was used because it has been shown to reliably predict flow field properties in human upper respiratory airways, especially in relation to aerosol transport and deposition (Xi, et al., 2008).

Lagrangian transport equations were implemented to execute particle trajectory calculations, which included predictions of hygroscopic size change (Longest & Hindle, 2010). A random walk method was utilized to estimate turbulent dispersion of particle trajectories, and user-defined functions (UDFs) were used to model Brownian motion and near-wall corrections of turbulence and fluid velocities. The near-wall velocity and turbulence correction UDFs updated in Chapter 4 were used with a slight modification that marginally increased NMT deposition. Particle size change was also predicted, in particular as it relates to the Kelvin effect, hygroscopicity of the drug and excipient, and the effect of vapor pressure. The system was modeled as one-way coupled in that influences of the discrete phase on the continuous phase were neglected. The equations used have been described in more detail by Longest et al. (2011) and Tian et al. (2013).

Previously established best practices were followed with regard to ANSYS FLUENT 14.5 solution methods (Longest, et al., 2012c). Accuracy was improved through the use of double precision for all calculations. The SIMPLEC algorithm was selected to model the pressure-velocity coupling and a second-order upwind scheme was utilized for the spatial discretization of all convective terms. To define flow field convergence, the simulations were monitored to detect both a five order of magnitude reduction in the global mass-residual and the approach of mass and momentum residual rates to the numerical precision limit.

The *in vitro* models were built once the steady state CFD simulations were complete, including the newly designed mask which showed the highest predicted drug delivery, the commercial mask, and the FNMT model. The computational models were altered with ANSYS Workbench/DesignModeler to create hollow versions with a 2 mm outer thickness. Rather than using the commercially available mask directly and an altered version of that mask to represent the new design, the masks were constructed with rapid prototyping. To accomplish this, stereolithography with a Viper SLA system (3D Systems, Valencia, GA, USA) was used with Accura 60 clear plastic resin. Rapid prototyping was chosen for mask creation because the mask seal was not a study design variable and also because it allowed for both the *in vitro* and *in silico* models to have identical dead space volumes. This provided a more exact comparison with the transient CFD simulations that followed the completion of the *in vitro* experiments. To aid with complete sealing of the mask-face interface, a bracket around the face region of the FNMT model was added. Additionally, the FNMT model was built in sections and assembled using epoxy rather than created as a whole piece due to difficulties associated with rapid prototyping. It was during this process that it was discovered the Viper SLA system required that the septum of the FNMT model have a minimum 0.4 mm thickness, and as mentioned above the septum was thickened to solve the issue. The final *in vitro* FNMT model is shown in Figure 7.3.

A series of *in vitro* experiments were completed by Dr. Michael Hindle and co-workers in the VCU Department of Pharmaceutics. For the experiments, a Galileo critical care ventilator (Hamilton Medical, Bonaduz, Switzerland) was used to provide NPPV support applied to the FNMT model. As is consistent with a critical care setting, a heated and humidified dual limb circuit was selected, and the ventilator was operated using a manufacturer defined 'NPPV' setting. The 'NPPV' setting defined a pressure support mode, where the peak end expiratory

pressure (PEEP) was set to 5 cm H_20, while the inspiratory positive airway pressure (IPAP) was varied from 10-15 cm H_20 to achieve a mean flow rate of ~30 L/min. The ventilator was connected to the FNMT geometry, which was in turn connected to a Dual Adult Test Lung (Michigan Instruments, Grand Rapids, MI), which was controlled with a breath simulation module (Michigan Instruments) and supplied by a tank of pressurized air. A breathing rate of 15 breaths per minute was selected for the Dual Adult Test Lung, while the inspiratory time was 1 or 2 s, which provided 400 or 800 mL of tidal volume to the system. The compliance of the lung was 50 mL/cm H_20 and the lung resistance was 5 cm H_20/L/s. For conventional and EEG drug delivery, inspiratory and expiratory drug filters were placed in the system to measure inhaled and exhaled dose. A high-performance liquid chromatography (HPLC) method was used to measure drug deposition in the connecting tubing, mask, face, and NMT.

Conventional drug delivery was assessed with a 0.5% AS w/v in water solution nebulized with an Aeroneb Pro (Aerogen, Galway, Ireland) mesh nebulizer. The nebulizer was inserted in-line using an Aerogen T-connector with a single section of tubing between the FNMT model and the junction at the dual limb exit. The expiratory filter was placed between the dual limb junction and the nebulizer. The process diagram is shown in Figure 7.4 and the experimental setup is pictured in Figure 7.5. For each trial, the nebulizer was operated for 2 min, which resulted in 30 periods of 4 s each. The rapid prototyped version of the commercially available PerformaTrak SE® mask was used for all conventional aerosol experiments.

Considering EEG delivery, the transient flow aerosol mixer-heater developed in Chapter 5 and reported by Golshahi et al. (2014b) was modified to receive inspiratory flow from the ventilator instead of the previously-used blowers. The EEG aerosol was a 50:50 combination of AS and NaCl that was initially dissolved as 0.5% AS and 0.5% NaCl w/v in water and nebulized

with the Aeroneb Pro. The mixer-heater was placed in-line with the inspiratory section of the dual limb circuit, which was mated to a Y-connector at the entrance to the mask. The rapid prototyped version of the commercially available PerformaTrak SE® mask was used, even though it had been previously decided to use the best of the new mask designs as indicated by the steady state simulations. The reasoning for this is described in the results section. The inspiratory filter is just downstream of the FNMT model, while the expiratory filter is in-line with expiratory section of the dual limb circuit. The process diagram for the EEG drug delivery experiments is shown in Figure 7.6 while the experimental setup is depicted in Figure 7.7. As with the conventional drug delivery trials, the nebulizer was operated for 2 min.

To provide further insight into the deposition patterns of the four experimental cases, flow and particle transport was modeled with four corresponding transient CFD simulations. To provide velocity inlet boundary conditions for those predictions, experimental flow rate profiles were sampled from the ventilator flow meter in 0.032 s intervals. It was observed for each case that when the system was started the flow profile underwent an initial period of rapid change as the ventilator adjusted to meet the defined pressure limits in response to the inhalation and exhalation of the Dual Adult Test Lung. After this period, the flow rate profile in each case demonstrated a pattern with no visibly significant changes. Thus, it was decided to sample the profiles from one period of ~4 s, which were then used as representative boundary conditions for the transient CFD predictions. To enhance convergence of the simulations, a series of linear and sinusoidal regressions were applied to each flow rate profile and expressed in terms of average inlet velocity. The sampled data and accompanying regressions are pictured in Figure 7.8. It is notable that for both the 1 s and 2 s inhalation cases, the conventional and EEG experimental systems produced similar inlet velocity profiles. Also noteworthy is the fact that for both cases

the inhalation flow terminates at ~1.6 s rather than at ~1 s and ~2 s as expected, but it is recalled that the ventilator acts in response to the inhalation flow it detects from the Dual Adult Test Lung to meet the preset IPAP and PEEP values. Thus, the values measured by the flow meter are reflective of the influences of both the ventilator and the test lung.

To reduce simulation times, the transient CFD predictions were executed using parallel processing with ANSYS FLUENT 14.5 on four 2.93 GHz processors in a Windows 7 environment. Auto-partitioning was used to separate the mesh into four regions. The shared memory option was chosen for the particle trajectory predictions because it was noted that certain variables were re-set when the particles crossed from one partition to the next. As compared with serial simulations, the run times were reduced from ~1 month to ~1 week. The other primary change to the transient predictions was the application of gradual particle release as opposed to a single bolus injection. The user-defined functions (UDFs) developed to facilitate parallel processing are described in more detail in Appendix A, and are titled "face_centroids_1.3.c", "near_wall_dist_1.4.c", "cell_num_1.1.c", "nw_cd_3.1.c", and "nw_turb_3.3.c".. A grouping of 450 particles was released after every 0.032 s time step during inhalation, resulting in ~23,000 particles total. The time step value was chosen to be consistent with the sampling rate of the ventilator flow meter. Droplet and particle formulations were chosen to be consistent with the *in vitro* experiments, namely 0.5% AS for the conventional cases and 50:50 AS:NaCl for the EEG cases. With the conventional cases, the polydisperse experimental distribution was used, but for the EEG cases a monodisperse distribution was assumed with an aerodynamic diameter of 0.9 μm, similar to the steady state CFD predictions performed earlier. Other simulation parameters and boundary conditions related to heat transfer,

species transport, and size change remained the same for the transient predictions as with the steady state simulations.

Deposition fraction (DF) as expressed by Equation 3.3 was the metric used for all CFD and *in vitro* characterizations of nebulized aerosol delivery through the mask-FNMT combinations. The DF calculations for the transient simulations required an adjustment factor to enable comparison with *in vitro* results, because the recovered dose for the experimental setup was measured from the amount that exited the nebulizer and used as the estimate for the nominal dose, but the transient CFD predictions required that the nominal dose represent the amount of drug entering the mask. However, the amount entering the mask in the experiments was difficult to ascertain because the fraction of the reported DF value that was deposited in a given region during either inhalation or exhalation was not evident. The fraction remaining (FR) of drug exiting the mask inlet after exhalation was also calculated for the transient CFD cases, which, as described in Section 3.2, is calculated in the same manner as DF. The amount of drug exiting the mask outlet was expressed as a DF value since it approximates experimentally determined inspiratory filter deposition. To assess condensational growth, the average residence time of injected particles that exit through the throat is found for each case, as well as the throat outlet mass median aerodynamic diameter (MMAD).

Some assumptions were made to estimate the nominal dose for the transient predictions. The objective was to determine the amount of experimentally determined recovered dose available to the mask by estimating how much deposition occurred in a given region during inhalation or exhalation. A trapezoidal rule approximation was used to estimate the amounts of flow volumes entering the system during inhalation and exhalation, which were used to estimate

experimentally recovered dose produced during inhalation and exhalation ($RD_{conv,inhale}$ and $RD_{conv,exhale}$) as

$$RD_{conv,inhale} = RD_{conv}\frac{V_{inhale}}{V_{total}} \quad (7.1)$$

$$RD_{conv,exhale} = RD_{conv}\frac{V_{exhale}}{V_{total}} \quad (7.2)$$

where RD_{conv} is the total amount of experimentally determined recovered dose for each conventional case, V_{total} is the total amount of flow volume delivered, and V_{inhale} and V_{exhale} are the inhalation and exhalation flow volumes. The amount of drug depositing on the nebulizer and T-connector was assumed to deposit in an inversely proportional fashion with respect to V_{inhale} and V_{exhale}, since it was theorized that most of the deposition in this region occurred when the flow rate was closer to zero. The tubing in the system consisted of an expiratory tube that connected the T-connector to the expiratory filter and an inspiratory tube connected the T-connector to the mask. Since the inspiratory tube was approximately twice as long as the expiratory tube, it was assumed that one third of the recovered dose in the tubing was deposited into the expiratory tube while the other two thirds deposited in the inspiratory tube. Furthermore, the amount of drug that deposited during inhalation or exhalation for each tube was estimated. It was assumed that 10% of the experimentally recovered drug in the expiratory tube was entrained during the inhalation flow cycle. For the inspiratory tube, the estimated DF values during inhalation and exhalation were determined by requiring that deposition efficiency (DE) was the same during both cycles, accounting for the fact that the drug deposited on the model and the inspiratory filter were not available during exhalation. For the expiratory filter the distribution of DF values was determined by requiring that the amount of drug assumed to enter the system from the inhalation and exhalation cycles balance with the amount of drug in each

region that was estimated to be associated with each cycle. The estimated DF values for both inhalation cases (1 s and 2 s) are tabulated in the results section.

Once the estimated DF values for the inhalation and exhalation cycles were found, the amount assumed to enter the mask ($ND_{CFD,conv}$), given as a percentage, was calculated as

$$ND_{CFD,conv} = \frac{DF_{insp}+DF_{model}+\left(DF_{exp}+DF_{tubing}\right)_{\text{inhalation}}}{\text{RD}_{\text{conv}}} \quad (7.3)$$

where DF_{insp} refers to the amount recovered on the inspiratory filter, DF_{model} is the combined deposition fraction of the mask and FNMT, DF_{exp} is the amount recovered on the expiratory filter, and DF_{tubing} is the amount on the tubing. All DF numbers are expressed as percentages. The values of DF_{exp} and DF_{tubing} were those estimated to have been produced by drug delivered to the system during the inhalation cycle. The value of RD_{conv} is the experimentally determined recovered dose, expressed as a fraction.

As illustrated by Figure 7.4 and Figure 7.6, the experimental setup for the EEG case was significantly different than the conventional case, and thus a different adjustment factor was required to account for deposition in regions not included in the CFD model. The fact that the nebulizer was isolated from the filters for EEG delivery simplified the process of estimating the transient CFD nominal dose. It was assumed that none of the *in vitro* recovered dose on the tubing in the inspiratory line or the nebulizer was available to the model. The total amount of drug recovered on the inspiratory filter, the model (including the mask and FNMT), and the expiratory filter were assumed to be available to the mask inlet during inhalation. An adjustment factor was applied to the Y-connector which joined the inspiratory and expiratory limbs to the model, and to the ventilator flow meter which was positioned proximal to the mask. The EEG adjustment factor was calculated as

$$ADJ_{EEG} = \frac{\text{DF}_{\text{model}}+\text{DF}_{\text{insp}}}{\text{DF}_{\text{exp}}+\text{DF}_{\text{model}}+\text{DF}_{\text{insp}}} \quad (7.4).$$

The amounts of Y-connector and flow meter recovered dose delivered to the mask were estimated as $DF_{Y\text{-}con}$*ADJ_{EEG} and DF_{meter}*ADJ_{EEG}, respectively. The nominal dose at the mask entrance for the EEG delivery transient CFD simulations ($ND_{CFD,EEG}$) was then approximated as

$$ND_{CFD,EEG} = \frac{DF_{insp}+DF_{model}+DF_{exp}+(DF_{Y-con}+\mathrm{DF_{meter}})ADJ_{\mathrm{EEG}}}{\mathrm{RD_{EEG}}+0.2(1-\mathrm{RD_{EEG}})} \quad (7.5)$$

where RD_{EEG} is the experimentally determined recovered dose, expressed as a fraction. The value of RD_{EEG} is adjusted to assume that 80% of the dose not recovered was deposited in the mixer-heater (which was not measured), resulting in a mixer-heater depositional loss of 7.1% and 4.9% for the 1 s and 2 s inhalation cases, respectively.

The values of FR at the mask inlet after exhalation based on the experimental data were estimated for both the conventional and EEG drug delivery cases based on the approximations of mask inlet nominal dose (i.e. $ND_{CFD,conv}$ and $ND_{CFD,EEG}$). Since the amounts of drug deposited in the model and the inspiratory filter were already measured from the *in vitro* experiments, the experimental FR at the mask inlet after exhalation ($FR_{exp,\ exhaled}$) was estimated as

$$FR_{exp,exhaled} = ND_{CFD} - DF_{model} - DF_{exp} \quad (7.6)$$

where ND_{CFD} is the estimated mask inlet nominal dose for either conventional or EEG delivery.

Approximation of inspiratory filter deposition with the transient CFD predictions was complicated by the inclusion of a numerical extension in the FNMT model. During the transition from inhalation to exhalation, some particles that are entrained in the volume enclosed by the extension reverse course and re-enter the volume enclosed by the FNMT model. For the sake of comparison, the FNMT model volume is 260.5 mL (as shown in Table 7.1) while the dead space volume of the extension is 54.7 mL. Re-entering of the particles into the FNMT model does not occur with the *in vitro* setup, since the filter is directly downstream of the throat exit. However, the extension was included with the CFD simulations to aid with increased accuracy in

turbulence modeling at the throat outlet, which is expected to balance out to some degree any loss in accuracy due to re-entering of particles. Moreover, the continuous release of particles (which is consistent with the experiments) ensures that only a small fraction of the total number of particles released may be present in the extension volume at any given moment.

7.3 Results

The steady state CFD prediction of conventional drug delivery through the commercial mask with polydisperse 0.2% AS is pictured in Figure 7.9. The deposition fraction of AS in the nose-mouth-throat (DF_{NMT}) shows a loss of 25.8%, while the values of DF_{face} and DF_{mask} are much smaller at 0.8% and 0.9%, respectively. The total loss in the model (27.5%) indicates lung delivery of about 70%, which is much higher than indicated in the literature for both *in vivo* and *in vitro* studies (Chatmongkolchart, et al., 2002; Dai, et al., 2013; Fauroux, et al., 2000; White, et al., 2013), which employ more realistic cyclic breathing. The applied assumptions of steady state flow and a perfect mask seal explain the high prediction of drug delivery, since transient flow with an imperfect seal would certainly decrease the delivered dose. However, it is important to note that the steady state predictions are not intended to model actual delivery but to serve as a basis for comparison with the steady state EEG monodisperse predictions that follow, which in turn are intended to serve as a means for comparing the mask designs.

Steady state DF predictions of 50:50 AS:NaCl and 75:25 AS:NaCl using EEG methods through the commercial mask and the three new mask designs are presented in Table 7.2 and Table 7.3 and pictured in Figure 7.10 and Figure 7.11, respectively. For all four mask designs and with both aerosol types, the amount of drug delivered to the face and mask in each case is negligible, with DF values between 0.0% and 0.2%. The predictions of DF in the NMT showed

that for both aerosol types, Mask Design #1.1 showed the highest values at 3.4% and 4.1% for 50:50 AS:NaCl and 75:25 AS:NaCl. The lowest values of DF in the NMT were in Mask Design #1.2 and Mask Design #1.3, which both had virtually identical values of DF for the 50:50 AS:NaCl aerosol (1.8% and 1.7%, respectively) and the 75:25 AS:NaCl aerosol (1.63% and 1.61%, respectively). The commercial mask showed loss in the NMT that was between Mask Design #1.1 and Mask Designs #1.2 and #1.3.

The values of MMAD and average particle residence time at the throat outlet showed similar results with the three new mask designs, with average figures of 2.09 μm and 0.27 s for the 50:50 AS:NaCl cases and 1.84 μm and 0.27 s for the 75:25 AS:NaCl cases. The commercial mask produced higher values of MMAD and average residence time, with the 50:50 AS:NaCl case resulting in 2.49 μm and 0.55 s and the 75:25 AS:NaCl case resulting in 2.19 μm and 0.54 s. This is most likely due to the reduced average particle velocity of the particles released from the 22 mm inlet of the commercial mask at 1.3 m/s, as compared with the velocities of those released from the 8 mm aerosol inlets of the three new mask designs, which were 5.0 m/s with Mask Designs #1.1 and #1.3 and 2.5 m/s with Mask Design #1.2. Additionally, the new mask designs implemented aerosol release proximal to the nostril openings in a more directed manner, as compared with the commercial mask which relied on aerosol release from the distal elbow inlet. Though the higher MMAD in the commercial cases is advantageous for enhanced thoracic deposition, the higher residence time is disadvantageous because of the short inhalation times (1 s and 2 s) that will be used in the transient *in vitro* experiments and CFD simulations.

Results of DF, MMAD, and average residence time indicated that the best case for future study was represented by either Mask Design #1.2 or Mask Design #1.3. The CFD predictions indicated that both designs resulted in about 40% as much drug loss in the NMT region as

compared with Mask Design #1.1, and about 60% as much drug loss as compared with the commercial mask. It was considered that the higher outlet MMAD from the commercial mask case may outweigh the increased drug loss in the NMT region, but the doubled average residence time of the commercial case as compared with the other three cases was considered to be problematic. To distinguish between Mask Design #1.2 and Mask Design #1.3, practicality was considered. The fully protruding inlet tube of Mask Design #1.3 may be an issue of compliance for conscious patients who may find the contact of the inlet tube with the right nostril uncomfortable. Additionally, differing nasal and facial anatomy may lead to difficulties with fitting the mask to some patients. Thus, Mask Design #1.2 was selected for *in vitro* and transient CFD study. The choice of drug:excipient combination for *in vitro* study was based on the balance between the delivery of a higher amount of drug with the 75:25 ratio as opposed to the expected increase in thoracic deposition due to the higher throat outlet MMAD of the 50:50 ratio. However, in the absence of data on the expected exhalation losses with one MMAD value versus another, it was decided to use the 50:50 drug:excipient combination, which has been studied extensively (Hindle & Longest, 2012; Longest & Hindle, 2011, 2012; Tian, et al., 2013; Walenga, et al., 2014) as opposed to the 75:25 combination which is not nearly as well represented in previous studies. Nonetheless, the data from the 75:25 predictions are included here as a reference for future study.

Early *in vitro* trials performed by Dr. Michael Hindle and co-workers in the VCU Department of Pharmaceutics indicated that Mask Design #1.2 would not provide the most efficient delivery as expected. The use of Mask Design #1.2 required a separate flow source for the mixer-heater which was also available from the ventilator and could be synchronized with inhalation. However, this flow source only provided about 10 L/min of gas delivery, which did

not provide the optimal conditions for emptying the mixer-heater during inhalation and for preventing overheating of the aluminium plates. It was decided that the most efficient means of accomplishing those two goals was to place the mixer-heater in-line with the inhalation limb of the dual limb circuit and to remove the extra flow source altogether. This setup then made the commercially available PerformaTrak® SE mask the most practical choice for further study.

The DF data from the conventional drug delivery *in vitro* experiments are presented in Table 7.4. The initial hypothesis was that an additional second of inhalation from the Dual Adult Test Lung would approximately double the amount of drug delivered to the model and subsequently double the amount deposited in the model and on the inspiratory filter. Consistent with that assumption, a significantly higher value of DF was observed on the inspiratory filter for the 2 s inhalation case as opposed to the 1 s case, with the average DF decreasing from 18.7% to 10.3%. Since nearly twice as much drug was available to the model for the 2 s case, nearly twice as much drug is lost for that case, with an average DF of 12.2% as compared to 7.2% for the 1 s case. The total DF in the nebulizer, Aerogen T-connector, tubing, and expiratory filter decreased from 73.5% for the 1 s inhalation case to 63.5% for the 2 s case. However, the amount of drug on the expiratory filter increased from 21.8% for the 1 s case to 45.0% for the 2 s case, while DF values decreased in the nebulizer, T-connector, and tubing. The reasons for this shift are unclear, but it is suggested that the increased average flow rate during inhalation for the 2 s case facilitates provided more efficient emptying of the nebulizer chamber and left more drug available for expiratory filter deposition.

Deposition fraction (DF) values from the EEG drug delivery *in vitro* experiments are given in Table 7.5. Delivery is significantly improved with the EEG method as compared to the conventional mode, with average inspiratory filter DF increasing from 10.3% to 27.1% for the 1

s inhalation case, and from 18.7% to 39.3% for the 2 s case. Model deposition was low for both EEG cases with average DF values of 1.9% for the 1 s inhalation case and 1.5% for the 2 s case. This showed some consistency with the steady state CFD predictions that indicated an order of magnitude reduction in model DF from the conventional estimate to the EEG prediction. Unlike the conventional *in vitro* data, the deposition in the rest of the system did not show a drastic change from one case to the next. The amounts of drug deposited in the nebulizer, tubing, and Y-connector were nearly identical for both cases. Some decrease in DF was observed in the mixer-heater outlet, the flow meter, and the expiratory filter from the 1 s inhalation case to the 2 s case. The deposition in the mixer-heater was not measured due to the difficulty of washing the part while preventing a short in the Kapton® film heaters. However the amount of recovered dose (>90% for each case) indicated that the amount of drug lost in the mixer-heater was low.

The regional estimates of DF contributions during inhalation and exhalation from the experimental data are given for the four delivery cases in Tables 7.6-7.9. The V_{inhale}/V_{total} and V_{exhale}/V_{total} ratios for conventional drug delivery were found to be 0.529 and 0.471 for the 1 s inhalation case and 0.542 and 0.458 for the 2 s inhalation case. In both cases, since the ratios were near 0.5, the amounts of nebulizer/T-connector recovered dose estimated to deposit during inhalation and exhalation were nearly the same. Using the results of Table 7.6 and Table 7.7, the values of $ND_{CFD,conv}$ were estimated to be 23.9% and 44.0% for the 1 s and 2 s inhalation cases, respectively. This led to estimates for $FR_{exp,exhaled}$ for the two conventional cases of 6.4% and 13.1%. For EEG delivery, the values of ADJ_{EEG} were calculated for the 1 s and 2 s inhalation cases and found to be 0.562 and 0.672, respectively. These factors were used to tabulate the results of Table 7.8 and Table 7.9 and estimate the amounts of $ND_{CFD,EEG}$ for both inhalation

cases, which were approximated as 59.2% and 65.2%. From this, the values $FR_{exp,exhaled}$ for the two EEG cases were estimated to be 30.2% and 24.8%.

Transient CFD predictions of DF in the model and at the mask outlet are illustrated in Figure 7.12, along with the CFD estimate of FR at the mask inlet. Also provided in the figure are the experimental DF results and the estimated values of $FR_{exp,\ exhaled}$ for each case. On the whole, the predictions of DF and FR show very good agreement with the experimental results of DF and the estimate of $FR_{exp,\ exhaled}$, especially considering the complexity of the system and the number of assumptions required to provide a one-to-one comparison of experimental and CFD results. The values of DF in the model are over-predicted by the CFD results in three of four cases, but are all within approximately 5%. Predictions of DF on the inspiratory filter show agreement within 3% for all cases and the estimates of FR at the mask inlet show agreement within 4% for all cases. The DF and FR results are also given in Table 7.10, along with the MMAD at the mask outlet and the average particle residence time for particles that exit through the model outlet. The particle residence times were slightly smaller for the EEG cases as compared with the conventional cases which are desirable in that it reduces the amount of drug lost to exhalation. Somewhat unexpectedly, the values of MMAD from conventional drug delivery were similar to those from EEG, with estimates of 2.26 μm and 2.17 μm for the 1 s inhalation cases, respectively, and 2.44 μm and 2.31 μm for the 2 inhalation cases. This provides confidence that condensational growth with the EEG delivery in this system is sufficient to produce efficient lung deposition.

7.4 Discussion

A direct comparison of *in vitro* DF results obtained by Dr. Hindle and co-workers in the Department of Pharmaceutics for this study with data from other *in vitro* studies is desired. However, the methods in the literature have a variety of significant differences as compared with this study. The closest comparisons may be drawn with three studies in the literature that model jet nebulized delivery of AS through an *in vitro* system with an adult test lung, a single limb circuit, and imperfect mask sealing. Chatmongkolchart et al. (2002) showed that 0.5% AS delivery from a jet nebulizer in a single limb circuit in a system with a tidal volume of 313 mL and a duty cycle of 0.41 yielded delivered doses of 8.5% or 15.6% on a filter at the inlet of the test lung model (without a mask in the circuit) for two different nebulizer positions with respect to the circuit valve (Chatmongkolchart, et al., 2002). The system included a BiPAP ventilator and a dual adult test lung (Chatmongkolchart, et al., 2002). For a tidal volume of 860 mL and a duty cycle of 0.48, delivery was 5.2% or 24.5% depending on nebulizer placement (Chatmongkolchart, et al., 2002). Dai et al. (2013) employed a similar experimental setup as compared with Chatmongkolchart et al. (2002) and measured delivery of 0.5% AS to a filter at the inlet of a dual adult test lung in a system with a critical care ventilator and a single limb circuit. The type of exhalation valve was varied, and for a variety of valve types, valve locations, and ventilator pressure settings, and delivery was measured between 15.99% and 28.22% (Dai, et al., 2013). The tidal volumes were not measured by Dai et al. (2013), so a direct comparison with the results of Chatmongkolchart et al. (2002) was not possible but the results were on the same order of magnitude. Additionally, Branconnier and Hess (2005) used a similar setup as compared with Chatmongkolchart et al. (2002), who showed 9% delivery of 0.125% AS through a commercial mask in a single limb circuit with a BiPAP ventilator and a dual adult test

lung. Since the tidal volume in the setup used by Branconnier and Hess (2005) was 400 mL, this is most directly comparable to the 15.6% delivery shown by Chatmongkolchart et al. (2002) with a tidal volume of 313 mL and a similar positioning of the jet nebulizer, though the inclusion of the mask by Branconnier and Hess (2005) represents a significant methodological difference.

Values of $ND_{CFD,conv}$ estimated for this study provide the most direct comparison with the results of the three studies described aboThorve, which for this study were 23.9% and 44.0% for the 1 s and 2 s inhalation cases and correspond to tidal volumes of about 400 mL and 800 mL, respectively. The duty cycle was ~0.4 for all cases in this study. However, the *in vitro* system modeled for this study employed a perfect mask seal, a dual limb circuit and a vibrating mesh nebulizer, which has entirely different flow and aerosol transport characteristics as compared with a system that has an imperfect mask seal, a single limb circuit, and a jet nebulizer. Nonetheless, the fact that the order of magnitude of $ND_{CFD,conv}$ was the same for this study as compared with the literature indicates that methods employed for the *in vitro* experiments were sound. Moreover, the perfect mask seal used in this study would be expected to improve delivered dose as compared with an imperfect seal, which is shown in the results.

Considering the experimental results of EEG delivery, the *in vitro* measurements of DF on the inspiratory filter, which ranged between 27.1% and 39.3%, compare well with the results of Chatmongkolchart et al. (2002), Dai et al. (2013), and Branconnier and Hess (2005), which collectively ranged between 5.2% and 28.22%. Also, those three studies did not include the effect of an FNMT model on delivered dose, which is expected to significantly reduce delivery of a conventionally sized aerosol, and only one of the three studies included the effect of a mask. The values of $ND_{CFD,EEG}$ were found by attempting to remove the effects of the mask and the FNMT model on delivered dose, and were 59.2% and 65.2% for the two inhalation cases.

However, the perfect mask seal in the system used for this study is again expected to artificially enhance delivered dose. Despite this limitation, the differences between the estimates of $ND_{CFD,conv}$ and $ND_{CFD,EEG}$ found in this study give confidence that EEG delivery through a system with an imperfect mask seal would exhibit significantly improved performance as compared with conventional aerosol delivery.

One of the objectives for this study was to use steady state CFD predictions to identify an improved mask design for EEG delivery. The results showed that Mask Design #1.2, a mask with two aerosol inlets aimed at the two nostril inlets, would provide the lowest FNMT depositional losses as compared with the commercial mask and two other proposed designs. However, *in vitro* experiments revealed that optimal emptying of the mixer-heater required that aerosol delivery be combined with the delivered gas flow upstream of the mask inlet. The primary limitation of the steady state CFD predictions then was the absence of other aspects of the system, such as the mixer-heater and delivery tubing. These aspects were left out because they would have increased the mesh size and complexity for each mask design substantially, and it was believed that emptying of the mixer-heater with the separate 10 L/min flow source would be adequate. The lesson learned is that the isolation of one region to the exclusion of another is difficult with a system as complicated as aerosol delivery during NPPV. Steady state CFD predictions are still believed to be useful for NPPV mask design purposes, but only if aerosol delivery characteristics are not affected by the aspects of the *in vitro* system external to the mesh domain.

Transient CFD predictions were shown to provide good agreement with *in vitro* results after a series of assumptions were applied to account for upstream deposition in the experiments and allow for a direct comparison. As mentioned above, the MMAD at the throat outlet was

surprisingly comparable for the conventional and EEG delivery cases, especially considering the large difference in the initial MMAD (~5 μm vs. 0.9 μm). It would be useful for future experimental work to confirm this result, and for any future CFD or experimental study to model the deposition characteristics of both delivery methods in the tracheobronchial region, particularly as they relate to lung targeting and total lung deposition. Another interesting finding is the significant amount of deposition found in the throat region. Previous study in Chapter 6 and Walenga et al. (2014) focused on nasal cavity deposition since that region is expected to have the highest losses, due to the narrow passageways as compared with the throat. However, both conventional and EEG delivery throat deposition was found to be significant, making up 31.8% to 43.4% of all NMT deposition, where the smallest relative amount was for EEG delivery and 1 s of test lung inhalation and the largest relative amount was for conventional delivery and the 2 s inhalation case. It suggests that the throat region may play an important role in variability of extrathoracic deposition of lung targeted, nasally delivered pharmaceutical aerosols.

As discussed above, the assumption of a perfect mask seal was applied to remove a design variable, which allowed for a more concentrated focus on the optimization of mask design and system setup. This significant limitation will be addressed in future study, including Chapter 8 of this dissertation. CFD predictions were limited by the omission of system components such as connecting tubing and the mixer-heater, which proved to be a significant limitation for steady state simulations where the initially determined optimal mask design did not perform as well as expected with *in vitro* experiments. However, the transient simulations were not as affected by this limitation, as evidenced by the good agreement of results with experimental data. Though the transient mixer-heater used for EEG delivery in the *in vitro* experiments for this study

showed improvement in delivered dose by a factor of two, it is believed that alterations to the outlet tubing and the Y-connector may further reduce system losses. Modifications have been made to enhance streamlining and reduce dead space volume in the tubing, which will be applied to future study. Results from this study are restricted to a critical care ventilator with a dual limb circuit and AS delivery, and so it is unknown how EEG delivery would perform in a different system with a different drug, and Chapter 8 will explore drug delivery with dry powder ciprofloxacin. Depositional intersubject variability with respect to extrathoracic dimensions was not explored and will be a focus of Chapter 8. Other study design aspects that were not explored for this study were mask design as it relates to dead space and open mouth versus closed mouth extrathoracic modeling. Mask design was explored in this study as it related to aerosol delivery methods, but dead space is known to impact drug delivery and represents a potential area of improvement. A closed mouth model was used based on the observation that many critical care patients are sedated, but an open mouth model would be an interesting case study, particularly as it relates to drug delivery during home ventilation.

Nebulized drug delivery of AS during NPPV was assessed for this study using experimental and CFD predictions based on both conventional and EEG methods. A new face-nose-mouth-throat (FNMT) model was constructed based on CT scan data from the Constricted2 model developed for Chapter 6 of this dissertation, with some modifications to allow for rapid prototyping. Steady state CFD predictions evaluated four oronasal mask designs for EEG drug delivery, including a commercial mask and three derivatives of that mask. The optimal mask identified by steady state CFD results implemented aerosol delivery through two separate inlets directed at the nostril openings. Dr. Michael Hindle and colleagues in the VCU Department of Pharmaceutics conducted experiments to assess both conventional and EEG delivery using a

rapid prototyped version of the FNMT model and a critical care ventilator with an adult test lung. A previously developed transient mixer-heater (Golshahi, et al., 2014b) was used to produce a submicrometer particle for EEG delivery. Early *in vitro* experiments showed that the commercial mask performed better with EEG methods as compared with the mask selected based on steady state CFD results because aerosol delivery through the ventilation inlet was required. Experimental data showed that drug delivery to an inspiratory filter downstream of the FNMT model was improved by a factor of two when EEG methods were used as opposed to conventional methods, for both 1 s and 2 s test lung induced inhalation. Subsequent transient CFD predictions of experimental conditions showed good agreement and indicated that significant condensational growth of EEG delivered aerosol occurred.

Table 7.1 Dead space volume of mask, nasal valve area, nasal cavity, mouth, nasopharynx, and throat regions of the face-nose-mouth-throat (FNMT) model with the commercial mask. The nasal cavity is defined as the region between the nasal valve area and the end of the septum. The mouth includes the entire oral pathway, the nasopharynx terminates above the mouth pathway, and the throat begins where the nasopharynx ends.

Region	Volume (mL)
Mask	207.9
Nasal Valve Area	7.9
Nasal Cavity	15.5
Mouth	7.1
Nasopharynx	8.4
Throat	13.7
Total	260.5

Table 7.2 Deposition fraction (DF) predictions (given in %) using CFD for EEG drug delivery at steady state flow with a monodisperse aerosol composed of **50:50** albuterol sulfate (AS):sodium chloride (NaCl). The initial aerodynamic diameter of the particles is 0.9 μm. Four mask designs are considered and DF is reported for the face, mask, and nose-mouth-throat (NMT) regions. Also given are the throat outlet mass median aerodynamic diameter (MMAD) due to EEG size increase and the average residence time of injected particles exiting the throat.

	Deposition Fraction (DF)			Outlet MMAD (μm)	Average Residence Time (s)
	Mask	Face	NMT		
Commercial	0.1	0.2	2.9	2.49	0.55
Mask Design #1.1	0.0	0.1	3.4	2.13	0.30
Mask Design #1.2	0.0	0.0	1.8	2.05	0.27
Mask Design #1.3	0.0	0.0	1.7	2.09	0.24

Table 7.3 Deposition fraction (DF) predictions (given in %) using CFD for EEG drug delivery at steady state flow with a monodisperse aerosol composed of **75:25** albuterol sulfate (AS):sodium chloride (NaCl). The initial aerodynamic diameter of the particles is 0.9 μm. Four mask designs are considered and DF is reported for the face, mask, and nose-mouth-throat (NMT) regions. Also given are the throat outlet mass median aerodynamic diameter (MMAD) due to EEG size increase and the average residence time of injected particles exiting the throat.

	Deposition Fraction (DF)			Outlet MMAD (μm)	Average Residence Time (s)
	Mask	Face	NMT		
Commercial	0.1	0.2	2.6	2.19	0.54
Mask Design #1.1	0.0	0.1	4.1	1.88	0.30
Mask Design #1.2	0.0	0.0	1.6	1.80	0.26
Mask Design #1.3	0.0	0.0	1.6	1.83	0.24

Table 7.4 Deposition fraction (DF) values (given in %) from *in vitro* experiments for conventional drug delivery. The T-connector refers to the connection between the nebulizer and the tubing between the dual limb circuit and the mask, while the DF in the tubing is the sum of all deposited drug elsewhere. The model refers to the combination of the commercial mask and the face-nose-mouth-throat (FNMT) model. These *in vitro* experiments were performed by Dr. Michael Hindle and co-workers in the VCU Department of Pharmaceutics and are presented here for comparison to CFD predictions.

	Deposition Fraction (DF)	
Region	**1 s Inhalation**	**2 s Inhalation**
Nebulizer	9.0 ± 1.6	2.1 ± 2.0
T-connector	26.4 ± 4.3	4.7 ± 0.5
Tubing	16.3 ± 2.5	11.7 ± 1.3
Expiratory Filter	21.8 ± 0.8	45.0 ± 2.0
Model	7.2 ± 0.7	12.2 ± 1.9
Inspiratory Filter	10.3 ± 3.2	18.7 ± 2.1

Table 7.5 Deposition fraction (DF) values (given in %) from *in vitro* experiments for EEG drug delivery. The mixer-heater outlet refers to a rapid prototyped 90 degree bend attached to the outlet, while the DF in the tubing is the sum of all deposited drug up to the Y-connector and flow meter combination, which is directly attached to the mask. The model refers to the combination of the commercial mask and the face-nose-mouth-throat (FNMT) model. These *in vitro* experiments were performed by Dr. Michael Hindle and co-workers in the VCU Department of Pharmaceutics and are presented here for comparison to CFD predictions.

	Deposition Fraction (DF)	
Region	**1 s Inhalation**	**2 s Inhalation**
Nebulizer	0.5 ± 0.4	0.8 ± 0.5
Mixer-heater Outlet	16.5 ± 1.5	12.2 ± 1.4
Tubing	7.5 ± 1.1	7.6 ± 3.5
Y-connector	1.1 ± 0.2	1.2 ± 0.3
Flow Meter	13.9 ± 0.7	11.4 ± 2.5
Expiratory Filter	22.6 ± 1.0	19.9 ± 3.3
Model	1.9 ± 0.2	1.5 ± 0.8
Inspiratory Filter	27.1 ± 0.8	39.3 ± 2.7

Table 7.6 Regional estimates of deposition fraction (DF) contributions during inhalation and exhalation (given in %) from *in vitro* experimental data for conventional drug delivery with 1 s inhalation from the Dual Adult Test Lung. The recovered dose refers to the estimate of total recovered drug deposited during inhalation or exhalation. These *in vitro* experiments were performed by Dr. Michael Hindle and co-workers in the VCU Department of Pharmaceutics and are presented here for comparison to CFD predictions.

	Recovered Dose	Nebulizer/ T-Connector	Expiratory tube	Inspiratory tube	Expiratory Filter	Model	Inspiratory Filter
Inhalation	48.2	16.7	0.5	9.6	2.5	7.2	10.3
Exhalation	42.9	18.7	4.9	1.3	19.3	0.0	0.0
Total	91.1	35.4	5.4	10.9	21.8	7.2	10.3

Table 7.7 Regional estimates of deposition fraction (DF) contributions during inhalation and exhalation (given in %) from *in vitro* experimental data for conventional drug delivery with 2 s inhalation from the Dual Adult Test Lung. The recovered dose refers to the estimate of total recovered drug deposited during inhalation or exhalation. These *in vitro* experiments were performed by Dr. Michael Hindle and co-workers in the VCU Department of Pharmaceutics and are presented here for comparison to CFD predictions.

	Recovered Dose	Nebulizer/ T-Connector	Expiratory tube	Inspiratory tube	Expiratory Filter	Model	Inspiratory Filter
Inhalation	51.2	3.1	0.4	6.4	8.8	12.2	18.7
Exhalation	43.2	3.7	3.5	1.4	36.2	0.0	0.0
Total	94.4	6.8	3.9	7.8	45.0	12.2	18.7

Table 7.8 Regional estimates of deposition fraction (DF) contributions during inhalation and exhalation (given in %) from *in vitro* experimental data for EEG drug delivery with 1 s inhalation from the Dual Adult Test Lung. The mixer-heater tubing refers to the amount of drug recovered on the nebulizer and the mixer-heater outlet tubing. These *in vitro* experiments were performed by Dr. Michael Hindle and co-workers in the VCU Department of Pharmaceutics and are presented here for comparison to CFD predictions.

	Mixer-Heater Tubing	Y-connector	Flow Meter	Expiratory Filter	Model	Inspiratory Filter
Inhalation	24.5	0.6	7.8	0.0	1.9	27.1
Exhalation	0.0	0.5	6.1	22.6	0.0	0.0
Total	24.5	1.1	13.9	22.6	1.9	27.1

Table 7.9 Regional estimates of deposition fraction (DF) contributions during inhalation and exhalation (given in %) from *in vitro* experimental data for EEG drug delivery with 2 s inhalation from the Dual Adult Test Lung. The mixer-heater tubing refers to the amount of drug recovered on the nebulizer and the mixer-heater outlet tubing. These *in vitro* experiments were performed by Dr. Michael Hindle and co-workers in the VCU Department of Pharmaceutics and are presented here for comparison to CFD predictions.

	Mixer-Heater Tubing	Y-connector	Flow Meter	Expiratory Filter	Model	Inspiratory Filter
Inhalation	20.6	0.8	7.7	0.0	1.5	39.3
Exhalation	0.0	0.4	3.7	19.9	0.0	0.0
Total	20.6	1.2	11.4	19.9	1.5	39.3

Table 7.10 Transient CFD predictions of deposition fraction (DF) on the model (mask and FNMT combination) and the inspiratory filter (given in %), where DF on the inspiratory filter represents delivered dose. Additionally, the values of fraction remaining (FR) of exhaled 50:50 albuterol sulfate (AS): sodium chloride (NaCl) at the mask elbow bend inlet (given in %) are tabulated. The model outlet mass median aerodynamic diameter (MMAD) and average particle residence time are also given, where the residence time only considers particles exiting the model outlet.

		Deposition Fraction (DF)		Fraction Remaining (FR)	Outlet MMAD (μm)	Average Residence Time (s)
		Model	Inspiratory Filter	Exhaled		
Conventional	**1 s**	5.7	7.3	9.4	2.26	0.67
	2 s	13.5	9.4	19.5	2.44	0.70
EEG	**1 s**	2.6	30.8	23.6	2.17	0.58
	2 s	3.6	19.0	40.3	2.31	0.58

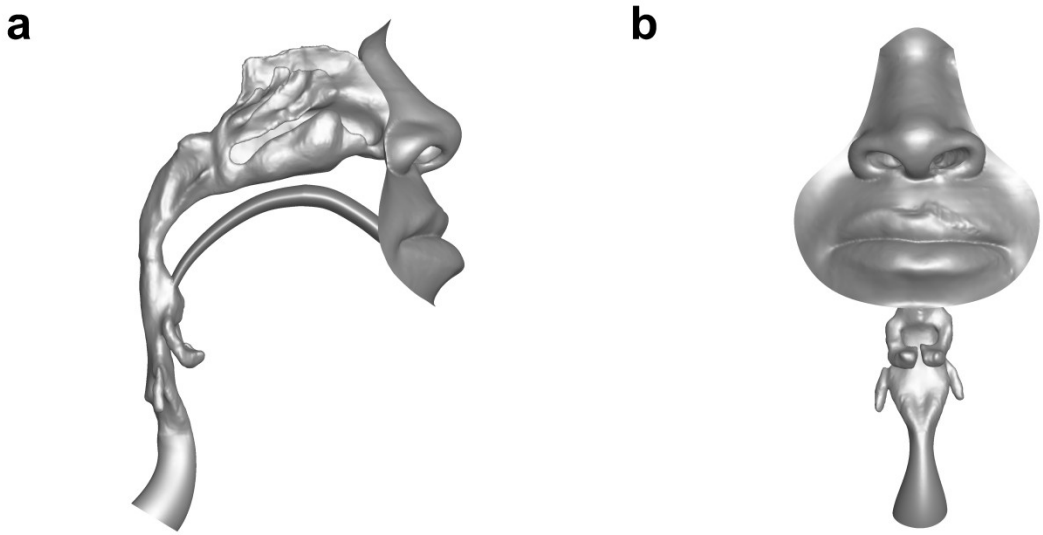

Figure 7.1 Surfaces of the face and interior airway of the face-nose-mouth-throat (FNMT) model, shown in (a) side view and (b) front view. The numerical extension is omitted from both views.

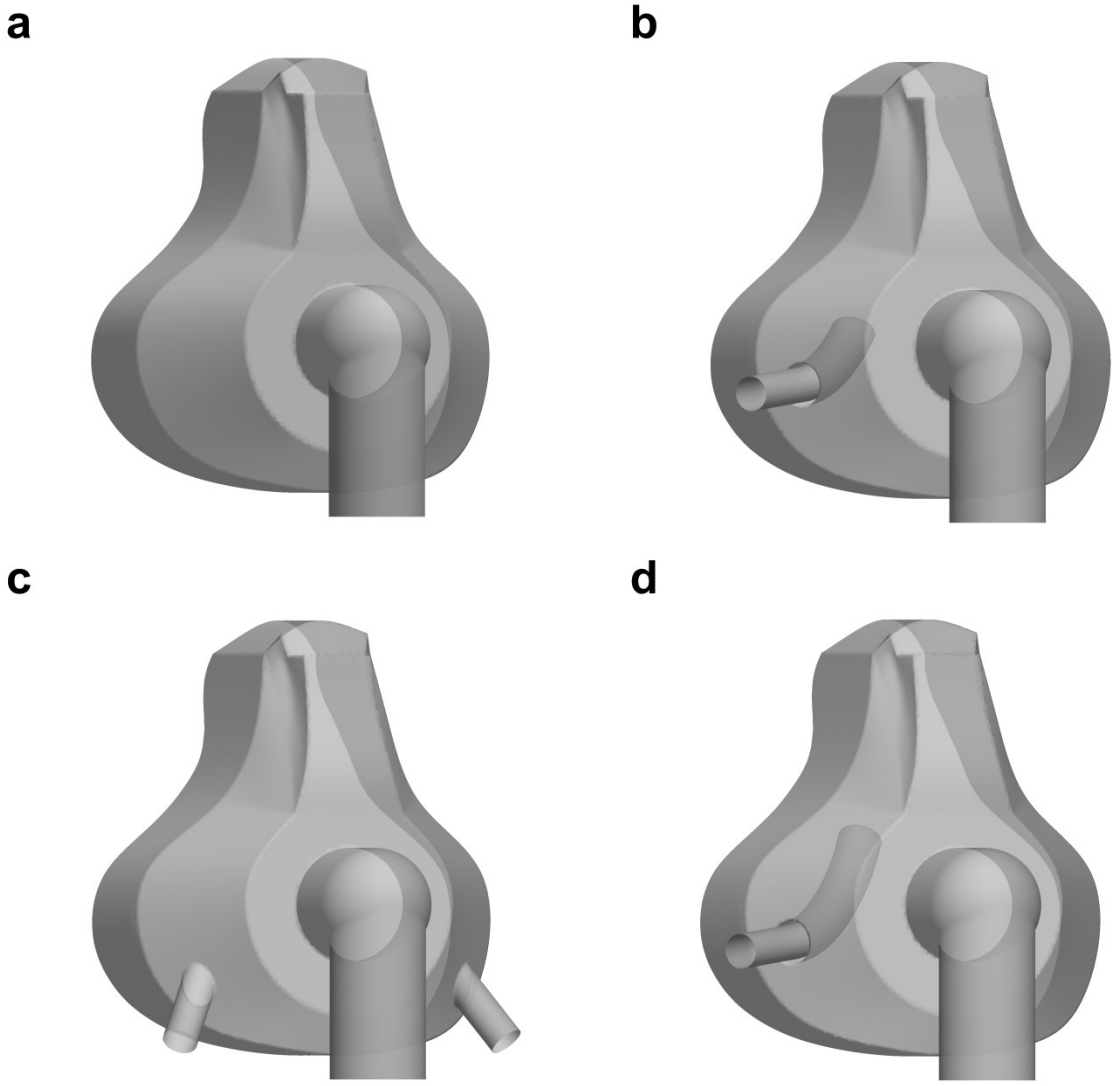

Figure 7.2 Four mask designs tested using steady state CFD simulations, including (a) the commercially available PerformaTrak® SE mask (Philips Respironics, Inc.). The three other designs are modifications of the commercial mask, which include (b) one 8 mm aerosol inlet tube extending halfway to the nostril opening, (c) two 8 mm aerosol inlets not protruding inside the mask and aimed at both nostrils, and (d) one 8 mm inlet tube extending all the way to the nares opening.

Figure 7.3 Rapid prototyped hollow geometry of face-nose-mouth-throat (FNMT) model used with *in vitro* experiments, constructed using stereolithography with a Viper SLA system (3D Systems, Valencia, GA) that used Accura 60 clear plastic resin.

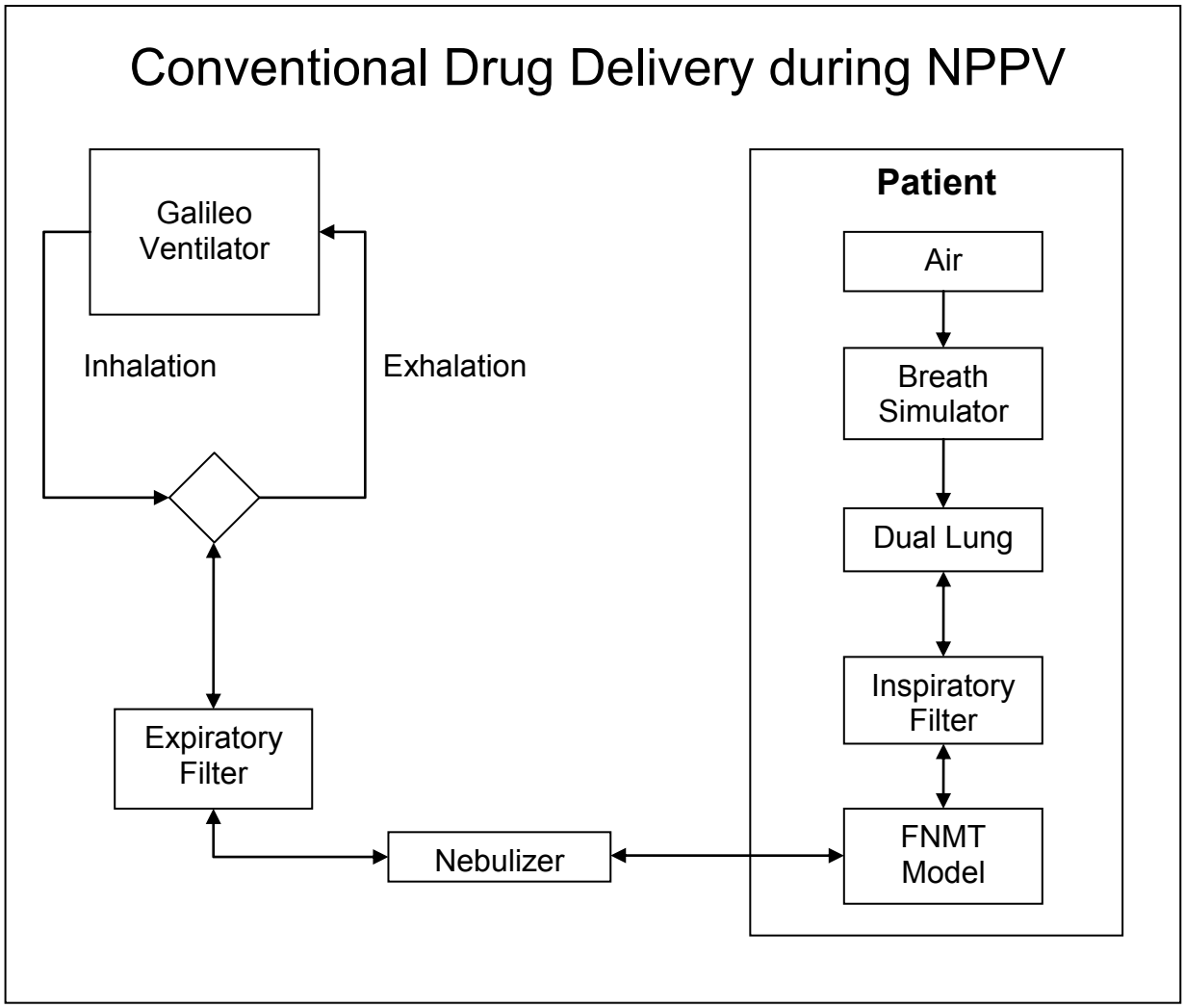

Figure 7.4 Process diagram of conventional drug delivery during NPPV.

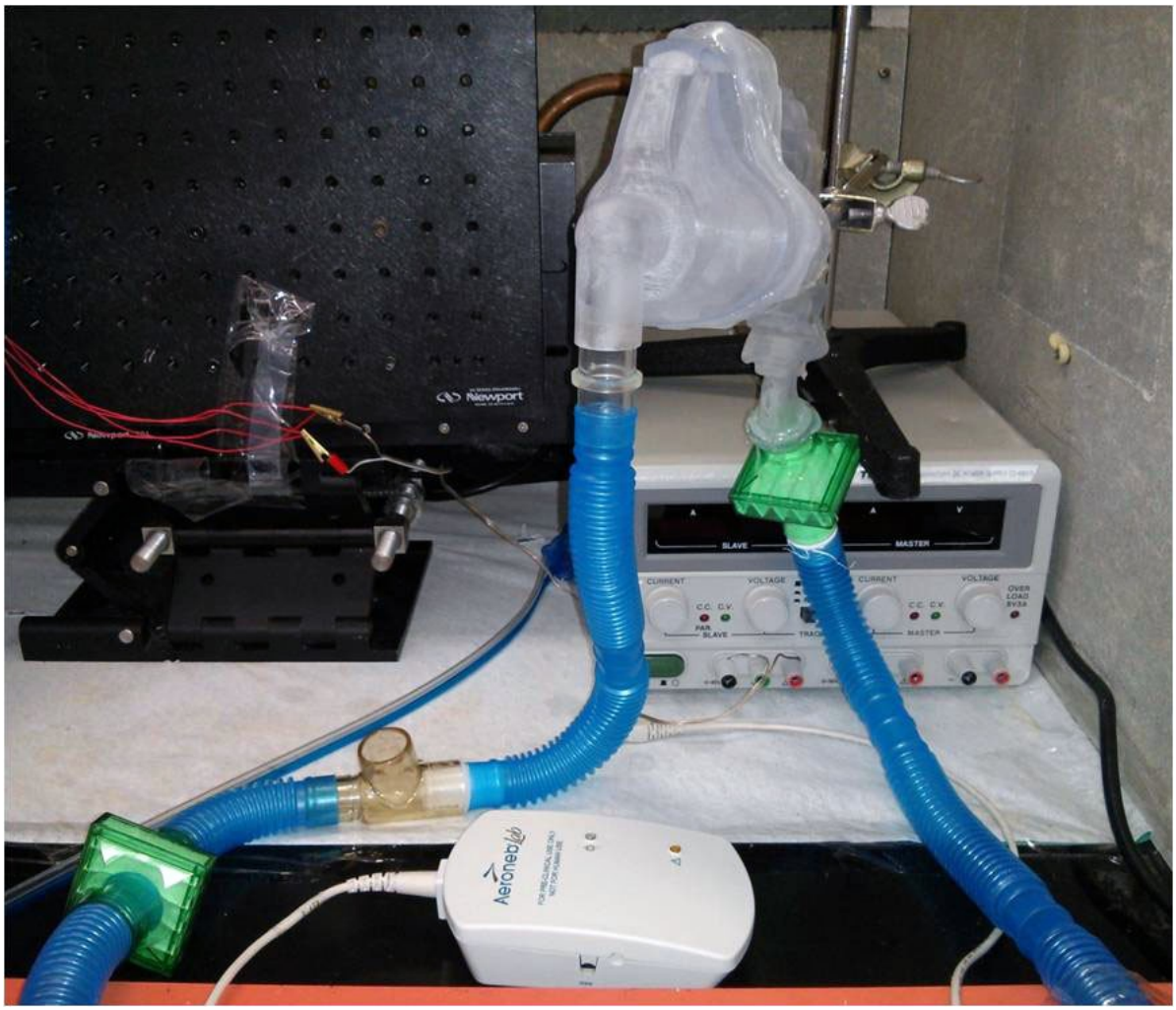

Figure 7.5 Experimental setup of conventional drug delivery during NPPV trials. The expiratory filter is pictured in the bottom left, while the Aerogen T-connector that interfaces with the Aeroneb Pro nebulizer (removed for washing in this image) is to the right of the expiratory filter. The FNMT model with the commercial mask is pictured at the top of the image, and the inspiratory filter is directly downstream.

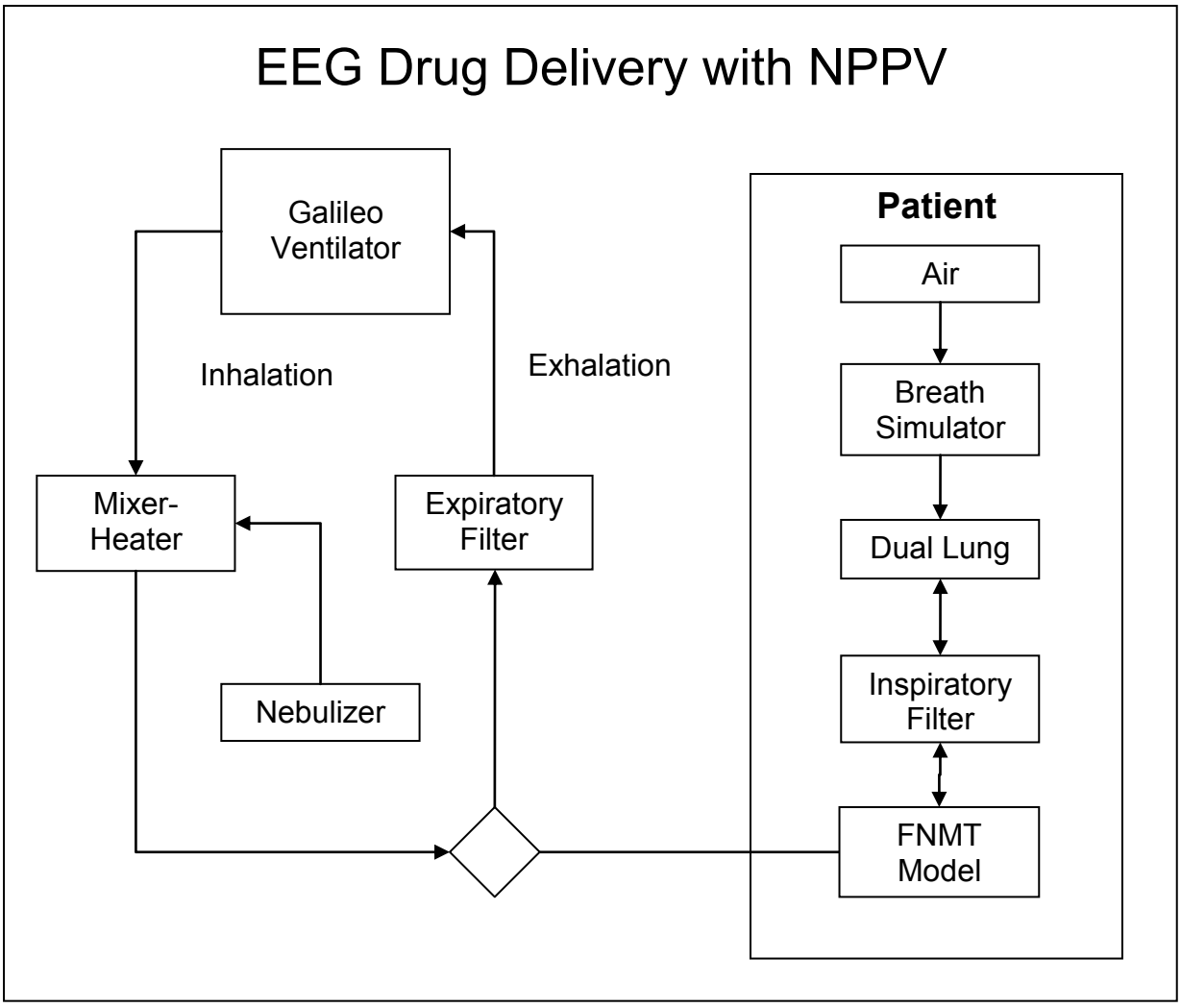

Figure 7.6 Process diagram of EEG drug delivery during NPPV.

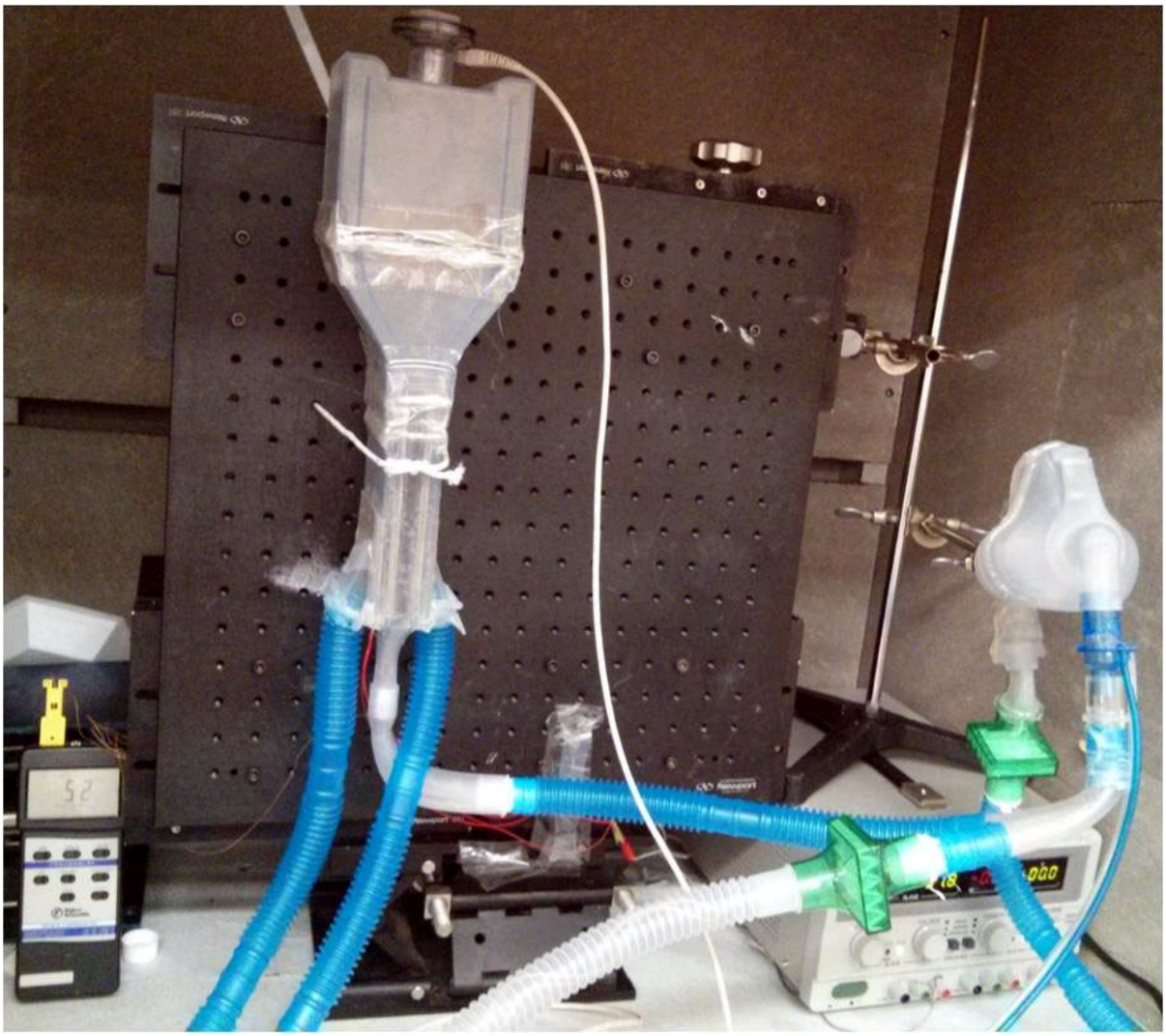

Figure 7.7 Experimental setup of EEG drug delivery during NPPV trials. The Aeroneb Pro nebulizer is pictured on the top left, attached to the mixer-heater. The inspiratory lines from the ventilator are attached to the sides of the mixer-heater, while the inspiratory tubing leaving the mixer-heater extends to the streamlined Y-connector. The ventilator flow meter is between the Y-connector and the FNMT model, while the inspiratory and expiratory filters are pictured downstream of the FNMT model and the Y-connector, respectively.

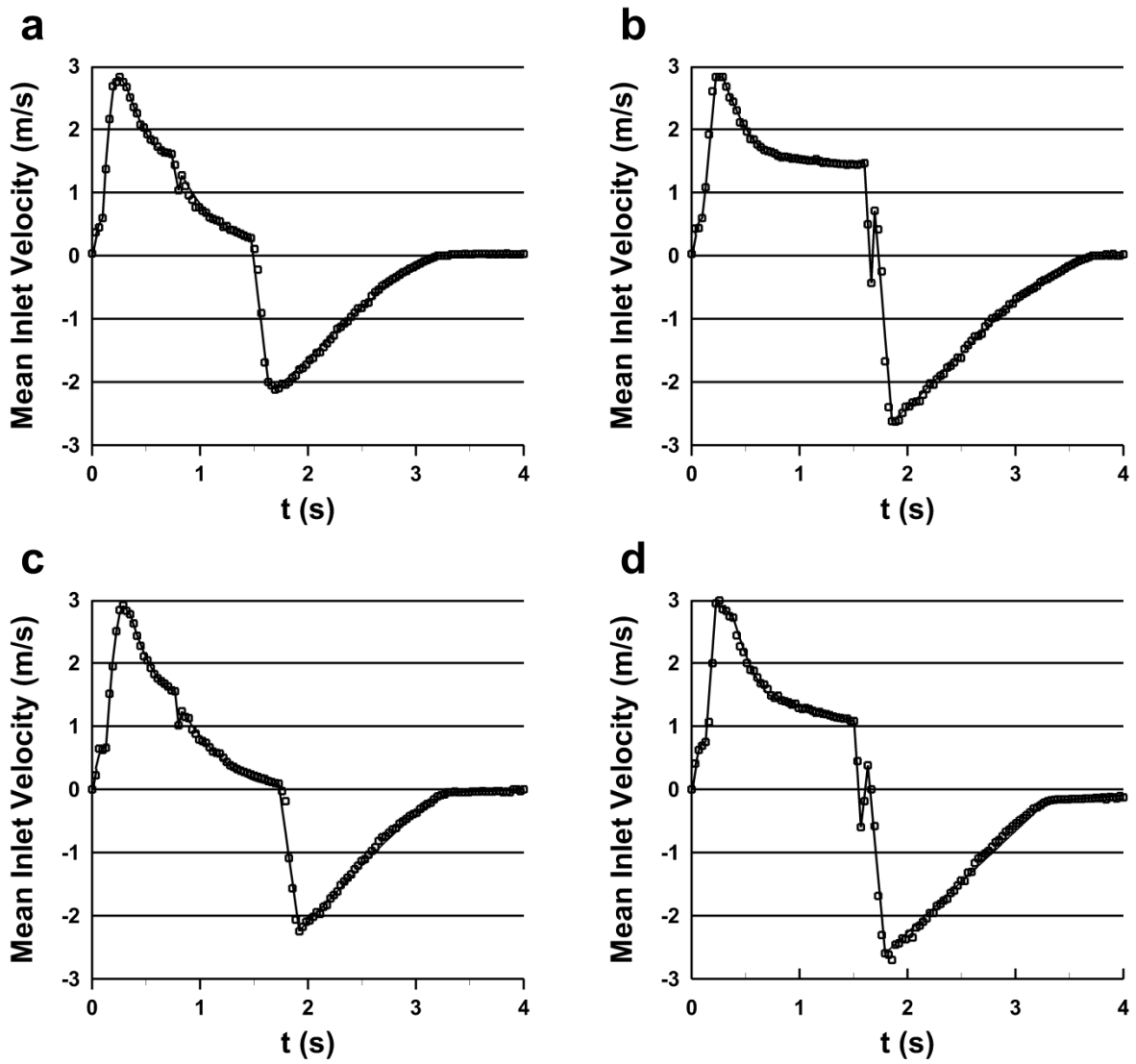

Figure 7.8 Mean mask inlet flow velocity (given in m/s for a 1520.5 cm^2 cross-sectional area) for conventional drug delivery during noninvasive positive pressure ventilation (NPPV) for (a) 1 s and (b) 2 s test lung inhalation, and for excipient enhanced growth (EEG) delivery during NPPV for (c) 1 s and (d) 2 s test lung inhalation.

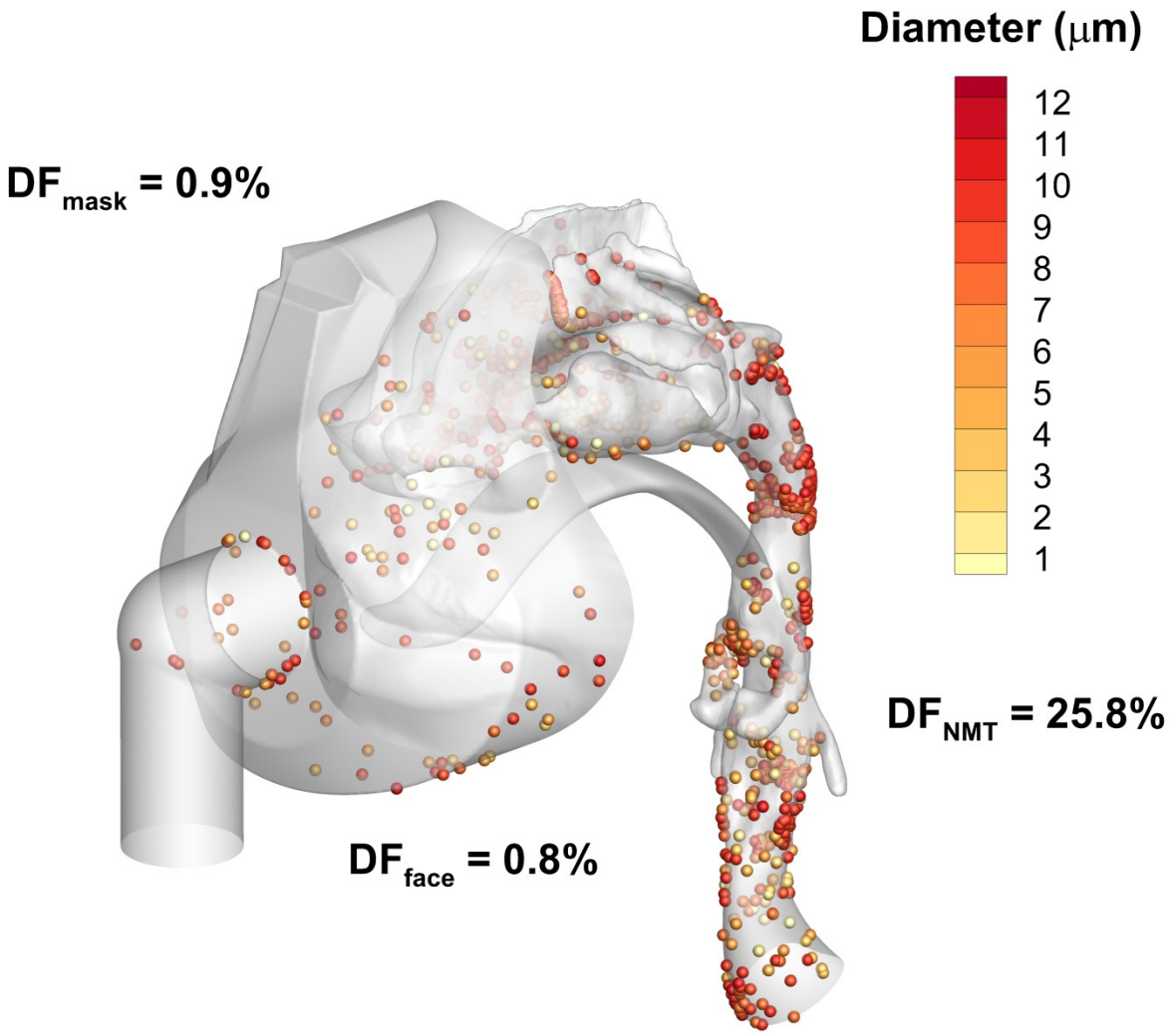

Figure 7.9 Steady state CFD prediction of conventional drug delivery with polydisperse 0.2% albuterol sulfate (AS) delivery through the commercial mask at 30 L/min.

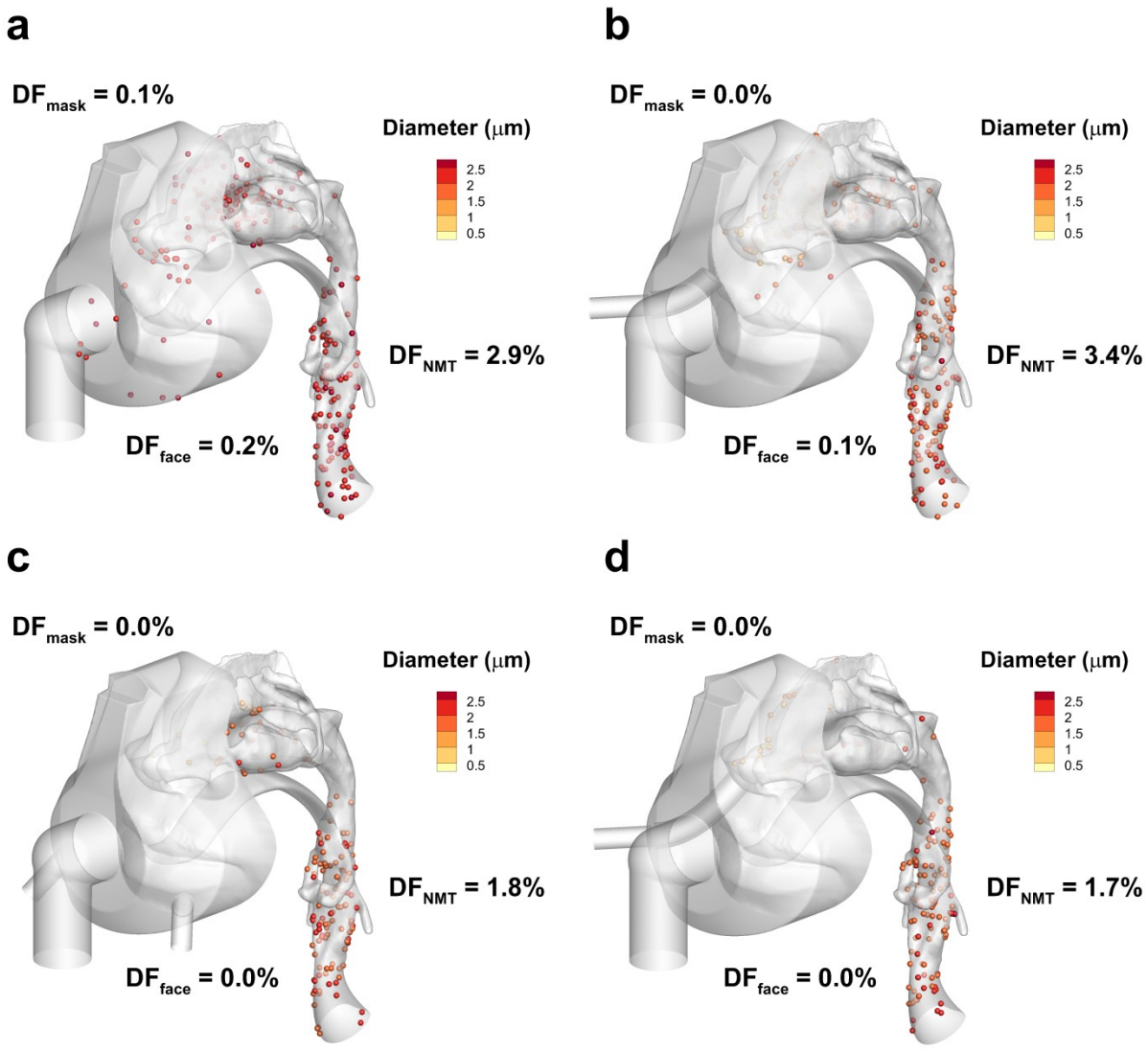

Figure 7.10 Steady state CFD predictions of deposition fraction (DF) for EEG drug delivery with monodisperse 50:50 albuterol sulfate (AS): sodium chloride (NaCl) particles at 30 L/min for the (a) commercial mask (PerformaTrak® SE, Philips Respironics, Inc.), (b) Mask Design #1.1, (c) Mask Design #1.2, and (d) Mask Design #1.3. Initial aerodynamic diameter of the EEG particles was 0.9 μm.

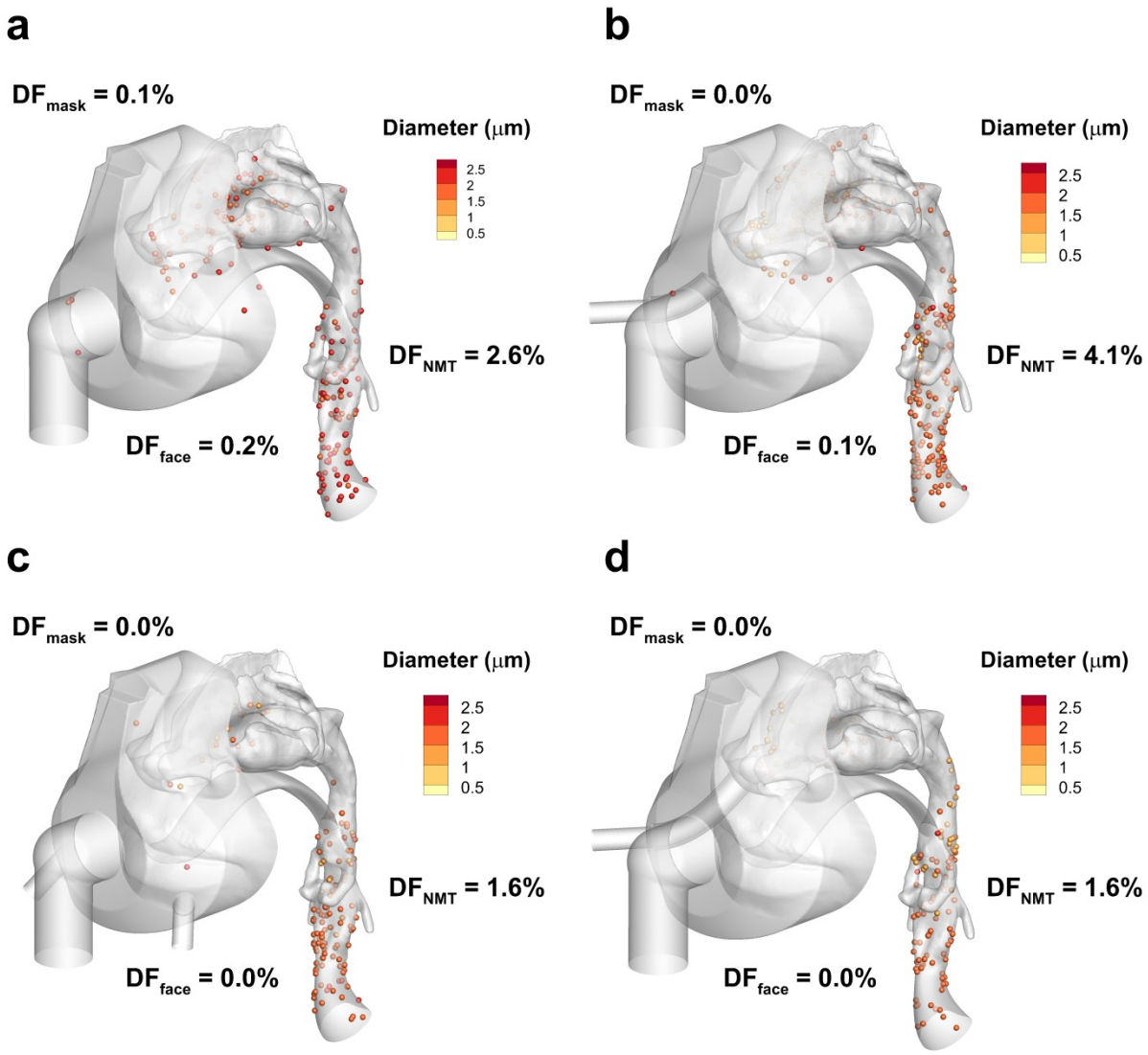

Figure 7.11 Steady state CFD predictions of deposition fraction (DF) for EEG drug delivery with monodisperse 75:25 albuterol sulfate (AS): sodium chloride (NaCl) particles at 30 L/min for the (a) commercial mask (PerformaTrak® SE, Philips Respironics, Inc.), (b) Mask Design #1.1, (c) Mask Design #1.2, and (d) Mask Design #1.3. Initial aerodynamic diameter of the EEG particles was 0.9 μm.

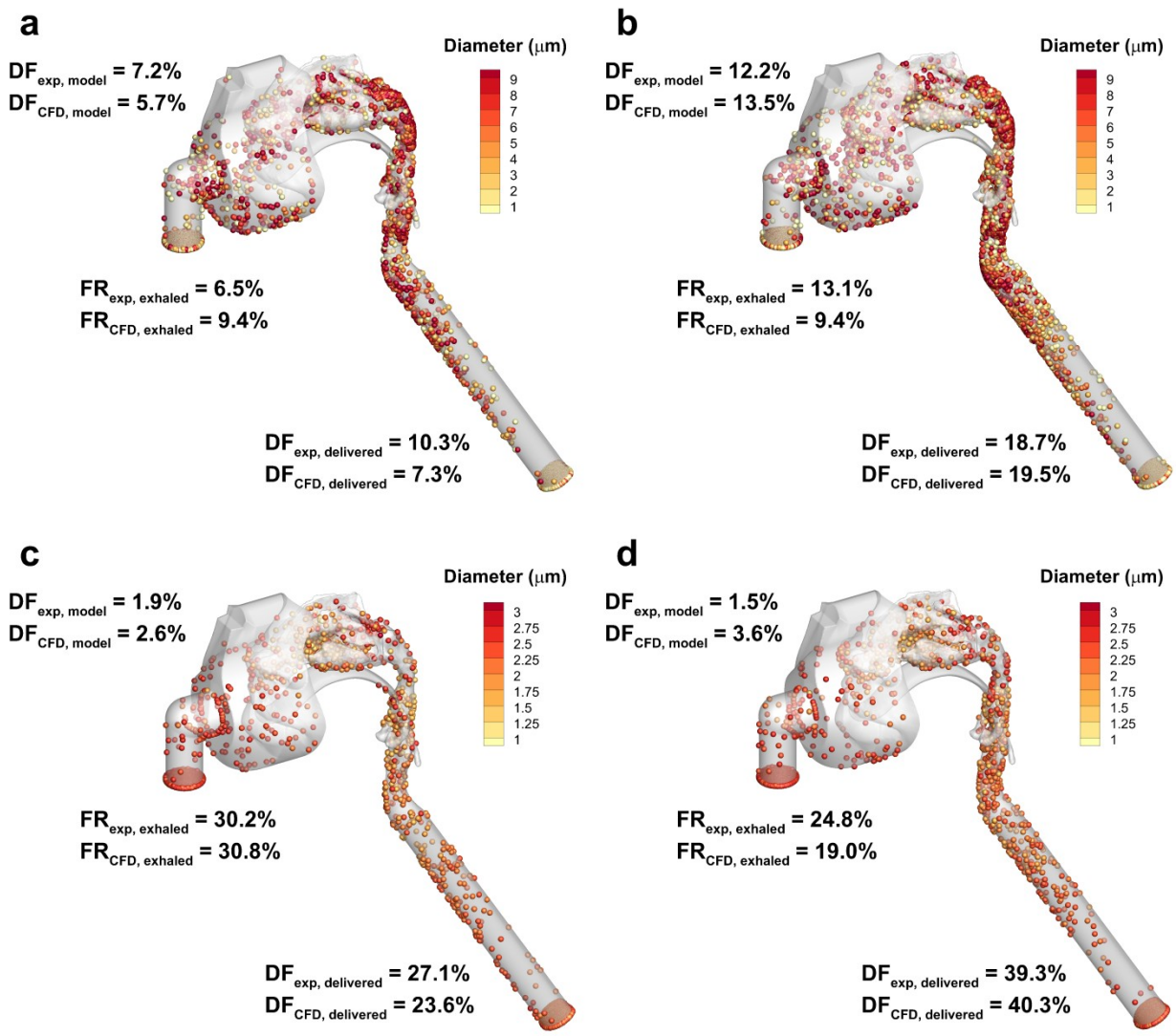

Figure 7.12 Transient CFD predictions of deposition fraction (DF) for the model and delivered dose for conventional drug delivery with (a) 1 s of inhalation and (b) 2 s of inhalation and for EEG drug delivery with (a) 1 s of inhalation and (b) 2 s of inhalation. Also shown is the estimate for fraction remaining of exhaled drug ($FR_{CFD,\ exhaled}$). The experimental values of DF are shown as well, while $FR_{exp,\ exhaled}$ is estimated based on Tables 7.6-7.9.

Chapter 8 Dry Powder Aerosol Delivery during NPPV

The objective of this study is to evaluate two oronasal mask designs as they relate to the efficiency of active dry powder aerosol delivery during noninvasive positive pressure ventilation (NPPV). Excipient enhanced growth (EEG) delivery was assessed with the antibiotic ciprofloxacin (CP), formulated as a combination particle with the hygroscopic excipient mannitol (MN) and the dispersibility enhancer L-leucine. Intersubject variability is explored using the face-nose-mouth-throat (FNMT) model from Chapter 7 and a second face-nose-mouth-throat (FNMT2) model constructed for this study. The effects of mask seal on drug deposition and variability are also explored. Conventional aerosol delivery was also considered to serve as a basis for comparison to newly proposed dry powder aerosol delivery during NPPV using the EEG approach.

8.1 Introduction

Characterization of intersubject variability with conventional and dry powder excipient enhanced growth (EEG) drug delivery through a mask during noninvasive positive pressure ventilation (NPPV) required the creation of a new face-nose-mouth-throat model in addition to the previously existing FNMT model from Chapter 7. The new model was created using CT scan data previously collected to form the data set used in Chapter 6 and Walenga et al. (2014), and was named the FNMT2 model. The FNMT2 model, pictured in Figure 8.1, was selected to

have a low value of nasopharynx exit hydraulic diameter ($d_{h,nasopharynx}$) as opposed to the FNMT model which had a higher value, since a weak inverse correlation between $d_{h,nasopharynx}$ and PF was noted in Chapter 6. The surface-area-to-volume ratio (SA/V) of the FNMT2 model was low (0.75 mm^{-1}) in the anatomical left side, but high (1.33 mm^{-1}) on the right side, indicating that significant nasal cycling was present, a phenomenon described in more detail by Gungor et al. (1999). The commercially available PerformaTrak SE® oronasal mask (Philips Respironics, Inc., Pittsburgh, PA, USA) served as a basis for the design of two new masks which both implemented separate aerosol inlets. One mask added an inlet targeted at the left nostril of the FNMT model (Mask Design #2.1), while the other mask placed a new inlet in the ventilation exchange elbow (Mask Design #2.2) (Figure 8.2). Conventional drug delivery was assessed for the four mask-model combinations with a 6 μm droplet and without size change of the aerosol. For dry powder EEG drug delivery, a drug:excipient combination similar to those described by Longest et al. (2014b) and Son et al. (2013a) was considered, which consisted of ciprofloxacin (CP), mannitol (MN), and also the dispersibility enhancer L-leucine. Both delivery methods were assessed through a series of monodisperse steady state CFD simulations that included an imperfect mask seal with a 5.2% leak which was the maximum amount identified by Schettino et al. (2001) for NPPV to still be effective. Following those simulations, the optimal mask was identified with regard to penetration fraction (PF) average value and variability. This mask was then simulated for both delivery methods and both face-nose-mouth-throat models with a perfect mask seal, to assess the effects of mask sealing on aerosol transport and deposition.

Results from the steady state CFD simulations showed a significant increase in delivered dose as expressed by PF for EEG drug delivery as opposed to the conventional method, by approximately a factor of two from 35.5% to 80.2% for Mask Design #2.1 and 36.2% to 78.2%

for Mask Design #2.2. The amount of drug lost through the mask seal, expressed by mask seal loss (MSL), was not greatly affected by the delivery method, but much more so by the mask design. For Mask Design #2.1, the MSL values with the FNMT model were 2.4% and 2.6% for conventional and EEG methods, respectively, but were 15.9% and 12.9% with the FNMT2 model for the same methods. Conversely, the MSL values for Mask Design #2.2 were nearly the same for all delivery methods and models, ranging from 4.8% to 5.9%. For both mask designs, significant variability of PF and deposition fraction (DF) in the nose-mouth-throat (NMT) was evident for both aerosol delivery methods between the FNMT and FNMT2 models, but Mask Design #2.2 showed much less variability of DF in the mask and face regions and of PF. For nearly all regions and cases, the amount of drug lost in the FNMT2 model was significantly higher, which was the opposite of what was expected. It is theorized that the lower value of $d_{h,nasopharynx}$ in the FNMT2 model greatly increased throat region deposition, a region which was not considered in Chapter 6. Considering that the average PF values for EEG delivery with both mask designs were similar, the reduction in delivered dose variability shown by Mask Design #2.2 indicated that it was the optimal design. The following steady state CFD simulations indicated that a perfect mask seal improved average PF for EEG delivery with Mask Design #2.2 by 3.6%, suggesting that drug lost through an imperfect mask seal for dry powder delivery during NPPV may not be large.

8.2 Methods

The previously developed FNMT model was used to evaluate dry powder delivery during NPPV. To assess the effects of intersubject variability on aerosol transport and deposition, a second face-nose-mouth-throat (FNMT2) model was constructed for this study. The absence of

readily available CT scan data that included a complete face, nasal cavity, and throat precluded the creation of a larger data set from which the range of dimensional characteristics could be represented. However, the dimensional data compiled in Chapter 6 and Walenga et al. (2014) served as a useful guide for the selection of scan data. Specifically, since the EEG technique is implemented for this study, $d_{h,nasopharynx}$ is used as a guiding measurement because a weak inverse correlation was observed in Chapter 6 between $d_{h,nasopharynx}$ and PF of EEG delivered drug through the nasal cavity. The demographic data for the two models are given in Table 8.1, where age, height, and weight were available in 10 year, 5 cm, and 5 kg increments. Both subjects were identified as female. The nasal cavity dimensions of the FNMT and the FNMT2 models are given in Table 8.2. Considering that the range of $d_{h,nasopharynx}$ values measured in Chapter 6 was 5.87-9.74 mm, the FNMT model is on the high end with a measured $d_{h,nasopharynx}$ of 8.78 mm, while the FNMT2 model was below the range of values with a value of 4.50 mm. It is then hypothesized that the FNMT2 model may provide further enhanced PF values with EEG delivery compared with conventional aerosol administration.

Other parameters, including surface-area-to-volume ratio (SA/V) and average nostril hydraulic diameter ($d_{h,nostril}$) were not controlled for in the selection of the FNMT2 model. The results of Chapter 6 and Walenga et al. (2014) showed a strong correlation between SA/V and PF for conventionally sized aerosols. For those studies SA/V was characterized by the anatomical side of the nasal cavity that showed the smallest value (i.e. the least constricted) to eliminate the effects of mild nasal cycling from the mean SA/V value. Additionally, for these previous studies, CT scans were selected to eliminate subjects with more extreme nasal cycling, which is evident in similar SA/V values on both sides of the FNMT model. However, the FNMT2 model shows significant nasal cycling as evidenced by very different values of SA/V on both sides,

with 0.75 mm^{-1} on the left and 1.33 mm^{-1} on the right. The effect of nasal cycling on PF is hypothesized to have a greater effect on aerosols delivered with a conventional method as opposed to the EEG technique, based on the previously identified correlation of SA/V with PF for conventionally sized droplets in Chapter 6. The reported range of values from Chapter 6 for $d_{h,nostril}$ was narrow, with values between 11.21 and 13.00 mm. The FNMT model is on the high end with a $d_{h,nostril}$ of 13.00 mm, while the FNMT2 model is outside of the lower bounds of the range with a value of 9.30 mm. It is unknown how much, if any, the smaller value of $d_{h,nostril}$ with the FNMT2 model as compared with the FNMT model will affect values of PF, but the similarity of $d_{h,nostril}$ as compared with $d_{h,nasopharynx}$ suggests that the PF of EEG delivered drugs is more likely to be affected by $d_{h,nostril}$ than those delivered by conventional means.

A similar method used to create the FNMT model for Chapter 7 was used to create the FNMT2 model. The CT scan data was segmented using the commercial software package Mimics 16.0 (Materialise, Belgium) to include the face, nasal cavity, and the throat. Then, a 3D surface file with an .stl extension was produced by Mimics 16.0, which was subsequently imported into 3-matic (Materialise, Belgium), and exported as a volumetric file with an .igs extension to be imported into SolidWorks 2011 (Dassault Systèmes Solidworks Corp., Waltham, MA, USA). Finally, the .igs file was saved as an .x_t file in SolidWorks, which allowed for modification to the model in ANSYS Workbench/DesignModeler 14.5 (ANSYS, Inc., Canonsburg, PA, USA). One limitation of the CT scan data set was incomplete imaging of the tip of the nose, which was reconstructed to approximate a hemispherical shape. This small modification (~5 mm extension) is not expected to significantly affect flow and aerosol transport. As with the FNMT model in Chapter 7, the face of the FNMT2 model not included in the mask area was truncated to allow for de-identification of the subject. Additionally, in the same manner

as Chapter 7, a closed mouth pathway was designed using similar dimensions as the nose-mouth-throat (NMT) model of Golshahi et al. (2013). The throat of the FNMT2 model was modified in the same manner as the FNMT model in Chapter 7 to allow for connection with Model D from Chapter 3 for future study. A numerical extension is added to the throat outlet in an identical manner as with the FNMT model. The final model is illustrated in Figure 8.1 without the numerical extension, and the dead space volumes of the various regions of the FNMT2 model are given in Table 8.3, including the volume of one the two mask designs used in this study (which were similar in shape and size).

Two new mask designs were created that used the commercially available PerformaTrak® SE oronasal mask as a basis. Despite the difficulties encountered with implementing a separate aerosol inlet for nebulized aerosol delivery during NPPV in the Chapter 7 study, the idea was introduced again for this study. The primary difference between the two studies is found in the aerosol delivery method, where in Chapter 7 the transient mixer-heater from Golshahi et al. (2014b) was utilized to create a submicrometer particle for the EEG method, while an active DPI was chosen for this study. The findings of Chapter 7 showed that the mixer-heater required in-line placement within the NPPV system, but for this study the selected active DPI would only be actuated approximately 4-8 times in a clinical setting. The in-line placement is logical for a continuously operating aerosol delivery system such as the mixer-heater, but not for the infrequently applied active DPI. As pictured in Figure 8.2, an inlet directed at the left nostril of the FNMT model and an inlet in the elbow bend of the commercial mask were used to modify the PerformaTrak® SE mask and create the two new designs, named Mask Design #2.1 and Mask Design #2.2, respectively. Both inlets were 8 mm in diameter and were external to the mask (i.e. did not protrude inward). The choice of face-nose-mouth-throat model used for the

target of the left nostril directed inlet in Mask Design #2.1 was arbitrary, which indicates that drug delivery through this mask design is more likely to be subject to issues of intersubject variability. However, Mask Design #2.2 may potentially produce higher values of face and mask DF because the elbow inlet is directed at the face. This study will attempt to assess which of these two limiting effects are greater.

The commercially available meshing software ICEM CFD 12.0.1 (ANSYS, Inc., Canonsburg, PA, USA) was used to create the computational meshes for this study. The two mask designs were joined to the two models in a manner that approximated a comfortable fit while maintaining a seal with each of the faces. It is notable that the mask dead space volume was greatly reduced with the FNMT2 model as compared with the FNMT model (157.5 mL vs. 207.9 mL), which was a result of mating the masks to different face shapes and positions. The imperfect mask seal was modeled by including a 0.5 mm thick ribbon between the face and the mask that followed the curvature of that boundary. The meshing procedure was identical to the method used in Chapter 7, where a tetrahedral Delauney mesh was applied to the entire volume of each mask-model combination. The boundary layers were approximated with seven near-wall prism layers, where the initial near-wall control volume height was 0.011 mm. The two meshes with the FNMT model had ~7 million cells each, while the two FNMT2 meshes had ~5.8 million cells each. As before, the y^+ values of the near-wall control volumes were checked to ensure mesh independence, and it was found that the maximum value for each case was 2.7 or less, which is within the range ($1< y^+ < 5$) of accuracy for the turbulence model selected for this study.

A series of steady state CFD simulations were conducted to evaluate the performance of the two mask designs, the variability of depositional loss and delivered dose, and to compare

performance of the EEG technique with a conventional delivery method. The steady state assumption was used because *in vitro* data were not yet available for comparison with CFD data, and it also allowed for greater computational efficiency. Initially, the four mask-model combinations were simulated using conventional and EEG delivery methods with a fraction of the flow exiting through the mask seal interfaces, while the rest penetrated to the throat outlets. Once the eight initial cases were complete, the mask with the best performance in terms of average PF was selected for further study. To explore the effect of mask sealing on PF and variability, four cases were conducted that considered a perfect mask seal with conventional and EEG methods with the higher performing mask and the two extrathoracic geometries.

Schettino et al. (2001) evaluated mask sealing during NPPV using a commercial mask with a mannequin at various inlet airway pressure settings, and found that the leak flow rate was nearly constant when the difference between the inlet airway pressure and mask pressure was above 1.7 ± 0.1 cm H_2O, and that a volumetric leak of 5.2% was observed at this threshold. Taking this into account, an outflow boundary condition was used for the CFD predictions in this study that applied the leak flow split identified by Schettino et al. (2001). For all cases, ventilation gas delivery was modeled as heated and humidified at an inlet temperature and relative humidity (RH) of 37 °C and 99%. Identical to Chapter 7, the flow rate was set at 30 L/min, which approximated mean flow rate of a real system. Flow from each of the aerosol inlets was modeled at room temperature (25 °C) with an RH of 99%, since the active DPI was not in-line with the system, but flow from the inlet entered into a relatively large volume of humidified air. The flow rate for the aerosol inlets was determined by the specific active DPI implemented, as described below.

Conventional aerosol delivery was modeled for this study by considering a generic droplet or particle with an initial aerodynamic diameter of 6 μm and assuming that size change is negligible, which is considered a good assumption for pharmaceutical aerosols with aerodynamic diameters greater than 3 μm (Finlay & Stapleton, 1995; Finlay, 1998). This particle size is considered to be typical for mesh nebulizers and DPIs (Borgström *et al.*, 1994; Kuhli *et al.*, 2009; Longest, et al., 2012a; Son, et al., 2013a). A ventilation bag actuated dry powder inhaler developed by Behara et al. (2014b) was selected for modeling EEG aerosol boundary conditions in this study. As described in Section 2.3.4, the ventilation bag provides external energy to a DPI system that implements a 3D rod array to enhance deagglomeration and a flow control orifice (Behara, et al., 2014b). The design selected for study here is a the 2.3-212-ECG device, which has a flow control orifice diameter of 2.3 mm, a 3D rod arrangement of 212, and was initially tested for enhanced condensational growth (ECG) delivery through a specially designed nasal cannula (Behara, et al., 2014b). The measured root-mean-square (RMS) flow rate of the device was 11.6 ± 0.6 L/min, where the mean was used for this study. The drug chosen for study was the antibiotic ciprofloxacin (CP), which was formulated as a combination particle with the hygroscopic excipient mannitol (MN), in a similar manner as described by Longest et al. (2014b), who modeled CP in combination with MN, L-leucine (a dispersibility enhancer), and polaxamer 188 (a surfactant) in a 30:48:20:2 ratio, based on a previous study by Son et al. (2013a). For this study, the surfactant polaxamer 188 was omitted, and the new ratio with CP, MN, and L-leucine was 30:50:20. A particle sizing experiment was conducted by Dr. Michael Hindle and colleagues in the VCU Department of Pharmaceutics for this study, and the mass median aerodynamic diameter (MMAD) of the combination particle at the active DPI exit was found to be 1.59 μm. A monodisperse particle profile of 9,000 particles with the measured

MMAD was used for all CFD simulations, because the added complexity of a polydisperse distribution was not expected to greatly contribute to the comparison of masks and airway models.

The combination of the commercially available CFD package ANSYS FLUENT 14.5 (ANSYS, Inc., Canonsburg, PA, USA) and several user-defined routines was used to model steady state flow through the various mask and model arrangements. Particle deposition, size change, and trajectories were modeled for all CFD predictions, as well as fluid mass and heat transfer. Parallel processing was utilized using the same user-defined functions (UDFs) developed for transient CFD predictions in Chapter 7. A low-Reynolds number (LRN) k-ω model was selected for simulating laminar and turbulent flow, since it has been shown by Xi et al. (2008) to provide reliable predictions of flow field characteristics in human upper respiratory airways, particularly as they relate to pharmaceutical aerosol deposition and transport.

Particle trajectory calculations, including predictions of hygroscopic size change for EEG delivery, were produced using Lagrangian transport modeling (Longest & Hindle, 2010). Turbulent dispersion of particle trajectories was simulated using a random walk method, while user-defined functions (UDFs) were implemented to model near-wall corrections of fluid velocities and turbulence. The updated UDFs for near-wall turbulence and velocity correction developed in Chapter 4 were used. Hygroscopicity of the drug and excipient, the Kelvin effect, and the effect of vapor pressure were all considered for particle size change predictions. One-way coupled modeling was applied to the system, which neglected the effects of the discrete phase on the continuous phase. Longest et al. (2011) and Tian et al. (2013) describe the equations used in greater detail.

Best practices for ANSYS FLUENT 14.5 solution methods as established by Longest et al. (2012c) were followed. Double precision was enforced to improve the accuracy of all calculations. Pressure-velocity coupling was modeled using the SIMPLEC algorithm, while spatial discretization of all convective terms was handled with a second-order upwind scheme. Both the approach of momentum and mass residual rates to the numerical precision limit and a five order of magnitude reduction in the global mass-residual were monitored to define flow field convergence.

Deposition of conventional and EEG delivered drug is measured on the face, mask, and NMT using DF as described by Equation 3.3. The MSL of drug exiting through the face and mask boundary for the imperfect sealing cases is reported, which is calculated in the same manner as DF. To assess the amount of delivered dose for each case, PF is used as described by Equation 6.12, where only the drug exiting from the throat is considered. To characterize condensational growth, throat outlet MMAD is reported for each case, as well as the average residence time of injected particles that exit from the throat. Deposition efficiency (DE), as calculated by Equation 3.4, was used to characterize total nasal region deposition for the optimal mask with a 5.2% mask seal leak to provide a basis for comparison with the results of Chapter 6.

8.3 Results

Values of DF and MSL for conventional and EEG drug delivery through Mask Design #2.1 with an imperfect mask seal are given in Table 8.4 and illustrated in Figure 8.3. Depositional losses in the mask, face, and NMT are all significantly higher for conventional as opposed to EEG drug delivery, with as high as an order of magnitude difference between the two methods. The average values of MSL are similar for both methods, with 9.1% for conventional

delivery and 7.8% for EEG delivery. Significant intersubject variability in DF and MSL values is evident considering the FNMT and FNMT2 models, with significant relative differences in every region, which were as high as a factor of ten for the mask and face regions with conventional delivery and for the mask with EEG delivery. Mask Design #2.1 includes a left nostril inlet that was targeted using the FNMT model but not the FNMT2 model. Then, the heightened values of DF in the mask and face regions for the FNMT2 model as compared with the FNMT model may be caused by the mismatched inlet aerosol stream from Mask Design #2.1 with the left nostril opening of the FNMT2 model. Values of PF, outlet MMAD, and average particle residence time for Mask Design #2.1 with an imperfect mask seal are given in Table 8.5. Average PF is much greater for the EEG aerosol as compared with the conventional aerosol, with delivered dose of 80.2% versus 35.5%. Again, intersubject variability is evident, with PF values for conventional delivery of 62.8% and 8.1% for the FNMT and FNMT2 models, respectively, but it is much less for EEG delivery with values of 90.3% and 70.1% for the two models. The outlet MMADs for EEG delivery show significant condensational growth with an average value of 2.70 μm, while the average particle residence time values show that particles are in the FNMT2 model nearly twice as long as for the FNMT model.

Depositional loss for conventional and EEG delivery through Mask Design #2.2 with an imperfect mask seal is characterized by values of DF and MSL given in Table 8.6 and pictured in Figure 8.4. Similar to the Mask Design #2.1 results, regional DF values are much higher for conventional delivery as compared with EEG delivery, but the MSL values are nearly identical. As with Mask Design #2.1, significant intersubject variability is present in the NMT considering the FNMT and FNMT2 models, with DF amounts of 25.4% and 73.0% using conventional methods, respectively, and 4.3% and 15.9% using the EEG approach in the two models.

However, the face and mask regions show similar values of DF in both models, which is true for both delivery methods even though the values are higher for conventional delivery as opposed to EEG delivery. The amount of MSL is nearly the same regardless of model or method, with about 5% leaving the system through the mask leak for all cases. Delivered dose for Mask Design #2.2 with an imperfect seal is assessed in Table 8.7, with values of PF, outlet MMAD, and average particle residence time. As with Mask Design #2.1, average PF is much greater for EEG as opposed to conventional delivery, with averaged values of 78.2% versus 36.2%, respectively. Again, variability of PF between the FNMT and FNMT2 models is significant, particularly for conventional delivery where values of 59.0% and 13.6% are reported, respectively. The difference in PF values for EEG delivery in the two models is much less, with 84.6% and 71.8% for the FNMT and FNMT2 models, respectively, and is also less than for the same delivery method with Mask Design #2.1. Significant condensational growth with the EEG technique is again evidenced by an average MMAD of 2.89 μm, while average particle residence time is nearly the same for both face-nose-mouth-throat models.

Results from Mask Design #2.1 and Mask Design #2.2 are compared to assess relative performance with respect to PF, outlet MMAD, regional DF, and MSL values for EEG drug delivery. Average PF is slightly higher for Mask Design #2.1 with 80.2% as compared with 78.2% for Mask Design #2.2, but the absolute difference in PF values between the geometries with Mask Design #2.2 is 12.8%, which is much less than the absolute difference of 20.2% reported for Mask Design #2.1. Regarding regional DF amounts in the NMT, variability is still high for both mask designs. However, a significant reduction in variability is also evident for Mask Design #2.2 in the regional DF values for the face and mask, which for Mask Design #2.1 are five to ten times greater with the FNMT2 model as compared with the FNMT model, but for

Mask Design #2.2 are only two times greater. The amount of drug lost through the mask seal as expressed by MSL is nearly four times greater for the FNMT2 model as for the FNMT model with Mask Design #2.1, but it is nearly the same with Mask Design #2.2. The reduced variability in the face DF, mask DF, and MSL values for Mask Design #2.2 is most likely due to the centrally located aerosol inlet in the ventilation exchange elbow, as opposed to the left nostril targeted aerosol inlet which does not account for intersubject variability of nostril size and location. The average outlet MMAD is improved for Mask Design #2.2 as compared with Mask Design #2.2, indicating another advantage. Overall, despite the small reduction in average PF value, the reduction in variability and increase in outlet MMAD shown for Mask Design #2.2 as opposed to Mask Design #2.1 suggests that it is the better performing mask, and is selected for further study.

To quantify the effect of mask sealing, regional predictions of DF for Mask Design #2.2 with a perfect mask seal were performed for both conventional and EEG drug delivery. The results are shown in Table 8.8 and illustrated in Figure 8.5. Considering the mask seal, very little difference is observed in the face and mask DF values for all models and methods. In contrast, the values of DF on the NMT increase for the perfect mask seal case as compared with the 5.2% leak case by as much as 8.5% with the FNMT2 model and EEG delivery. However, regarding EEG delivery, when the DF values in the NMT are summed with the MSL values for the 5.2% leak case, these total losses are reduced when compared with the DF values in the NMT for the perfect seal case, with an average decrease of 3.6%. Thus, the CFD predictions suggest that the presence of the leak does show some effect on regional losses with the EEG technique, albeit a small one. The values of PF given in Table 8.9 also indicate that a perfect mask seal improves EEG delivery, with an average PF value of 81.8% for a perfect seal as opposed to 78.2% with a

leak. The values of outlet MMAD and average particle residence time in Table 8.9 are nearly the same as for the imperfect mask seal cases, indicating that condensational growth may not be greatly affected by the mask seal.

Previously in Chapter 6, the effect of intersubject variability on DF and DE values in the nasal region was studied for conventional and EEG delivery of AS through a high flow therapy (HFT) nasal cannula at 30 L/min. To provide a basis for comparison with the results of that study, the values of DF in the NMT region of the FNMT and FNMT2 models for conventional and EEG delivery through Mask Design #2.2 with a 5.2% mask seal leak (available in Table 8.6) were segmented into the regions defined by Chapter 6 and listed in Table 8.10. The nasal regions from Chapter 6 were the nasal valve area, nasal cavity, and nasopharynx (not listed in the Chapter 6 tables but available), while the throat region was absent in that study but is included here. The DE of the total nasal region, which includes the nasal valve area, nasal cavity, and nasopharynx, is also included. Significant relative variability is visible for both delivery methods in the nasal valve area, nasopharynx, and throat regions, with values of DF in the FNMT2 model three to ten times greater than the in the FNMT model. However, nasal cavity DF is nearly identical for EEG delivery with drug losses of 2.1% and 2.4% in the FNMT and FNMT2 models, respectively, while it is similar for conventional delivery with values of 12.0% and 10.1% in the two models. The value of nasal cavity DF for conventional drug delivery through the FNMT2 model with Mask Design #2.2 and a 5.2% leak is the only instance in the study where the deposition amount is less than for the FNMT model. Throat deposition is significant for all cases, with 42-75% of the total DF value for the NMT region depositing in that sub-region. Intersubject variability is evident regarding total nasal DE, with an increase by a

factor of three for conventional delivery from the FNMT to the FNMT2 model, and an increase by a factor of two for EEG delivery.

Particle trajectories for conventional and EEG drug delivery through Mask Design #2.1 with imperfect mask sealing are pictured for the two face-nose-mouth-throat models in Figure 8.6. Regarding Mask Design #2.1, it is clear that for both conventional and EEG delivery through the FNMT2 model that injected particles travel past the left nostril opening and around the perimeter of the mask before entering the NMT. In contrast, conventional and EEG results for Mask Design #2.1 and the FNMT model indicate that injected particles are directly delivered to the left nostril, which is not surprising considering that the aerosol inlet for this mask was designed to target the left nostril of the FNMT model. The results from Figure 8.6 explain the long residence times observed for the FNMT2 model as compared with the FNMT model, which were observed in Table 8.5 to be approximately twice as long for the FNMT2 model.

Illustrated in Figure 8.7 and Figure 8.8 are particle trajectories for conventional and EEG drug delivery through Mask Design #2.2 with imperfect and perfect mask sealing, respectively, for the two face-nose-mouth-throat models. Large recirculation areas are visible in the mask regions of both models for both delivery methods with imperfect and perfect mask sealing. For the imperfect mask sealing cases, many of the recirculating particles appear to exit through the leak. The FNMT2 model has more recirculation in the top portion of the mask volume for both delivery methods and sealing conditions, and some of the particles appear to move to the top of the mask and then enter through the nostrils. This may reduce particle velocities and consequently increase depositional loss in the nasal cavity. Recirculation regions are also visible in the throat sections of both models for both delivery methods, which may explain the high deposition in those regions. Also notable is that noticeably fewer particle trajectories are

observed after the nasopharynx exit in the FNMT2 model with the conventional aerosol. Another factor that may play a role is dead space volume, since it appears that for both delivery methods and sealing conditions with the FNMT model, which has the larger mask dead space volume as compared with the FNMT2 model, the distance between the entrance from the ventilation inlet to the nostrils is longer and that allows for slower particle delivery to the NMT which may potentially enhance efficiency.

8.4 Discussion

Considering that the CFD simulations performed for this study used a steady state assumption, a direct comparison with *in vitro* and *in vivo* data from the literature is not sought, since it is well known that transient flow significantly reduces delivered dose through human upper airways. However, to assess the effects of drug:excipient combination particle type and mask sealing, a comparison of the EEG delivery results for the FNMT model with 30:50:20 CP:MN:L-leucine from this study is made with the 50:50 AS:NaCl EEG delivery steady state CFD results using the same nasal model from Chapter 7. The DF results in the NMT are similar for both particle types, with a range of 1.7% to 3.4% for 50:50 AS:NaCl with the four mask designs from that study, while for Mask Design #2.2 with a perfect mask seal the DF value for 30:50:20 CP:MN:L-leucine was 5.1%. In all cases for both studies, DF values in the mask and face regions were negligible. The higher initial diameter of 30:50:30 CP:MN:L-leucine of 1.59 μm as compared with 0.9 μm initially sized 50:50 AS:NaCl may explain the small increase in DF in the NMT. When an imperfect seal was considered with the two mask designs in this study, the amount of DF in the NMT was reduced to 2.0% and 4.3% for Mask Design #2.1 and Mask Design #2.2, respectively. However, In addition to losses in the NMT, between 2.6% and

4.9% of the dry powder nominal dose was lost through the imperfect mask seal for the two mask designs with the FNMT model, indicating total losses in the NMT and through the seal of 4.6% and 9.2% for Mask Design #2.1 and Mask Design #2.2. Altogether, results from this chapter indicated that the use of 30:50:20 CP:MN:L-leucine increased DF in the NMT by about 2-3%. The inclusion of an imperfect mask seal further increased the total drug loss in the geometry by about 4% as compared with the results of Chapter 7.

A primary hypothesis of this study was that the FNMT2 model would increase EEG delivered dose because of its small $d_{h,nasopharynx}$ value as compared with the FNMT model. It was thought that increased resistance produced by a small value of $d_{h,nasopharynx}$ would decrease residence time, and since the particle is initially in the submicrometer range it would not increase deposition by impaction greatly. However, the steady state CFD predictions indicated that delivered dose was significantly worse for conventional and EEG delivery through the FNMT2 model as compared with the FNMT model, though the absolute difference was much greater for the conventional method. Many factors may explain this unexpected outcome, including dead space volume, the presence of nasal cycling in the FNMT2 model, the relatively small value of $d_{h,nostril}$ as compared with the data from Chapter 6, or the change in size of the extrathoracic airways. Also, the correlation between PF and $d_{h,nasopharynx}$ developed in Chapter 6 was based on EEG delivery through a nasal cannula during HFT, not through a mask. The measured values of DF in the nasal valve area are higher for the FNMT2 model than the FNMT model with both delivery methods, suggesting that $d_{h,nostril}$ may play a larger role than previously thought and may affect nasal cavity deposition. The particle trajectories in Figure 8.7 and Figure 8.8 for imperfect and perfect sealing with Mask Design #2.2, respectively, show more recirculation above the nostrils for the FNMT2 model than for the FNMT model, which may be the result of a smaller

mask dead space volume for the FNMT2 model as compared with the FNMT model. The decrease in size of the extrathoracic airways may play a role. From Figures 8.3-8.5 it is evident that the FNMT2 model is smaller than the FNMT model (which are both scaled to the same viewing magnification in those views), which may be partly explained by looking at the demographic data, since the subject for the FNMT2 model is approximately 10 cm shorter than the subject for the FNMT model.

The regional nasal DF and total nasal DE data from Table 8.10 indicates that throat deposition is likely an important factor for intersubject variability. As discussed in Chapter 7, the amount of NMT deposition in the throat for the FNMT model was significant, which suggested that the correlation observed in Chapter 6 between PF and $d_{h,nasopharynx}$ may be only applicable to delivered dose at the nasopharynx exit, while the delivered dose at the throat exit is truly required. The relative amount of NMT deposition in the throat for Mask Design #2.2 with an imperfect seal ranges from 42-45% for the FNMT model with both delivery methods and with the FNMT2 model with the conventional method, but the relative amount for the FNMT2 model with the EEG technique is 75%. It appears that the smaller $d_{h,nasopharynx}$ acts to increase the already significant amount of throat deposition when EEG delivery is employed.

The effect of a mask interface as compared with a nasal cannula on aerosol delivery during the application of ventilation support is examined by comparing the results of Table 8.10 with those of Table 6.7 and Table 6.8. The 6 μm conventional aerosol from this study is most directly comparable with the 5 μm conventional aerosol without size change from Chapter 6. Both the FNMT and FNMT2 models have total nasal cavity SA/V values that are most directly comparable to the Average model from Chapter 6, though the FNMT and Average models are more similar in terms of $d_{h,nasopharynx}$. Nasal cavity DF values are similar for all conventional

cases, with 11.2% in the Average model and 12.0% and 10.1% in the FNMT and FNMT2 models. However, variability is observed in the nasal valve area, where the Average model is observed to have 5.1% drug loss in that region as compared with 1.1% and 8.3% in the FNMT and FNMT2 models. The total nasal DE is similar for the Average and FNMT2 models with values of 38.6% and 44.2%, respectively, but much less for the FNMT model with 15.8%. Regarding EEG delivery, the initially sized 1.5 μm 50:50 AS:NaCl (Chapter 6) combination particles with size change considered provide the best comparison for delivery of 30:50:20 CP:MN:L-leucine with an initial size of 1.59 μm (Chapter 8). The amount of drug lost in the nasal cavity is less for the FNMT and FNMT2 models than for the Average model, with DF values of 2.1% and 2.4% as opposed to 3.5%. For nasal valve area, the amount of DF in the FNMT2 model is 1.0% as compared with 0.2% and 0.3% for the FNMT and Average models. It is observed that total nasal DE values are nearly the same for the Average and FNMT2 models for EEG delivery (4.1% and 4.3%), but less for the FNMT model (2.5%). The trends for both conventional and EEG delivery seem to indicate that for the two most similar geometries, the Average and FNMT models, the presence of the cannula increases nasal valve area DF and also total nasal DE. It is believed that the same effect applies to the FNMT2 model as compared with the Average model, but that other factors contribute to the higher values of nasal valve area DF and the comparable values of total nasal DE. As suggested above, there are many geometric dimensions which may play a role in the dramatic increase in deposition in the nasal regions of the FNMT2 model, including $d_{h,nasopharynx}$, $d_{h,nostril}$, or the presence of nasal cycling.

A steady state assumption was applied to all CFD simulations for this study to facilitate a comparison of dry powder EEG delivery during NPPV to two different human extrathoracic geometries and to identify which new mask design showed the best performance with respect to

depositional loss and variability. Transient predictions, which are known to be more accurate, were not implemented due to a lack of *in vitro* data that would provide a meaningful comparison. Though steady state CFD predictions in Chapter 7 proved to be problematic for mask design due to system effects not included in the mesh domain, they are not expected to have the same issue for this system since the EEG aerosol delivery flow source is separate from the ventilator tubing. Nonetheless, to confirm the results of this study, it would be useful for future transient simulations to be performed when relevant *in vitro* data becomes available. Another limitation of the study is the small sample size (n = 2) for assessing intersubject variability, which will be an obstacle for future study due to the limited availability of CT scan data sets that include the face, nasal cavity, and throat. If possible, the acquisition of additional CT scan data would allow for a more complete characterization of the effects of nasal cycling, $d_{h,nostril}$, $d_{h,nasopharynx}$, and perhaps throat characteristics as they relate to delivered dose of lung-targeted aerosols. CFD results quantify the expected throat outlet MMAD values for each case, but in the absence of a thoracic geometry it is not possible to measure thoracic deposition and lung targeting, and so future work may include thoracic predictions using Model D, which was developed in Chapter 3. The effects of dead space volume were only touched upon by visual analysis of Figure 8.7 and Figure 8.8, and require more analysis to provide a fuller understanding of their impact on a realistic system. Though a smaller dead space volume for the FNMT2 model as compared with the FNMT model appeared to reduce drug delivery efficiency, this may not be the case for transient predictions, since smaller volumes are expected to decrease injected particle residence time. As mentioned in Chapter 7, the FNMT model employs a closed mouth design, and the FNMT2 model does as well. It may be of interest to model open mouth drug delivery during NPPV in the future.

Dry powder drug delivery of ciprofloxacin (CP) with the EEG method during NPPV was assessed for this study using steady state CFD simulations and compared with conventional drug delivery for the same system. In addition to the previously existing FNMT model which was created for Chapter 7, a second face-nose-mouth-throat (FNMT2) model was created to assess intersubject variability of dry powder delivery during NPPV, using data from a CT scan which was chosen because its low value of nasopharynx exit hydraulic diameter ($d_{h,nasopharynx}$) was expected to enhance penetration fraction (PF). Two new oronasal mask designs based on the commercially available PerformaTrak SE® were evaluated based on the results of the steady state CFD predictions. Conventional drug delivery was assessed to provide a basis for comparison with the dry powder selected, which was based on the formulations of Longest et al. (2014b) and Son et al. (2013a) and presumed to be introduced to the masks via an active DPI device developed by Behara et al. (2014b). An imperfect mask seal was included to assess the effects of leakage on drug delivery. Results showed that PF was improved by a factor of two with EEG delivered drug as opposed to conventional aerosols. The mask which showed greater performance implemented an aerosol inlet in the ventilation exchange elbow, which reduced variability in the face and mask regions as well as through the mask leak when compared with the other mask design which utilized a left nostril targeted aerosol inlet. Drug lost through the mask seal was found to be on the order of ~5%, which was found to be approximately the same for conventional and EEG delivery methods. Significant intersubject variability was observed between the FNMT and FNMT2 models, and contrary to expectations, the FNMT2 model showed greater drug loss and consequently less delivered dose. It is hypothesized that throat deposition, which was not considered in Chapter 6, may be greatly increased by smaller values of $d_{h,nasopharynx}$ and may at least partly account for the greater losses observed in the FNMT2

model. Other factors are considered, including the presence of nasal cycling in the FNMT2 model, which may increase nasal cavity drug loss, and average nostril hydraulic diameter ($d_{h,nostril}$).

Table 8.1 Demographic data for the FNMT and FNMT2 models, including age, height, and weight, which were available in 10 year, 5 cm, and 5 kg increments. Both subjects were identified as female.

Model	Age (years)	Height (cm)	Weight (kg)
FNMT	30	180	75
FNMT2	20	170	60

Table 8.2 Geometric measurements of the nasal cavity from the face-nose-mouth-throat (FNMT) and second face-nose-mouth-throat (FNMT2) models. The dimensions tabulated are the surface area-to-volume ratio (SA/V) of the anatomical left and right sides, the average nostril hydraulic diameter ($d_{h,nostril}$), and the nasopharynx exit hydraulic diameter ($d_{h,nasopharynx}$).

	SA/V (mm^{-1})			
Model	**Left**	**Right**	**$d_{h,nostril}$ (mm)**	**$d_{h,nasopharynx}$ (mm)**
FNMT	1.14	1.05	13.00	8.78
FNMT2	0.75	1.33	9.30	4.50

Table 8.3 Dead space volume of mask, nasal valve area, nasal cavity, mouth, nasopharynx, and throat regions of the two face-nose-mouth-throat (FNMT and FNMT2) models. Also included is the volume of Mask Design #2.1, which is nearly the same as for Mask Design #2.2. The nasal cavity is defined as the region between the nasal valve area and the end of the septum. The mouth includes the entire pathway, the nasopharynx terminates above the mouth pathway, and the throat begins where the nasopharynx ends.

	Volume (mL)	
Region	**FNMT**	**FNMT2**
Mask	207.9	157.5
Nostril	7.9	3.3
Nasal Cavity	15.5	14.3
Mouth	7.1	7.8
Nasopharynx	8.4	3.5
Throat	13.7	11.5
Total	260.5	197.9

Table 8.4 Steady state CFD deposition fraction (DF) predictions (given in %) for both conventional and EEG drug delivery to the two face-nose-mouth-throat (FNMT and FNMT2) models with Mask Design #2.1 and an imperfect mask seal (5.2% leak). The conventional aerosol is considered without size change, while the EEG combination particle is considered with size change and is composed of 30:50:20 ciprofloxacin (CP): mannitol (MN): L-leucine. The initial aerodynamic diameters of the conventional and EEG particles are 6.0 μm and 0.9 μm, respectively. Values of DF are reported for the face, mask, and nose-mouth-throat (NMT) regions. Also given is the mask seal loss (MSL), given in %, of drug exiting through the mask seal.

		Deposition Fraction (DF)			
		Mask	**Face**	**NMT**	**Mask Seal Loss (MSL)**
Conventional	**FNMT**	0.4	0.6	27.7	2.4
	FNMT2	3.8	7.1	60.5	15.9
EEG	**FNMT**	0.1	0.2	2.0	2.6
	FNMT2	1.1	0.7	8.4	12.9

Table 8.5 Steady state CFD penetration fraction (PF) predictions (given in %) for both conventional and EEG drug delivery to the two face-nose-mouth-throat (FNMT and FNMT2) models with Mask Design #2.1 and an imperfect mask seal (5.2% leak). Also given are the throat outlet mass median aerodynamic diameter (MMAD) due to EEG size increase and the average residence time of injected particles exiting the throat. Outlet MMAD is identical to initial aerodynamic diameter for the conventional cases since size change is assumed to be negligible for those predictions.

		Penetration Fraction (PF)	Outlet MMAD (μm)	Average Residence Time (s)
Conventional	**FNMT**	62.8	6.00	0.24
	FNMT2	8.1	6.00	0.50
EEG	**FNMT**	90.3	2.81	0.22
	FNMT2	70.1	2.60	0.42

Table 8.6 Steady state CFD deposition fraction (DF) predictions (given in %) for both conventional and EEG drug delivery to the two face-nose-mouth-throat (FNMT and FNMT2) models with Mask Design #2.2 and an imperfect mask seal (5.2% leak). The conventional aerosol is considered without size change, while the EEG combination particle is considered with size change and is composed of 30:50:20 ciprofloxacin (CP): mannitol (MN): L-leucine. The initial aerodynamic diameters of the conventional and EEG particles are 6.0 μm and 0.9 μm, respectively. Values of DF are reported for the face, mask, and nose-mouth-throat (NMT) regions. Also given is the mask seal loss (MSL), given in %, of drug exiting through the mask seal.

		Deposition Fraction (DF)			
		Mask	**Face**	**NMT**	**Mask Seal Loss (MSL)**
Conventional	**FNMT**	0.7	1.1	25.4	4.8
	FNMT2	1.7	1.4	73.0	5.9
EEG	**FNMT**	0.2	0.2	4.3	4.9
	FNMT2	0.4	0.4	15.9	5.9

Table 8.7 Steady state CFD penetration fraction (PF) predictions (given in %) for both conventional and EEG drug delivery to the two face-nose-mouth-throat (FNMT and FNMT2) models with Mask Design #2.2 and an imperfect mask seal (5.2% leak). Also given are the throat outlet mass median aerodynamic diameter (MMAD) due to EEG size increase and the average residence time of injected particles exiting the throat. Outlet MMAD is identical to initial aerodynamic diameter for the conventional cases since size change is assumed to be negligible for those predictions.

		Penetration Fraction (PF)	Outlet MMAD (μm)	Average Residence Time (s)
Conventional	**FNMT**	59.0	6.00	0.34
	FNMT2	13.6	6.00	0.31
EEG	**FNMT**	84.6	2.91	0.32
	FNMT2	71.8	2.86	0.28

Table 8.8 Steady state CFD deposition fraction (DF) predictions (given in %) for both conventional and EEG drug delivery to the two face-nose-mouth-throat (FNMT and FNMT2) models with Mask Design #2.2 and a perfect mask seal. The conventional aerosol is considered without size change, while the EEG combination particle is considered with size change and is composed of 30:50:20 ciprofloxacin (CP): mannitol (MN): L-leucine. The initial aerodynamic diameters of the conventional and EEG particles are 6.0 μm and 0.9 μm, respectively. Values of DF are reported for the face, mask, and nose-mouth-throat (NMT) regions.

		Deposition Fraction (DF)		
		Mask	**Face**	**NMT**
Conventional	**FNMT**	0.6	0.9	30.3
	FNMT2	1.1	1.3	81.5
EEG	**FNMT**	0.1	0.2	5.1
	FNMT2	0.2	0.4	18.3

Table 8.9 Steady state CFD penetration fraction (PF) predictions (given in %) for both conventional and EEG drug delivery to the two face-nose-mouth-throat (FNMT and FNMT2) models with Mask Design #2.2 and a perfect mask seal. Also given are the throat outlet mass median aerodynamic diameter (MMAD) due to EEG size increase and the average residence time of injected particles exiting the throat. Outlet MMAD is identical to initial aerodynamic diameter for the conventional cases since size change is assumed to be negligible for those predictions.

		Penetration Fraction (PF)	Outlet MMAD (μm)	Average Residence Time (s)
Conventional	**FNMT**	59.0	6.00	0.34
	FNMT2	11.6	6.00	0.32
EEG	**FNMT**	88.9	2.90	0.33
	FNMT2	74.7	2.85	0.27

Table 8.10 Steady state CFD deposition fraction (DF) predictions (given in %) of nasal valve area, nasal cavity, nasopharynx, and throat regions of nose-mouth-throat (NMT) for both conventional and EEG drug delivery to the two face-nose-mouth-throat (FNMT and FNMT2) models with Mask Design #2.2 and an imperfect mask seal (5.2% leak). Also shown is the deposition efficiency (DE) of the total nasal region including the nasal valve area, nasal cavity, and nasopharynx.

		Deposition Fraction (DF)				Deposition Efficiency (DE)
		Nasal Valve Area	**Nasal Cavity**	**Nasopharynx**	**Throat**	**Total Nasal**
Conventional	**FNMT**	1.1	12.0	1.7	10.6	15.8
	FNMT2	8.3	10.1	21.8	32.9	44.2
EEG	**FNMT**	0.2	2.1	0.1	1.9	2.5
	FNMT2	1.0	2.4	0.6	11.9	4.3

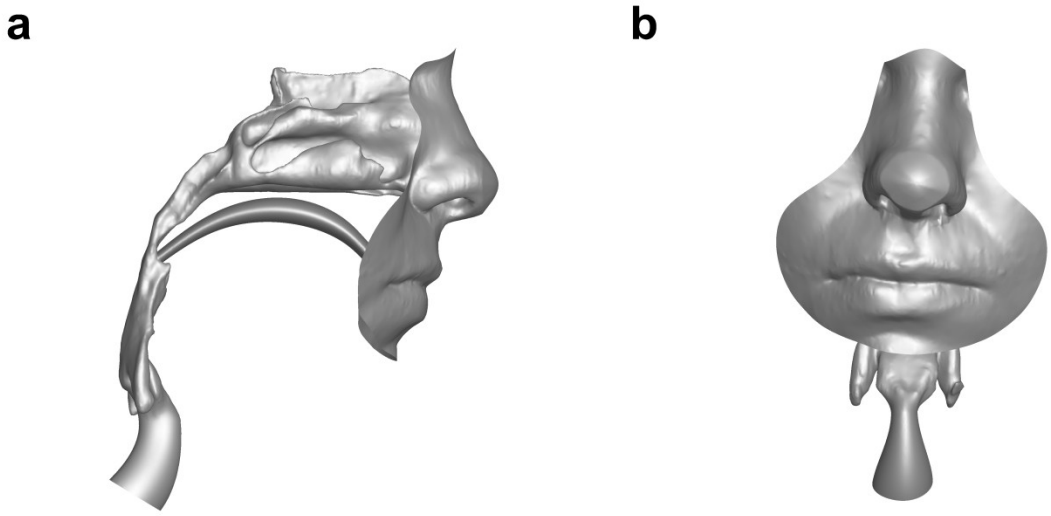

Figure 8.1 Surfaces of the face and interior airway of the second face-nose-mouth-throat (FNMT2) model, shown in (a) side view and (b) front view. The numerical extension is omitted from both views.

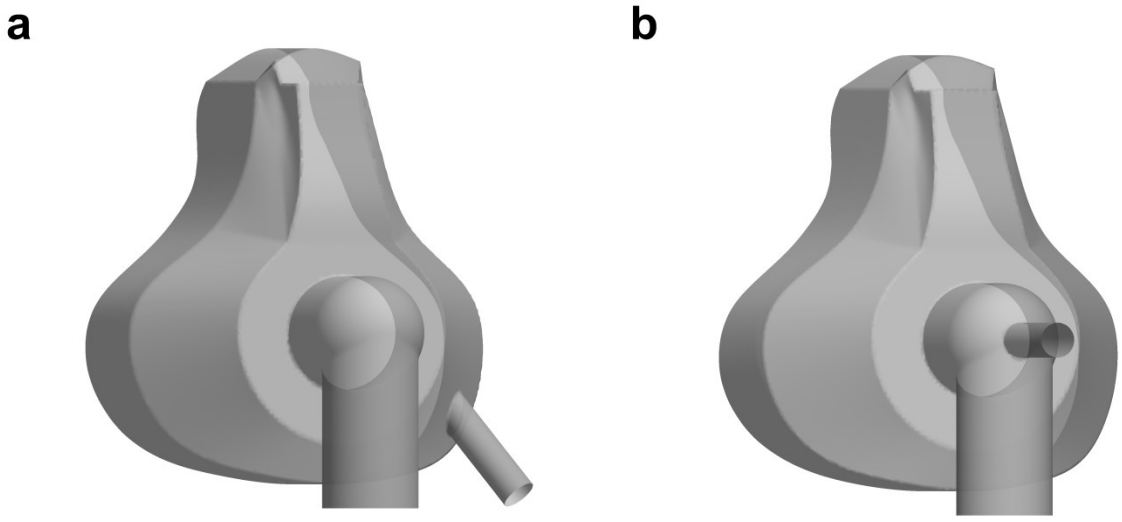

Figure 8.2 Two mask designs tested for dry powder delivery using steady state CFD simulations, both based on the commercially available PerformaTrak® SE mask (Philips Respironics, Inc.). The initial commercial design is altered to include an 8 mm inlet (a) directed at the left nostril (Mask Design #2.1) and (b) directed into the ventilation exchange elbow (Mask Design #2.2).

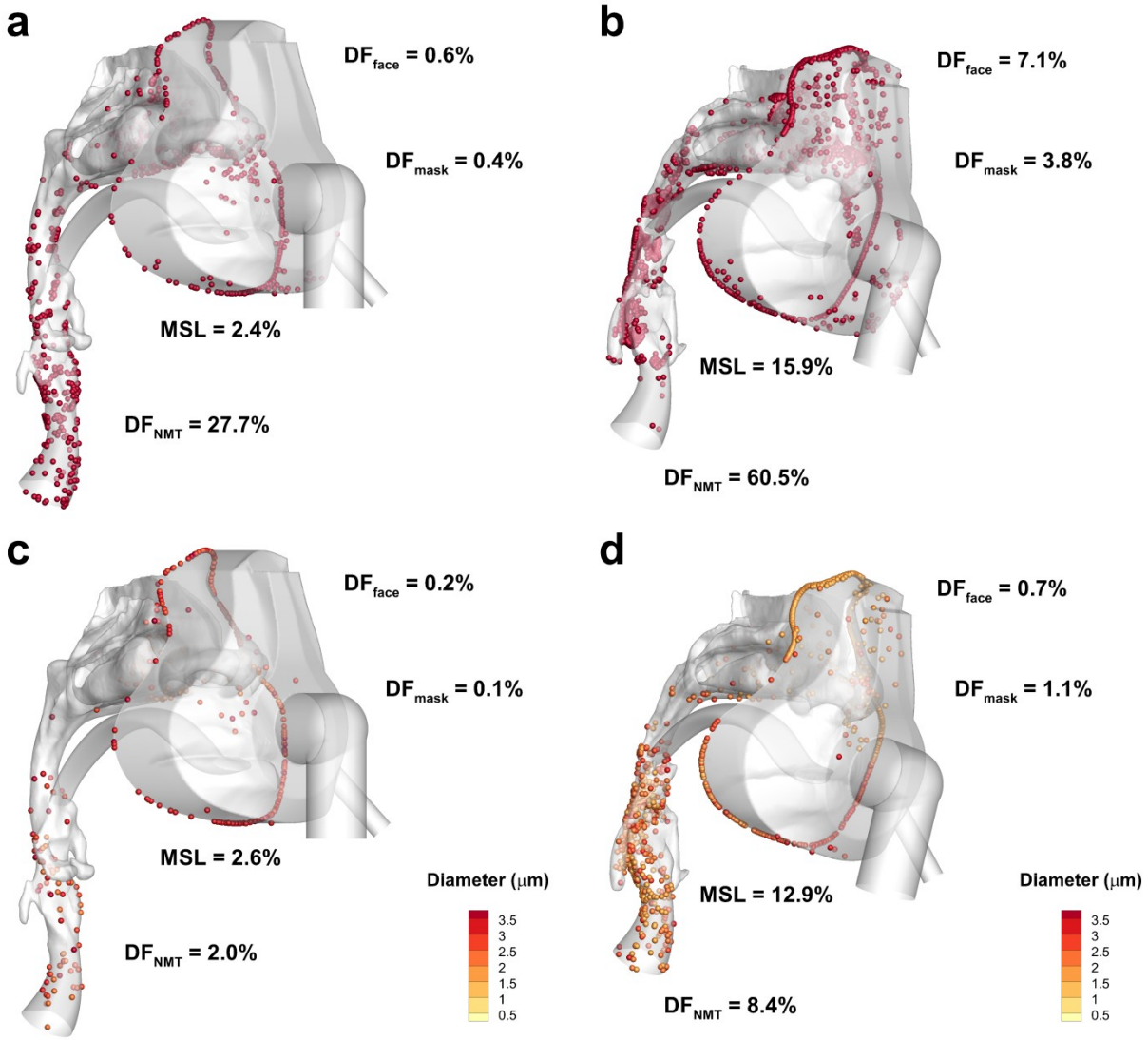

Figure 8.3 Steady state CFD simulations of 30 L/min flow through Mask Design #2.1 and a 5.2% leak through the mask seal. Results are given for conventional aerosol delivery to (a) the face-nose-mouth-throat (FNMT) and (b) the second face-nose-mouth-throat (FNMT2) models, and for EEG drug delivery with ciprofloxacin (CP): mannitol (MN): L-leucine (LC) combination particles to the (c) FNMT and (d) FNMT2 models.

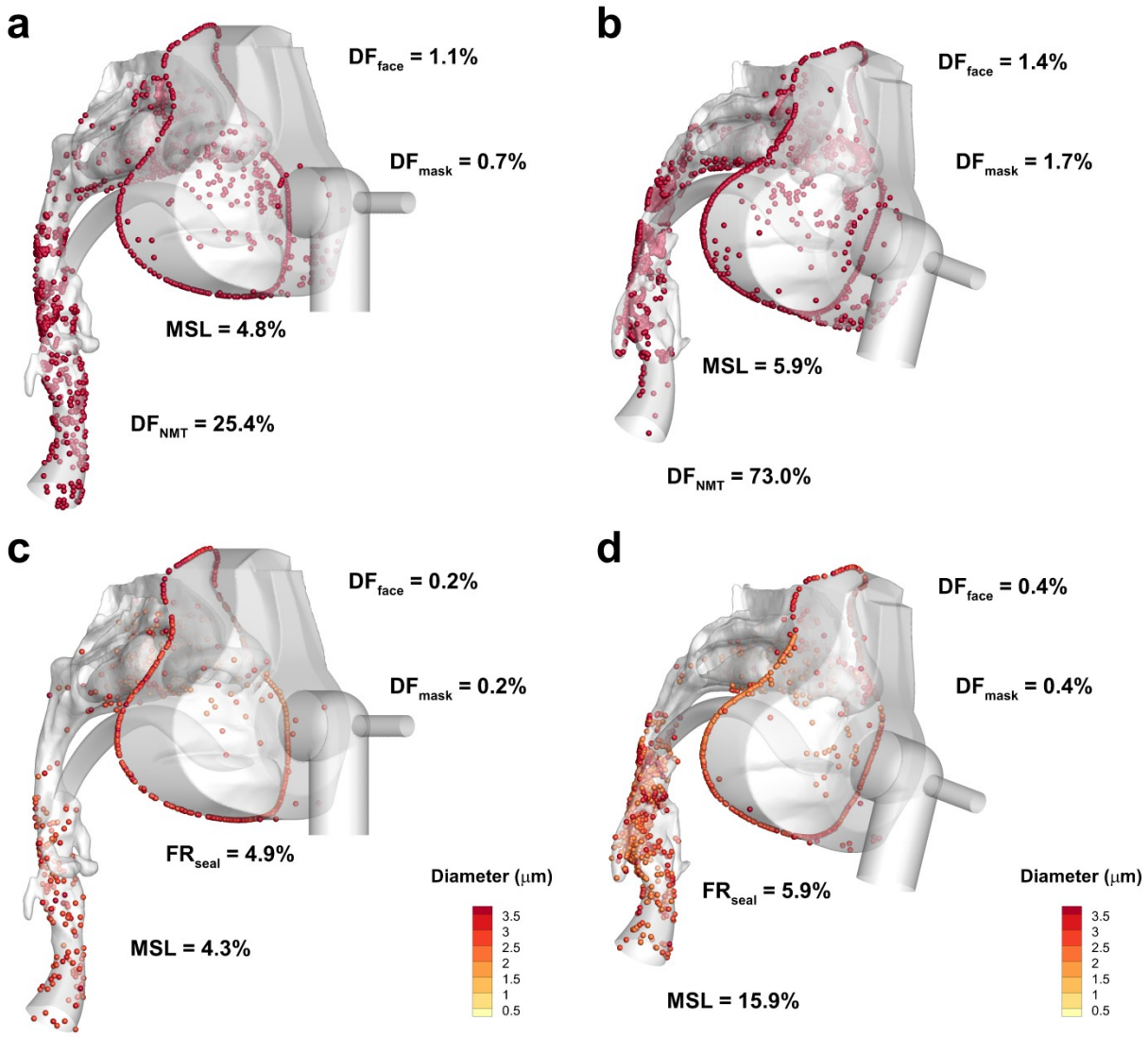

Figure 8.4 Steady state CFD simulations of 30 L/min flow through Mask Design #2.2 and a 5.2% leak through the mask seal. Results are given for conventional aerosol delivery to (a) the face-nose-mouth-throat (FNMT) and (b) the second face-nose-mouth-throat (FNMT2) models, and for EEG drug delivery with ciprofloxacin (CP): mannitol (MN): L-leucine (LC) combination particles to the (c) FNMT and (d) FNMT2 models.

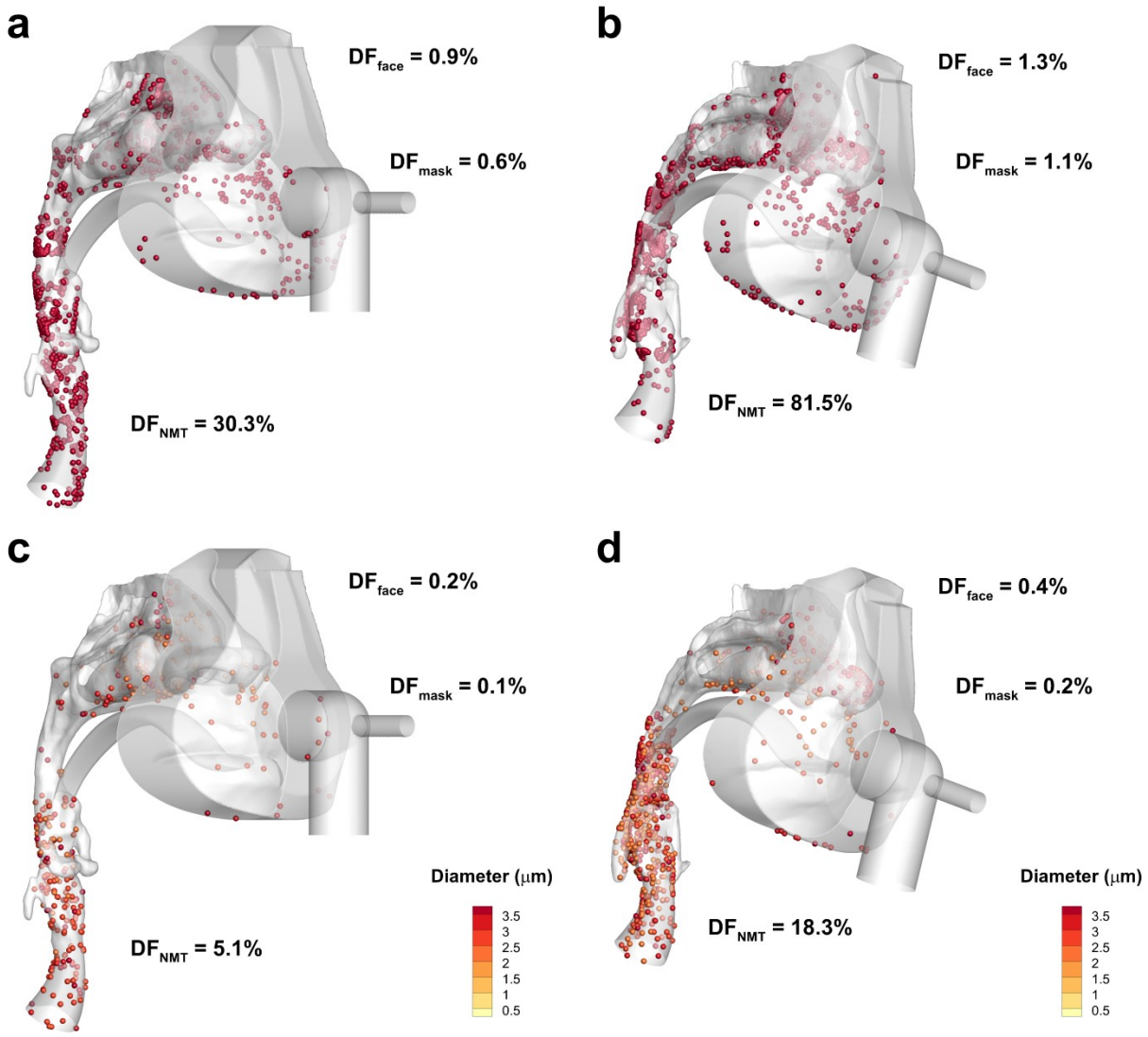

Figure 8.5 Steady state CFD simulations of 30 L/min flow through Mask Design #2.2 and a perfect mask seal. Results are given for conventional aerosol delivery to (a) the face-nose-mouth-throat (FNMT) and (b) the second face-nose-mouth-throat (FNMT2) models, and for EEG drug delivery with ciprofloxacin (CP): mannitol (MN): L-leucine (LC) combination particles to the (c) FNMT and (d) FNMT2 models.

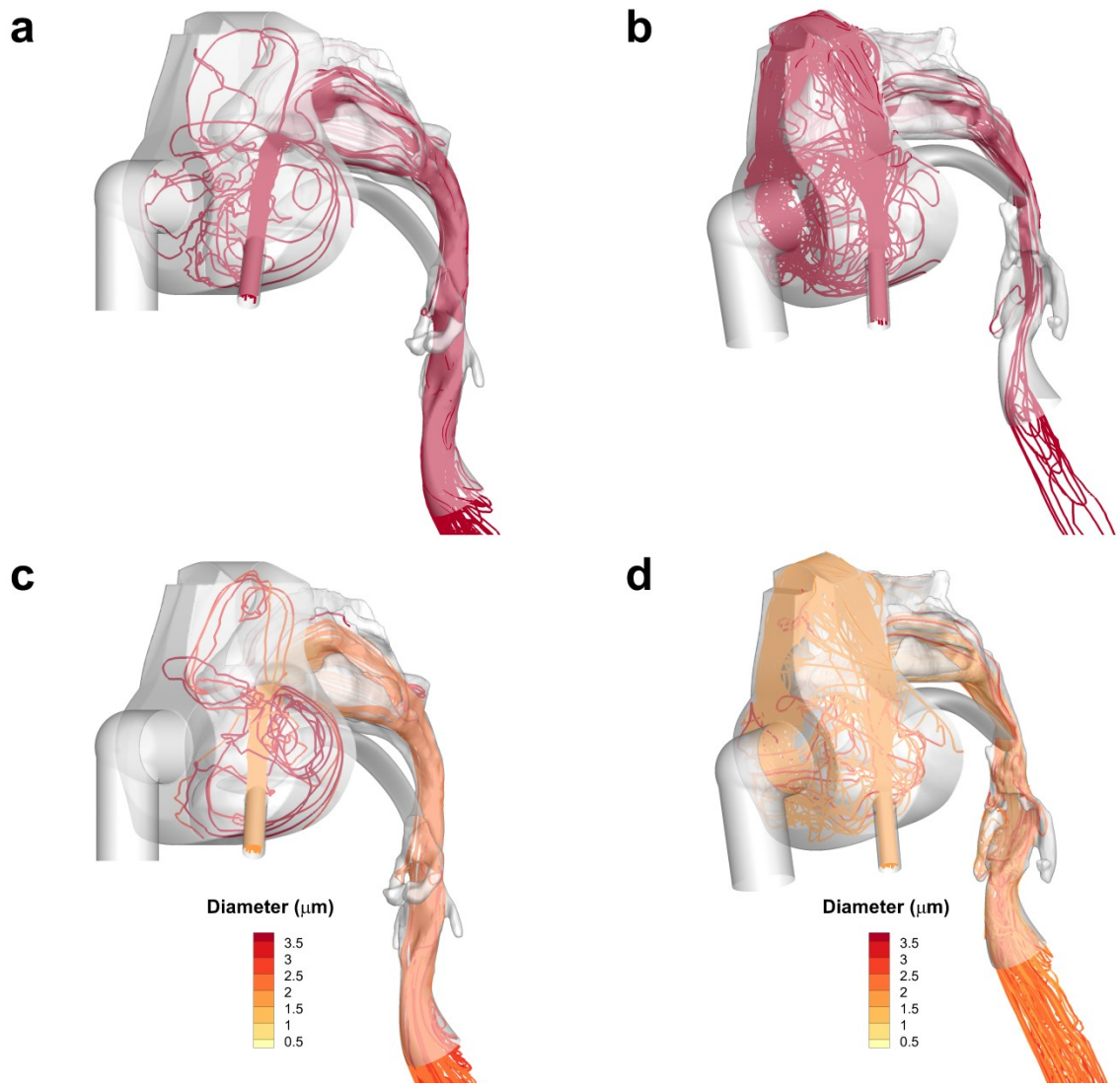

Figure 8.6 Particle trajectories through Mask Design #2.1 with a 5.2% mask seal leak for the conventionally sized 6 μm aerosol the (a and b) FNMT and FNMT2 models and for the EEG formulation through the (c and d) FNMT and FNMT2 models. Growth and evaporation is shown for the EEG particles that have an initial aerodynamic diameter of 0.9 μm. The conventionally sized aerosol was considered without size change.

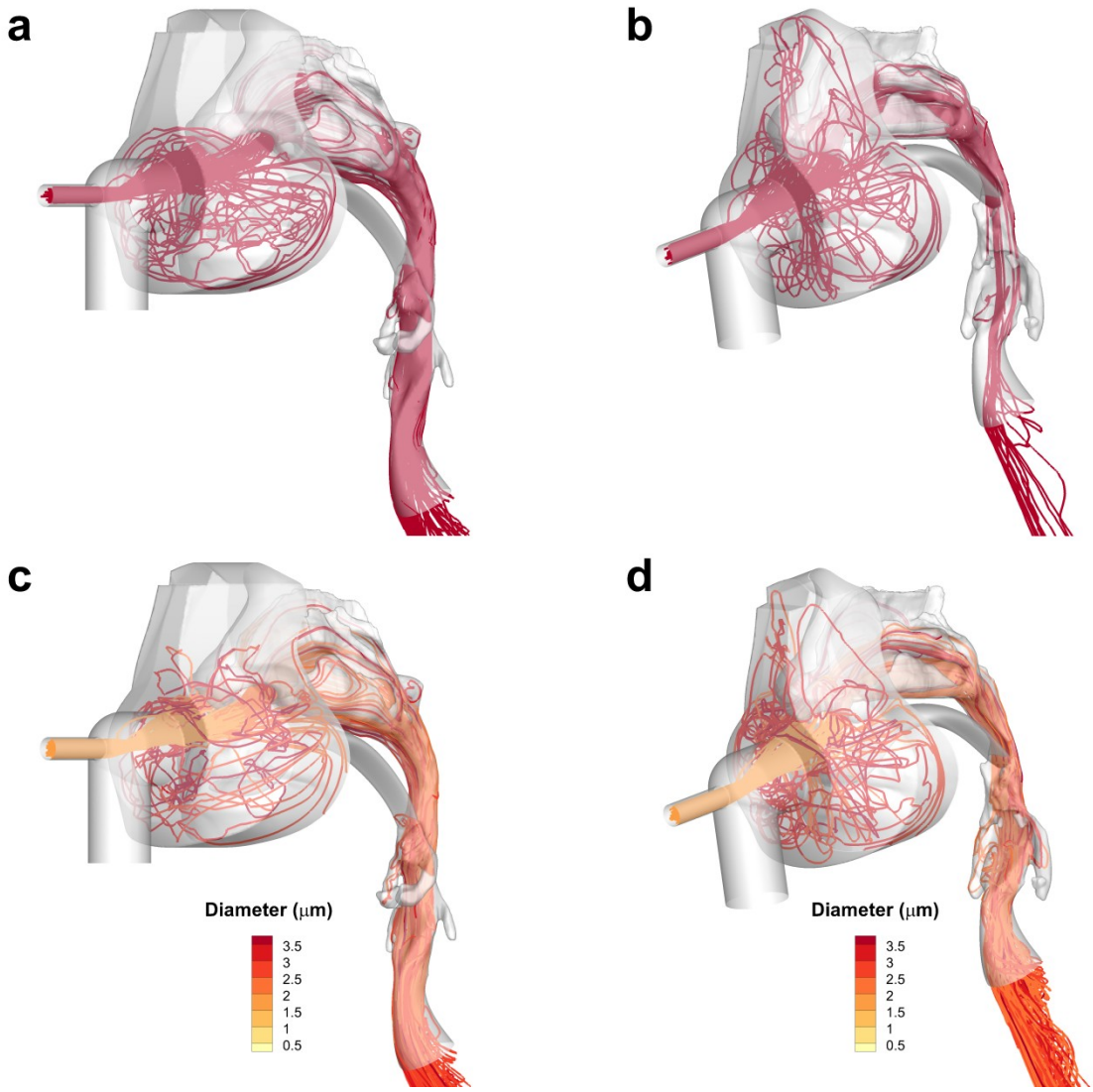

Figure 8.7 Particle trajectories through Mask Design #2.2 with a 5.2% mask seal leak for the conventionally sized 6 μm aerosol the (a and b) FNMT and FNMT2 models and for the EEG formulation through the (c and d) FNMT and FNMT2 models. Growth and evaporation is shown for the EEG particles that have an initial aerodynamic diameter of 0.9 μm. The conventionally sized aerosol was considered without size change.

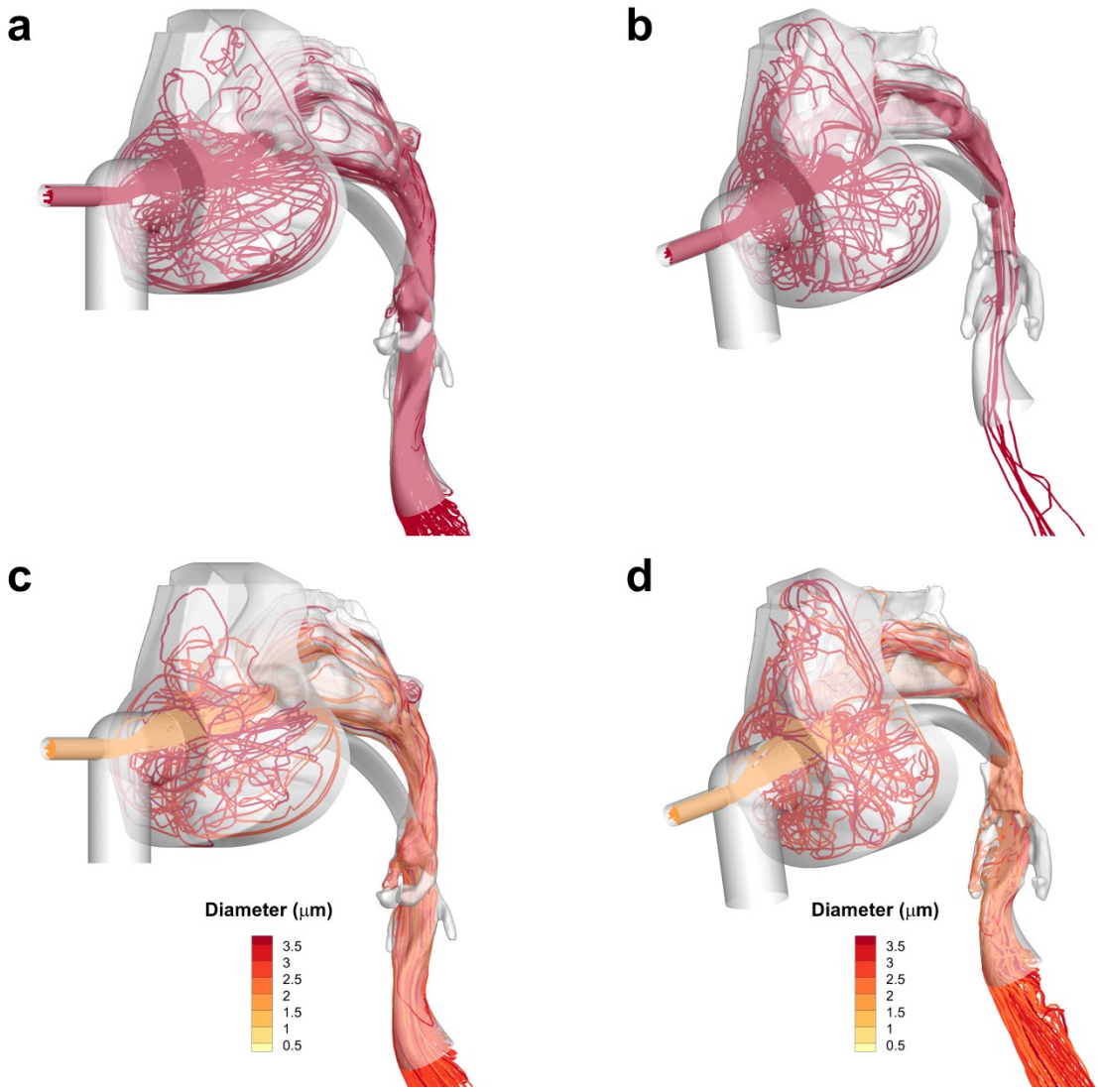

Figure 8.8 Particle trajectories through Mask Design #2.2 with perfect mask seal for the conventionally sized 6 μm aerosol the (a and b) FNMT and FNMT2 models and for the EEG formulation through the (c and d) FNMT and FNMT2 models. Growth and evaporation is shown for the EEG particles that have an initial aerodynamic diameter of 0.9 μm. The conventionally sized aerosol was considered without size change.

Chapter 9 Conclusions and Future Work

The specific aims outlined in Chapter 1 described three objectives, all of which have been accomplished for this dissertation. In summary: (1.1) a characteristic upper tracheobronchial (TB) airway model (Model D) was developed based on average anatomical dimensions of an adult male as indicated by collected computed tomography (CT) scan data; (1.2) four nasal models were constructed based on collected CT scan data and selected to cover the measured range of surface-area-to-volume ratio (SA/V) values; (1.3) a literature review of noninvasive ventilation (NIV) interfaces for aerosol delivery was performed and new mask designs were introduced for nebulized and dry powder aerosol delivery during NPPV; (2.1) CFD simulation methods were validated for metered dose inhaler (MDI) and dry powder inhaler (DPI) delivery through a characteristic TB airway model (Model C) and then applied to compare regional deposition fraction (DF) in Model C and Model D; (2.2) a stochastic individual pathway (SIP) modeling approach was used to evaluate the effect of asthma constriction on Model C from the mouth-throat (MT) region to the fifteenth bifurcation (B15); (3.1) an aerosol conditioning device was constructed, tested, and optimized for use with enhanced condensational growth (ECG) or excipient enhanced growth (EEG) drug delivery; (3.2) the four models developed for Task 1.2 were used to evaluate delivered dose of conventional and EEG drug formulations during high flow therapy (HFT) through a nasal cannula; (3.3) a new face-nose-mouth-throat (FNMT) model was used for CFD simulations and for *in vitro* testing by Dr. Michael Hindle and colleagues,

which integrated the EEG delivery method into a noninvasive positive pressure ventilation (NPPV) system with an oronasal mask and showed significant improvement in aerosolized drug delivery; (3.4) steady state CFD simulations with two face-nose-mouth-throat (FNMT and FNMT2) models and with two new oronasal mask designs showed that EEG drug delivery greatly improved drug delivery of a dry powder aerosol during NPPV as opposed to a conventionally sized droplet; (3.5) intersubject variability of dry powder EEG drug delivery through a mask interface was assessed with the two new face-nose-mouth-throat models. Conclusions from these studies are summarized below in greater detail, and areas of future study are identified.

9.1 Objective 1: Airway and Mask Model Development

Characteristic anatomical models include realistic features relevant to the variable of interest while omitting unnecessary features to improve manufacturability and computational efficiency. To create a new characteristic upper airway tracheobronchial (TB) model, a collection of computed tomography (CT) scan data was compiled (n = 21) from reported upper TB airway dimensions in the literature and from measurements of scans obtained from VCU Medical Center, which identified ranges of parameters that were intended to represent a population of adults, including tracheal diameter, left and right main bronchial lengths, and left and right main bronchial diameters. From available CT scan data sets, a scan was selected with airway dimensions within or nearly within two standard deviations of the mean of the selected parameters. Since the subject of the selected average scan was an adult male and the dimensions were near the upper ends of the ranges of values, it was interpreted as an average adult male TB model. The new TB model, titled Model D, was created using CAD software and converted into

a hexahedral computational mesh. Model D features added anatomical realism as compared with Model C, particularly with curvature in the trachea that accounts for the presence of the aorta, irregular cross sections, curvature in the main bronchi, and an accurate tracheal gravity angle. It has been used in several other CFD and *in vitro* studies from our group since its creation (Longest, et al., 2014b; Longest & Tian, 2014; Tian *et al.*, 2014). One future direction for characteristic upper TB model development may include the creation of new geometries that represent other segments of the population. In particular, infant and pediatric drug delivery is of interest due to the significantly smaller average anatomical dimensions and lower drug delivery efficiency to younger as opposed to older patients. To this end, further collection of a data set representing upper airway dimensions of infants and children would be useful. Adult female and geriatric TB models would be helpful as well for understanding differences in those population groups. Another research direction involves the creation of stochastic individual path (SIP) models with greater realism as opposed to the existing geometries, which are idealized extensions of Model C constructed of physically realistic bifurcation (PRB) units as defined by Heistracher and Hofmann (1995). These new models would include irregular cross sections and curvature, features that are absent in the PRB units of the existing SIP models, and the effects of these realistic characteristics on branch-averaged deposition efficiency (DE) are unknown.

Four nasal models were created with the guidance of a compiled CT scan data set (n = 66) of surface-area-to-volume ratio (SA/V) measurements to represent 84% of the theoretical variation of a normal distribution, with values between 0.74-1.42 mm^{-1}. The models included nostrils, the nasal cavity, and the nasopharynx, but did not include a throat because not all CT scans included that region. Three of the models were built from collected scans, and one was selected from a previously existing study (Xi & Longest, 2008b). The models were used for

Task 3.2 to assess intersubject variability of nasal deposition during nose-to-lung excipient enhanced growth (EEG) aerosol delivery through a nasal cannula. However, the results of Chapters 7 and 8 indicated that the throat region may be important for a more complete understanding of intersubject variability as it relates to EEG drug delivery. Also, some of the measurements taken for the four models ($d_{h,nasopharynx}$, $d_{h,nostril}$) were not tabulated in the full data set and may be important parameters for future study. This issue may be addressed by expanding the current data set to include these measurements, and by the collection of more CT scans that include the throat region. It may be useful to characterize geometric features of the throat as well. Beyond this, it would be helpful to understand how anatomical dimensions relevant to drug deposition change dynamically, and how these dynamic changes may be incorporated into CFD or *in vitro* testing.

Existing interfaces for NIV delivery to patients with respiratory insufficiency were reviewed in Section 2.1.3, with a particular emphasis on the relationship between interface type and pharmaceutical aerosol delivery. A nasal cannula is the typical interface for high flow therapy (HFT) delivery, while noninvasive positive pressure ventilation (NPPV) utilizes a range of different interfaces, including helmets, nasal pillows, mouthpieces, and facial, nasal, and oronasal masks, all of which may be paired with aerosol administration. Low amounts of emitted dose through a nasal cannula for low flow therapy (LFT) with a conventional aerosol have been reported (Ari, et al., 2011; Bhashyam, et al., 2008), with measured values in the range of approximately 10-25%. However, a new streamlined nasal cannula developed by Longest et al. (2013a) showed emitted dose of 40% and higher for a conventionally sized aerosol during HFT, which implements flow rates of ~30 L/min and consequently is expected to decrease delivered dose during HFT as compared with LFT. This nasal cannula was adopted for further

study in the nasal variability study of Chapter 6 for the completion of Task 3.2. Aerosol delivery through a mask during NPPV has not been well characterized with *in vivo* data, but one study indicated 1-7% delivery to asthmatic adults receiving continuous positive airway pressure (CPAP) (Parkes & Bersten, 1997), and *in vitro* studies have indicated low delivery as well (Branconnier & Hess, 2005; Chatmongkolchart, et al., 2002; Dai, et al., 2013; White, et al., 2013). Several new mask designs were introduced for the completion of Task 3.3, which utilized a separate aerosol inlet for EEG drug delivery during NPPV and used the commercially available PerformaTrak SE® oronasal mask (Philips Respironics, Inc., Pittsburgh, PA, USA) as a basis. These mask designs did not produce the expected increase in delivery efficiency when tested with *in vitro* experiments by Dr. Michael Hindle and colleagues in the VCU Department of Pharmaceutics, since it was discovered that the most effective placement of the aerosol delivery device, the transient mixer-heater, required that the aerosol enter through the ventilation inlet. However, the idea of a separate aerosol inlet was re-introduced for steady state CFD predictions of dry powder EEG drug delivery during NPPV for the completion of Task 3.4, and the early CFD results are promising. As with the previous mask designs though, these results will be assessed with future *in vitro* experiments to better understand their performance within the context of the system. Further research in the design of masks for EEG drug delivery during NPPV may focus on the continued optimization of the aerosol inlet with respect to placement and size. Other aspects of the mask design, such as mask seal, dead space volume, and ventilation inlet size and placement, have been unexplored as of yet by our group. However, it would be useful for future study to better understand these effects, particularly as they relate to aerosol delivery, with the aim of eventually creating a fully optimized and entirely original design. In particular, future designs will seek to minimize dead space volume in the mask with

the objective of reducing aerosolized drug loss due to transient effects. Specifically, minimizing dead space volume reduces the distance that the aerosol is required to travel during inhalation, which lessens the amount of drug lost during exhalation.

9.2 Objective 2: CFD Assessment of MDI and DPI Delivery

A comparison of metered dose inhaler (MDI) and dry powder inhaler (DPI) drug delivery through upper airway TB models using CFD was performed using the pre-existing Model C and the newly created Model D. The primary function of these predictions was to evaluate both geometries as potential characteristic upper airway TB models. CFD methods, which included the simulation of polydisperse particle MDI and DPI distributions in a transient flow field, were validated with existing *in vitro* data. The total upper airway deposition was similar for both models, but the additional realistic anatomical features of Model D produced different regional and local estimates. These results led to the conclusion that while both models may be considered characteristic for total deposition of MDI and DPI drug delivery to the mouth-throat (MT) through the third bifurcation (B3), but only Model D may be considered characteristic for regional and local deposition. Since Model C and Model D were based on average adult male dimensions, those models should only be considered characteristic for that specific population segment. As mentioned in Section 3.4, future research with Model D will seek to compare Model D results with existing *in vivo* data that includes central lung to peripheral lung deposition, expressed as a C/P ratio (Newman, et al., 2000), as well as *in vivo* data that is now becoming available in the literature on a branch-averaged DE basis (Conway, et al., 2012; Majoral, et al., 2014). Additionally, as proposed in Section 9.1, new models based on other

segments of the population may be created which would require CFD or other data to confirm the characteristic nature of the new geometries.

The effects of asthma constriction on upper airway TB regional deposition fraction (DF) and lower airway TB branch-averaged DE measurements of MDI and DPI delivered drug were assessed using CFD methods. Model C was chosen to represent the upper airways because Model D was not yet available when the study commenced. The lower airways were represented by five previously existing SIP models (Tian, et al., 2011b). To create asthma constricted counterparts to the existing healthy models, a 30% diameter reduction was applied to the TB airways, based on the canine *in vivo* data of Brown and Mitzner (2003). A primary challenge of the study was the extrapolation of transient flow field data in Model C to steady state simulation boundary conditions in the SIP models, and to handle this difficulty previously existing near-wall turbulence and fluid velocity user-defined routines were updated to allow for mesh-independent application. Comparison of the relative differences in branch-averaged DE with those measured by application of a previously existing correlation (Chan & Lippmann, 1980) showed good agreement, which gave confidence that the CFD methods used for this study were sound. For both MDI and DPI predictions, DF values in the TB region were increased by a factor of two for the asthma constricted airways as compared with the healthy models. Considering DF values in the small lower airways (B8-B15), the delivered dose was reduced from the healthy to the asthmatic airways by 0.24% and 0.27% for MDI and DPI delivery, respectively. Comparison of asthma constricted model results with newly available *in vivo* data (Majoral, et al., 2014) would be a useful topic for further study. As mentioned in Section 4.4, adjustment of interpolated flow rate from the transient Model C to the steady state SIP models may be a factor to consider for any validation with *in vivo* data. Also, future research may include CFD simulations or *in vitro*

experiments to evaluate a constricted version of Model D in comparison with the existing healthy version as a means for enhancing branch-averaged DE predictions in the trachea through B3.

9.3 Objective 3: Improved Aerosol Delivery during NIV

To facilitate *in vitro* experiments for enhanced condensational growth (ECG) and EEG drug delivery, a device that heats and dries nebulized droplets to a submicrometer size was constructed, tested, and optimized using the computational design of Longest et al. (2013c). The first version of the mixer-heater system was built for steady state operation, and testing of the optimized system showed delivery of particles that were in the submicrometer range, as measured by Dr. Michael Hindle and colleagues in the VCU Department of Pharmaceutics, and outlet flow heated to an acceptable temperature (35°C) for inhalation. A transient mixer-heater was constructed as well, which utilized blowers controlled by a waveform generator and an amplifier to deliver flow with an approximately sinusoidal profile and a 4 s period. Other studies showed both systems to be capable of high values of emitted dose, with the steady state mixer-heater producing a measured increase by a factor of three as compared with an existing radial design (Longest, et al., 2013c), and the transient version showing 96.9% stand-alone delivery of 0.2% AS: 0.2% NaCl in water (Golshahi, et al., 2014b). Regarding future development, the transient mixer-heater has been altered to enhance streamlining of the outlet, and to accommodate connecting tubing with a smaller diameter. The aim of this modification is to reduce dead space volume for the transient NPPV system with the expected outcome of improving delivered dose. Future *in vitro* trials will be conducted to assess the effect of these improvements. Another area for development is the adaptation of the stand-alone version of the

transient mixer-heater for synchronization with a real patient's variable breathing patterns, since the current version only responds to a pre-determined waveform.

The four nasal models selected for Task 1.2 to cover the range of SA/V values based on the collected data set were used to assess conventional and EEG delivery of albuterol sulfate (AS) during HFT through the streamlined nasal cannula developed by Longest et al. (2013a). Using a steady state CFD method as a basis for comparison, results showed average total loss in the nasal region and device for conventional delivery of an initially sized 5 μm aerosol of about 80%, while for EEG delivery only about 20% of the initially sized 0.9 μm particle was lost. It was also noted that when tracheal inhalation flow rate was higher than device delivered flow rate the EEG delivered dose, as expressed by penetration fraction (PF), was increased to 90%. Variability expressed as coefficient of variation (CV) was reduced from 15% to 3-4% for the EEG technique as compared with the conventional method. A strong correlation between PF and SA/V was found for conventional delivery of AS, but not for EEG delivery. However, a weak correlation between PF and nasopharynx exit hydraulic diameter ($d_{h,nasopharynx}$) was noted for the EEG method. Further study may include transient CFD predictions using a realistic inhalation waveform or *in vitro* experiments to obtain a more accurate measurement of delivered dose with the EEG method. Additionally, a better understanding of intersubject variability of EEG delivered aerosols through a nasal cannula may be sought, since only a weak correlation between PF and $d_{h,nasopharynx}$ was observed. As observed in Chapter 8 for dry powder EEG delivery through a mask during NPPV, throat deposition played an important role in variability, and that may be true for nasal cannula delivery as well. It would be useful to further develop the existing four models to include throat regions. Also, the expansion of the data set to include a full range of $d_{h,nasopharynx}$ and $d_{h,nostril}$ values would be useful to explore the effect of those dimensions on PF.

Conventional and EEG delivery of nebulized albuterol sulfate (AS) during NPPV was considered using CFD and experimental *in vitro* methods with a newly created face-nose-mouth-throat (FNMT) model. The CT scan data used to create the Constricted2 model for the completion of Task 1.2 was used to develop the FNMT model, with some modifications to the septum to allow for *in vitro* model construction with rapid prototyping. As described above in Section 9.1, four new mask designs for EEG drug delivery were introduced, that implemented an aerosol inlet separate from the ventilation flow source and used the commercially available PerformaTrak SE® oronasal mask (Philips Respironics, Inc., Pittsburgh, PA, USA) as a basis. A critical care ventilator was used with an adult test lung by Dr. Michael Hindle and colleagues in the VCU Department of Pharmaceutics to evaluate conventional and EEG delivery of AS during NPPV. Initial *in vitro* testing of EEG delivery during NPPV revealed that the previously developed transient mixer-heater (Golshahi, et al., 2014b), which was used to generate the EEG submicrometer aerosol, was optimally located in-line with the inspiratory limb of the ventilation dual-limb circuit, which eliminated the usefulness of a separate aerosol inlet. This discovery led to the adoption of the commercial mask for use with EEG delivery rather than any of the four new masks. The adult test lung was set to 1 s or 2 s of inhalation for both delivery methods, and *in vitro* data indicated that delivered dose to an inspiratory filter immediately downstream of the FNMT model increased twofold for EEG delivery as compared with the conventional method. The system was then modeled using transient CFD predictions, which simulated condensational growth during EEG delivery and resulted in significant growth of the initially submicrometer aerosol. As mentioned in Section 7.4, modifications to the transient mixer-heater have been made to enhance streamlining and reduce device dead space volume. Dr. Michael Hindle and colleagues in the VCU Department of Pharmaceutics are currently conducting experiments to

evaluate the performance of the new transient mixer-heater with NPPV, which will potentially increase the currently demonstrated EEG delivered dose of 27.1% and 39.3% with 1 s and 2 s test lung inhalation. Another future direction for EEG delivery of a nebulized aerosol during NPPV may be the assessment of intersubject variability, which is evaluated for a dry powder EEG aerosol in Chapter 8. Additionally, delivery of other drug:excipient combinations with the system are currently uncharacterized and may vary substantially from the recently acquired results for 50:50 AS:NaCl. It would also be desirable to assess the performance of any new masks which may be designed to optimize dead space volume, ventilation inlet placement and size, and mask seal, as described in Section 9.1.

Steady state CFD simulations were used to evaluate EEG delivery during NPPV of a dry powder formulation introduced by Longest et al. (2014b) and Son et al. (2013a) that includes the antibiotic ciprofloxacin (CP), which was compared with CFD predictions of a conventionally sized aerosol in the same system. Aerosol transport and deposition for both delivery methods were modeled using the previously existing FNMT model and a newly created face-nose-mouth-throat (FNMT2) model. The concept of a separate aerosol inlet was revisited for dry powder delivery during NPPV with the creation of two mask designs that use the PerformaTrak SE® oronasal mask as their basis. The effects of an imperfect mask seal were not considered previously for nebulized aerosol delivery during NPPV, but were included here and modeled as 5.2% volumetric leak based on the study of Schettino et al. (2001). Steady state CFD results indicated that average delivered dose through four mask-model combinations, expressed as PF, was increased twofold for EEG delivery as compared with the conventional method. For the mask identified as the higher performing interface, which included an aerosol inlet in the ventilation exchange elbow, variability of DF on the face and mask and of fraction remaining

(FR) through the mask seal were greatly reduced as compared with the other mask design. The imperfect mask seal was predicted to lose about 5% of the nominal dose for both delivery methods through the higher performance mask. Regarding the future of this research, these initial CFD results will be tested by Dr. Michael Hindle and colleagues in the VCU Department of Pharmaceutics using experimental methods with rapid prototyped versions of the FNMT model and perhaps the FNMT2 model. Unlike the experiments for nebulized aerosol delivery during NPPV, modified versions the actual commercial masks are recommended rather than rapid prototyped masks, to aid with the assessment of imperfect mask sealing effects on drug delivery. Initial testing has revealed that some backflow occurs in the aerosol delivery line, which impedes DPI capsule emptying. This difficulty will be addressed through the course of *in vitro* testing. Similar to the methods used in Chapter 7, transient CFD predictions may be performed after *in vitro* testing to assess condensational growth.

Intersubject variability of dry powder drug delivery during NPPV was assessed using the steady state CFD results described above. The CT scan data for the FNMT2 model was selected because of its small measured value of $d_{h,nasopharynx}$, but it was not controlled for other anatomical dimensions, including SA/V. It was expected that the FNMT2 model might have higher values of PF for EEG delivery as compared with the FNMT model, due to the inverse correlation noted in Chapter 6 between PF and $d_{h,nasopharynx}$ for EEG delivery during HFT. However, CFD results indicated PF values that were increased to 84.6% and 59.0% for EEG and conventional drug delivery for the FNMT model as compared with 71.8% and 13.6% for the FNMT2 model. The primary hypothesis for this departure from expected results was that throat deposition was not considered for the results of Chapter 6, which accounts for a significant amount of extrathoracic drug loss and appears to be affected by small values of $d_{h,nasopharynx}$. Also, the different NIV

means of respiratory support, namely HFT and NPPV, may be a significant factor. Additionally, the presence of nasal cycling, a small value of average nostril hydraulic diameter ($d_{h,nostril}$) in the FNMT2 model, or the smaller mask dead space volume in the FNMT2 model may account for the unexpected decrease in PF in comparison to the FNMT model. As mentioned above, Dr. Michael Hindle and colleagues in the VCU Department of Pharmaceutics will be performing *in vitro* experiments with the two face-nose-mouth-throat models and a modified commercial mask to assess delivery of the same dry powder formulation during NPPV, and these results are expected to enhance the understanding of the intersubject variability evident in the CFD results. Also, as described in Section 9.1, it would be helpful to further develop the existing nasal dimension data set to include measurements of $d_{h,nostril}$ and $d_{h,nasopharynx}$, which will provide a more complete estimate of the population range for those parameters. The selection of future CT scan data for CFD and *in vitro* testing should aim to isolate the variables of interest if possible, with the caveat that currently available CT scans do not often include the face, nasal region, and throat in one set.

List of References

List of References

Aboussouan, L.S., & Ricaurte, B. (2010). Noninvasive positive pressure ventilation: Increasing use in acute care. *Cleveland clinical journal of medicine,* **77**, 307-316.

Amirav, I., Balanov, I., Gorenberg, M., Luder, A.S., Newhouse, M.T., & Groshar, D. (2002). β-Agonist aerosol distribution in respiratory syncytial virus bronchiolitus in infants. *The Journal of Nuclear Medicine,* **43**, 487-491.

Amirav, I., Balanov, I., Gorenberg, M., Groshar, D., & Luder, A.S. (2003). Nebuliser hood compared to mask in wheezy infants: aerosol therapy without tears! *Archives of Disease in Childhood,* **88**, 719-723.

Ari, A., Harwood, R., Sheard, M., Dailey, P., & Fink, J.B. (2011). In vitro comparison of heliox and oxygen in aerosol delivery using pediatric high flow nasal cannula. *Pediatric Pulmonology,* **46**, 795-801.

Asgharian, B., Hofmann, W., & Bergmann, R. (2001). Particle deposition in a multiple-path model of the human lung. *Aerosol Science and Technology,* **34**, 332-339.

Asgharian, B., & Price, O.T. (2006). Airflow distribution in the human lung and its influence on particle deposition. *Inhalation Toxicology,* **18**, 795-801.

Bach, J.R., Robert, D., Leger, P., & Langevin, B. (1995). Sleep fragmentation in kyphoscoliotic individuals with alveolar hypoventilation treated by NIPPV. *CHEST Journal,* **107**, 1552-1558.

Balashazy, I., Hofmann, W., & Heistracher, T. (1999). Computation of local enhancement factors for the quantification of particle deposition patterns in airway bifurcations. *Journal of Aerosol Science,* **30**, 185-203.

Behara, S.R.B., Farkas, D.R., Hindle, M., & Longest, P.W. (2013). Development and comparison of new high efficiency dry powder inhalers for carrier-free formulations. *Journal of Pharmaceutical Sciences,* **103**, 465-477.

Behara, S.R.B., Farkas, D.R., Hindle, M., & Longest, P.W. (2014a). Development of a high efficiency dry powder inhaler: Effects of capsule chamber design and inhaler surface modifications. *Pharmaceutical Research,* **31**, 360-372.

Behara, S.R.B., Longest, P.W., Farkas, D.R., & Hindle, M. (2014b). Development of high efficiency ventilation bag actuated dry powder inhalers. *International Journal of Pharmaceutics,* **465**, 52-62.

Bersten, A.D., Holt, A.W., Vedig, A.E., Skowronski, G.A., & Baggolery, C.J. (1991). Treatment of severe cardiogenic pulmonary edema with continuous positive airway pressure delivered by face mask. *The New England Journal of Medicine,* **325**, 1825-1830.

Bhashyam, A.R., Wolf, M.T., Marcinkowski, A.L., Saville, A., Thomas, K., Carcillo, J.A., & Corcoran, T.E. (2008). Aerosol delivery through nasal cannulas: An in vitro study. *Journal of Aerosol Medicine and Pulmonary Drug Delivery,* **21**, 181-187.

Bollert, F.G.E., Matusiewicz, S.P., Dewar, M.H., Brown, G.M., McLean, A., Greening, A.P., & Crompton, G.K. (1997). Comparative efficacy and potency of ipratropium via Turbuhaler(R) and pressurized metered-dose inhaler in reversible airflow obstruction. *European Respiratory Journal,* **10**, 1824-1828.

Bondesson, E., Friberg, K., Soliman, S., & Lofdahl, C.G. (1998). Safety and efficacy of a high cumulative dose of salbutamol inhaled via Turbuhaler (R) or via a pressurized metered-dose inhaler in patients with asthma. *Respiratory Medicine,* **92**, 325-330.

Borgström, L., Bondesson, E., Moren, F., Trofast, E., & Newman, S.P. (1994). Lung deposition of budesonide inhaled via Turbuhaler: A comparison with terbutaline sulphate in normal subjects. *European Respiratory Journal,* **7**, 69-73.

Borgström, L., Derom, E., Ståhl, E., Wåhlin-Boll, E., & Pauwels, R. (1996). The inhalation device influences lung deposition and bronchodilating effect of terbutaline. *American Journal Of Respiratory And Critical Care Medicine,* **153**, 1636-1640.

Borgström, L., Olsson, B., & Thorsson, L. (2006). Degree of throat deposition can explain the variability in lung deposition of inhaled drugs. *Journal of Aerosol Medicine,* **19**, 473-483.

Branconnier, M.P., & Hess, D.R. (2005). Albuterol delivery during noninvasive ventilation. *Respiratory Care,* **50**, 1649-1653.

Brandão, D.C., Lima, V.M., Filho, V.G., Silva, T.S., Campos, T.F., Dean, E., & de Andrade, A.D. (2009). Reversal of bronchial obstruction with bi-level positive airway pressure and nebulization in patients with acute asthma. *Journal of Asthma,* **46**, 356-361.

Broeders, M.E.A.C., Molema, J., Hop, W.C.J., & Folgering, H.T.M. (2003). Inhalation profiles in asthmatics and COPD patients: Reproducibility and effect of instruction. *Journal of Aerosol Medicine,* **16**, 131-141.

Brown, R.H., & Mitzner, W. (2003). Functional imaging of airway narrowing. *Respiratory Physiology and Neurobiology,* **137**, 327-337.

Burnell, P.K.P., Asking, L., Borgström, L., Nichols, S.C., Olsson, B., Prime, D., & Shrubb, I. (2007). Studies of the human oropharyngeal airspaces using magnetic resonance imaging

IV-The oropharyngeal retention effect for four inhalation delivery systems. *Journal of Aerosol Medicine,* **20**, 269-281.

Byron, P.R. (2004). Drug delivery devices: Issues in drug development. *Proc. Am. Thorac. Soc.,* **1**, 321-328.

Byron, P.R., Hindle, M., Lange, C.F., Longest, P.W., McRobbie, D., Oldham, M.J., Olsson, B., Thiel, C.G., Wachtel, H., & Finlay, W.H. (2010). In Vivo-In Vitro Correlations: Predicting Pulmonary Drug Deposition from Pharmaceutical Aerosols. *Journal Of Aerosol Medicine And Pulmonary Drug Delivery,* **23**, S59-S69.

Carrigy, N.B., Ruzycki, C.A., Golshahi, L., & Finlay, W.H. (2014). Pediatric in vitro and in silico models of deposition via oral and nasal inhalation. *Journal of Aerosol Medicine and Pulmonary Drug Delivery,* **27**, 149-169.

Celikel, T., Sungur, M., Ceyhan, B., & Karakurt, S. (1998). Comparison of noninvasive positive pressure ventilation with standard medical therapy in hypercapnic acute respiratory failure. *CHEST Journal,* **114**, 1636-1642.

Chan, T.L., & Lippmann, M. (1980). Experimental measurement and empirical modeling of the regional deposition of inhaled particles in humans. *American Industrial Hygiene Association Journal,* **41**, 399-409.

Chatmongkolchart, S., Schettino, G.P.P., Dillman, C., Kacmarek, R.M., & Hess, D.M. (2002). In vitro evaluation of aerosol bronchodilator delivery during noninvasive positive pressure ventilation: effect of ventilator settings and nebulizer position. *Critical Care Medicine,* **30**, 2515-2519.

Cheng, K.H., Cheng, Y.S., Yeh, H.C., & Swift, D.L. (1997). Measurements of airway dimensions and calculation of mass transfer characteristics of the human oral passage. *Journal of Biomechanical Engineering,* **119**, 476-482.

Cheng, Y.S. (2003). Aerosol deposition in the extrathoracic region. *Aerosol Science and Technology,* **37**, 659-671.

Choi, J., Tawhai, M., Hoffman, E.A., & Lin, C.L. (2009). On intra- and intersubject variabilities of airflow in the human lungs. *Physics of Fluids,* **21**, 101901-101901-101917.

Chua, H.L., Collis, G.G., Newbury, A.M., Chan, K., Bower, G.D., Sly, P.D., & Le Souef, P.N. (1994). The influence of age on aerosol deposition in children with cystic fibrosis. *European Respiratory Journal,* **7**, 2185-2191.

Conway, J., Fleming, J., Majoral, C., Katz, I., Perchet, D., Peebles, C., Tossici-Bolt, L., Collier, L., Caillibotte, G., Pichelin, M., Sauret-Jackson, V., Martonen, T., Apiou-Sbirlea, G., Muellinger, B., Kroneberg, P., Gleske, J., Scheuch, G., Texereau, J., Martin, A., Montesantos, S., & Bennett, M. (2012). Controlled, parametric, individualized, 2-D and 3-D imaging measurements of aerosol deposition in the respiratory tract of healthy human subjects for model validation. *Journal Of Aerosol Science,* **52**, 1-17.

Crimi, C., Noto, A., Princi, P., Esquinas, A., & Nava, S. (2010). A European survey of noninvasive ventilation practices. *European Respiratory Journal,* **36**, 362-369.

Crowder, T., & Hickey, A. (2006). Powder specific active dispersion for generation of pharmaceutical aerosols. *International Journal of Pharmaceutics,* **327**, 65-72.

Dai, G., Kang, J., Sun, L., Tan, W., & Zhao, H. (2013). Influence of exhalation valve and nebulizer position on albuterol delivery during noninvasive positive pressure ventilation. *Journal of Aerosol Medicine and Pulmonary Drug Delivery,* **26**, 1-8.

De Backer, J.W., Vos, W.G., Vinchurkar, S.C., Claes, R., Drollmann, A., Wulfrank, D., Parizel, P.M., Germonpre, P., & De Backer, W. (2010a). Validation of Computational Fluid Dynamics in CT-based Airway Models with SPECT/CT. *Radiology,* **257**, 854-862.

De Backer, W., Devolder, A., Poli, G., Acerbi, D., Monno, R., Herpich, C., Sommerer, K., Meyer, T., & Mariotti, F. (2010b). Lung deposition of BDP/Formoterol HFA pMDI in Healthy Volunteers, Asthmatic, and COPD Patients. *Journal of Aerosol Medicine and Pulmonary Drug Delivery,* **23**, 137-148.

DeHaan, W.H., & Finlay, W.H. (2001). In vitro monodisperse aerosol deposition in a mouth and throat with six different inhalation devices. *Journal of Aerosol Medicine,* **14**, 361-367.

DeHaan, W.H., & Finlay, W.H. (2004). Predicting extrathoracic deposition from dry powder inhalers. *Journal of Aerosol Science,* **35**, 309-331.

Delvadia, R., Longest, P.W., & Byron, P.R. (2012). In vitro tests for aerosol deposition. I. Scaling a physical model of the upper airways to predict drug deposition variation in normal humans. *Journal of Aerosol Medicine,* **25**, 32-40.

Delvadia, R., Hindle, M., Longest, P.W., & Byron, P.R. (2013). In vitro tests for aerosol deposition. II: IVIVCs for different dry powder inhalers in normal adults. *Journal of Aerosol Medicine and Pulmonary Drug Delivery,* **26**, 138-144.

Dhand, R. (2008). Aerosol delivery during mechanical ventilation: From basic techniques to new devices. *Journal of Aerosol Medicine and Pulmonary Drug Delivery,* **21**, 45-60.

Dhand, R. (2012). Aerosol therapy in patients receiving noninvasive positive pressure ventilation. *Journal of Aerosol Medicine and Pulmonary Drug Delivery,* **25**, 63-78.

DiMarco, A.F., Onders, R.P., Ignagni, A., Kowalski, K.E., & Mortimer, J.T. (2005). Phrenic nerve pacing via intramuscular diaphragm electrodes in tetraplegic subjects. *CHEST Journal,* **127**, 671-678.

Diot, P., Morra, L., & Smaldone, G.C. (1995). Albuterol delivery in a model of mechanical ventilation. Comparison of metered-dose inhaler and nebulizer efficiency. *American Journal of Respiratory and Critical Care Medicine,* **152**, 1391-1394.

Dysart, K., Miller, T.L., Wolfson, M.R., & Shaffer, T.H. (2009). Research in high flow therapy: Mechanisms of action. *Respiratory Medicine,* **103**, 1400-1405.

Ehrmann, S., Roche-Campo, F., Papa, G.F.S., Isabey, D., Brochard, L., & Apiou-Sbirlea, G. (2013). Aerosol therapy during mechanical ventilation: an international survey. *Intensive Care Medicine,* **39**, 1048-1056.

Erzinger, S., Schuepp, K.G., Brooks-Wildhaber, J., Devadason, S.G., & Wildhaber, J.H. (2007). Facemasks and aerosol delivery in vivo. *Journal of Aerosol Medicine,* **20**, S78-S84.

Esteban, A., Frutos-Vivar, F., Ferguson, N.D., Arabi, Y., Apezteguia, C., Gonzalez, M., Epstein, S.K., Hill, N.S., Nava, S., Soares, M.-A., D'Empaire, G., Alia, I., & Anzueto, A. (2004). Noninvasive positive-pressure ventilation for respiratory failure after extubation. *The New England Journal of Medicine,* **350**, 2452-2460.

Everard, M.L., Devadason, S.G., & LeSouef, P.N. (1996). In vitro assessment of drug delivery through an endotracheal tube using a dry powder inhaler delivery system. *Thorax,* **51**, 75-77.

Farkas, A., & Balashazy, I. (2007). Simulation of the effect of local obstructions and blockage on airflow and aerosol deposition in central human airways. *Journal of Aerosol Science,* **38**, 865-884.

Fauroux, B., Itti, E., Pigeot, J., Isabey, D., Meignan, M., Ferry, G., Lofaso, F., Willemot, J.M., Clement, A., & Harf, A. (2000). Optimization of aerosol deposition by pressure support in children with cystic fibrosis - An experimental and clinical study. *American Journal Of Respiratory And Critical Care Medicine,* **162**, 2265-2271.

Fink, J.B., Dhand, R., Grychowski, J., Fahey, P.J., & Tobin, M.J. (1999). Reconciling in vitro and in vivo measurements of aerosol delivery from a metered-dose inhaler during mechanical ventilation and defining efficiency-enhancing factors. *American Journal of Respiratory Critical Care Medicine,* **159**, 63-68.

Finlay, W.H., & Stapleton, K.W. (1995). The effect on regional lung deposition of coupled heat and mass-transfer between hygroscopic droplets and their surrounding phase. *Journal of Aerosol Science,* **26**, 655-670.

Finlay, W.H. (1998). Estimating the type of hygroscopic behavior exhibited by aqueous droplets. *Journal of Aerosol Medicine,* **11**, 221-229.

Finlay, W.H. (2001). *The Mechanics of Inhaled Pharmaceutical Aerosols*. Academic Press, San Diego.

Finlay, W.H., & Martin, A.R. (2007). Modeling of aerosol deposition within interface devices. *Journal of Aerosol Medicine,* **20**, S19-S28.

Fok, T.F., Monkman, S., Dolovich, M., Gray, S., Coates, G., Paes, B., Rashid, F., Newhouse, M., & Kirpalani, H. (1996). Efficiency of aerosol medication delivery from a metered dose

inhaler versus jet nebulizer in infants with bronchopulmonary dysplasia. *Pediatric Pulmonology,* **21**, 301-309.

França, E.E.T., De Andrade, A.D., Cabral, G., Almeida-Filho, P., Silva, K.C., Galindo-Filho, V.C., Marinho, P.E.M., Lemos, A., & Parreira, V.F. (2006). Nebulization associated with bi-level noninvasive ventilation: analysis of pulmonary radioaerosol deposition. *Respiratory Medicine,* **100**, 721-728.

Galindo-Filho, V.C., Brandão, D.C., Ferreira, R., Menezes, M.J.C., Almeida-Filho, P., Parreira, V.F., Silva, T.N., Rodrigues-Machado, M., Dean, E., & De Andrade, A.D. (2013). Noninvasive ventilation coupled with nebulization during asthma crises: a randomized controlled trial. *Respiratory Care,* **58**, 241-249.

Garcia, G.J.M., Tewksbury, E.W., Wong, B.A., & Kimbell, J.S. (2009). Interindividual variability in nasal filtration as a function of nasal cavity geometry. *Journal of Aerosol Medicine and Pulmonary Drug Delivery,* **22**, 139-155.

Girault, C., Briel, A., Benichou, J., Hellot, M.-F., Dachraoui, F., Tamion, F., & Bonmarchand, G. (2009). Interface strategy during noninvasive positive pressure ventilation for hypercapnic acute respiratory failure. *Critical Care Medicine,* **37**, 124-131.

Golshahi, L., Noga, M.L., Thompson, R.B., & Finlay, W.H. (2011). In vitro deposition measurement of inhaled micrometer-sized particles in extrathoracic airways of children and adolescents during nose breathing. *Journal of Aerosol Science,* **42**, 474-488.

Golshahi, L., Tian, G., Azimi, M., Son, Y.-J., Walenga, R.L., Longest, P.W., & Hindle, M. (2013). The use of condensational growth methods for efficient drug delivery to the lungs during noninvasive ventilation high flow therapy. *Pharmaceutical Research,* **30**, 2917-2930.

Golshahi, L., Longest, P.W., Azimi, M., Syed, A., & Hindle, M. (2014a). Intermittent aerosol delivery to the lungs during high flow nasal cannula therapy. *Respiratory Care,* **59**, 1476-1486.

Golshahi, L., Walenga, R.L., Longest, P.W., & Hindle, M. (2014b). Development of a transient flow aerosol mixer-heater system for lung delivery of nasally-administered aerosols using a nasal cannula. *Aerosol Science and Technology,* **48**, 1009-1021.

Grgic, B., Finlay, W.H., Burnell, P.K.P., & Heenan, A.F. (2004a). In vitro intersubject and intrasubject deposition measurements in realistic mouth-throat geometries. *Journal of Aerosol Science,* **35**, 1025-1040.

Grgic, B., Finlay, W.H., & Heenan, A.F. (2004b). Regional aerosol deposition and flow measurements in an idealized mouth and throat. *Aerosol Science,* **35**, 21-32.

Griscom, N.T., & Wohl, M.E.B. (1986). Dimensions of the growing trachea related to age and gender. *American Journal of Roentgenology,* **146**, 233-237.

Guilmette, R.A., Cheng, Y.S., Yeh, H.C., & Swift, D.L. (1994). Deposition of 0.005 - 12 micrometer monodisperse particles in a computer-milled, MRI-based nasal airway replica. *Inhalation Toxicology,* **6 (Suppl. 1)**, 395-399.

Gungor, A., Moinuddin, R., Nelson, R.H., & Corey, J.P. (1999). Detection of the nasal cycle with acoustic rhinometry: techniques and applications. *Otolaryngology - Head and Neck Surgery,* **120**, 238-247.

Gupta, D., Nath, A., Agarwal, R., & Behara, D. (2010). A prospective randomized controlled trial on the efficacy of noninvasive ventilation in severe acute asthma. *Respiratory Care,* **55**, 536-543.

Hammersley, J.R., & Olson, D.E. (1992). Physical models of the smaller pulmonary airways. *Journal of Applied Physiology,* **72**, 2402-2414.

Hayden, J.T., Smith, N., Woolf, D.A., Barry, P.W., & O'Callaghan, C. (2004). A randomised crossover trial of facemask efficacy. *Archives of Disease in Childhood,* **89**, 72-73.

Heistracher, T., & Hofmann, W. (1995). Physiologically realistic models of bronchial airway bifurcations. *Journal of Aerosol Science,* **26**, 497-509.

Hess, D.R. (2007). The mask of noninvasive ventilation: Principles of design and effects on aerosol delivery. *Journal of Aerosol Medicine,* **20**, S85-S99.

Heyder, J., & Rudolf, G. (1975). Deposition of aerosol particles in the human nose. *Inhaled Particles,* **4**, 107-126.

Hindle, M., Newton, D.A.G., & Chrystyn, H. (1995). Dry powder inhalers are bioequivalent to metered dose inhalers: a study using a new urinary albuterol (salbutamol) assay technique. *Chest,* **107**, 629-633.

Hindle, M., & Longest, P.W. (2010). Evaluation of enhanced condensational growth (ECG) for controlled respiratory drug delivery in a mouth-throat and upper tracheobronchial model. *Pharmaceutical Research,* **27**, 1800-1811.

Hindle, M., & Longest, P.W. (2012). Condensational growth of combination drug-excipient submicrometer particles for targeted high efficiency pulmonary delivery: Evaluation of formulation and delivery device. *Journal of Pharmacy and Pharmacology,* **64**, 1254-1263.

Hirst, P.H., Bacon, R.E., Pitcairn, G.R., Silvasti, M., & Newman, S.P. (2001). A comparison of the lung deposition of budesonide from Easyhaler (R), Turbuhaler (R) and pMDI plus spacer in asthmatic patients. *Respiratory Medicine,* **95**, 720-727.

Horsfield, K., Dart, G., Olson, D.E., Filley, G.F., & Cumming, G. (1971). Models of the human bronchial tree. *Journal of Applied Physiology,* **31**, 207-217.

Hounam, R.F., Black, A., & Walsh, M. (1971). The deposition of aerosol particles in the nasopharyngeal region of the human respiratory tract. *Aerosol Science,* **2**, 47-61.

Hui, D.S., Hall, S.D., Chan, M.T.V., Chow, B.K., Tsou, J.Y., Joynt, G.M., Sullivan, C.E., & Sung, J.J.Y. (2006). Noninvasive positive-pressure ventilation: an experimental model to assess air and particle dispersion. *CHEST Journal,* **130**, 730-740.

ICRP. (1994). *Human Respiratory Tract Model for Radiological Protection* (Vol. 66). Elsevier Science Ltd., New York.

Ilie, M., Matida, E.A., & Finlay, W.H. (2008). Asymmetrical aerosol deposition in an idealized mouth with a DPI mouthpiece inlet. *Aerosol Science and Technology,* **42**, 10-17.

Inthavong, K., Choi, L.-T., Tu, J., Diang, S., & Thien, F. (2010a). Micron particle deposition in a tracheobronchial airway model under different breathing conditions. *Medical Engineering and Physics,* **32**, 1198-1212.

Inthavong, K., Tu, J., Ye, Y., Ding, S., Subic, A., & Thien, F. (2010b). Effects of airway obstruction induced by asthma attack on particle deposition. *Journal of Aerosol Science,* **41**, 587-601.

Inthavong, K., Ge, Q.J., Se, C.M.K., Yang, W., & Tu, J.Y. (2011). Simulation of sprayed particle deposition in a human nasal cavity including a nasal spray device. *Journal of Aerosol Science,* **42**, 100-113.

Isaacs, K.K., Schlesinger, R.B., & Martonen, T.B. (2006). Three-dimensional computational fluid dynamics simulations of particle deposition in the tracheobronchial tree. *Journal of Aerosol Medicine,* **19**, 344-352.

Islam, N., & Cleary, M.J. (2012). Developing an efficient and reliable dry powder inhaler for pulmonary drug delivery - A review for multidisciplinary researchers. *Medical Engineering and Physics,* **34**, 409-427.

Jin, H.H., Fan, J.R., Zeng, M.J., & Cen, K.F. (2007). Large eddy simulation of inhaled particle deposition within the human upper respiratory tract. *Aerosol Science,* **38**, 257-268.

Kelly, J.T., Asgharian, B., Kimbell, J.S., & Wong, B. (2004a). Particle deposition in human nasal airway replicas manufactured by different methods. Part II: Ultrafine particles. *Aerosol Science and Technology,* **38**, 1072-1079.

Kelly, J.T., Asgharian, B., Kimbell, J.S., & Wong, B. (2004b). Particle deposition in human nasal airway replicas manufactured by different methods. Part I: Inertial regime particles. *Aerosol Science and Technology,* **38**, 1063-1071.

Kesavanathan, J., Bascom, R., & Swift, D.L. (1998). The effect of nasal passage characteristics on particle deposition. *Journal of Aerosol Medicine,* **11**, 27-39.

Kim, C.S. (2009). Deposition of aerosol particles in human lungs: in vivo measurement and modeling. *Biomarkers,* **14(S1)**, 54-58.

Kim, J., Moin, P., & Moser, R.D. (1987). Turbulence statistics in fully developed channel flow at low Reynolds number. *Journal of Fluid Mechanics,* **177**, 133-166.

Kimbell, J.S., Segal, R.A., Asgharian, B., Wong, B.A., Schroeter, J.D., Southall, J.P., Dickens, C.J., Brace, G., & Miller, F.J. (2007). Characterization of deposition from nasal spray devices using a computational fluid dynamics model of the human nasal passages. *Journal Of Aerosol Medicine-Deposition Clearance And Effects In The Lung,* **20**, 59-74.

Kleinstreuer, C., & Zhang, Z. (2009). An adjustable triple-bifurcation unit model for air-particle flow simulations in human tracheobronchial airways. *Journal of Biomechanical Engineering,* **131**, 021007.

Kuhli, M., Weiss, M., & Steckel, H. (2009). A sampling and dilution system for droplet aerosols from medical nebulisers developed for use with an optical particle counter. *Aerosol Science,* **40**, 523-533.

Kuo, T., Tully, E.A., & Galea, M.P. (2009). Video analysis of sagittal spinal posture in healthy young and older adults. *Journal of Manipulative and Physiological Therapeutics,* **32**, 210-215.

Kwok, H.M., J., Cece, R., Houtchens, J., & Hill, N.S. (2003). Controlled trial of oronasal versus nasal mask ventilation in the treatment of acute respiratory failure. *Critical Care Medicine,* **31**, 468-473.

Lambert, A.R., O'Shaughnessy, P.T., Tawhai, M.H., Hoffman, E.A., & Lin, C.-L. (2011). Regional deposition of particles in an image-based airway model: Large-eddy simulation and left-right lung ventilation asymmetry. *Aerosol Science and Technology,* **45**, 11-25.

Lang, C., Grützenmacher, S., Mlynski, B., Plontke, A., & Mlynski, G. (2003). Investigating the nasal cycle using endoscopy, rhinoresistometry, and acoustic rhinometry. *The Laryngoscope,* **113**, 284-289.

Laube, B.L., Sharpless, G., Shermer, C., Sullivan, V., & Powell, K. (2012). Deposition of dry powder generated by solovent in Sophia Anatomical infant nose-throat (SAINT) model. *Aerosol Science and Technology,* **46**, 514-520.

Leach, C.L., Davidson, P.J., & Bouhuys, A. (1998). Improved airway targeting with the CFC-free HFA-beclomethasone metered-dose inhaler compared with CFC-beclomethasone. *European Respiratory Journal,* **12**, 1346-1353.

Lightowler, J.V., Wedzicha, J.A., Elliott, M.W., & Ram, F.S.F. (2003). Non-invasive positive pressure ventilation to treat respiratory failure resulting from exacerbations of chronic obstructive pulmonary disease: Cochrane systematic review and meta-analysis. *British Medical Journal,* **326**, 185-187.

Lin, C.-L., Tawhai, M.H., McLennan, G., & Hoffman, E.A. (2007). Characteristics of the turbulent laryngeal jet and its effect on airflow in the human intra-thoracic airways. *Respiratory Physiology and Neurobiology,* **157**, 295-309.

Lin, C.-L., Tawhai, M.H., McLennan, G., & Hoffman, E.A. (2009). Multiscale simulation of gas flow in subject-specific models of the human lung. *IEEE Engineering in Medicine and Biology,* **28**, 25-33.

Lin, M., & Chiang, H. (1991). The efficacy of early continuous positive airway pressure therapy in patients with acute cardiogenic pulmonary edema. *Journal of Formosan Medical Association,* **90**, 736-743.

Lin, M., Yang, Y., Chiany, H., Chang, M., Chiany, B.N., & Chitlin, M.D. (1995). Reappraisal of continuous positive airway pressure therapy in acute cardiogenic pulmonary edema: short-term results and long-term follow-up. *CHEST Journal,* **107**, 1379-1386.

Liu, Y., Matida, E.A., Gu, J., & Johnson, M.R. (2007). Numerical simulation of aerosol deposition in a 3-D human nasal cavity using RANS, RANS/EIM, and LES. *Aerosol Science,* **38**, 683-700.

Liu, Y., Johnson, M.R., Matida, E.A., Kherani, S., & Marsan, J. (2009). Creation of a standardized geometry of the human nasal cavity. *Journal of Applied Physiology,* **106**, 784-795.

Longest, P.W., Vinchurkar, S., & Martonen, T.B. (2006). Transport and deposition of respiratory aerosols in models of childhood asthma. *Journal of Aerosol Science,* **37**, 1234-1257.

Longest, P.W., Hindle, M., Das Choudhuri, S., & Byron, P.R. (2007). Numerical simulations of capillary aerosol generation: CFD model development and comparisons with experimental data. *Aerosol Science and Technology,* **41**, 952-973.

Longest, P.W., & Vinchurkar, S. (2007a). Effects of mesh style and grid convergence on particle deposition in bifurcating airway models with comparisons to experimental data. *Medical Engineering and Physics,* **29**, 350-366.

Longest, P.W., & Vinchurkar, S. (2007b). Validating CFD predictions of respiratory aerosol deposition: effects of upstream transition and turbulence. *Journal of Biomechanics,* **40**, 305-316.

Longest, P.W., & Xi, J. (2007). Effectiveness of direct Lagrangian tracking models for simulating nanoparticle deposition in the upper airways. *Aerosol Science and Technology,* **41**, 380-397.

Longest, P.W., Hindle, M., Das Choudhuri, S., & Byron, P.R. (2008a). Developing a better understanding of spray system design using a combination of CFD modeling and experiment. In R.N. Dalby, Byron, P.R., Peart, J., Suman, J.D., Farr, S.J. & Young, P.M. (Ed.), *Proceedings of Respiratory Drug Delivery 2008*. Davis Healthcare International Publishing: Illinois, pp. 151-163.

Longest, P.W., Hindle, M., Das Choudhuri, S., & Xi, J. (2008b). Comparison of ambient and spray aerosol deposition in a standard induction port and more realistic mouth-throat geometry. *Journal of Aerosol Science,* **39**, 572-591.

Longest, P.W., & Xi, J. (2008). Condensational growth may contribute to the enhanced deposition of cigarette smoke particles in the upper respiratory tract. *Aerosol Science and Technology,* **42**, 579-602.

Longest, P.W., & Hindle, M. (2009a). Evaluation of the Respimat Soft Mist inhaler using a concurrent CFD and in vitro approach. *Journal of Aerosol Medicine and Pulmonary Drug Delivery,* **22**, 99-112.

Longest, P.W., & Hindle, M. (2009b). Quantitative analysis and design of a spray aerosol inhaler. Part 1: Effects of dilution air inlets and flow paths. *Journal of Aerosol Medicine and Pulmonary Drug Delivery,* **22**, 271-283.

Longest, P.W., Hindle, M., & Das Choudhuri, S. (2009). Effects of generation time on spray aerosol transport and deposition in models of the mouth-throat geometry. *Journal of Aerosol Medicine and Pulmonary Drug Delivery* **22**, 67-84.

Longest, P.W., & Hindle, M. (2010). CFD simulations of enhanced condensational growth (ECG) applied to respiratory drug delivery with comparisons to in vitro data. *Journal of Aerosol Science,* **41**, 805-820.

Longest, P.W., McLeskey, J.T., & Hindle, M. (2010). Characterization of nanoaerosol size change during enhanced condensational growth. *Aerosol Science and Technology,* **44**, 473-483.

Longest, P.W., & Hindle, M. (2011). Numerical model to characterize the size increase of combination drug and hygroscopic excipient nanoparticle aerosols. *Aerosol Science and Technology,* **45**, 884-899.

Longest, P.W., Tian, G., & Hindle, M. (2011). Improving the lung delivery of nasally administered aerosols during noninvasive ventilation - An application of enhanced condensational growth (ECG). *Journal of Aerosol Medicine and Pulmonary Drug Delivery,* **24**, 103-118, DOI: 110.1089/jamp.2010.0849.

Longest, P.W., & Hindle, M. (2012). Condensational growth of combination drug-excipient submicrometer particles: Comparison of CFD predictions with experimental results. *Pharmaceutical Research,* **29**, 707-721.

Longest, P.W., & Holbrook, L.T. (2012). In silico models of aerosol delivery to the respiratory tract - Development and applications. *Advanced Drug Delivery Reviews,* **64**, 296-311.

Longest, P.W., Spence, B.M., Holbrook, L.T., Mossi, K.M., Son, Y.-J., & Hindle, M. (2012a). Production of inhalable submicrometer aerosols from conventional mesh nebulizers for improved respiratory drug delivery. *Journal of Aerosol Science,* **51**, 66-80.

Longest, P.W., Tian, G., Delvadia, R., & Hindle, M. (2012b). Development of a stochastic individual path (SIP) model for predicting the deposition of pharmaceutical aerosols: Effects of turbulence, polydisperse aerosol size, and evaluation of multiple lung lobes. *Aerosol Science and Technology,* **46**, 1271-1285.

Longest, P.W., Tian, G., Li, X., Son, Y.-J., & Hindle, M. (2012c). Performance of combination drug and hygroscopic excipient submicrometer particles from a softmist inhaler in a characteristic model of the airways. *Annals of Biomedical Engineering,* **40**, 2596-2610.

Longest, P.W., Tian, G., Walenga, R.L., & Hindle, M. (2012d). Comparing MDI and DPI aerosol deposition using in vitro experiments and a new stochastic individual path (SIP) model of the conducting airways. *Pharmaceutical Research,* **29**, 1670-1688.

Longest, P.W., Golshahi, L., & Hindle, M. (2013a). Improving pharmaceutical aerosol delivery during noninvasive ventilation: Effects of streamlined components. *Annals of Biomedical Engineering,* **41**, 1217-1232.

Longest, P.W., Son, Y.-J., Holbrook, L.T., & Hindle, M. (2013b). Aerodynamic factors responsible for the deaggregation of carrier-free drug powders to form micrometer and submicrometer aerosols. *Pharmaceutical Research,* **30**, 1608-1627.

Longest, P.W., Walenga, R.L., Son, Y.-J., & Hindle, M. (2013c). High efficiency generation and delivery of aerosols through nasal cannula during noninvasive ventilation. *Journal of Aerosol Medicine and Pulmonary Drug Delivery,* **26**, 266-279.

Longest, P.W., Azimi, M., Golshahi, L., & Hindle, M. (2014a). Improving aerosol drug delivery during invasive mechanical ventilation with redesigned components. *Respiratory Care,* **59**, 686-698.

Longest, P.W., Golshahi, L., Behara, S.R.B., Tian, G., Farkas, D.R., & Hindle, M. (2014b). Efficient nose-to-lung (N2L) aerosol delivery with a dry powder inhaler. *Journal of Aerosol Medicine and Pulmonary Drug Delivery,* **27**, 1-13.

Longest, P.W., & Tian, G. (2014). Development of a new technique for the efficient delivery of aerosolized medications to infants on mechanical ventilation. *Pharmaceutical Research,* **(in press)**.

Lopes, A.J., Nery, F.P.O.S., Sousa, F.C., Guimaraes, F.S., Dias, C.M., Oliveira, J.F., & Menezes, S.L.S. (2011). CPAP decreases lung hyperinflation in patients with stable COPD. *Respiratory Care,* **56**, 1164-1169.

Ma, B., & Lutchen, K.R. (2009). CFD simulations of aerosol deposition in an anatomically based human large-medium airway model. *Annals of Biomedical Engineering,* **37**, 271-285.

Majoral, C., Fleming, J., Conway, J., Katz, I., Tossici-Bolt, L., Pichelin, M., Montesantos, S., & Caillibotte, G. (2014). Controlled, parametric, individualized, 2D and 3D imaging measurements of aerosol deposition in the respiratory tract of human volunteers: in vivo data analysis. *Journal of Aerosol Medicine and Pulmonary Drug Delivery,* **27**, 349-362.

Mallol, J., Rattray, S., Walker, G., Cook, D., & Robertson, C.F. (1996). Aerosol deposition in infants with cystic fibrosis. *Pediatric Pulmonology,* **21**, 276-281.

Martin, A.R., Gleske, J., Katz, I.M., Hartmann, M., Mullinger, B., Haussermann, S., Caillibotte, G., & Scheuch, G. (2010). Laser diffraction characterization of droplet size distributions produced by vibrating mesh nebulization of air and a helium-oxygen mixture. *Journal of Aerosol Science,* **41**.

Martin, G.P., Marriott, C., & Zhang, X.M. (2007). Influence of realistic inspiratory flow profiles on fine particle fractions of dry powder aerosol formulations. *Pharmaceutical Research,* **24**, 361-369.

Martonen, T., Fleming, J., Schroeter, J., Conway, J., & Hwang, D. (2003). In silico modeling of asthma. *Advanced Drug Delivery Reviews,* **55**, 829-849.

Martonen, T.B., Musante, C.J., Segal, R.A., Schroeter, J.D., Hwang, D., Dolovich, M.A., Burton, R., Spencer, R.M., & Fleming, J.S. (2000). Lung Models: Strengths and Limitations. *Respiratory Care,* **45**, 712-736.

Masip, J. (2007). Non-invasive ventilation. *Heart Failure Reviews,* **12**, 119-124.

Matida, E.A., Nishino, K., & Torii, K. (2000). Statistical simulation of particle deposition on the wall from turbulent dispersed pipe flow. *International Journal of Heat and Fluid Flow,* **21**, 389-402.

Matida, E.A., DeHaan, W.H., Finlay, W.H., & Lange, C.F. (2003). Simulation of particle deposition in an idealized mouth with different small diameter inlets. *Aerosol Science and Technology,* **37**, 924-932.

Matida, E.A., Finlay, W.H., & Grgic, L.B. (2004). Improved numerical simulation of aerosol deposition in an idealized mouth-throat. *Journal of Aerosol Science,* **35**, 1-19.

McDaid, C., Griffin, S., Weatherly, H., Duree, K., van der Burgt, M., van Hout, S., Akers, J., Davies, R.J.O., Sculpher, M., & Westwood, M. (2009). A systematic review of continous positive airway pressure for obstructive sleep apnoea-hypopnoea syndrome. *Sleep Medicine Reviews,* **13**, 427-426.

Mehta, S., & Hill, N.S. (2001). Noninvasive ventilation. *American Journal of Respiratory and Critical Care Medicine,* **163**, 540-577.

Meyer, T., Brand, P., Ehlich, H., Kobrich, R., Meyer, G., Reidinger, F., Sommerer, K., Weuthen, T., & Scheuch, G. (2004). Deposition of Foradil P in Human Lungs: Comparison of In Vitro and In Vivo Data. *Journal of Aerosol Medicine,* **17**, 43-49.

Miyoshi, E., Fujino, Y., Uchiyama, A., Mashimo, T., & Nishimura, M. (2005). Effects of gas leak on triggering function, humidification, and inspiratory oxygen fraction during noninvasive positive airway pressure ventilation. *CHEST Journal,* **129**, 3691-3698.

Montesantos, S., Fleming, J.S., & Tossici-Bold, L. (2010). A spatial modelof the human airway tree: The hybrid conceptual model. *Journal of Aerosol Medicine and Pulmonary Drug Delivery,* **23**, 59-68.

Nava, S., & Hill, N. (2009). Non-invasive ventilation in acute respiratory failure. *The Lancet,* **374**, 250-259.

Nava, S., Navalesi, P., & Gregoretti, C. (2009). Interfaces and humidification for noninvasive mechanical ventilation. *Respiratory Care,* **54**, 71-84.

Navalesi, P., Fanfulla, F., Frigerio, P., Gregoretti, C., & Nava, S. (2000). Physiologic evaluation of noninvasive mechanical ventilation delivered with three types of masks in patients with chronic hypercapnic respiratory failure. *Critical Care Medicine,* **28**, 1785-1790.

Newman, S.P., Pitcairn, G.R., Hirst, P.H., Bacon, R.E., O'Keefe, E., Reiners, M., & Hermann, R. (2000). Scintigraphic comparison of budesonide deposition from two dry powder inhalers. *European Respiratory Journal,* **16**, 178-183.

Newman, S.P., & Busse, W.W. (2002). Evolution of dry powder inhaler design, formulation, and performance. *Respiratory Medicine,* **96**, 293-304.

Newman, S.P. (2005). Principles of metered-dose inhaler design. *Respiratory Care,* **50**, 1177-1190.

O'Driscoll, B.R., Howard, L.S., & Davison, A.G. (2008). BTS guideline for emergency oxygen use in adult patients. *Thorax,* **63**, vi1-vi68.

Parke, R.L., Eccleston, M.L., & McGuinness, S.P. (2011a). The effects of flow on airway pressure during nasal high-flow oxygen therapy. *Respiratory Care,* **56**, 1151-1155.

Parke, R.L., McGuinness, S.P., & Eccleston, M.L. (2011b). A preliminary randomized controlled trial to assess effectiveness of nasal high-flow oxygen in intensive care patients. *Respiratory Care,* **56**, 265-270.

Parkes, S.N., & Bersten, A.D. (1997). Aerosol kinetics and bronchodilator efficacy during continuous positive airway pressure delivered by face mask. *Thorax,* **52**, 171-175.

Perry, S.A., Kesser, K.C., Geller, D.E., Selhorst, D.M., Rendle, J.K., & Hertzog, J.H. (2013). Influences of cannula size and flow rate on aerosol drug delivery through the Vapotherm humidified high-flow nasal cannula system. *Pediatric Critical Care Medicine,* **14**, e250-e256.

Phalen, R.F., Oldham, M.J., Beaucage, C.B., Crocker, T.T., & Mortensen, J.D. (1985). Postnatal enlargement of human tracheobronchial airways and implications for particle deposition. *Anat. Rec.,* **212**, 368-380.

Pohlmann, G., Iwatschenko, P., Koch, W., Windt, H., Rast, M., Gama de Abreu, M., Taut, F.J.H., & De Muynck, C. (2013). A novel continuous powder aerosolizer (CPA) for

inhalative administration of highly concentrated recombinant surfactant protein-C (rSP-C) surfactant to perterm neonates. *Journal of Aerosol Medicine and Pulmonary Drug Delivery,* **26**, 370-379.

Pollack, C.V., Fleisch, K.B., & Dowsey, K. (1995). Treatment Of Acute Bronchospasm With Beta-Adrenergic Agonist Aerosols Delivered By A Nasal Bilevel Positive Airway Pressure Circuit. *Annals Of Emergency Medicine,* **26**, 552-557.

Price, A.M., Plowright, C., Makowski, A., & Misztal, B. (2008). Using a high-flow respiratory system (Vapotherm) within a high dependency setting. *Nursing in Critical Care,* **13**, 298-304.

Raabe, O.G., Yeh, H.C., Schum, G.M., & Phalen, R.F. (1976). Tracheobronchial Geometry: Human, Dog, Rat, Hamster. *Report No. LF-53*.

Rao, N., Kadrichu, N., & Ament, B. (2010). Application of a droplet evaporation model to aerodynamic size measurement of drug aerosols generated by a vibrating mesh nebulizer. *Journal of Aerosol Medicine and Pulmonary Drug Delivery,* **23**, 295-302.

Rasanen, J., Heikkila, J., Downs, J., Nikki, P., Vaisanen, I.T., & Viitanen, A. (1985). Continuous positive airway pressure by face mask in acute cardiogenic pulmonary edema. *American Journal of Cardiology,* **55**, 296-300.

Rea, H., McAuley, S., Jayaram, L., Garrett, J., Hockey, H., Storey, L., O'Donnell, G., Haru, L., Payton, M., & O'Donnell, K. (2010). The clinical utility of long-term humidification therapy in chronic airway disease. *Respiratory Medicine,* **104**, 525-533.

Robinson, R.J., Russo, J., & Doolittle, R.L. (2009). 3D airway reconstruction using visible human data set and human casts with comparison to morpometric data. *The Anatomical Record,* **292**, 1028-1044.

Roca, O., Riera, J., Torres, F., & Masclans, J.R. (2010). High-Flow Oxygen Therapy in Acute Respiratory Failure. *Respiratory Care,* **55**, 408-413.

Ross, D.L., & Schultz, R.K. (1996). Effect of inhalation flow rate on the dosing characteristics of dry powder inhaler (DPI) and metered dose inhaler (MDI) products. *Journal of Aerosol Medicine,* **9**, 215-226.

Russo, J., Robinson, R., & Oldham, M.J. (2008). Effects of cartilage rings on airflow and particle deposition in the trachea and main bronchi. *Medical Engineering and Physics,* **30**, 581-589.

Sangwan, S., Gurses, B.K., & Smaldone, G.C. (2004). Facemasks and facial deposition of aerosols. *Pediatric Pulmonology,* **37**, 447-452.

Sauret, V., Halson, P.M., Brown, I.W., Fleming, J.S., & Bailey, A.G. (2002). Study of the three-dimensional geometry of the central conducting airways in man using computed tomographic (CT) images. *J. Anat.,* **2002**, 123-134.

Scherer, T., Geller, D.E., Owyang, L., Tservistas, M., Keller, M., Boden, N., Kesser, K.C., & Shire, S.J. (2011). A technical feasibility study of dornase alfa delivery with eFlow® vibrating membrane nebulizers: aerosol characteristics and physicochemical stability. *Journal of Pharmaceutical Sciences,* **100**, 98-109.

Schettino, G.P.P., Tucci, M.R., Sousa, R., Barbas, C.S.V., Amato, M.B.P., & Carvalho, C.R.R. (2001). Mask mechanics and leak dynamics during noninvasive pressure support ventilation: a bench study. *Intensive Care Medicine,* **27**, 1887-1891.

Scheuch, G., Bennett, W., Borgström, L., Clark, A., Dalby, R., Dolovich, M., Fleming, J., Gehr, P., Gonda, I., O'Callaghan, C., Taylor, G., & Newman, S. (2010). Deposition, Imaging, and Clearance: What Remains to be Done? *Journal Of Aerosol Medicine And Pulmonary Drug Delivery,* **23**, S39-S57.

Schwab, R.J., Gefter, W.B., Pack, A.I., & Hoffman, E.A. (1993). Dynamic imaging of the upper airway during respiration in normal subjects. *Journal of Applied Physiology,* **74**, 1504-1514.

Segal, R.A., Kepler, G.M., & Kimbell, J.S. (2008). Effects of differences in nasal anatomy of airflow distribution: A comparison of four individuals at rest. *Annals of Biomedical Engineering,* **36**, 1870-1882.

Shivaram, U., Donath, J., Khan, F.A., & Juliano, J. (1987). Effects of continuous positive pressure airway pressure in acute asthma. *Respiration,* **52**, 157-162.

Smaldone, G.C., Berg, E., & Nikander, K. (2005). Variation in pediatric aerosol delivery: Importance of facemask. *Journal of Aerosol Medicine-Deposition Clearance And Effects In The Lung,* **18**, 354-363.

Son, Y.-J., Longest, P.W., & Hindle, M. (2013a). Aerosolization characteristics of dry powder inhaler formulations for the excipient enhanced growth (EEG) application: Effect of spray drying process conditions on aerosol performance. *International Journal of Pharmaceutics,* **443**, 137-145.

Son, Y.-J., Longest, P.W., Tian, G., & Hindle, M. (2013b). Evaluation and modification of commercial dry powder inhalers for the aerosolization of submicrometer excipient enhanced growth (EEG) formulation. *European Journal of Pharmaceutical Sciences,* **49**, 390-399.

Soong, T.T., Nikolaides, P., Yu, C.P., & Soong, S.C. (1979). A statistical description of the human tracheobronchial tree geometry. *Respiratory Physiology,* **37**, 161-172.

Stahlhofen, W., Rudolf, G., & James, A.C. (1989). Intercomparison of experimental regional aerosol deposition data. *Journal of Aerosol Medicine,* **2**, 285-308.

Stapleton, K.W., Guentsch, E., Hoskinson, M.K., & Finlay, W.H. (2000). On the suitability of k-epsilon turbulence modeling for aerosol deposition in the mouth and throat: A comparison with experiment. *Journal of Aerosol Science,* **31**, 739-749.

Stein, S.W., & Myrdal, P.B. (2006). The relative influence of atomization and evaporation on metered dose inhaler drug delivery efficiency. *Aerosol Science and Technology,* **40**, 335-347.

Storey-Bishoff, J., Noga, M., & Finlay, W.H. (2008). Deposition of micrometer-sized aerosol particles in infant nasal airway replicas. *Aerosol Science,* **39**, 1055-1065.

Sullivan, C., Berthon-Jones, M., Issa, F., & Eves, L. (1981). Reversal of obstructive sleep apnoea by continuous positive airway pressure applied through the nares. *The Lancet,* **317**, 862-865.

Swift, D.L. (1991). Inspiratory inertial deposition of aerosols in human nasal airway replicate casts: implication for the proposed NCRP lung model. *Radiation Protection Dosimetry,* **38**, 29-34.

Swift, D.L., & Strong, J.C. (1996). Nasal deposition of ultrafine 218Po aerosols in human subjects. *J. Aerosol Science,* **27**, 1125-1132.

Tang, P., Chan, H.K., Rajbhandari, D., & Phipps, P. (2011). Method to introduce mannitol powder to intubated patients to improve sputum clearance. *Journal of Aerosol Medicine and Pulmonary Drug Delivery,* **24**, 1-9.

Tarsin, W.Y., Pearson, S.B., Assi, K.H., & Chrystyn, H. (2006). Emitted dose estimates from Seretide (R) Diskus (R) and Symbicort (R) Turbuhaler (R) following inhalation by severe asthmatics. *International Journal Of Pharmaceutics,* **316**, 131-137.

Taylor, D.J., Doorly, D.J., & Schroter, R.C. (2010). Inflow boundary profile prescription for numerical simulation of nasal airflow. *Journal of the Royal Society Interface,* **7**, 515-527.

Tian, G., Longest, P.W., Su, G., & Hindle, M. (2011a). Characterization of respiratory drug delivery with enhanced condensational growth (ECG) using an individual path model of the entire tracheobronchial airways. *Annals of Biomedical Engineering,* **39**, 1136-1153.

Tian, G., Longest, P.W., Su, G., Walenga, R.L., & Hindle, M. (2011b). Development of a stochastic individual path (SIP) model for predicting the tracheobronchial deposition of pharmaceutical aerosols: Effects of transient inhalation and sampling the airways. *Journal of Aerosol Science,* **42**, 781-799.

Tian, G., Longest, P.W., Li, X., & Hindle, M. (2013). Targeting aerosol deposition to and within the lung airways using excipient enhanced growth. *Journal of Aerosol Medicine and Pulmonary Drug Delivery,* **26**, 248-265.

Tian, G., Hindle, M., & Longest, P.W. (2014). Targeted lung delivery of nasally administered aerosols. *Aerosol Science and Technology,* **48**, 434-449.

Trudo, F.J., Gefter, W.B., Welch, K.C., Gupta, K.B., Maislin, G., & Schwab, R.J. (1998). State-related changes in upper airway caliber and surrounding soft-tissue structures in normal subjects. *American Journal of Respiratory and Critical Care Medicine,* **158**, 1259-1270.

Vaisanen, I.T., & Rasanen, J. (1987). Continuous positive airway pressure and supplemental oxygen in the treatment of cargiogenic pulmonary edema. *CHEST Journal,* **92**, 481-485.

Van Holsbeke, C.S., Stijn, L.V., Wim, G.V., De Backer, J.W., Vinchurkar, S.C., Verdonck, P.R., van Doorn, J.W.D., Nadjmi, N., & De Backer, W.A. (2013). Change in upper airway geometry between upright and supine position during tidal nasal breathing. *Journal of Aerosol Medicine and Pulmonary Drug Delivery,* **26**, 1-7.

Vinchurkar, S., & Longest, P.W. (2008). Evaluation of hexahedral, prismatic and hybrid mesh styles for simulating respiratory aerosol dynamics. *Computers and Fluids,* **37**, 317-331.

Vinchurkar, S., De Backer, L., Vos, W.G., Van Holsbeke, C., De Backer, J., & De Backer, W. (2012). A case series on lung deposition analysis of inhaled medication using functional imaging based computational fluid dynamics in asthmatic patients: effect of upper airway morphology and comparision with in vivo data. *Inhalation Toxicology,* **24**, 81-88.

Walenga, R.L., Tian, G., & Longest, P.W. (2013). Development of characteristic upper tracheobronchial airway models for testing pharmaceutical aerosol delivery. *ASME Journal of Biomechanical Engineering,* **135**, 091010.

Walenga, R.L., Tian, G., Hindle, M., Yelverton, J., Dodson, K., & Longest, P.W. (2014). Variability in nose-to-lung aerosol delivery. *Journal of Aerosol Science,* **78**, 11-29.

Walters, D.K., & Luke, W.H. (2011). Computational fluid dynamics simulations of particle deposition in large-scale multigenerational lung models. *Journal Of Biomechanical Engineering,* **133**, 011003.

Wang, Y., & James, P.W. (1999). On the effect of anisotropy on the turbulent dispersion and deposition of small particles. *International Journal of Multiphase Flow,* **22**, 551-558.

Wang, Z.L., Grgic, B., & Finlay, W.H. (2006). A dry poweder inhaler with reduced mouth-throat deposition. *Journal of Aerosol Medicine,* **19**, 168-174.

Weibel, E.R. (1963). *Morphometry of the Human Lung*. Springer Verlag, Berlin.

White, C.C., Crotwell, D.N., Shen, S., Salyer, J., Yung, D., & DiBlasi, R.M. (2013). Bronchodilator delivery during simulated pediatric noninvasive ventilation. *Respiratory Care,* **58**, 1459-1466.

Wildhaber, J.H., Dore, N.D., Wilson, J.M., Deavadason, S.G., & LeSouef, P.N. (1999). Inhalation therapy in asthma: nebulizer or pressurized metered-dose inhaler with holding chamber? In vivo comparison of lung depositon in children. *J. Pediatr,* **135**, 28-33.

Xi, J., & Longest, P.W. (2007). Transport and deposition of micro-aerosols in realistic and simplified models of the oral airway. *Annals of Biomedical Engineering,* **35**, 560-581.

Xi, J., & Longest, P.W. (2008a). Evaluation of a novel drift flux model for simulating submicrometer aerosol dynamics in human upper tracheobronchial airways. *Annals of Biomedical Engineering,* **36**, 1714-1734.

Xi, J., & Longest, P.W. (2008b). Numerical predictions of submicrometer aerosol deposition in the nasal cavity using a novel drift flux approach. *International Journal Of Heat And Mass Transfer,* **51**, 5562-5577.

Xi, J., Longest, P.W., & Martonen, T.B. (2008). Effects of the laryngeal jet on nano- and microparticle transport and deposition in an approximate model of the upper tracheobronchial airways. *Journal of Applied Physiology,* **104**, 1761-1777.

Xi, J., Si, X.H., Kim, J.W., & Berlinski, A. (2011). Simulation of airflow and aerosol deposition in the nasal cavity of a 5-year-old child. *Journal Of Aerosol Science,* **42**, 156-173.

Xi, J., Berlinski, A., Zhou, Y., Greenberg, B., & Ou, X.W. (2012). Breathing Resistance and Ultrafine Particle Deposition in Nasal-Laryngeal Airways of a Newborn, an Infant, a Child, and an Adult. *Annals Of Biomedical Engineering,* **40**, 2579-2595.

Yang, X.L., Liu, Y., & Luo, H.Y. (2006). Respiratory flow in obstructed airways. *Journal of Biomechanics,* **39**, 2743-2751.

Yeh, H.C., & Schum, G.M. (1980). Models of human lung airways and their application to inhaled particle deposition. *Bull. Math. Biology,* **42**, 461–480.

Yin, Y., Choi, J., Hoffman, E.A., Tawhai, M.H., & Lin, C.-L. (2010). Simulation of pulmonary air flow with a subject-specific boundary condition. *Journal of Biomechanics,* **43**, 2159-2163.

Yokley, T.R. (2006). *The functional and adaptive significance of anatomical variation in recent and fossil human nasal passages.* Unpublished Doctoral Dissertation, Duke University, Durham, NC.

Zhang, H., & Papadakis, G. (2010). Computational analysis of flow structure and particle deposition in a single asthmatic human airway bifurcation. *Journal of Biomechanics,* **43**, 2453-2459.

Zhang, Y., Finlay, W.H., & Matida, E.A. (2004). Particle deposition measurements and numerical simulations in a highly idealized mouth-throat. *Journal of Aerosol Science,* **35**, 789-803.

Zhang, Y., & Finlay, W.H. (2005). Measurement of the effect of cartilaginous rings on particle deposition in a proximal lung bifurcation model. *Aerosol Science and Technology,* **39**, 394-399.

Zhang, Y., Gilbertson, K., & Finlay, W.H. (2007). In vivo-in vitro comparison of deposition in three mouth-throat models with Qvar and Turbuhaler inhalers. *Journal of Aerosol Medicine,* **20**, 227-235.

Zhang, Z., Kleinstreuer, C., & Kim, C.S. (2002). Cyclic micron-size particle inhalation and deposition in a triple bifurcation lung airway model. *Journal of Aerosol Science,* **33**, 257-281.

Zhang, Z., Kleinstreuer, C., Donohue, J.F., & Kim, C.S. (2005). Comparison of micro- and nano-size particle depositions in a human upper airway model. *Journal of Aerosol Science,* **36**, 211-233.

Zhang, Z., Kleinstreuer, C., & Kim, C.S. (2009). Comparison of analytical and CFD models with regard to micron particle deposition in a human 16-generation tracheobronchial airway model. *Aerosol Science,* **40**, 16-28.

Zhang, Z., & Kleinstreuer, C. (2011). Computational analysis of airflow and nanoparticle deposition in a combined nasal-oral-tracheobronchial airway model. *Journal of Aerosol Science,* **42**, 174-194.

Zhou, Y., & Cheng, Y.S. (2005). Particle deposition in a cast of human tracheobrochial airways. *Aerosol Science and Technology,* **39**, 492-500.

Zhou, Y., Sun, J., & Cheng, Y.S. (2011). Comparison of deposition in the USP and physical mouth-throat models with solid and liquid particles. *Journal of Aerosol Medicine and Pulmonary Drug Delivery,* **24**, 277-284.

Zhu, J.H., Lee, H.P., Lim, K.M., Lee, S.J., & Wang, D.Y. (2011). Evaluation and comparison of nasal airway flow patterns among three subjects from Caucasian, Chinese and Indian ethnic groups using computational fluid dynamics simulation. *Respiratory physiology & neurobiology,* **175**, 62-69.

Appendix A

The user-defined functions (UDFs) used for this dissertation are listed and described in this appendix. All UDFs are developed in Microsoft Visual Studio 2005 and 2008 (Microsoft, Redmond, WA, USA) using the C programming language. They are all intended for use with ANSYS FLUENT 12.0.16 and 14.5 (ANSYS, Inc., Canonsburg, PA, USA). The routines were developed by Dr. P. Worth Longest, Dr. Geng Tian, and the author. The original developer is listed in parentheses next to each file name, while the developer for each updated version is indicated in its description with initials (PWL, GT, RLW). Only UDFs with multiple versions applied for this dissertation include separate version information, and only the versions used are included. The description for each UDF also includes the number of user-defined memory (UDM) locations and discrete phase scalars (DPS), if required by that UDF. Similar functions are grouped together.

nw_flag_2.1.c

Original developer: Dr. P. Worth Longest

Chapter(s): 3,4,5,6,7

Near-wall fluid velocity and turbulence corrections as defined by nw_cd_2.*.c and nw_turb_2.*.c use values determined by this UDF, which is run after initialization of the simulation and prior to resolving the flow field. This code calculates the distance from the center of each cell in the mesh domain to the nearest wall face centroid, and identifies the zone and face ID numbers of the nearest wall face. Additionally, all wall faces are "flagged" with a value of one for coordination with nw_cd_2.*.c and nw_turb_2.*.c. This code requires 12 UDM locations to be allocated prior to operation, is suitable for serial processing, and is run with the Execute on Demand option. The zone_ID variable definition must be edited for each code to include all wall zones.

face_centroids_1.3_<zone name>.c

near_wall_dist_1.4.c

cell_num_1.1.c

Original developer: Ross L. Walenga

Chapter(s): 7,8

These three UDFs replace nw_flag_2.1.c to provide compatibility with parallel processing, and are run prior to use with nw_cd_3.*.c and nw_turb_3.*.c. All three files are run in sequence using the Execute on Demand option after solution initialization and prior to resolving the flow field. First, a text file with the face centroid coordinates of all wall faces is produced using face_centroids_1.3_<zone name>.c, where a separate file is created for each zone and named accordingly. Then, the face centroids are read into dynamically allocated memory using near_wall_dist_1.4.c, and calculations are performed to find the distance from the center of each cell in the mesh domain to the nearest wall face centroid, and also the zone number and face ID number of the nearest wall face. Finally, the cell numbers of each wall adjacent cell are updated from a parallel numbering system to a serial numbering system using cell_num_1.1.c, to allow for particle trajectory calculations using the shared memory option. These UDFs require 20 UDM locations to be allocated prior to operation, and are suitable for serial or parallel processing. The WALL_ID identifier must be updated for face_centroids_1.3.c and the <zone name>_ID identifiers must be updated for near_wall_dist_1.4.c. The total number of wall faces must be assigned to NUM_FACES for near_wall_dist_1.4.c, and the summation of partition (P) cells up to P-1 are assigned to NODE_<P> for cell_num_1.1.c.

nw_cd_*.*.c

Original developer: Dr. P. Worth Longest

Chapter(s): 3,4,5,6,7,8

This code applies a near-wall fluid velocity correction for all Lagrangian particle trajectory calculations using linear interpolation. It is run in conjunction with nw_flag_2.1.c for nw_cd_2.*.c versions, and with face_centroids_1.3_<zone_name>.c, near_wall_dist_1.4.c, and cell_num_1.1.c for nw_cd_3.*.c versions. Also, it is run with nw_turb_*.*.c and when applicable, custom_evap_law_*.*.c, and that combination of UDFs requires the allocation of 10 DPS locations for versions 2.1 and 2.1c, and between 14 and 20 for version 3.1, depending on the version of custom_evap_law_*.*.c used (if implemented). It is activated in the Drag Law field of the Discrete Phase Model definition in ANSYS FLUENT. The nw_limit variable must be defined prior to use, which has multiple definitions for versions 2.1c and 3.1. Also, for versions 2.1c and 3.1, the zone_ID variable must be updated to reflect the correct zone that each nw_limit is to be applied to.

Version	Improvements	Chapter(s)	Developer
2.1	Original inherited version	3,5	PWL
2.1c	Mesh independent application	4,6,7	RLW
	Variable nw_limit may change by zone		
3.1	Compatible with parallel processing	7,8	RLW

nw_turb_*.*.c

Original developer: Dr. P. Worth Longest

Chapter(s): 3,4,5,6,7,8

This function applies a near-wall fluid turbulence correction for all Lagrangian particle trajectory calculations using linear interpolation. It is run in conjunction with nw_flag_2.1.c for nw_turb_2.*.c versions, and with face_centroids_1.3_<zone_name>.c, near_wall_dist_1.4.c, and cell_num_1.1.c for nw_turb_3.*.c versions. Also, it is run with nw_cd_*.*.c and when applicable, custom_evap_law_*.*.c, and that combination of UDFs requires the allocation of 10 DPS locations for versions 2.4, 2.4c, and 2.5, and between 14 and 20 for versions 3.3 and 3.4, depending on the version of custom_evap_law_*.*c used (if implemented). It is activated in the UDF Scalar Update field of the Discrete Phase Model definition in ANSYS FLUENT. Reduced near-wall particle velocities are only applied for locations within y_p_limit, which must be updated. The nw_limit variable must be defined prior to use for versions 2.4c, 2.5, 3.3, and 3.4. Also, for versions 2.4c, 2.5, 3.3, and 3.4, the zone_ID variable must be updated to reflect the correct zone that each nw_limit is to be applied to.

Version	Improvements	Chapter(s)	Developer
2.4	Original inherited version	3,5	PWL
2.4c	Mesh independent application Includes nw_limit definition	4,6,7	RLW
2.5	Implements particle tracking for serial processing	6	RLW
3.3	Compatible with parallel processing	7,8	RLW
3.4	Implements particle tracking for parallel processing	8	RLW

custom_evap_law_*.*.c

Original developer: Dr. P. Worth Longest

Chapter(s): 5,6,7,8

Condensational evaporation and growth are modeled using this UDF for all Lagrangian particle trajectory calculations. It is run in conjunction with nw_flag_2.1.c for nw_cd_2.*.c and nw_turb_2.*.c versions, and with face_centroids_1.3_<zone_name>.c, near_wall_dist_1.4.c, and cell_num_1.1.c for nw_cd_3.*.c and nw_turb_3.*.c versions. The combination of custom_evap_law_*.*.c, nw_cd_*.*.c and nw_turb_*.*.c requires the allocation of between 10 and 14 DPS locations when paired with nw_flag.c, and between 14 and 20 when paired with face_centroids_1.3_<zone_name>.c, near_wall_dist_1.4.c, and cell_num_1.1.c. Each component adds two DPS locations so a two component code has either 12 or 16 DPS locations for serial or parallel processing, for example. The application of particle trajectory tracking through nw_turb_3.4.c requires an additional 2 DPS locations. It is activated in the Custom Law field of the Set Injection Properties definition in ANSYS FLUENT. Values of density, molecular weight, and van 't Hoff factor must be entered for each component of the particle combination, which includes the drug as the first component. Also, the mass fraction is entered for each component of the combination.

Version	Improvements	Chapter(s)	Developer
1.7c	Avoids rapid evaporation with single component	7,8	PWL
2.5	Adapted for two components	5,6,7	PWL
3.1C	Adapted for three components	8	GT

DPM_source_1.3s.c

Original developer: Dr. P. Worth Longest

Chapter(s): 5

This UDF is used for two-way coupled particle trajectory predictions and calculates heat and mass sources for condensing and evaporating particles. It is run with nw_cd_*.*.c, nw_turb_*.*.c, and custom_evap_law_*.*.c, and it is activated in the UDF Source field of the Discrete Phase Model definition in ANSYS FLUENT. It is hooked while the steady state flow field calculation is performed, then un-hooked for the particle trajectory calculations after the flow field solution is reached.

WaveformInlet_<inhalation flow field name>.c

WaveformInlet_Massflux_<inhalation flow field name>.c

Original developer: Dr. P. Worth Longest

Chapter(s): 4,7

The velocity inlet profiles for transient flow field simulations are defined with these UDFs. They are given unique names for the type of flow field (e.g. 'QD', 'SD', etc.). The WaveformInlet_<inhalation_flow_name>.c function defines the profile as a blunt velocity field, while the WaveformInlet_MassFlux_<inhalation_flow_name>.c defines it as a blunt mass flux field (used for the MDI simulations). For WaveformInlet_<inhalation_flow_name>.c, it is activated in the Velocity Magnitude field of the Velocity Inlet boundary condition definition in ANSYS FLUENT, while for WaveformInlet_MassFlux_<inhalation_flow_name>.c, it is activated in the Mass Flux field of the Mass-Flow Inlet boundary condition.

Outlet_flow_interpolation_<lobar branch>.c

Outlet_particle_update.c

Profile_inlet_ss_<lobar branch>.c

Original developer: Dr. Geng Tian

Chapter(s): 4

These routines are used to apply flow field and particle interpolation from one adjoining mesh to another when the two meshes are simulated separately. The Outlet_flow_interpolation_<lobar branch>.c function is used to interpolate outlet flow at each time step from the transient upper airway tracheobronchial (TB) model at the lobar branch outlets, where five UDFs are required to represent the five branches. This code is applied in the Execute at End field of the Function Hooks option. The zone_ID variable must be updated for each branch UDF. Outlet particle interpolation from the TB model is performed by Outlet_particle_update.c, which produces a .dat file that accumulates all particles that pass through each lobar outlet over the course of the transient simulation. It is set through the Discrete Phase BC function field in the Pressure Outlet or Outflow boundary condition windows. Steady state stochastic individual path (SIP) models use Profile_inlet_ss_<lobar branch>.c to define the inlet velocity profile in the Velocity Magnitude field.

RH_1.2.c

VD_1.2s_mp_try1.c

Original developer: Dr. P. Worth Longest

Chapter(s): 5,6

Relative humidity and other mass transfer related properties are calculated by these two UDFs and stored in UDM locations. The same UDM locations allocated by nw_flag_2.1.c are used for these calculations. The RH_1.2.c code was used in Chapter 5 while the VD_1.2s_mp_try1.c code was used in Chapter 6. They are activated in the Execute at End field of the Function Hooks option. The zone_ID variable must be updated to reflect all wall and velocity inlet boundary zone ID numbers.

particle_path_report_2.4.c

Original developer: Dr. P. Worth Longest

Chapter(s): 5

Particle trajectory tracking is enabled by this UDF, which is activated in the Scalar Update field of the Discrete Phase Model. It requires that near-wall fluid velocity and turbulence corrections be disabled. It is replaced by nw_turb_2.5.c for serial processing and nw_turb_3.4.c for parallel processing, which include the near-wall corrections to the trajectory calculations.

DEF_drugmass.c

Original developer: Dr. P. Worth Longest

Chapter(s): 3

This UDF calculates the deposition enhancement factor (DEF), which is a measure of localized deposition. It is activated by the Execute on Demand option after the flow field solution has been obtained. The zone_ID variable must be updated to reflect all wall boundary zone ID numbers.

Vita

ROSS WALENGA

3507 Wilmington Ave., Hopewell, VA, 23860

(804)-519-7075, ross.walenga@gmail.com

Education

- **Ph.D. Candidate in Engineering (Mechanical track)** (Fall, 2014)

  Virginia Commonwealth University (VCU), Richmond, VA, USA

- **Bachelor of Fine Arts in Painting & Printmaking and Art Education** (2007)

  Virginia Commonwealth University (VCU), Richmond, VA, USA

- **Bachelor of Science in Aerospace Engineering** (2000)

  Virginia Polytechnic Institute and State University, Blacksburg, VA, USA

Journal Articles

- Tian, G., Longest, P. W., Su, G., Walenga, R.L., Hindle, M. (2011). Development of a Stochastic Individual Path (SIP) Model for Predicting the Tracheobronchial Deposition of

Pharmaceutical Aerosols: Effects of Transient Inhalation and Sampling the Airways. Journal of Aerosol Science, 42, 781-799.

- Longest, P., Tian, G., Walenga, R.L., Hindle, M. (2012). Comparing MDI and DPI Aerosol Deposition Using In Vitro Experiments and a New Stochastic Individual Path (SIP) Model of the Conducting Airways. Pharmaceutical Research, 29, 1670-1688.

- Longest, P.W., Walenga, R.L., Son, Y.J., and Hindle, M. (2013). High-Efficiency Generation and Delivery of Aerosols Through Nasal Cannula During Noninvasive Ventilation. Journal of Aerosol Medicine and Pulmonary Drug Delivery, 26, 266-279.

- Golshahi, L., Tian, G., Azimi, M., Son, Y-J., Walenga, R.L., Longest, P.W., Hindle, M. (2013). The Use of Condensational Growth Methods for Efficient Drug Delivery to the Lungs during Noninvasive Ventilation High Flow Therapy. Pharmaceutical Research, 30, 2917-2930.

- Walenga, R.L., Tian, G., and Longest, P. W. (2013). Development of Characteristic Upper Tracheobronchial Airway Models for Testing Pharmaceutical Aerosol Delivery. ASME Journal of Biomechanical Engineering, 135, 091010.

- Walenga, R.L, Longest, P.W., Sundaresan, G. (2014). Creation of an *In Vitro* Biomechanical Model of the Trachea using Rapid Prototyping. Journal of Biomechanics, 47, 1861-1868.

- Golshahi, L., Walenga, R.L, Longest, P.W., Hindle, M. (2014). Development of a Transient Flow Aerosol Mixer-Heater System for Lung Delivery of Nasally-Administered Aerosols using a Nasal Cannula. Aerosol Science & Technology, 48, 1009-1021.

- Walenga, R.L., Hindle M., Tian, G., Longest, P.W. (2014). Variability in Nose-to-Lung Aerosol Delivery. Journal of Aerosol Science, 78, 11-29.

Conference Abstracts

- Walenga, R., Longest, P.W., Son, Y., Hindle, M. (2013). Generation and Effective Delivery of Submicrometer Aerosols through High Flow Nasal Cannula During Noninvasive Ventilation. ISAM Annual meeting (April 6-10), Chapel Hill, NC. (Poster and peer-reviewed abstract)

- Walenga, R.L., Tian, G., Hindle, M., Longest, P.W. (2014). Variability of Lung Targeted Aerosol Delivery during High Flow Nasal Cannula Therapy. AAAR Annual meeting (October 20-24), Orlando, FL. (Presentation and peer-reviewed abstract)